DISSERTATION

submitted to the

COMBINED FACULTY OF NATURAL SCIENCES AND MATHEMATICS

of the

RUPERTO-CAROLA-UNIVERSITY OF HEIDELBERG, GERMANY

for the degree of

DOCTOR OF NATURAL SCIENCES

Put forward by

Michael HANKE

born in Balingen, Germany

Oral examination: July 17th, 2020

PROBING THE EARLY MILKY WAY WITH STELLAR SPECTROSCOPY

Supervisor:

Prof. Dr. Eva K. GREBEL

Co-supervisors:

Dr. Camilla J. HANSEN

Priv.-Doz. Dr. Andreas KOCH

Referees:

Prof. Dr. Eva K. GREBEL

Prof. Dr. Norbert CHRISTLIEB

Co-examiners:

Prof. Dr. Björn Malte SCHÄFER

Prof. Dr. Mario TRIELOFF

Abstract

Probing the early Milky Way with stellar spectroscopy

Stars preserve the fossil records of the kinematical and chemical evolution of individual building blocks of the Milky Way. In its efforts to excavate this information, the astronomical community has recently seen the advent of massive astrometric and spectroscopic observing campaigns that are dedicated to gather extensive data for millions of stars. The exploration of these vast datasets is at the heart of the present thesis. First, I introduce `ATHOS`, a data-driven tool that employs spectral flux ratios for the determination of the fundamental stellar parameters effective temperature, surface gravity, and metallicity, upon which all higher-order parameters like detailed chemical abundances critically rely. `ATHOS`' robustness and widespread applicability is not only showcased in a comparison to large-scale spectroscopic surveys and their dedicated pipelines, but it is also demonstrated to be able to compete with highly specialized parameterization methods that are tailored to high-quality data in the realm of studies with low target numbers. An in-depth study of the latter kind is outlined in the second part of this thesis, where I present a chemical abundance investigation of the metal-poor Galactic halo star HD 20. Using spectra and photometric time series of utmost quality in combination with modern asteroseismic and spectroscopic analysis techniques, I deduce a comprehensive, highly accurate, and precise chemical pattern that proves HD 20 worthy of being added to the short list of metal-poor benchmark stars, both for nuclear astrophysics and in terms of stellar parameters. The decomposition of the chemical pattern shows an imprint from *s*-process nucleosynthesis on top of the already in itself rarely encountered enhancement of *r*-process elements. In the absence of a companion that could act as polluter, this poses a striking finding that points towards fast and efficient mixing in the early interstellar medium prior to HD 20's formation. In the third and last part, spectroscopic data from the SDSS/SEGUE surveys are combined with astrometry from the *Gaia* mission to form a sample of several hundred thousand chemodynamically characterized halo stars that is scrutinized to establish links between globular clusters and the general halo field star population. Based on the identified sample of probable cluster escapees that includes both first-generation and second-generation (former) cluster stars, I provide important observational constraints on the overall cluster contribution to the buildup of the Galactic halo. A highly interesting – yet tentative – finding is that for those populations of stars that were lost early on, the first-generation fraction appears higher compared to groups that are currently being stripped or still bound to clusters. This observation could indicate either a dominant contribution from since dissolved low-mass clusters or that early cluster mass loss preferentially affected first-generation stars.

Zusammenfassung

Die Erforschung der frühen Milchstraße mittels stellarer Spektroskopie

Sterne konservieren die fossilen Zeugnisse der kinematischen und chemischen Entwicklung einzelner Grundbausteine der Milchstraße. Im Bestreben diese Informationen auszugraben fand in der Astronomie jüngst ein Aufbruch im Hinblick auf großskalige astrometrische und spektroskopische Kampagnen statt. Diese haben zum Ziel umfangreiche Datensätze über Millionen von Sternen zu erlangen. Die Untersuchung jener Datensätze stellt das Herzstück der vorgelegten Dissertation dar. Zunächst präsentiere ich `ATHOS`, ein datengesteuertes Werkzeug, welches spektrale Flussverhältnisse einsetzt, um die grundlegenden stellaren Parameter Effektivtemperatur, Oberflächengravitation und Metallizität zu bestimmen. Auf diese sind alle höhergelagerten Parameter wie zum Beispiel detaillierte chemische Häufigkeiten kritisch angewiesen. Die Robustheit von `ATHOS` und seine weitgestreuten Einsatzmöglichkeiten werden nicht nur im Rahmen von großangelegten spektroskopischen Durchmusterungen und deren Pipelines vorgeführt, sondern es wird auch demonstriert, dass `ATHOS` es mit hochspezialisierten Parameterbestimmungsmethoden, die auf die Anwendung in Studien mit kleiner Anzahl von Zielen und hoher Datenqualität zugeschnttten sind, aufnehmen kann. Eine solch detaillierte Studie wird im zweiten Teil dieser Arbeit dargelegt, indem ich eine chemische Häufigkeitsuntersuchung des metallarmen Halosterns HD 20 präsentiere. Unter Benutzung von Spektren und zeitaufgelöster Photometrie von höchster Qualität in Kombination mit modernen astroseismologischen und spektroskopischen Analysetechniken bestimme ich ein umfassendes, hoch akkurates und präzises chemisches Häufigkeitsmuster, welches HD 20 als würdig auszeichnet, der kurzen Liste von metallarmen Referenzsternen – sowohl im Hinblick auf nukleare Astrophysik als auch mit Blick auf stellare Parameter – hinzugefügt zu werden. Die Zerlegung des chemischen Häufigkeitsmusters zeigt eine Einprägung von *s*-Prozess-Nukleosynthese über einer bereits alleine selten auftretenden Anreicherung von *r*-Prozess-Elementen. Aufgrund der Abwesenheit eines Begleiters, der als Verschmutzer dienen könnte, stellt dies eine bedeutende Erkenntnis dar, welche in Richtung einer schnellen und effizienten Durchmischung des frühen interstellaren Mediums noch vor der Formierung von HD 20 zeigt. Im dritten und letzten Teil der Arbeit werden spektroskopische Daten der SDSS/SEGUE Durchmusterungen mit Astrometrie der *Gaia*-Mission kombiniert um eine Sammlung von mehreren hunderttausend chemodynamisch charakterisierter Sterne zu formieren. Diese wird verwendet um Verbindungen zwischen Kugelsternhaufen und der generellen Feldsternpopulation des Halos zu etablieren. Basierend auf der Kollektion von wahrscheinlichen Haufenausbrechern, welche sowohl Sterne erster als auch zweiter Generation enthält, stelle ich wichtige beobachtungsgestütze Erkenntnisse für den Beitrag von Haufen zur Bildung des Galaktischen Halos zur Verfügung. Eine sehr interessante – jedoch schwach hinterlegte – Erkenntnis ist, dass in der Population von früh verloren gegangenen Sternen der Anteil von Sternen der ersten Generation größer zu sein scheint im Vergleich zu solchen Gruppen, die dem Haufen derzeit entrissen werden oder immer noch gebunden sind. Diese Beobachtung könnte entweder auf einen dominanten Beitrag seither aufgelöster Haufen mit niedriger Masse hinweisen, oder sie könnte anzeigen, dass der frühe Massenverlust bevorzugt Sterne der ersten Generation betraf.

"Another star has fallen without sound
Another spark has burned out in the cold
Another door to barrens standing open
And who is there to tell me not to give in, not to go?

How could I know? How could I know?
That I'll get lost in space to roam forever"

Lost in Space, AVANTASIA

Contents

IV Chemodynamical association of halo stars with Milky Way globular clusters 159

V Concluding remarks and Outlook 203

A Additional material for Chapter IV 209

List of Figures

List of Tables

Für meine Familie…

This figure shows the surroundings of Andromeda (M 31) and its southeastern neighbor M 33, which are two out of the three massive spiral galaxies in the Local Group. The illustration is a false-color image obtained via the matched-filter technique using density maps and colors for individual stars from the Pan-Andromeda Archaeological Survey (PAndAS). This way, the three *rgb* channels correspond to dominant contributions from stellar populations with metallicites that are indicated on the *upper left*. The extended streams reveal a snapshot of ongoing accretion events onto M 31. Similar events have been proposed to have had considerable contributions to the buildup of the Milky Way – the other massive spiral in the Local Group – throughout its history. **Image credit.** Figure 2 in Martin et al. (2013). Reproduced by permission of the author and the AAS.

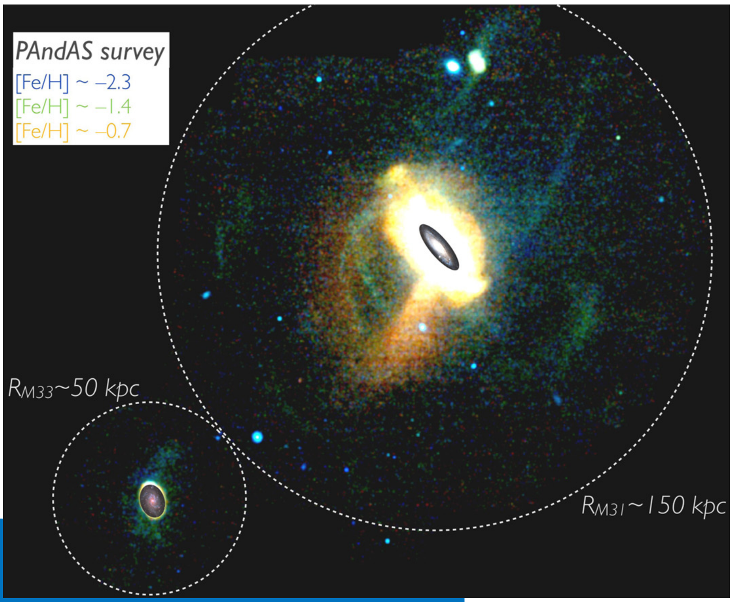

CHAPTER I

Introduction

This chapter in brief

In this introduction, the basic theoretical framework and scientific background in the context of this dissertation are set out. It starts off with a summary of the astrophysical subfield of Galactic archaeology, including a brief overlook of observational methods that are in use. The summary is followed by a more detailed description of the Milky Way and its major components together with a concise outline of their currently favored formation scenarios. The subsequent chapter deals with the various channels of nucleosynthesis throughout cosmic time, before eventually the theoretical foundations and applications of contemporary stellar spectroscopy are elaborated on with a special focus on chemical abundances.

1 Galactic Archaeology – a chemodynamical perspective

A major cornerstone in the field of contemporary astrophysics is striving to understand the buildup and evolution of stellar systems across time. In this respect, a sound comprehension of the large-scale cosmic structure formation is already in place, which involves a hierarchical formation through mergers of smaller galaxies to ever larger stellar systems in a universe that is governed by dark energy and cold dark matter (the so-called ΛCDM model; e.g., Dekel & Silk 1986; Bullock & Johnston 2005). Yet, on the level of individual, presently observable galaxies, there is a wealth of unanswered fundamental questions concerning the origin and development of various substructures. Among those questions is the role of the first stars, not only with respect to them being building blocks of primordial stellar systems but, in particular, to their contribution to the chemical evolution of the cosmos. With this in mind, a key part of the puzzle is the in-depth understanding of nucleosynthetic processes that led to the transformation of the chemical inventory of the Universe from purely consisting of H and He to exhibiting the wide variety of elements we see nowadays. Another mechanism that remains to be fully understood is the formation of stellar halos; the diffuse, old, and (to first order) spherical envelopes surrounding disk galaxies like our own home galaxy, the Milky Way. For instance, it is a long-standing question whether halos formed "in-situ" – that is, from gas attributable to the host galaxies – or are in fact the result of accretion from disrupted satellites such as dwarf galaxies or maybe even globular clusters (i.e., ex-situ formation channels; e.g., Searle & Zinn 1978).

Most of the above challenges can only be addressed by studying individual stars. Astronomers are thus inevitably limited to the Local Group and its constituents – the only place where it is and will be possible to resolve and characterize resolved stars in the foreseeable future. As a consequence, the subfield of astrophysics has sometimes been termed near-field cosmology to emphasize its impact on cosmology as a whole whilst being informed from a rather localized volume. More specifically, Galactic archaeology is the scientific field seeking to answer the raised questions for our own Galaxy (thus the capitalized "G" in Galactic). Much like traditional archaeologists, Galactic archaeologists infer the history of the Galaxy by "excavating" the fossil records that are preserved in the currently observable stellar populations and trace their whereabouts back in space and time. The main differences to classical archaeology are, of course, that the time scales involved commonly span many billion years as opposed to a few thousand years, and – against the strong beliefs of some individuals of a certain species inhabiting a rocky planet that orbits a G dwarf – that the Universe could exist (e.g., Dicke 1961; Carter 1974; Carr & Rees 1979) just fine in the absence of primates with upright stance and the ability to speak.

Thanks to their proximity, for a substantial fraction of Milky Way stars, there is a number of directly accessible observables with relevance to Galactic archaeology. On top of the most obvious one – the position of a star in the sky – important parameters are the distance and both the line-of-sight velocity and the proper motions running perpendicular to it. Together, these enable the full characterization of the stars' location in the six-dimensional phase space, which already in itself is a powerful means to attribute stars to a broader population sharing the same properties. Still, the dimensionality of the information space can be expanded almost indefinitely by adding quantities such as stellar age, mass, or a collection of photospheric chemical abundances. Owing to the circumstance that the Galaxy as we see it nowadays is a highly complex system of entangled subcomponents (see next section), such high-dimensional chemodynamical data are of prime importance to reveal the conserved memory of individual building blocks.

Observationally, the methods used to obtain the above parameters for Galactic archaeology can be broadly divided into three categories: Photometry, astrometry, and spectroscopy.

Photometry quantifies the amount of photons collected through imaging of a source in a given interval of time. Combined with a myriad of available systems of broadband (e.g., the optical Johnson-Cousins system; Johnson & Morgan 1953; Cousins 1976) and medium-/narrow-passband filters (e.g., Strömgren 1966), valuable information about fundamental stellar parameters for stellar astrophysics such as the effective temperature (T_{eff}, Alonso et al. 1999a,b), surface gravity ($\log g$), and sometimes even chemical abundances (e.g., Piotto et al. 2007) of large populations of stars can be obtained. Large-scale surveys like the Sloan Digital Sky Survey (SDSS, York et al. 2000), the Panoramic Survey Telescope And Rapid Response System (Pan-STARRS) imaging survey (Kaiser et al. 2010), or the upcoming Rubin Observatory Legacy Survey of Space and Time (LSST, Tyson 2002; Ivezić et al. 2019) have pioneered or will revolutionize the possibilities in this respect. The latter two campaigns shed light on an additional prospect of photometry when conducted repeatedly for the same patch of the sky over time – the so-called time-domain astronomy. For stellar astrophysics, short-cadence surveys such the National Aeronautics and Space Administration's (NASA) *Kepler* and K2 space missions (Borucki et al. 2010; Howell et al.

2014), as well as the Transiting Exoplanet Survey Satellite (TESS[1], Ricker et al. 2015) and the European Space Agency's (ESA) future PLAnetary Transits and Oscillation of stars (PLATO) mission (Rauer et al. 2014) bear the advantage of mapping miniscule periodic brightness variations that can be used to infer stellar ages, masses, and radii of unprecedented precision by virtue of asteroseismology.

Taking the idea of the time domain one step further, one can precisely track the position of stellar objects over time and infer both distances from trigonometric parallaxes and proper motions on the celestial sphere. While this field of astronomy – termed astrometry – has a history that reaches back to Hipparchus in the 2nd century BC and the year 1838 when Friedrich Bessel measured the first parallax of a star (61 Cyg) outside of the Solar System, large number statistics with meaningful precisions could not be achieved until the emergence of ESA's Hipparcos satellite (ESA 1997). More than two decades later, we have now entered a whole new era where high-precision astrometry is radically changing our views on Galactic astronomy, which is made possible by the *Gaia* space mission (Gaia Collaboration et al. 2016). Its latest Data Release 2 (DR2, Gaia Collaboration et al. 2018a) provides positions, parallaxes, and proper motions for approximately one billion stars (Lindegren et al. 2018). Moreover, for about 7 million targets it offers the full, 3D space-motion vector by adding radial velocities (Cropper et al. 2018). With future data releases, these numbers will increase even more and the dataset will additionally comprise, for instance, binary solutions and spectra for a subset of the targets.

Finally, in order to push the envelope of stellar astrophysics to its fullest potential, one can gather spectra of stars, which not only allows for radial velocity measurements but for the inference of ever more detailed information about the chemical composition encoded in them. Most science cases in Galactic archaeology that are investigated through spectroscopy, in order to be addressed in detail, require a substantial number of targets being observed. This may be the case either due to the occurrence rate of an observable being low (for example, as demonstrated by Christlieb et al. 2002, there are only few field stars revealing extremely low metallicities[2] or nitrogen enhancements; see Chapter IV), or because the effect under scrutiny is frequent but its expression is subtle in magnitude such that large number statistics are needed for robust sample estimates (e.g., when using chemical tagging to dissect chemodynamical substructures in the Galaxy). To meet these goals, multiplex capabilities of fiber-fed spectrographs are key. Here, the Radial Velocity Experiment (RAVE, Steinmetz et al. 2006), the Sloan Extension for Galactic Understanding and Exploration (SEGUE-1 and SEGUE-2, Yanny et al. 2009; Eisenstein et al. 2011), and

---

[1] Not to be confused with TE$_{\nu}$SS (Günther & Berardo 2020).

[2] Here, chemical abundances of "metals", that is, elements heavier than He.

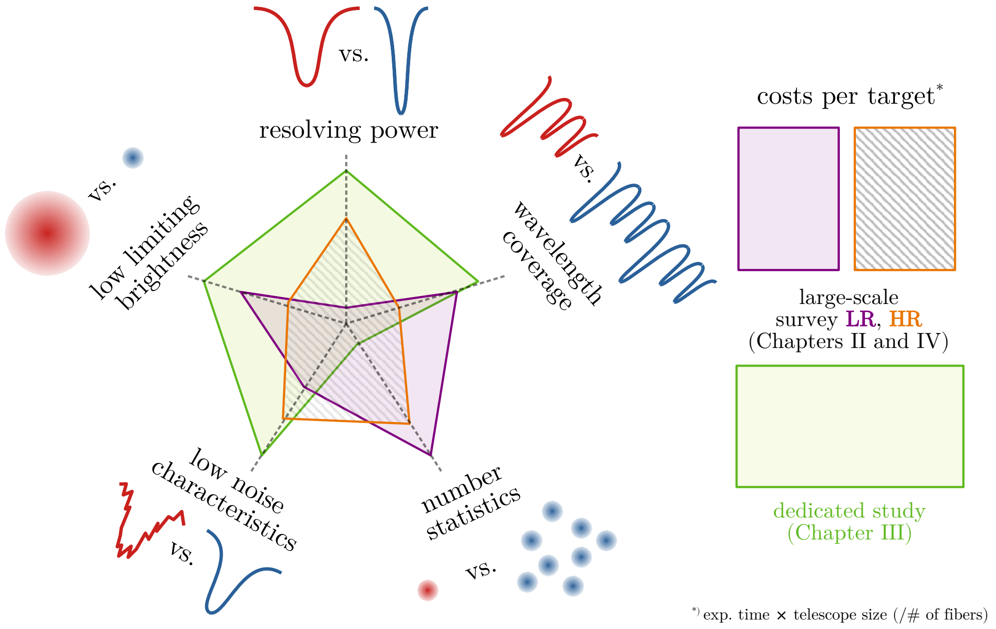

FIGURE I.1: Schematic representation of trade-offs made when designing spectroscopic observing programs. Shown are three exemplary realizations: the low-resolution (LR, purple) and high-resolution (HR, orange) channels of a generic large survey, and a dedicated study that is tailored to a specific science case (green; here, one could think of a study aiming for abundances of exotic neutron-capture elements or isotopic ratios measured in well-resolved features with hyperfine splitting). The costs per target are represented by the area spanned by the polygons. These are commonly lower for large surveys due to optimized observing strategies that minimize overheads and, more importantly, due to (mostly) using smaller telescopes.

the LAMOST spectroscopic survey (Luo et al. 2015) were ground-breaking at the low-resolution[3] end, whereas the *Gaia*-ESO spectroscopic survey (Gilmore et al. 2012), the Galactic Archaeology with HERMES (GALAH, De Silva et al. 2015) survey, or the Apache Point Observatory Galactic Evolution Experiment (APOGEE, Majewski et al. 2017) pioneered the mid- to high-resolution domains. Furthermore, large-scale future surveys like the ones conducted with WEAVE (Dalton et al. 2012) or the Galactic surveys (Helmi et al. 2019; Christlieb et al. 2019; Chiappini et al. 2019; Bensby et al. 2019) of the 4-meter Multi-Object Spectroscopic Telescope (4MOST, de Jong et al. 2012) will enter unprecedented terrain and obtain low- and medium-resolution spectra for several million targets to complement – among others – space missions like *Gaia* and PLATO.

---

[3] Throughout the literature, there is a certain degree of arbitrariness when it comes to pinpointing the definitions of low, medium, and high resolution (or resolving power, $R = \lambda/\mathrm{FWHM}$, where FWHM denotes the full width at half maximum, to use the more accurate term). A major factor undoubtedly is the field of research the term is used in. For example, when studying unresolved populations of galaxies with their intrinsically broad spectra (velocity dispersions $> 100\,\mathrm{km\,s^{-1}}$), an R of 20 000 is unquestionably (and unreasonably) “high”. The same does not necessarily hold true in the realm of resolved stars in the absence of significant rotation. In any case, claiming to be using “high-resolution” spectra is certainly always a good selling point (cf., Chapter III).

Despite the enormous efforts and manpower that is currently devoted to such spectroscopic surveys, it is important to bear in mind that a number of stellar science goals cannot be achieved in the scope of these programs. In the design of streamlined surveys, there are five main contradicting parameters that need to be balanced: spectral resolving power, wavelength coverage, number statistics, noise characteristics of the data, and survey depth by means of limiting magnitude at the faint end. This circumstance is schematically illustrated in Figure I.1. To some extent the gravity of having to make trade-off decisions is mitigated by the usage of spectrographs of two distinct resolving powers within one consortium. Nonetheless, science cases requiring at the same time large wavelength coverages, high resolutions, and little to no noise in the spectrum are notoriously hard to fulfill in the scope of big surveys. As a consequence, even in light of a seemingly shifting focus, dedicated smaller programs with a much higher degree of flexibility will still be strongly called for in the years to come.

1.1 This thesis

In my research, I have employed all of the observational techniques described above – be it performing asteroseismology with a single target or mining datasets obtained by large photometric, astrometric, and spectroscopic surveys – to investigate kinematic and chemical properties of stellar populations in the Milky Way both from a methodological and a scientific point of view. A specific emphasis is put on the development and application of spectroscopic techniques. In this thesis, I provide a detailed report of my three main projects that were published in the following peer-reviewed journal articles:

- **HANKE, M.**, HANSEN, C.J., KOCH, A., and GREBEL, E.K.
  "ATHOS: On-the-fly stellar parameter determination of FGK stars based on flux ratios from optical spectra"
  2018, Astronomy & Astrophysics, 619, A134
- **HANKE, M.**, HANSEN, C.J., LUDWIG, H.-G., CRISTALLO, S., MCWILLIAM, A., GREBEL, E.K., and PIERSANTI, L.
  "A high-precision abundance analysis of the nuclear benchmark star HD 20"
  2020a, Astronomy & Astrophysics, 635, A104
- **HANKE, M.**, KOCH, A., PRUDIL, Z., GREBEL, E.K., and BASTIAN, U.
  "Purveyors of fine halos. II. Chemodynamical association of halo stars with Milky Way globular clusters"
  2020b, Astronomy & Astrophysics, in press [arXiv:2004.00018]

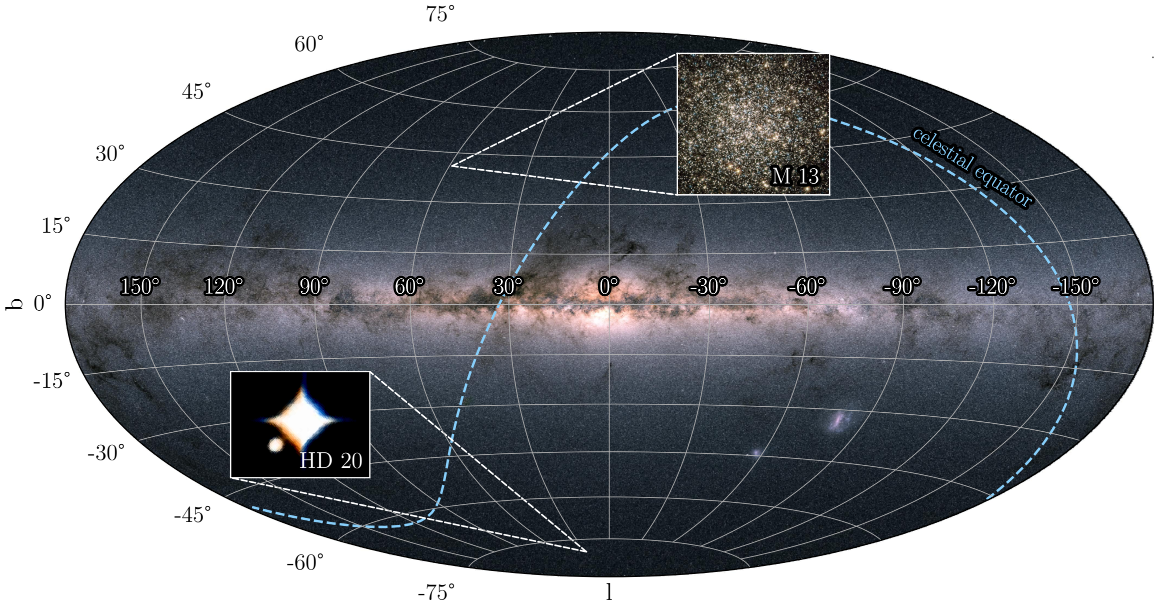

FIGURE I.2: All-sky view of the Milky Way in Galactic coordinates as seen by *Gaia*. This color image was created using the integrated flux – both from the blue and red *Gaia* channels – of $\approx 1.7 \cdot 10^9$ sources and therefore is not a real image of the sky but a reconstruction from photometry. The bright overdensity in the very center of the frame represents the Galactic bulge (Sect. 2.1), whereas the slightly less luminous bands to either side around $b \sim 0°$ mark the disk (Sect. 2.2). Elongated dark regions along the Galactic plane indicate dust lanes that are merely indirectly seen because they create voids in *Gaia*'s target density distribution due to drastically increased line-of-sight extinction. The two pronounced extended structures towards the lower right from the Galactic center are the Small and Large Magellanic Clouds. The fiducial blue-dashed line separates the northern from the southern celestial hemisphere. Two examples for the main science targets of this thesis are highlighted using inlay panels – that is, the halo giant star HD 20 (Chapter III) and the globular cluster M 13 as one representative of the objects studied in Chapter IV. **Image credits.** Milky Way all-sky map: *Gaia* Data Processing and Analysis Consortium (DPAC); A. Moitinho / A. F. Silva / M. Barros / C. Barata, University of Lisbon, Portugal; H. Savietto, Fork Research, Portugal; licensed under CC BY-SA 3.0 IGO. *M 13*: NASA, ESA, and the *Hubble* Heritage Team (STScI/AURA). *HD 20*: Digitized Sky Survey 2.

First, I will embed this thesis into a broader context by introducing the main scientific backgrounds and their underlying physical processes (this chapter). This introduction is then followed by a description of the newly developed, fundamentally new method for the determination of fundamental stellar parameters from optical spectra (Chapter II). The technique is a data-driven classifier that employs ratios of the fluxes contained in dedicated spectral windows that can be related to the main, fundamental stellar parameters, that is, effective temperature, surface gravity, and metallicity. The computational implementation of the method is called A Tool for HOmogenizing Stellar parameters (`ATHOS`). `ATHOS` is not only highly competitive and unprecedented in terms of demand for computational resources and speed, but also covers a wide range of stellar parameters. It successfully reaches its main objective, that is, bridging the gaps between spectroscopic surveys by being applicable in combination with most existing and future optical spectrographs. Hence, without being specifically tailored to individual specifications, `ATHOS` can provide a homogeneous parameter scale that enables cross-survey comparisons of stellar-parameter and – by extension – chemical-abundance scales.

As stressed in the previous section, there is commonly a trade-off between large number statistics achieved by surveys and the target-by-target detail that can be obtained through in-depth studies of smaller samples of stars. This usually implies that much more comprehensive information can be gained from a spectrum of the latter kind, which frequently leads to the application of different parameterization methods. This, in turn, opens Pandora's box in terms of biases between these studies and the less accurately parametrized survey targets[4]. In this respect, Chapter III is important as it shows that `ATHOS` can easily compete with the most sophisticated parameter scales. In the respective study, the metal-poor halo star HD 20 is studied in great detail using spectra of exquisite quality. Dedicated care is devoted to the stellar parameters and – thanks to the outstanding data quality – an almost complete chemical pattern is deduced. Thereby, HD 20 is added to the short list of benchmark stars (e.g., Jofré et al. 2014), both in terms of stellar parameters and for nuclear astrophysics. Connected to the latter point, the obtained detailed chemical abundances are used to disentangle the various nucleosynthetic sites that led to to the currently observed pattern in HD 20 – most notably the rarely observed enhancement of elements attributed to the rapid neutron-capture process that has been linked to scarce kinds of core-collapse supernovae and neutron star mergers (see Section 3.4).

The subsequent chapter moves away from the meticulous analysis of a single target to the other extreme in terms of number statistics. In Chapter IV, a long-standing question in Galactic archaeology is addressed: The contribution of stars stripped from globular clusters to the buildup of the Galactic halo. By exploiting the kinematic memory and chemical composition of a large sample of halo field stars, we mined the information contained in low-resolution SDSS spectra to establish links between the halo field and the presently observed population of clusters. An invaluable tracer in this regard are stars showing peculiar chemical imprints that are otherwise only found in globular clusters. By estimating the share these stars make up amongst all stars lost from clusters – that is, chemically normal and peculiar – an important missing piece in the modeling of cluster evolution is provided.

Finally, Chapter V summarizes the main findings of all three main topics, encompasses an outlook for studies that could be envisioned, and furthermore outlines

---

[4] Which cannot ever be overcome by enlarging the number statistics.

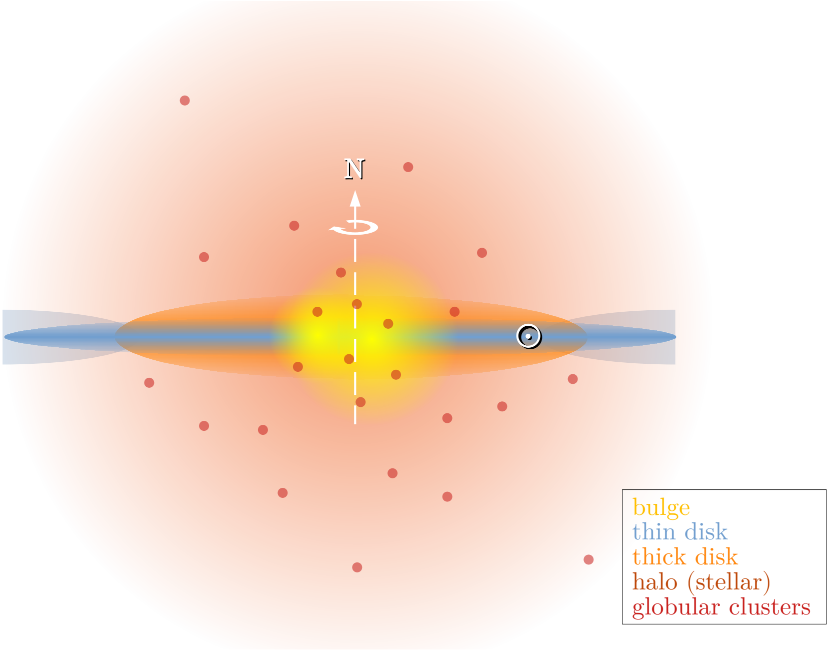

FIGURE I.3: Edge-on schematic illustration of the four main stellar components of the Milky Way (not to scale). The bulge is shown in yellow, the thin and thick subcomponents of the disk in blue and orange, respectively, and the stellar halo is represented by a diffuse brown spheroid. The rotation axis and sense of rotation of the plane is indicated by a white-dashed arrow pointing toward the Galactic north pole. The flaring of metal-poor disk stars with solar $[\alpha/\mathrm{Fe}]$[5] is indicated in light blue. Note that the bulge is displayed slightly asymmetric to mimic the projection effect of its barred shape (i.e., the right component is closer to the observer than the left). In addition, globular clusters are depicted by filled red circles. The position of the Sun about 8 kpc from the Galactic center is marked by its designated symbol, $\odot$.

projects that were inspired by this work and are already under way.

2 The Milky Way and its constituents

Naturally, by mere proximity, the easiest testbeds for performing stellar archaeology are the populations associated with the Milky Way. Here, I will briefly describe its four major stellar components from inside out. These are the Galactic bulge, the thin and thick disks, and the stellar halo, which are depicted in Figure I.3 as a schematic representation. As this thesis is revolved around stellar physics, this section mostly focuses on the (optically) luminous stellar components of the respective parts of the Galaxy. Therefore, it neglects other important building blocks of the Milky Way, such as the gas and dust phases as well as its most massive component – the dark matter.

---

[5] Throughout this thesis, the standard bracket notation for abundances $[X/Y] = (\log\epsilon(X) - \log\epsilon(Y)) - (\log\epsilon(X) - \log\epsilon(Y))_{\odot}$ is employed, where $\log\epsilon(X) = \log(n_X/n_H) + 12$ is the abundance of the chemical element X.

2.1 The Galactic bulge

The bulge constitutes the most luminous component of the Milky Way (cf., central regions of Figure I.2) and is located in its very center. Bulges in galaxies are commonly separated into pseudo-bulges that are dominated by cylindrical rotation of a bar and, on the other hand, spheroidal classical bulges with pressure support (e.g., Rich 2013; Barbuy et al. 2018). The Galactic bulge has been shown to have a barred structure with the portion at positive Galactic longitudes ($l > 0°$) being closer to the Sun (Stanek et al. 1994). Nonetheless, there were findings indicating that the bulge could indeed be a mixture of both a pseudo- and a classical bulge (Zoccali et al. 2008), although the latter component is small in number (Howard et al. 2008, 2009; Shen et al. 2010) and predates the dynamically formed pseudo-bulge (Kunder et al. 2016). From studies of red clump stars it became apparent that the bulge has a pronounced X-structure that when viewed from the Sun resembles a so-called boxy/peanut shape (McWilliam & Zoccali 2010; Wegg & Gerhard 2013).

Stars with locations that coincide with the bulge are predominantly old (i.e., $\gtrsim$ 10 Gyr) and span a metallicity -1.5 dex $<$ [Fe/H] $<$ $+0.5$ dex (e.g., Zoccali et al. 2003, 2008). From their chemodynamical studies (viz. radial velocities and [Fe/H]), Ness et al. (2012, 2013a,b) concluded that only stars at [Fe/H] > -0.5 dex are bona fide bulge stars and constitute the boxy/peanut shape, whereas the more metal-poor components are likely to be attributable to the thick disk and inner halo (Koch et al. 2016; see also next sections).

Solidifying the evidence for/against mixed pseudo- and classical bulge contributions as well as the investigation of the interface with other Galactic components are among the key science goals for the BRAVA(-RR) surveys (Kunder et al. 2012) and the low- and high-resolution 4MOST consortium surveys[6] 4MIDABLE-LR and 4MIDABLE-HR (Chiappini et al. 2019; Bensby et al. 2019).

2.2 The disk(s)

The idea that the stellar disk of the Milky Way is a multicomponent structure dates back to the early 1980s. Based on stellar number counts, Gilmore & Reid (1983) reported that the density profile away from the Galactic midplane cannot be described by a single power law. Hence, the terminology of distinguishing the disk into a "thin" and "thick" structure emerged, which was owed to the different inferred scale heights (0.3 kpc compared to 1.35 kpc at the solar circle).

---

[6] In this context it is interesting to note that WEAVE – an instrument that is in a sense competing with 4MOST in terms of multiplexing capability and spectrograph design – will not be able to conduct such studies as the bulge is not accessible from the northern hemisphere (see, for instance, Figure I.2).

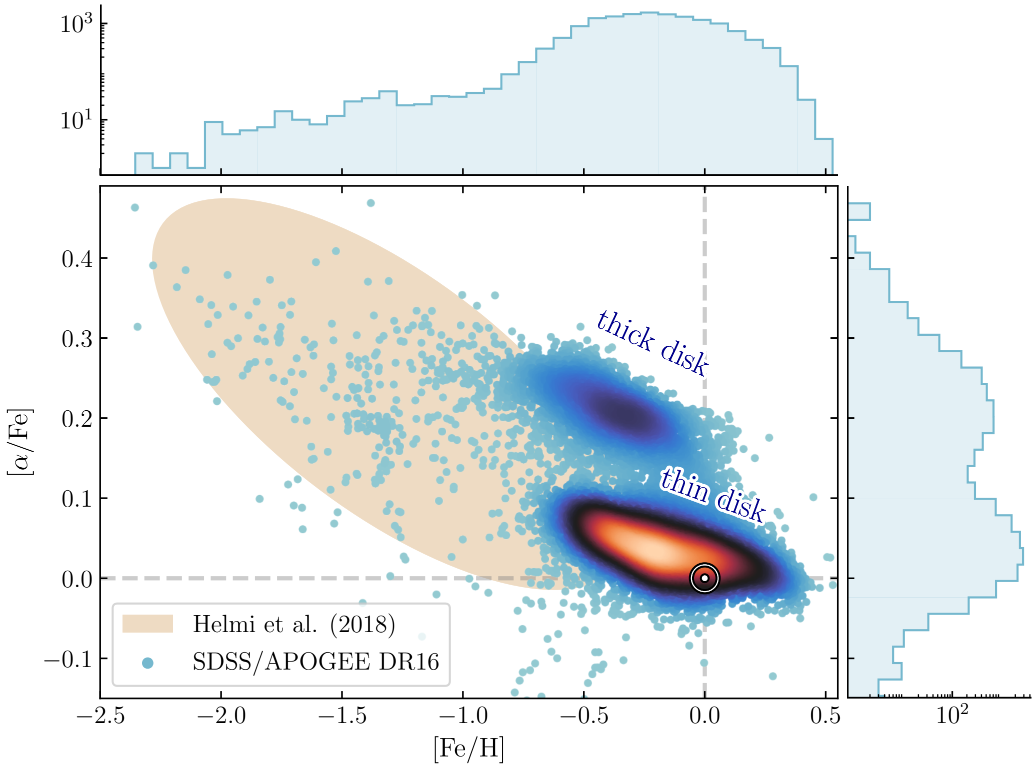

FIGURE I.4: Chemical evidence for a split in the population of disk stars. Shown are the abundance ratios [α/Fe] versus [Fe/H] of 14 963 giants ($\log g < 2.2$ dex) from SDSS-IV/APOGEE DR16 that obey $-15^\circ < b < 15^\circ$ and $\varpi/\sigma_\varpi > 5$. The color coding resembles the local point density, which is also represented by logarithmic number counts in the *upper* and *right panels*. Solar values are indicated by a $\odot$ marker. The parameter space occupied by the population of retrograde stars that were attributed to the now-dissolved *Gaia*-Enceladus dwarf galaxy (Helmi et al. 2018) is approximatively indicated by a light brown ellipse.

Since then, the picture has been much refined (or even refuted, see Bovy et al. 2012), particularly by introducing chemodynamical information. For instance, Bensby et al. (2003) and Haywood (2008), among others, showed the existence of two distinct abundance sequences with [Fe/H] of those elements that are subsumed in the group of α-elements (see Section 3.2). This finding is reflected in Figure I.4 where stars at low Galactic latitutes with abundances from APOGEE spectra of SDSS DR16 (Ahumada et al. 2019) are shown. Moreover, Hayden et al. (2015) reported that the α-rich thick disk has a shorter scale length (roughly out to the solar circle at a Galactocentric distance $R_{\mathrm{GC}} \approx 8$ kpc) and further revealed that the thin disk (solar[7] [α/Fe]) not only shows the already known metallicity gradient – that is, decreasing [Fe/H] with increasing R_{GC} (e.g., Friel 1995; Andrievsky et al. 2002a,b,c; Lemasle et al. 2008) – but that its more metal-poor component beyond the solar circle is flaring out to larger Galactic heights, z. From changes in the skewness of the metallicity distribution

---

[7] Note that here "solar" is preferred over the term "α-poor" that is frequently used in the literature. At values close to solar with even a tendency towards supersolar figures it would appear odd to follow that nomenclature.

function of stars close to the Galactic plane with R_{GC} Hayden et al. (2015) further provided strong evidence for radial migration within the disk (see also, e.g., Minchev & Famaey 2010). The outer regions of the Galactic disk exhibit a break in the axial symmetry, which manifests in a warping of the disk away from the midplane (e.g., Burke 1957; Djorgovski & Sosin 1989; Gaia Collaboration et al. 2018c). Recently, Poggio et al. (2020) argued that this warp is a transient phenomenon as opposed to a relic of the early Galaxy buildup. They further indicate that the structure may be caused by an ongoing interaction with a satellite galaxy, possibly the Canis Major overdensity (Momany et al. 2006).

With respect to the formation channel of the Galactic thick disk, Helmi et al. (2018) offered a powerful description using the mighty explanatory power of a dataset combining kinematical and chemical information from *Gaia* and APOGEE. They discovered that a prominent retrograde Galactic substructure (first reported by Koppelman et al. 2018) is remarkably similar in phase-space coordinates to a simulated merger of the precursor of todays stellar disk with a satellite of similar mass to the present-day Small Magellanic Cloud. The authors additionally proposed that roughly ~ 10 Gyr ago this major merger with the so-called *Gaia*-Enceladus galaxy (also known as the *Gaia*-Sausage; Belokurov et al. 2018; Myeong et al. 2018) led to a considerable dynamical heating of the disk and may have triggered the formation of a major part of what we today perceive as the thick disk.

2.3 The stellar halo

At a mass of about $10^9\,M_\odot$ and a mean metallicity ~ -1.5 dex (e.g., Deason et al. 2019), the stellar halo is the largest (out to ~ 160 kpc; Fukushima et al. 2019), yet least massive ($\sim 2\%$ of the Milky Way mass) stellar component of the Galaxy. It has been shown to have a metallicity distribution function that is highly skewed towards the regime of the lowest metallicities ($[\mathrm{Fe/H}] < 3$ dex; e.g., Hartwick 1976 and most recently Youakim et al. 2020), such that the most metal-poor stars in the Milky Way are to be found there. Pursuing the assumption that the oldest stars also expose the lowest metal abundances, these are vital in order to study early nucleosynthesis and the properties of the very first stars in the Universe (see, e.g., the review by Frebel & Norris 2015).

By mapping the distribution and chemodynamics of globular clusters and stellar populations, it has been demonstrated that the halo is separable into an "inner" and an "outer" halo component; the transition region residing at $R_{\mathrm{GC}} \approx 20\,\mathrm{kpc}$ (e.g., Zinn 1993; Carollo et al. 2007; Watkins et al. 2009; Carollo et al. 2010). Halo dichotomies appear to be common in other galaxies, too (e.g., Ibata et al. 2007; Koch et al. 2008b).

Buildup scenarios for the Galactic halo range from purely in-situ formation (e.g., Eggen et al. 1962) to mixtures of both in-situ and ex-situ channels, with the degree of ex-situ contributions varying with Galactocentric distance (e.g., Searle & Zinn 1978; Bell et al. 2008; De Lucia & Helmi 2008; Zolotov et al. 2009; Pillepich et al. 2015; Cooper et al. 2015). Already in the pre-*Gaia*-era, for example, Deason et al. (2013) proposed an explanation for the break in the halo density profile. These latter authors employed high-resolution N-body simulations to argue that a single massive merger about $\sim$ 6-9 Gyr in the past would be capable of reproducing a structure that is reminiscent of the inner halo as it is observed today.

Indeed, there is a wealth of observational evidence for ongoing accretion in the form of persistent stellar streams, which support the ex-situ scenarios. These streams range from events as massive as the accretion of the Sagittarius dwarf spheroidal galaxy (Ibata et al. 1994; Belokurov et al. 2006) to observations of more elusive, more dynamically cold stellar streams and envelopes attributed to globular clusters that are in the process of being tidally disrupted or that are already entirely dissolved (e.g., Odenkirchen et al. 2001; Grillmair & Dionatos 2006; Jordi & Grebel 2010; Kuzma et al. 2018; Malhan et al. 2018; Ibata et al. 2019; Borsato et al. 2020). However, proof for massive accretion events in the distant past has been lacking until recently, when *Gaia* DR2 enabled Koppelman et al. (2018), Helmi et al. (2018), and Belokurov et al. (2018) to unravel the imprints of the merger with *Gaia*-Enceladus, and Myeong et al. (2019) to discover a potential further event[8] – termed Sequoia – that is proposed to have happened at about the same time. Moreover, Koppelman et al. (2019) could tie the so-called Helmi streams to a slightly more recent merger of the Milky Way with yet another now dissolved dwarf galaxy.

In this thesis, an entire chapter (Chapter IV) is dedicated to investigating the interface of the halo and the Galactic globular cluster population where we additionally address the contribution stripped clusters may have had to the buildup of the halo.

2.4 Globular clusters – relics of the early Galaxy

Globular clusters (GCs) are found in all of the Milky Way's components discussed so far save for the actively star forming thin disk. The Harris catalog of parameters for Milky Way globular clusters (Harris 1996, 2010 edition) lists 157 such objects, and new ones at low Galactic latitutes are being discovered or confirmed in their nature every now and then (e.g., Minniti et al. 2017; Koch et al. 2017; Camargo 2018; Camargo & Minniti 2019; Barbá et al. 2019). Given that the knowledge of their existence reaches far back (e.g., Halley 1715; Herschel 1814), it may be surprising

---

[8] Note that such an event has already been postulated by Kruijssen et al. (2019) – The Kraken.

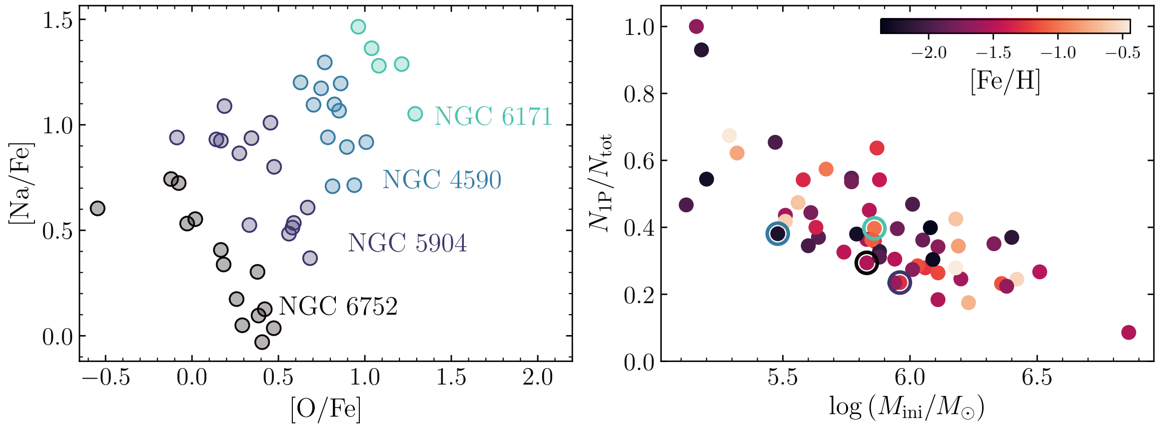

FIGURE I.5: Chemical evidence for multiple populations in Galactic globular clusters. *Left panel*: Na-O anticorrelation for a selection of four GCs (NGC 6752, NGC 5904, NGC 4590, and NGC 6171) that are representative for the range in strengths of the Na-O anticorrelation as deduced by Carretta et al. (2009). Stars belonging to one cluster are color coded in the same way and they were shifted by constant offsets both on the ordinate and the abscissa in order to facilitate the distinction of the GCs. *Right panel*: for individual clusters, the fraction of first-generation stars among all GC stars, N_{1P}/N_{tot}, is presented as a function of the initial cluster mass, M_{ini}. The data stem from the compilation by Gratton et al. (2019), which itself is based on Milone et al. (2017) and Baumgardt et al. (2019). Colors reflect the GCs' metallicities (see color bar on the *upper right*). The four clusters shown on the *left* are marked by circles of the same color.

that there is to this day no clear definition for globulars that is unanimously agreed upon. GCs rather appear to be objects of the you-know-it-when-you-see-it kind. A non-exhaustive list of properties shared by most – yet not necessarily all – GCs comprises old age ($\gtrsim 10$ Gyr), high densities ($\langle\rho\rangle \sim 0.1\,M_\odot\ \mathrm{pc}^{-3}$), small radii (a few pc), and the apparent lack of dark matter (though the latter was not necessarily the case at birth; see Beasley 2020, and references therein).

Historically, GCs were thought to be prototypes of simple stellar populations, in a sense that they would exclusively host stars of identical age and chemical composition. However, whilst otherwise indeed being (mostly) mono-metallic, GCs almost genuinely reveal at least some amount of variations in light-element abundances, which manifests in C-N and Na-O anticorrelations (e.g., Cohen 1978; Kraft 1979; Carretta et al. 2009; left-hand side of Figure I.5). This abundance anomaly is attributed to high-temperature proton burning in the CNO cycle and its NeNa chain. The less-frequently observed spreads in Mg, Al, Si, and potentially even K and Zn (e.g., Gratton et al. 2001; Hanke et al. 2017; Pancino et al. 2017; Gratton et al. 2019) are attributed to burning at even higher temperatures ($\gtrsim 70 \cdot 10^6$ K, Arnould et al. 1999; see Section 3.5 for more detailed discussions of proton burning and GC self-enrichment). Here, I follow the nomenclature of Bastian & Lardo (2018) and distinguish a second, chemically “enriched” GC population (2P[9]), which manifests in enhanced N and Na abundances at the expense of depleted C and O. Models suggest that this second generation was enriched by the aforementioned nucleosynthesis in massive stars of the first, chemically “normal” (i.e., C- and O-enhanced while being Na- and N-depleted) population (1P). Addressing the circumstance that some clusters do not show clear imprints of multiple populations, Gratton et al. (2019) caution that “lack of evidence“ does not imply ”evidence of lack“ since it may prove hard to find multiple populations; particularly in those cases where altered populations are less strongly enhanced or sparse in number. The latter authors further point out that the fraction of enriched stars, N_{1P}/N_{tot}, seems to be tightly related to the initial cluster mass (see right-hand side of Figure I.5), whereas they also mention that a similar trend is found with the escape velocity (Baumgardt & Hilker 2018), which would indicate that more massive clusters (or those with higher escape velocities) could more easily hold on to 1P ejecta to form the 2P. Still, it should be noted that there is an ongoing debate concerning the more fundamental cluster parameter – that is, either mass or age – for multiple populations, with authors like Bastian & Lardo (2018) advocating for the latter. The seemingly ubiquitous occurrence of multiple populations led Carretta et al. (2010) to propose a definition for GCs being stellar systems that exhibit the Na-O anticorrelation.

Moving away from the chemical vantage point, Kruijssen (2015) defines a GC in a rather different way:

> *”A gravitationally-bound, stellar cluster that in terms of its position and velocity vectors does not coincide with the presently star-forming component of its host galaxy.“*

None of the above directly reflects any of the properties of GCs that were mentioned earlier. Nevertheless, Kruijssen (2015) lays out a line of reasoning according to which those properties are a natural outcome for objects satisfying his definition and that were formed early on and survived until today.

---

[9] Throughout the literature, 1G/2G or FG/SG are used as alternatives. Furthermore, Carretta et al. (2010) coined a distinction between primordial (P), intermediate (I), and (E) components.

3 Cosmic nucleosynthesis – setting the preconditions for all life

Organic chemistry – and by extension all biological life as we know it – would be unthinkable in the absence of elements like H, C, N, O, P, and S (atomic numbers, Z, of 1, 6, 7, 8, 15, and 16, respectively) and their capability to bond to more than one other binding partner, which is paramount for the formation of complex molecules. A number of heavier chemical species are key ingredients for all technological advancements achieved in the era of digitalization. For example, this very thesis was written using a device that owes its existence to semiconductor materials like Si and to metals (in the customary, non-astronomical sense of the word) such as Cu. Nonetheless, all elements, except for H, have in common that they did not always exist in the Universe but were synthesized in astrophysical sites that emerged successively throughout cosmic history; long before the elements coagulated to form the Solar System some 4.5682 Gyr ago (Bouvier & Wadhwa 2010).

The cosmological history of the Universe and the instances of emergence of several nucleosynthesis sites are illustrated in Figure I.6 in a schematic manner. The first transformative event was about 15 minutes into the Universe's existence when primordial nucleosynthesis halted and left behind H, He, and trace amounts of Li. Another point is the appearance of the first stars and their products of hydrostatic burning and explosive nucleosynthesis. This latter point should not be considered one discrete instance in time but rather a starting point of a continuous enrichment process since then. The same applies for spallation processes (not discussed here as they are beyond the scope of this dissertation) and the emergence of the first rare types of supernovae, neutron star mergers, and low-mass stars evolving through the asymptotic giant branch (AGB) phase, which are among the sites thought to contribute neutron-capture elements (see following sections for details). Pioneering work in the field of nuclear astrophysics was performed by (Burbidge et al. 1957; hereafter B^{2}FH). B^{2}FH singled out eight distinct nucleosynthesis channels of the elements that are attributed to stars, some of which will be discussed here as they are of relevance for this thesis.

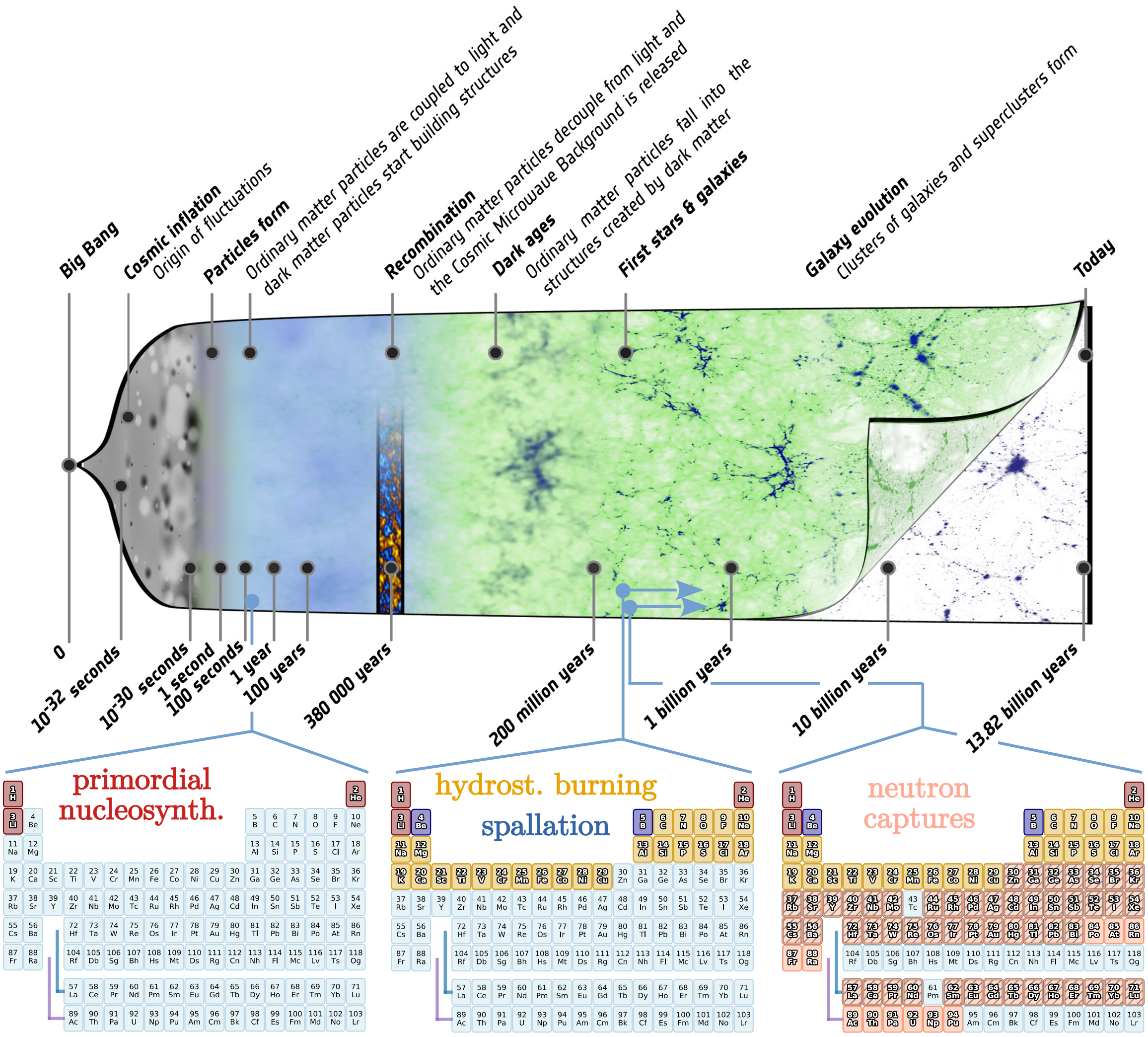

FIGURE I.6: A brief cosmological history of the Universe from the Big Bang until today as we currently understand it, largely thanks to NASA's Wilkinson Microwave Anisotropy Probe (WMAP; Hinshaw et al. 2013) and ESA's *Planck* mission (Planck Collaboration et al. 2018). Further indicated are the three pivotal points in time that are mentioned in the main text: the end of primordial nucleosynthesis, the onset of hydrostatic burning in stars, and the advent of neutron-capture events. Note that elements without stable isotopes on cosmological timescales[10]remain being shown in light blue in the third periodic table. **Image credits.** Planck history of Universe zoom (*upper part*): ESA / C. Carreau. The *rgb* channels of the original image were inverted.

3.1 Primordial nucleosynthesis

According to our current cosmological understanding, the history of the universe in its essence is a story of expansion, cooling, and condensation. Shortly after the Big Bang ($\sim$ 1 s), when the temperature had dropped below $T \approx \Delta m_{\mathrm{n,p}} c^2 / k_{\mathrm{B}} =$

---

[10] In this respect it is interesting to note that the short-lived element Tc is still of astrophysical relevance to identify stars that are currently undergoing the third dredge-up in the AGB phase (e.g., Smith & Lambert 1988). In fact, it's discovery in stellar spectra by Merrill (1952) was the first proof that neutron-capture reactions (see later in this sections) actually take place in stars.

$1.3\,\mathrm{MeV}/k_\mathrm{B} \approx 10^{10}\,\mathrm{K}$, with $\Delta m_\mathrm{n,p}$ being the rest-mass difference between a neutron and a proton and k_B the Boltzmann constant, neutrons and protons dropped out of thermal equilibrium such that the conversion reaction preferred the slightly less massive protons, which then became more numerous. This led to a neutron-to-proton ratio $n/p = 1/6$ by the time the conversion reaction came to a complete halt (e.g., Boesgaard & Steigman 1985). After cooling had proceeded further, the $n(p,\gamma)^2\mathrm{H}$[11] reaction could form deuteron – the second hydrogen isotope after $^1\mathrm{H}$ – without being destroyed immediately after. Subsequently, several additional reactions involving n, p, and $^2\mathrm{H}$ led to $^3\mathrm{H}$, $^3\mathrm{He}$, and $^4\mathrm{He}$ (see, e.g., Yang et al. 1984). Since isolated neutrons are unstable to β^--decay [$n(e^-\bar{\nu}_e)p$, with $\tau_{1/2} \approx 880$ s; Tanabashi et al. 2018], all neutrons were either bound in an isotope or decayed. By the time free neutrons ceased to exist, n/p had dropped to 1/7, which converts into a mass fraction of 75% and 25% for $^1\mathrm{H}$ and $^4\mathrm{He}$, respectively. Other nuclides like $^2\mathrm{H}$, $^3\mathrm{H}$, $^3\mathrm{He}$, $^7\mathrm{Li}$, and the radioactive isotope $^7\mathrm{Be}$ – the latter two by means of $^4\mathrm{He}(^3\mathrm{H},\gamma)^7\mathrm{Li}$ and $^4\mathrm{He}(^3\mathrm{He},\gamma)^7\mathrm{Be}$ – were merely produced in trace amounts. Due to the lack of stable elements with mass numbers (A) of 5 or 8, heavier elements could not form by fusion of the existing nuclides. This "bottleneck" effectively terminated primordial nucleosynthesis. The abundances of the primordial elements that are measured today are one of the cornerstone observables in support for the Big Bang scenario (e.g., Cyburt 2004; Steigman 2010; Hinshaw et al. 2013). Heavier elements ($A > 7$) were not synthesized for several 100 Myr until stars provided the necessary conditions for those elements to be generated.

3.2 Hydrostatic burning in stars

Photons decoupled from ordinary matter about 379 000 yr into the Universe's existence, which marks the time when the cosmic microwave[12] background was emitted (e.g., Penzias & Wilson 1965; Spergel et al. 2003; Planck Collaboration et al. 2018). At the same time, the Universe entered the epoch of the "dark ages", where predominantly neutral ordinary matter (H and He) fell into the potential wells created by filamentary dark matter overdensities. This era lasted for a few 100 Myr until gas clouds underwent gravitational collapse to form the first stars (also termed Population III or Pop III stars), which were forging heavier nuclei that settled in later generations of stars (Pop II and I; Baade 1944).

Stars are hot so that they do not become even hotter. This somewhat counterintuitive statement is a direct consequence of their negative heat capacity that follows from

---

[11] The nuclear reaction notation $a(b,c)d$ indicates that a and b react to form d by releasing c.

[12] At the time of release, considering that the Universe's temperature was ~ 1100 times hotter, it would rather have been termed the cosmic near-infrared background.

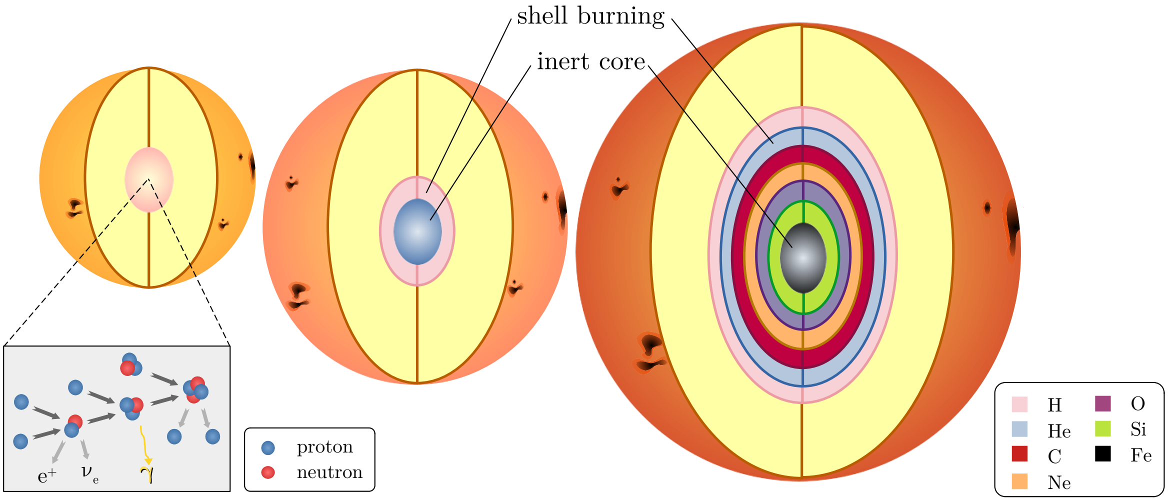

FIGURE I.7: Stellar structure during hydrostatic burning (not to scale). *Left*: Main sequence star with core H burning. The reaction chain of the dominant energy source in a solar-type star – the pp-I chain – is presented at the *lower left*. *Center*: H shell burning during the evolution on the RGB. The inert He core is depicted in blue. At this stage the outer envelope of the star is substantially enlarged and cooler as compared to the main sequence, which is only indicated to some extent here that does not reflect the true size change. *Right*: Onion structure of the shell-burning core of a massive star right before the core-collapse and the subsequent Type II supernova explosion. The burning shells are represented by different colors as indicated in the legend at the *lower right*.

the virial theorem for stable self-gravitating objects stating

$$\langle E_{\mathrm{kin}} \rangle = -\frac{1}{2} \langle E_{\mathrm{pot}} \rangle, \tag{I.1}$$

where $\langle E_{\mathrm{kin}} \rangle$ and $\langle E_{\mathrm{pot}} \rangle$ are the mean particle kinetic and potential energies. The virial theorem implies that such an object increases its particles' (in the case of stars mostly protons and H atoms) kinetic energy – that is, the object's temperature – when it contracts under the influence of gravity. However, a star is characterized by its capability to maintain hydrostatic equilibrium[13] by counteracting its gravitational collapse through thermal pressure that is induced by an internal heat source. That heat source is supplied exothermic nuclear fusion reactions in the stellar core (see Figure I.7 for an illustration).

In main sequence (MS) stars like the Sun, H is burnt into He in the *p*-*p* chain reaction, which itself has three branches with the same net reaction. The most dominant (84%) energy source in the Sun is the $^{1}\mathrm{H}(p,e^{+}\nu_{e})^{2}\mathrm{H}(p,\gamma)^{3}\mathrm{He}(^{3}\mathrm{He},2p)^{4}\mathrm{He}$ reaction, followed by the $^{1}\mathrm{H}(p,e^{+}\nu_{e})^{2}\mathrm{H}(p,\gamma)^{3}\mathrm{He}(\alpha,\gamma)^{7}\mathrm{Be}(e^{-},\nu_{e})^{7}\mathrm{Li}(p,\alpha)^{4}\mathrm{He}$ branch (16%) and the subordinate $^{1}\mathrm{H}(p,e^{+}\nu_{e})^{2}\mathrm{H}(p,\gamma)^{3}\mathrm{He}(\alpha,\gamma)^{7}\mathrm{Be}(p,\gamma)^{8}\mathrm{B}(e^{+}\nu_{e})^{8}\mathrm{Be}(\alpha)^{4}\mathrm{He}$

---

[13] It should be noted that some peculiar classes of pulsating variables such as RR Lyrae stars or Cepheids oscillate around this equilibrium state. More generally, all stars show oscillations, although those are typically many orders of magnitude less strong. These oscillations are the result of linear perturbations to the equilibrium state and constitute the basis for asteroseismology.

branch with its 0.1% share of the solar energy output (see, e.g., Wiescher et al. 2012). Stars that are more massive – and hence hotter – than the Sun (i.e., $\gtrsim 1.3 M_\odot$) produce the majority of their energy in the CNO cycle as it is the more efficient mechanism at these high temperatures ($\gtrsim 1.7 \cdot 10^7$ K; Schuler et al. 2009). The attributed burning phases are highly relevant to explain the abundance anomalies seen in GCs and I will discuss the details and possible polluters in Section 3.5 in order to further our understanding of their multiple stellar populations.

In the entire collection of the aforementioned nucleosynthesis reactions the heavier elements merely act as catalysts, in other words they do not participate in the net reaction, which solely fuses H into He. Facing a lack of such heavier nuclei to seed these processes, Pop III stars could not trigger the CNO cycle irrespective of their mass. Moreover, since at the time of their formation no carbon monoxide molecules (CO) were available to act as efficient coolant, the protostellar gas clouds cooled solely through molecular hydrogen, which prevented cloud fragmentation and typically favored the formation of very massive stars (Bromm & Larson 2004).

A star spends most of its lifetime on the MS where it sustains hydrostatic equilibrium via H burning. During that time, large amounts of He accumulate in the stellar core. Once the nuclear fuel is exhausted, the star evolves off the MS and becomes a red giant. The latter evolutionary state is characterized by an inert He core that contracts under its own gravity while being surrounded by an H-burning shell (see middle part of Figure I.7). As soon as this core turns hot enough ($\sim 10^8$ K), the triple-α reaction $^4\mathrm{He}(2\alpha,\gamma)^{12}\mathrm{C}$ followed by a further α-capture, $^{12}\mathrm{C}(\alpha,\gamma)^{16}\mathrm{O}$, ignites (e.g., Wiescher et al. 2012). The bottleneck of primordial nucleosynthesis was overcome for the first time in cosmic history when the first Pop III stars triggered this triple-α reaction.

During core He burning, similar to the earlier stage of core H burning, the ashes assemble in the core until eventually an inert CO core with a He-burning shell emerges. He burning marks the final stage of hydrostatic burning in low- to intermediate-mass stars (initial masses $\lesssim 8\,M_\odot$), which end up as CO white dwarfs (WDs) or ONeMg WDs, provided they had slightly larger initial masses (Werner & Herwig 2006). WDs are stellar remnants that are supported by electron-degeneracy pressure.

Stars with even larger initial masses reach sufficient core temperatures for the onset of C burning with its major reactions $^{12}\mathrm{C}(^{12}\mathrm{C},\alpha)^{20}\mathrm{Ne}$ and $^{12}\mathrm{C}(^{12}\mathrm{C},p)^{23}\mathrm{Na}$. Subsequently, these stars experience a rapid cascade of Ne, O, and finally Si shell-burning stages where the zones fusing lighter elements move outward to form an onion-like structure. This is illustrated on the right-hand side of Figure I.7. As opposed to prior reactions, Si burning is not a reaction of the $\mathrm{Si}(\mathrm{Si},x)y$ type but is

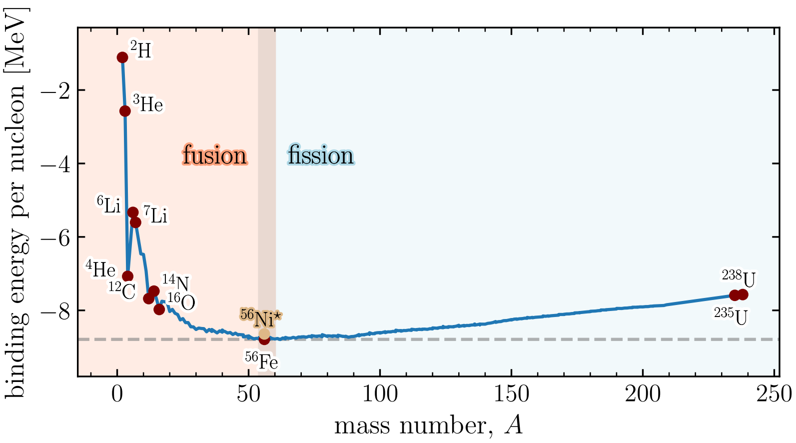

FIGURE I.8: Nuclear binding energy as a function of mass number, A. The graph shows the mean binding energy or mass defect per nucleon ($\Delta mc^2/A$) for stable nuclides. In this representation, the most strongly bound nuclei expose the lowest (most negative) binding energy. Several important nuclides in the context of this section are highlighted by red-filled circles and respective annotations. ^{56}Ni, the unstable end product of Si burning (see text), is given in orange. The iron peak with its most strongly bound nuclei is marked by a vertical band. At higher A than the iron peak, nuclear reactions release energy only via fission, while lighter elements can produce energy through fusion. The binding energies were computed from data that were extracted from the NuDat 2 database of the National Nuclear Data Center.

largely governed by photodisintegration. Photodisintegration is triggered by thermal γ-ray photons, which are available in the photon bath once temperatures are sufficiently high. Among other channels, photodisintegration liberates α-particles through, for instance, $^{28}\mathrm{Si}(\gamma,\alpha)^{24}\mathrm{Mg}$, which then may be captured in a series like $^{28}\mathrm{Si}(\alpha,\gamma)^{32}\mathrm{S}(\alpha,\gamma)^{36}\mathrm{Ar}(\alpha,\gamma)^{40}\mathrm{Ca}(\alpha,\gamma)^{44}\mathrm{Ti}(\alpha,\gamma)^{48}\mathrm{Cr}(\alpha,\gamma)^{52}\mathrm{Fe}(\alpha,\gamma)^{56}\mathrm{Ni}(\alpha,\gamma)^{60}\mathrm{Zn}$ (e.g., Clayton 1968). Figure I.8 presents the mean binding energy per nucleon for stable isotopes and demonstrates that the elements around the iron peak ($A \sim 56$) are the most strongly bound. Thus, fusion reactions with products beyond the iron peak are endothermic and cannot stabilize against gravitational collapse. The inevitable consequence is that a star that has converted the majority of its core material into iron-peak elements experiences a free-fall contraction of its core. This marks the end of hydrostatic equilibrium. A graphical summary showing stellar nucleosynthesis mechanisms as a function of the initial stellar mass of their host is given in Figure I.9.

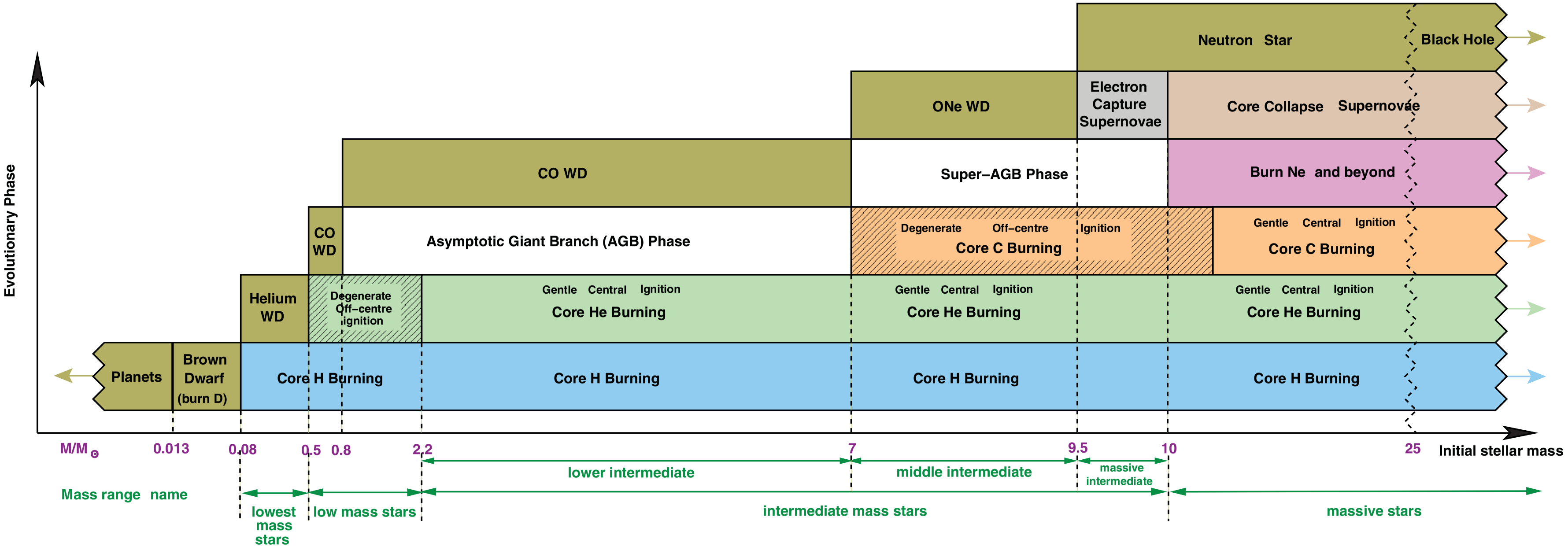

FIGURE I.9: Schematic of stellar nuclear burning phases at solar metallicity as a function of the initial stellar mass and the evolutionary stage. Blue colors represent the main sequence and successive phases after the H fuel is exhausted are stacked on top. The remnants left after the final evolution stages are shown at the top (highlighted in olive green). Reproduced by permission from figure 1 in Karakas & Lattanzio (2014). Copyright © 2014, Cambridge University Press.

3.3 Supernovae

As soon as the density of the collapsing core of a massive star reaches a critical threshold where neutron-degeneracy pressure abruptly counterbalances gravity, the still inward moving outer layers bounce off. This causes an outward-moving shock wave leading to an explosion that expels the stellar envelope, leaving behind only the core remnant. Depending on the initial stellar mass, this remnant ends up being either a neutron star or a black hole (see Figure I.9). The ejected material mixes into the interstellar medium (ISM) and enriches later stellar populations that form from this ISM. While the major production of elements from He up to and including Si is thought to be dominated by hydrostatic burning processes, the aforementioned Type II core-collapse supernovae (CCSNe) with their explosive nucleosynthesis are likely responsible for a substantial fraction of the iron-peak inventory ($14 \leq Z \leq 30$; Woosley & Weaver 1995; Nomoto et al. 2006).

Another important donor of iron-peak elements are thermonuclear supernovae (Type Ia; Kobayashi et al. 2019), which are attributed to exploding WDs that do not leave behind a core remnant. There is a variety of proposed characteristics for the progenitor systems and definitive proof for either one is yet to be revealed (see, e.g., the review by Soker 2019). Since Type Ia supernovae require intermediate-mass stars first to have evolved all the way to the WD stage, whereas CCSNe due to having high-mass progenitors occur almost instantly (a few Myr) after the onset of the initial burst of star formation, there is a considerable time delay between the two nucleosynthesis sites. This gave rise to the well renowned α-knee that is observed in all galaxies with prolonged star formation history (e.g., Matteucci & Brocato 1990; McWilliam 1997; Venn et al. 2004; Koch et al. 2008a; Reichert et al. 2020), which manifests in a plateau of high [α/Fe] at low(er) [Fe/H] and a downturn of [α/Fe] with [Fe/H] above a characteristic metallicity. This latter characteristic metallicity indicates the point in time at which SNe Ia yields (exclusively iron-peak elements) started contributing to the chemical enrichment.

3.4 Neutron-capture processes

Beyond the iron peak, electrostatic Coulomb repulsion ensures that charged-particle reactions play a minuscule role in element synthesis (with the possible exception of proton-rich isotopes). Temperatures high enough for charged particles to overcome the Coulomb barrier photo-dissociate the larger nuclei. Thus, most of the elements heavier than the iron peak result from neutron captures, which are divided into the slow (s) and rapid (r) processes by their capture rates with respect to the β-decay

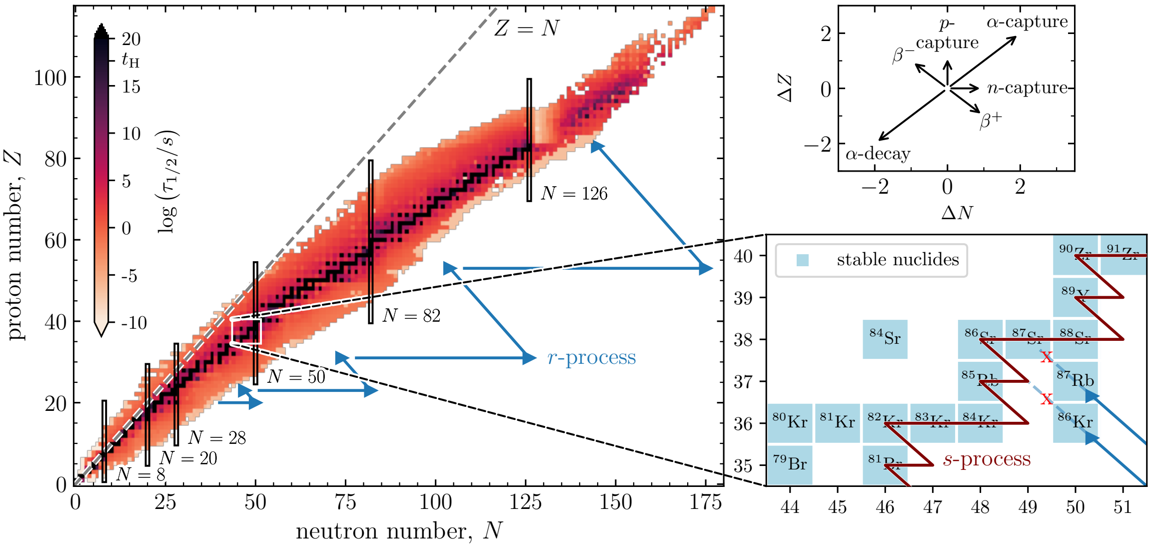

FIGURE I.10: Chart of nuclides based on data taken from the NuDat 2 database of the National Nuclear Data Center. *Left*: nuclides are represented by their proton number (Z) versus their neutron number (N) with their half-life time, $\tau_{1/2}$, being indicated by color. As the color bar on the *left* suggests, the darker the color of a nuclide is the less prone it is to radioactive decay. The age of the universe ($t_H \approx 13.8$ Gyr) is specifically labeled. The valley of stability can be seen as black track in the center of the distribution. Nuclides above the valley tend to decay via β^+-decay, while the ones below are mostly unstable to β^--decay (see *upper right panel* for some of the existing other reaction channels). Further indicated are the line of proton and neutron number equalities ($Z = N$, black-dashed), the magic neutron numbers, $N = 8$, 20, 28, 50, 82, and 126 (black rectangles), and possible realizations of r-process tracks before reaching the valley of stability (i.e., fractions of a second after the neutron exposure; blue arrows). *Zoom-in panel*: only stable nuclides are shown here in light blue. A possible s-process path in a low-mass AGB star is demonstrated in red. ^{86}Kr and ^{87}Rb exemplify production by the r-process[14]and their role in shielding the Sr isotopes ^{86}Sr and ^{87}Sr from the r-process is illustrated.

timescale (B^{2}FH; Cameron 1957). The involved neutron densities differ by many orders of magnitude and are thought to be $n < 10^8$ cm^{-3} and $n \gtrsim 10^{20}$ cm^{-3} for the s- and r-process, respectively (Busso et al. 2001; Meyer 1994). However, it should be noted that these limits are not set in stone but leave room for an i-process at intermediate densities (Cowan & Rose 1977; Malaney 1986; Hampel et al. 2016, 2019).

3.4.1 The *s*-process

The s-process is subdivided into a main and a weak component, which are separated based on their driving neutron source. The main s-process is believed to be active during the thermally pulsing phases of low-mass AGB stars (e.g., Gallino et al. 1998;

---

[14] Note that these are not necessarily r-only isotopes since intermediate-mass AGB stars with their capabilities to efficiently activate the $^{22}\mathrm{Ne}(\alpha,n)^{25}\mathrm{Mg}$ s-process neutron source generate neutron densities that are high enough to bypass the unstable isotope ^{85}Kr and produce the resistant ^{87}Rb nucleus with its stable neutron configuration via the channel $^{84}\mathrm{Kr}(n,\gamma)^{85}\mathrm{Kr}(n,\gamma)^{86}\mathrm{Kr}(n,\gamma)^{87}\mathrm{Kr}(e^-\bar{\nu}_e)^{87}\mathrm{Rb}$ (e.g., Karakas & Lattanzio 2014). This is important in the context of the line of reasoning in Section III.7.4.

Straniero et al. 2006; Lugaro et al. 2012; Karakas & Lattanzio 2014), where the required low neutron fluxes are provided through the $^{13}\mathrm{C}(\alpha,n)^{16}\mathrm{O}$ reaction (Lambert et al. 1995). The weak *s*-process, on the other hand, is characterized by the $^{22}\mathrm{Ne}(\alpha,n)^{25}\mathrm{Mg}$ neutron source, which prevails first during core He-burning in intermediate-/high-mass stars, and is reactivated at the later stage of C-burning when the necessary α-particles are produced by the $^{12}\mathrm{C}(^{12}\mathrm{C},\alpha)^{20}\mathrm{Ne}$ reaction (Arnett & Truran 1969; van Raai et al. 2012). The main *s*-process can produce elements as heavy as Bi, while the weak component does not produce sizable amounts of species beyond Zr (Raiteri et al. 1991; Pignatari et al. 2010). A detailed discussion of how certain abundance ratios measured in stars can give away the neutron source that is responsible for their enrichment can be found in Section III.7.4.

A characteristic feature of the *s*-process is that it never moves away from the "valley of stability", that is, the regime of stable isotopes in a chart of nuclides comparing the atomic number to the neutron number, N (Figure I.10). An *s*-process track starts with a seed nucleus and adds neutrons until an unstable configuration is reached. The respective nuclide decays via β^--decay before any more neutrons can be added, thereby increasing the atomic number by one incremental step (see illustration on the right-hand side of Figure I.10). This way, the (main) *s*-process can produce elements up to Bi, where it is terminated via the bottleneck reaction cycle $^{209}\mathrm{Bi}(n,\gamma e^-\bar{\nu}_e)^{210}\mathrm{Po}(\alpha)^{206}\mathrm{Pb}(3n,\gamma e^-\bar{\nu}_e)^{209}\mathrm{Bi}$. In between, particularly stable configurations are reached at the magic neutron numbers $N = 50$, 82, and 126, which indicate closed neutron shells that have a certain resistance against accumulating further neutrons. This leads to a pile up of stable nuclides in those regimes as can be seen in Figure I.11, where the three *s*-process peaks in the Solar System material are clearly identifiable.

3.4.2 The *r*-process

The existence of additional peaks towards lighter nuclei from each *s*-process peak led $\mathrm{B^2FH}$ to propose the *r*-process, which ought to bombard the seed nuclei with a large amount of neutrons well in advance of any β-decay occurrence. The highly neutron-rich species again concentrate around the magic neutron numbers; however, they are unstable to β-decay and therefore cluster at lower A once they reach the valley of stability. The *r*-process typically synthesizes the more neutron-rich isotopes of an element that are inaccessible by the *s*-process (hence they are referred to as *r*-only isotopes). On the other hand, there are also nuclides that are shielded from the *r*-process by stable nuclides that interrupt the β-decay tracks. This circumstance is illustrated in the lower right panel of Figure I.10. One distinctive trait of the *r*-process

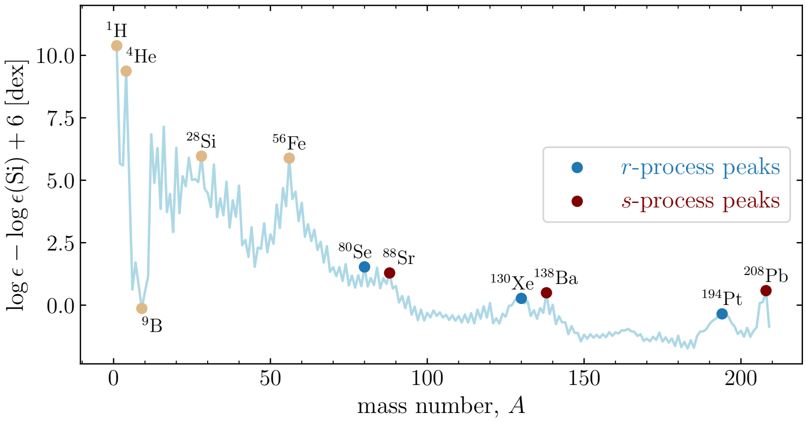

FIGURE I.11: Solar System abundances from Lodders (2003). Abundances are normalized to Si, which itself is set to 6 dex. The abundances are shown as a function of mass number and not atomic number. Due to this, the labels only indicate the dominant contributor to nuclides with their given A, although there may be more isotopes of different elements with the same A. To guide the eye in the light-element regime, ^{1}H, ^{4}He, ^{9}B, ^{28}Si, and ^{56}Fe are marked in dark yellow. Blue- and red-filled circles highlight the r-process (close to ^{80}Se, ^{130}Xe, and ^{194}Pt) and s-process peaks (around ^{88}Sr, ^{138}Ba, and ^{208}Pb), respectively.

is that it can produce elements heavier than Bi. Among those are, for example, Th and U, which are vital tracers for stellar age determinations via nuclear cosmochronology (see Section III.7.6).

Several astrophysical sites are under consideration for enabling extremely neutron-rich environments for the r-process to take place. Viable candidates are neutrino-driven winds in CCSNe (Arcones et al. 2007; Wanajo 2013), jets in magneto-rotational supernovae (MR SNe, Cameron 2003; Mösta et al. 2018), and neutron star mergers (NSMs, e.g., Lattimer & Schramm 1974; Chornock et al. 2017). The latter site recently gained a lot of attention since, for example, Pian et al. (2017) found indications for short-lived r-process isotopes in the spectrum of the electromagnetic afterglow of the gravitational wave event GW170817 that was detected and confirmed as an NSM by the LIGO experiment (Abbott et al. 2017). The authors, however, could not single out any individual elements. Only later, direct spectroscopic investigations revealed the newly produced neutron-capture element Sr in this NSM (Watson et al. 2019). Nonetheless, as stressed by, for instance, Côté et al. (2019) and Ji et al. (2019), other sites like MR SNe may still be needed to explain the full budget of r-process elements observed in the Galaxy.

3.5 Globular cluster self-enrichment

Given sufficiently high temperatures, the CNO cycle branches out to the NeNa ($\gtrsim 2 \cdot 10^7$ K) and MgAl ($\gtrsim 7 \cdot 10^7$ K) cycles, which are presented in Figure I.12.

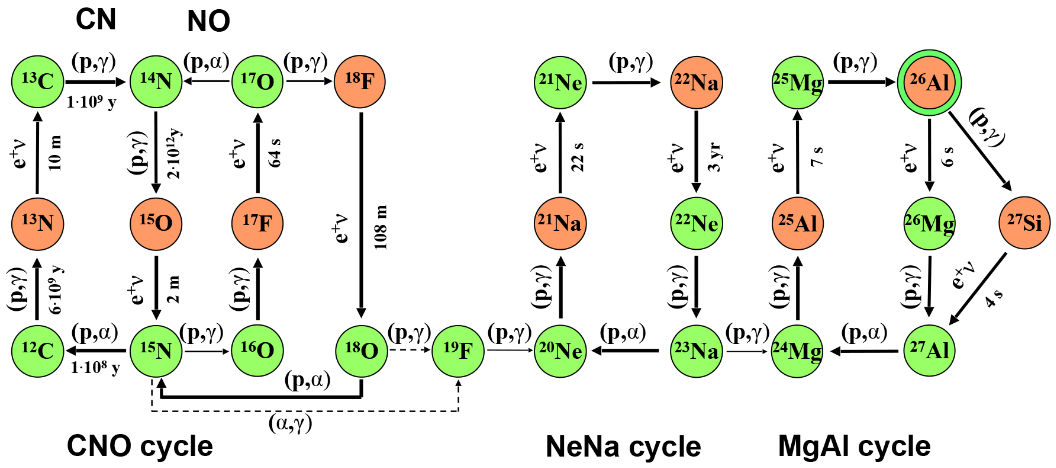

FIGURE I.12: CNO and higher H burning cycles, ordered by the temperatures that are required to trigger the reactions (increasing from *left* to *right*). Nuclides that are stable on the relevant timescales are shown in green, whereas unstable species are depicted by orange-filled circles. ^{26}Al has both a β^{+}-unstable excited state and a stable ground state. Reproduced by permission from figure 1 in Boeltzig et al. (2016). Copyright © 2016, Springer Nature.

Even higher temperatures in excess of $8 \cdot 10^7$ K and $18 \cdot 10^7$ K furthermore enable the penetration of the Coulomb barrier of heavier nuclei to produce Si and K, respectively (Prantzos et al. 2017). These H-burning reaction chains have been proposed to be the production mechanisms causing the anticorrelations seen in GCs (e.g., Prantzos et al. 2007).

There are three viable candidates for astrophysical sites that may host these processes and have led to the enrichment of the 2P. One possibility lies in hot bottom burning at the bottom of the convective envelope of intermediate-mass ($\sim$3-8 $M_\odot$) AGB stars as shown by, for instance, D'Antona et al. (2016). Another option are fast-rotating massive ($\gtrsim 15\,M_\odot$) stars that provide the necessary dredge-up of core-processed material to the surface via rotation-induced mixing (Krause et al. 2013). Finally, Denissenkov & Hartwick (2014) favor supermassive ($\sim 10^4\,M_\odot$) stars as production site. The authors propose that these exotic hypothetical objects may have formed either by a monolithic collapse of a primordial gas cloud, or by rapid mergers of massive stars. In spite of the tremendous modeling efforts made in the field, there are still various degrees of fine tuning needed to reproduce observational findings. The debate concerning which of the former nucleosynthesis sites (or combinations thereof) was responsible for 2P stars was reviewed by Bastian & Lardo (2018) and the authors show that it is far from being settled.

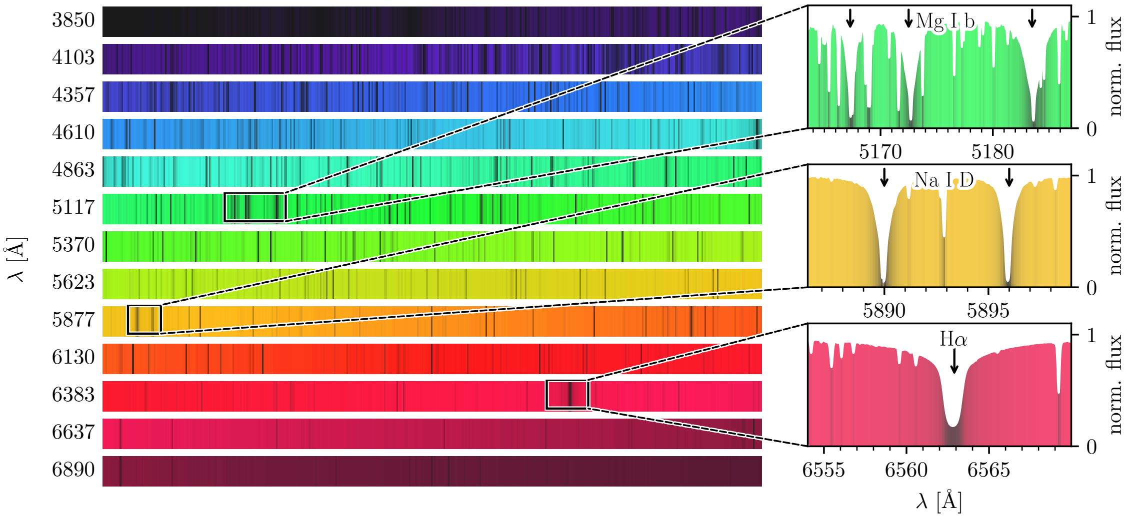

FIGURE I.13: Visual spectrum of the Sun at $R \sim 150\,000$. In the *left panel*, the continuous spectrum from 3850 Å to 7400 Å is shown in 13 parts, where the wavelength, λ, increases from the *upper left* to the *lower right* and is furthermore color-coded. Starting wavelengths for each part are presented on the *left*. The gradual darkening towards low and high λ is meant to represent the black-body emission spectrum (cf., Figure I.14), whereas localized dark vertical stripes indicate the position of absorption lines. Three of the more prominent absorption features – that is, the Mg I b triplet, the Na I D doublet, and the Hα profile – are shown as one-dimensional zoom-in spectra on the *right*. The data were obtained and published by Hinkle et al. (2000) using the echelle spectrograph at the Coudé Feed telescope on Kitt Peak, Arizona.

4 The characterization of stars through spectroscopy

As already indicated at the beginning of this introduction, spectroscopic studies of stars can reveal a detailed picture of their structure and composition, which is a pivotal piece of information for most – if not all – fields of astronomy. In order to split incoming stellar light into its colors (the energy or wavelength of the photons) it has to pass a dispersive element, which constitutes the integral part of any spectrograph[15]. The role of this optical element is to modify the incident light such that different wavelengths propagate on different spatial trajectories for them to be recorded separately by the detector. Dispersive elements range from being as simple as a transmission prism (typically low resolving power; used in the surveys by, e.g., Beers et al. 1985a and Christlieb 2003) to reflective diffraction gratings in echelle configuration that are operated at high angles of incidence to achieve high resolutions. Additionally, in order to achieve larger wavelength coverage given a

---

[15] Sometimes also termed spectrometer in resemblance of the process of measuring the spectrum.

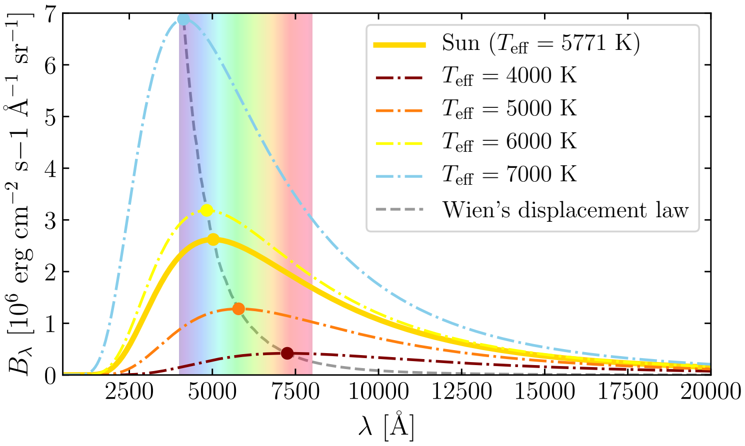

FIGURE I.14: Spectral energy distributions for black bodies of temperatures between 4000 K and 7000 K. A black body spectrum for the solar $T_{\rm eff}$ (5771; Heiter et al. 2015) is highlighted with a solid dark yellow line. Rainbow colors in the background show the visual wavelengths in the range $\sim$ 4000 to 8000 Å. The gray-dashed line represents Wien's displacement law, stating that the peak wavelength of the distribution behaves as $\lambda_{\rm peak} = 2.898 \cdot 10^7$ Å K$/T_{\rm eff}$.

fixed detector size, an additional low-dispersion grating can be operated as cross-disperser to separate spectral orders in perpendicular direction to the dispersion direction of the main grating. The latter setup was used to acquire the spectrum that creates the foundation of the illustration presented in Figure I.13. It shows the visual part of the solar spectrum where the Sun emits most of its electromagnetic radiation.

To first order, the spectral energy distribution of the Sun (and of every other star) in this regime resembles black-body radiation, which is entirely driven by the effective temperature, $T_{\rm eff}$, of the object it is emitted from as described in the works of Kirchhoff (1860), Wien (1893), and Planck (1901). For a black-body, the energy radiated away per unit area per unit wavelength per time takes the form

$$B_\lambda(\lambda, T_{\rm eff}) = \frac{2hc^2}{\lambda^5} \frac{1}{e^{ch/(\lambda k_{\rm B} T_{\rm eff})} - 1} \tag{I.2}$$

or

$$B_\nu(\nu, T_{\rm eff}) = \frac{2h\nu^3}{c^2} \frac{1}{e^{h\nu/(k_{\rm B} T_{\rm eff})} - 1} \tag{I.3}$$

in frequency notation. Here, c is the speed of light and h the Planck constant. This relation is also called Planck curve. Spectra of perfect black bodies at various $T_{\rm eff}$ are displayed in Figure I.14. Already more than 200 years ago, Fraunhofer (1817) found that the solar spectrum is in fact discontinuous and reported the existence of darker lines that are imprinted on the continuous component. Three of those discovered lines are highlighted on the right-hand side of Figure I.13. Kirchhoff & Bunsen (1860) associated the positions of the dark lines in the solar spectrum with the same lines measured in emission spectra of terrestrial chemical elements and proposed that the Sun contains those elements that act as absorbers in the solar photosphere – that is, the part of the atmosphere where its spectrum forms. In this section, I briefly summarize chief ingredients for the physical description of stellar atmospheres, line formation, and stars as a whole, which are ultimately used to deduce their systemic velocities and chemical composition by utilizing spectroscopic observations.

4.1 Radial velocities

For the purposes of Galactic archaeology, systemic radial velocities are commonly the most straightforward quantity to extract from stellar spectra. The restriction to Galactic archaeology is made here because precisions (and accuracies) of the order of a few 100 m s^{-1} are typically desired. Much greater care has to be taken, for example, when aiming for the detection of extrasolar planets using the radial velocity technique (e.g., Mayor & Queloz 1995; commonly rather $\sim$ 1-10 m s^{-1} precision), where the instrument stability over time and stellar activity pose challenges on their own (Queloz et al. 2001).

The spectrum of an object moving towards or away from the observer experiences a wavelength shift, the so-called Doppler-Fizeau shift

$$\Delta\lambda = \lambda_0 \left(\sqrt{\frac{1 + v_r/c}{1 - v_r/c}} - 1 \right), \tag{I.4}$$

with v_r being the line-of-sight radial velocity of the object (by convention negative for approaching sources) and λ_0 being the wavelength emitted in the rest frame of the source. The result of the relative movement is an effective blue- or redshift in the case of negative and positive v_r, respectively. In the non-relativistic regime (i.e., $v_r \ll c$), Equation I.4 simplifies to

$$\Delta\lambda = \lambda_0 \frac{v_r}{c}. \tag{I.5}$$

There are essentially two ways to determine v_r from stellar spectra. The first option is to directly measure $\Delta\lambda$ in the observed spectrum by identifying isolated lines, fitting their central position, and by comparison to the corresponding rest wavelengths. In practice, this is often hampered by too many lines being blended with other lines or other effects that lead to profile asymmetries. In addition, in case of noisy data[16], robust fits may not always be feasible. A method that is less prone to these obstacles

---

[16] Expressed by the signal-to-noise ratio, S/N, which is frequently given per pixel. Some other used variants are providing this value per Å or resolution element (i.e., FWHM).

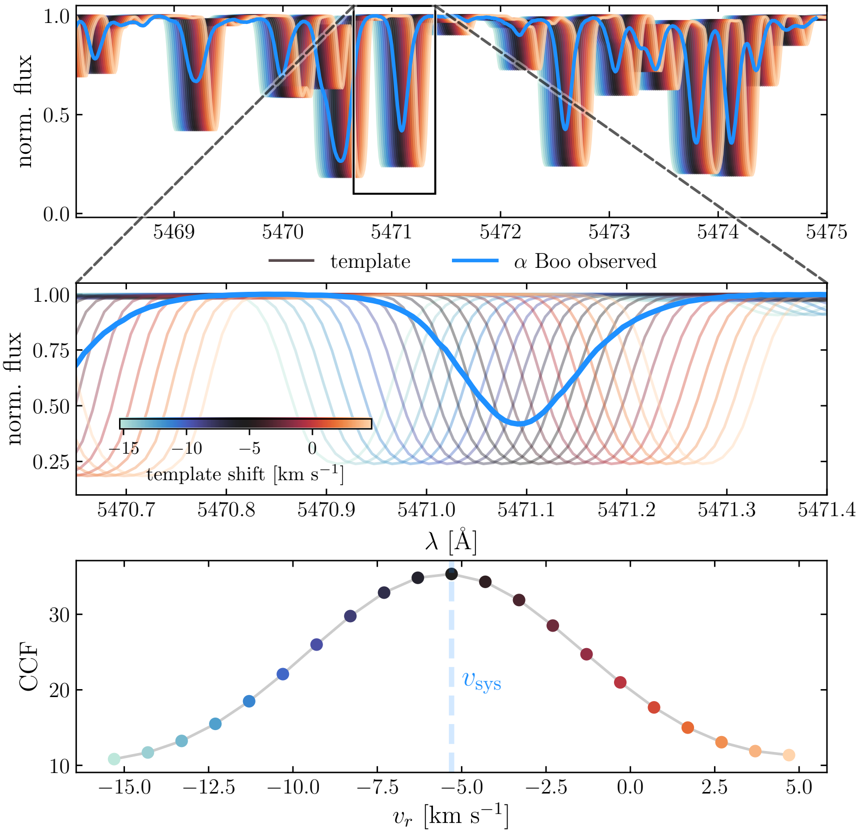

FIGURE I.15: Illustration of the cross-correlation technique for the determination of stellar radial velocities. *Top panel with zoom-in view*: the observed spectrum of α Boo by Hinkle et al. (2000) in the heliocentric rest frame (i.e., corrected for the motion of the Earth around the Sun) is visualized in blue. Colored curves in the background represent a synthetic spectrum that is shifted in velocity space from the systemic velocity, $v_{\mathrm{sys}} = 5.299$ km s^{-1} (Soubiran et al. 2018), by ±10 km s^{-1} in steps of 1 km s^{-1} (see color bar). *Bottom panel*: cross-correlation function (CCF). The systemic velocity is marked by a dashed vertical line.

employs the cross-correlation technique, which was introduced by Tonry & Davis (1979). In its essence, the method is a template matching approach where a template spectrum is shifted in radial velocity space with the best match to the observed spectrum marking v_r. Either synthetic spectra or observed spectra of known velocity (in the latter case of similar properties to the target as encountered in, e.g., studies of binaries or pulsating variables) can function as templates. The numerical formulation for the so-called cross-correlation function between the observed spectrum, o, and the template, t, is

$$\mathrm{CCF}(v_r) = \sum_i o(\lambda_i) t'(\lambda_i) \,, \tag{I.6}$$

where the spectrum t' corresponds to $t\left(\lambda \cdot \left(1 + \frac{v_r}{c}\right)\right)$ mapped onto the dispersion scale of the observed spectrum[17]. The latter rebinning becomes necessary because a

---

[17] In case of unnormalized spectra, it may be desirable to perform a Fourier filtering that removes large-scale fluctuations both from the observed spectrum and the template and thus prevents spurious peaks in the CCF. Moreover, for the purpose of

shift in velocity space does firstly not imply an integer pixel shift and secondly renders the pixel width itself a function of λ. An alternative approach is to perform the analysis in Fourier space, where the necessary convolution turns into a summation, which is computationally more efficient. Figure I.15 shows an example for a CCF that was obtained from a portion of a spectrum of the RGB star Arcturus (α Boo) and a synthetic template.

4.2 Fundamental stellar parameters

Moving away from the radial velocity – which is dependent on the observer's position – from now on intrinsic stellar properties will be discussed. Idealizing stars as black bodies allows for several profound deductions of interdependences among their structural properties when combined with the assumption of spherical symmetry. The Stefan-Boltzmann law for ideal black-bodies indicating the relation between the radiant flux (i.e., the total amount of energy that is emitted per unit area and unit time) and T_{eff} follows from integration of Equation I.3:

$$\mathcal{F} = \int_0^\infty B_\lambda \mathrm{d}\lambda = \sigma_{\mathrm{SB}} T_{\mathrm{eff}}^4, \tag{I.7}$$

where σ_{SB} is the Stefan-Boltzmann constant. Given a stellar radius, R[18], this can be utilized to deduce the total luminosity, L, by multiplying with the surface area:

$$L = A\mathcal{F} = 4\pi R^2 \sigma_{\mathrm{SB}} T_{\mathrm{eff}}^4. \tag{I.8}$$

Moreover, the gravitational surface acceleration, also called surface gravity, connects the stellar mass, M, to R via

$$g = \frac{GM}{R^2} \text{ or } \log g = \log g_\odot - \log \frac{M}{M_\odot} + 2\log \frac{R_\odot}{R}, \tag{I.9}$$

with the latter expression relating to the same properties for the Sun. Finally, the stellar age – in other words, the time that has passed since the star was formed from its natal gas cloud – together with M are the fundamental properties that dictate how the other properties manifest[19]. Both parameters combined indicate the evolutionary state of the star, which essentially maps the thermodynamic conditions in its core

---

estimating peak significances, the signal of the continuum can be removed by subtracting unity from the normalized spectra prior to the cross-correlation.

[18] In light of the fact that a star rather exposes a gradually changing density profile than an abrupt phase transition, the (effective) stellar radius is typically defined as the radius where a certain optical depth is reached, which makes the concept wavelength-dependent.

[19] Telling the whole truth, rotation and the chemical composition with its impact on the mean molecular weight also contribute to coining the stellar structure. However, the latter parameter will be dealt with later in this section as it is at the same time both an input and an output quantity in iterative chemical abundance studies.

(see Section 3.2) and the feedback in the outer layers in order to maintain hydrostatic equilibrium. The process of stellar evolution can be modeled by evolving a simulated core and by simultaneously solving for fundamental stellar structure equations, which results in a set of theoretical structural parameters for every instance in time throughout a star's evolution (Demarque et al. 2004; Dotter et al. 2008; Marigo et al. 2017).

Of the aforementioned fundamental properties, arguably the most important ones for chemical abundance studies are T_{eff} and $\log g$ because – apart from the elemental abundances themselves – they govern the formation of spectral lines (Sections 4.4 and 4.6). In the following, several techniques that are in use for the derivation of T_{eff} and $\log g$ are discussed. Since this thesis is focused on stars of spectral types F, G, and K, only methods of relevance for those are mentioned.

4.2.1 Stellar effective temperatures

The most direct way to constrain T_{eff} utilizes interferometric measurements of the angular extent of a resolved star. The concept of interferometric temperatures relies on the scaling of its bolometric flux with its angular diameter and temperature and directly follows from Equation I.7 (e.g., Heiter et al. 2015):

$$F_{\mathrm{bol}} = \sigma_{\mathrm{SB}} \left(\frac{\Theta_{\mathrm{LD}}}{2} \right)^2 T_{\mathrm{eff}}^4, \tag{I.10}$$

with σ_{SB} being the Stefan-Boltzmann constant and Θ_{LD} the limb-darkened angular diameter

$$\Theta_{\mathrm{LD}} = \frac{2R}{d}, \tag{I.11}$$

where d is the distance to the star. By measuring both F_{bol} and Θ_{LD}, one can directly infer the temperature of the star using the above relations.

Usually, flux-calibrated spectra of the studied targets for the purpose of direct integration are not readily available. An alternative is to calculate bolometric fluxes from the photometric magnitudes in the V-band via

$$F_{\mathrm{bol}} = \frac{1}{4\pi (10\,\mathrm{pc})^2} L_0 10^{-0.4(V - A(V) + BC_V(T_{\mathrm{eff}}, [\mathrm{Fe/H}]))}. \tag{I.12}$$

Here L_0 is the zero-point luminosity and BC_V is the bolometric correction. BC_V can be determined using, for instance, the empirical calibrations by Alonso et al. (1999b), which themselves depend on T_{eff} and [Fe/H].

Meaningful angular diameters can unfortunately only be obtained for nearby stars ($\lesssim$ 100 pc) and are therefore impractical for a broader application. Nevertheless, Blackwell & Shallis (1977) noted that it is possible to derive the angular diameter from the monochromatic flux in a photometric band together with the integrated flux, which can then be used to infer T_{eff}. Since the flux in the infrared is much less temperature dependent than in the visual (see Figure I.14), the monochromatic flux is derived from infrared bands. This is why the method is called infrared flux method (IRFM).

Throughout the years, several studies have compiled stellar samples for which IRFM temperatures could be derived (e.g., Alonso et al. 1996a, 1999a; Ramírez & Meléndez 2005). These were then used to constrain empirical relations between photometric colors and T_{eff} with some weak dependence on [Fe/H] (Alonso et al. 1996b, 1999b; Ramírez & Meléndez 2005; Casagrande et al. 2010). Using temperatures from colors has the tremendous advantage that their applicability is not limited to close-by stars but can be expanded out to large distances with the only requirement being that at least two photometric magnitudes are obtainable.

The main caveat of photometric T_{eff} scales is that they are sensitive to reddening, that is, the circumstance that interstellar dust has a stronger attenuation effect on bluer wavelengths than it has on, for instance, the infrared (Cardelli et al. 1989). If not taken into account, reddening therefore leads to systematically underestimated temperatures. This is problematic in particular for studies of stars with poorly constrained reddening estimates, which may be encountered close to the Galactic midplane or the bulge (cf., Figure I.2). For dense regions like the bulge or GCs further problems emerge from low-resolution photometric surveys due to crowding, which prevents the separation of sources. Not only – but especially – in these situations it may be desirable to deduct T_{eff} from the spectra under scrutiny themselves. Apart from fitting entire spectral regions (discussed in more detail in Section 4.7), three approaches shall be mentioned here:

The wings of spectral lines of the Balmer series of neutral H are highly sensitive to the stellar effective temperature with little to no dependence on any other stellar parameter. Vice versa, these profiles can be modeled in order to constrain T_{eff} from an observed spectrum, as has been showcased by Fuhrmann et al. (1993), Barklem et al. (2002), Amarsi et al. (2018), and Giribaldi et al. (2019). Nevertheless, a mentioning should be given to aspects of both theoretical and observational nature that complicate these measures. Section III.4.1.2 provides a detailed description of these aspects.

Another spectroscopic means to determine T_{eff} is the enforcement of excitation balance of lines at different lower excitation energy. These expose different sensitivities to T_{eff}. In the application of the method, abundances of spectral lines are inferred using a model with free parameters (see Sections 4.3, 4.4, and 4.6 for details). One of the free parameters is the temperature, which is tuned until the abundances from high-excitation lines equal the ones from low-excitation lines (e.g., chapter 16 in Gray 2005). The adopted input T_{eff} at equilibrium can then be assumed to be representative for the star. This method is applied and discussed in great depth in Sections II.2.1 and III.3.3. Furthermore, in the latter section, a discussion of problems that may arise is outlined, and strategies to overcome them are deployed.

A variation of the excitation balance approach is the line-depth ratio (LDR) method, which uses the same physical principle. The approach utilizes the ratio of line depths – that is, the fractional flux depressions of line cores with respect to the continuum level – of low-excitation and high-excitation features and relates them to T_{eff} via empirically determined relations (Gray & Johanson 1991; Kovtyukh et al. 2003). A variation of this principle is delineated in Chapter II.

4.2.2 Stellar surface gravities

Asteroseismology enables the most accurate and precise way to constrain $\log g$ by investigating periodic oscillations in stellar observables, which are mostly measured by means of brightness variations but sometimes also by mapping v_r changes. These oscillations are caused by small perturbations to the hydrostatic equilibrium state. If these perturbations are induced by surface convection (as is the case in the Sun), asteroseismologists refer to solar-like oscillations (e.g., Kjeldsen & Bedding 1995). The asteroseismic scaling relation

$$\log g_{\mathrm{seis.}} = \log g_{\odot} + \log\left(\frac{f_{\mathrm{max}}}{f_{\mathrm{max},\odot}}\sqrt{\frac{T_{\mathrm{eff}}}{T_{\mathrm{eff},\odot}}}\right) \tag{I.13}$$

relates the frequency of maximum power, f_{max}, of stars showing these solar-like oscillations to their $\log g$. Being largely model-independent (Gai et al. 2011) and highly sensitive to f_{max}, asteroseismic gravities that are inferred this way are unchallenged in terms of accuracy and precisions (with the possible exception of the few binary systems with known orbital parameters; see below), which are frequently superior to other methods by about one order of magnitude. As one of the first applications of its kind in the metal-poor regime, an asteroseismic gravity estimate for the giant star HD 20 is obtained from a TESS light curve in Section III.3.1.

Lacking high-precision time series, an alternative way to deduce surface gravities follows from the relation that is obtained when solving Equation I.8 for R and substituting it into Equation I.9:

$$\log g = \log g_{\odot} + \log \frac{M}{M_{\odot}} + 4 \log \frac{T_{\rm eff}}{T_{\rm eff,\odot}} + \log \frac{L_{\odot}}{L}. \tag{I.14}$$

The latter expression is useful if no prior estimates for R (e.g., by means of angular diameters) are available. Otherwise, Equation I.9 can be used directly. In either case, the stellar mass is the only hitherto unconstrained parameter (assuming L and $T_{\rm eff}$ have already been determined). In the literature, there is a variety of approaches to infer masses. One possibility is to assume a mass based on age and stellar evolution arguments, as is sometimes done in dwarf galaxy or GC studies, where $\sim$0.8 $M_{\odot}$ is a reasonable assumption for old RGB stars (e.g., Koch et al. 2008a; Koch & McWilliam 2008). In cases where nothing about the underlying population and therefore age/evolutionary stage is known in advance, theoretical stellar evolution tracks can be used to determine a mass from the position of a star in $T_{\rm eff}$-L-[Fe/H] space (e.g., Heiter et al. 2015). In the unlikely event of the star residing in a binary system (not very unlikely in itself) of known orbital parameters (rather unlikely), the mass can be trivially obtained from Kepler's laws of orbital motion (e.g., Pourbaix et al. 2002).

Spectroscopically, $\log g$ can be determined from pressure-broadened – and thus gravity-sensitive – strong lines like the ones belonging to the Mg I b triplet in metal-rich to moderately metal-poor dwarfs (e.g., Ramírez et al. 2006), or from the width of the chromospheric emission feature in the core of the Ca II K line in cool stars (spectral types G and later), which is also known as the Wilson-Bappu effect (Wilson & Vainu Bappu 1957). A spectroscopic routine to determine $\log g$ in a wider range of applicability lies in the so-called ionization balance. Similar to the method of excitation balance, this method strives to adjust model gravities until abundances from largely gravity-insensitive neutral lines and from gravity-sensitive ionized lines agree. Again, much like the excitation balance approach, ionization balance comes with its own shortcomings that are thoroughly discussed in Sections III.3.3 and III.3.4.

4.3 Modeling stellar atmospheres

Once the fundamental stellar structure parameters $T_{\rm eff}$, $\log g$, and metal content are set, a model of a star's photosphere can be constructed. Such models are the central prerequisites for solving the radiative transfer with the ultimate goal to compute synthetic line profiles that are used for the deduction of chemical abundances.

To approach real conditions in a star as close as possible, one would ideally require a detailed temporal and spatial description of its structure, in order words, it would be desirable to have a fully 3D and hydrodynamic model in which radiative transfer processes can be simulated. Tremendous steps in this direction have been made by, for example, Freytag et al. (2012) and Magic et al. (2013) who realistically simulated convection and as a consequence surface granulation patterns in stars that have proven to reproduce actual observations of the solar surface remarkably well.

Unfortunately, the handling of the available hydrodynamic models is as of yet not possible without investing considerable computational resources. This is a major inhibiting factor for their widespread usage, on top of the circumstance that many of the frequently used radiation transfer solvers cannot straightforwardly incorporate them. Still, with a few simplifying assumptions it is possible to construct atmospheric models that approximate stellar photospheres sufficiently well to procure accuracies that satisfy most scientific needs. In this respect, there are two grids of stellar atmospheres that are most commonly used. These are the grids generated with the `MARCS` code by Gustafsson et al. (2008) and the `ATLAS9` code by Castelli & Kurucz (2003), the latter of which is employed throughout the present work. Conceptually, both codes have very similar base presumptions: They rely on hydrostatic equilibrium conditions, a treatment of convection by means of the mixing-length theory with convective overshoot (see Castelli 1996 for details for the treatment in the `ATLAS9` code), and radiative transfer under the assumption of local thermodynamic equilibrium (LTE, discussed in more detail in the following section). While the `MARCS` grid offers spherical as well as plane-parallel atmospheres, `ATLAS9` only contains the plane-parallel option.

A model atmosphere constructed by the above codes is consisted of layers that are fully described by some variant of the thermodynamic properties temperature (T), gas pressure (P_g), electron density (n_e), and the Rosseland mean opacity on a mass scale (κ). The latter quantity is a weighted frequency average of the specific opacity, κ_ν, at frequency ν where the temperature derivative of the Planck curve (Equation I.2) acts as weight function. Since classical physical length scales (i.e., in units of m or km) do not have a lot of meaning in the realm of stellar atmospheres, a more convenient quantity is the unitless Rosseland optical depth

$$\tau_\mathrm{Ross} = \int_0^x \rho(x')\kappa(x')\mathrm{d}x', \tag{I.15}$$

which incorporates the attenuation along the line of sight from the observer ($x' = 0$) to the atmospheric layer at $x' = x$. In the latter expression $\rho(x')$ stands for the density profile. `ATLAS9` atmospheres consist of 72 layers with a log-linear spacing in

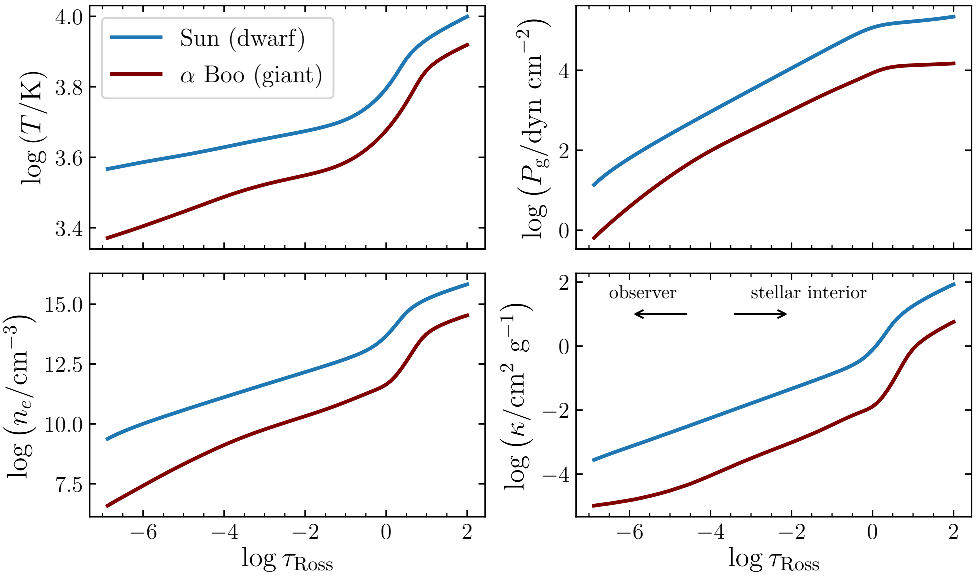

FIGURE I.16: Structure of `ATLAS9` atmospheres for the Sun (blue) and α Boo (red) as representatives for dwarf and giant stars, respectively. Shown are from the *upper left* to the *lower right* the common logarithm of the properties temperature, T, gas pressure, P_g, electron density, n_e, and the Rosseland mean opacity, κ, as a function of the optical depth, τ_Ross. The adopted input parameters are $T_\mathrm{eff} = 5771$ K, $\log g = 4.44$ dex, and $[\mathrm{M/H}] = 0.00$ dex for the Sun and $T_\mathrm{eff} = 4286$ K, $\log g = 1.64$ dex, and $[\mathrm{M/H}] = -0.57$ dex for α Boo (Heiter et al. 2015). Arrows in the *lower right panel* indicate the directions toward the observer and the stellar core and they apply analogously to the other panels.

$\log \tau_\mathrm{Ross}$ from -6.875 to $+2.000$ in steps of 0.125. Figure I.16 exemplarily illustrates the atmospheric structures for models of the Sun and α Boo, which function as examples for a dwarf and a giant, respectively.

4.4 Basics of radiative transfer

Having a suitable model atmosphere at hand, a stellar spectrum can be computed by solving the radiative transfer in that atmosphere. The key steps are mentioned here following derivations that were taken from Gray (2005). Since there are commonly no analytical solutions to the involved differential equations, for practical computational applications, numerical approximations are used and integrals are merely summations over atmospheric layers or wavelength/frequency intervals of finite width.

The idea behind radiative transfer calculations is to track the radiation field and its changes due to interaction with matter from the bottom to the top of the modeled photosphere in order to deduce the specific intensity, I_ν, as it emerges from the stellar surface. In each atmospheric layer of depth $\mathrm{d}x$ along the line of sight, the change in

I_ν as the radiation field propagates from the bottom to the top can be expressed as

$$\mathrm{d}I_\nu = (j_\nu - \kappa_\nu I_\nu)\rho \mathrm{d}x = (\frac{j_\nu}{\kappa_\nu} - I_\nu)\mathrm{d}\tau, \tag{I.16}$$

where the differential form of Equation I.15 was employed for the right-hand expression. The first component accounts for the two additive sources of radiation, which are emission from the layer itself and scattering of photons into the considered path of radiation. Both combined are represented by the emission coefficient j_ν. Analogously, the second term, parametrized by the extinction coefficient κ_ν, represents the radiation that is lost, both by scattering in a different direction and by absorption in the atmospheric layer. An important observation for the absorption term is that the amount of intensity that is lost is directly proportional to the incoming intensity. Using the expression of the source function

$$S_\nu = \frac{j_\nu}{\kappa_\nu}, \tag{I.17}$$

which encapsulates the total emitted intensity from the layer, Equation I.16 takes the commonly used form of the basic differential equation for radiative transfer

$$\mathrm{d}I_\nu = (S_\nu - I_\nu)\mathrm{d}\tau. \tag{I.18}$$

For realistic applications in stellar atmospheres, S_ν is composed of various continuous and discrete components, in other words there are contributors that vary gradually with wavelength and thereby shape the large scale structure of the final spectrum, and there are those that are very localized in wavelength/frequency. This latter component are the spectral lines. The source function can be decomposed into continuous and discrete (line) terms like so

$$S_\nu = \frac{j_\nu^\mathrm{l} + j_\nu^\mathrm{c}}{k_\nu^\mathrm{l} + \kappa_\nu^\mathrm{c}} = \frac{S_\mathrm{l} + (\kappa_\nu^\mathrm{c}/k_\nu^\mathrm{l})S_\mathrm{c}}{1 + \kappa_\nu^\mathrm{c}/k_\nu^\mathrm{l}}, \text{ where } S_\mathrm{l} = \frac{j_\nu^\mathrm{l}}{k_\nu^\mathrm{l}} \text{ and } S_\mathrm{c} = \frac{j_\nu^\mathrm{c}}{\kappa_\nu^\mathrm{c}}. \tag{I.19}$$

The superscipt indices l and c denote line and continuous quantities, respectively. The continuous absorption coefficient summarizes several free-free and bound-free (charged-)particle interactions like collisions and atomic transitions. In cool stars and at visual to infrared wavelengths, the continuous absorption is dominated by the bound-free transition of the loosely bound H^- ion[20], whereas metal absorption

---

[20] This source of continuous opacity is strongly governed by the α-elements O and Mg, whose loosely bound valence electrons render them important electron donors. The H^- opacity will become relevant again in Section III.6.2, where the impact of the temperature dependence of the H^- opacity explains temperature sensitivities of the abundances that are inferred from certain lines.

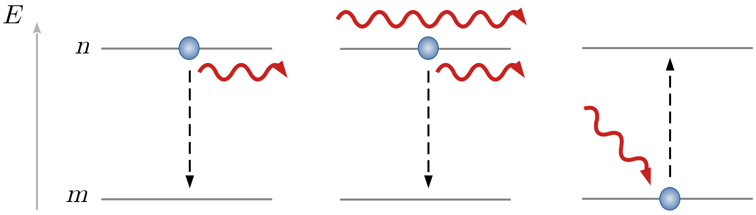

FIGURE I.17: Types of bound-bound transitions for an electron between the two energy states m and n. From *left* to *right*, these are emission, stimulated emission, and absorption. Photons are shown in red and electrons are represented by blue-filled circles with dashed arrows pointing in the direction of the end state of the respective transition.

dominates in the ultraviolet, and bound-bound transitions of H govern in the high-temperature regime.

A spectral line – be it in emission or absorption – involves the discrete transition between two bound energy levels of an electron in an ion or atom. From now on, the lower excitation state (χ_{ex}) shall be indicated by subscript m and the upper excitation state by subscript n. As illustrated in Figure I.17, there are three types of bound-bound transitions: emission, stimulated emission, and absorption, the latter of which are coupled to the radiation field. In LTE, it is assumed that inter-particle collisions are so frequent that they dominate the distribution of the available energy over the excitation and ionization stages. Then, the dependence of S_{l} on I_ν becomes negligible and the ratio between fractional population numbers at the upper and lower states is determined by the Boltzmann equation

$$\frac{N_n}{N_m} = \frac{g_n}{g_m} e^{-\Delta\chi_{\mathrm{ex},nm}/(k_{\mathrm{B}}T)}. \tag{I.20}$$

In this relation, g_n and g_m are statistical weights. Another important parameter is the fractional ionization of the ionization state to which the line is associated. The knowledge of this share is required in order to determine how many particles among all particles of a chemical species are even capable to undergo the bound-bound transition in the first place. The population of the ith ionization stage is computed through

$$\frac{n_i}{n_{\mathrm{tot}}} = \frac{n_i}{\sum_{j=0}^{Z} n_j}, \tag{I.21}$$

for which in the collision-dominated case the Saha equation dictates

$$\frac{n_{j+1}}{n_j} = \frac{2\,(2\pi m_e)^{3/2}\,(k_{\mathrm{B}}T)^{5/2}\,u_{j+1}(T)}{P_e h^3 u_j(T)} e^{-\Delta I_{j+1,j}/(k_{\mathrm{B}}T)}, \tag{I.22}$$

where m_e is the electron mass, P_e is the electron pressure, $\Delta I_{j+1,j}$ is the difference between the ionization potentials of the $j+1$th and jth ionization stages, and u_{j+1} and u_j are the respective partition functions.

The general line source function in Equation I.19 takes the form

$$S_l = \frac{j_\nu^l}{\kappa_\nu^l} = \frac{N_n A_{nm} \psi(\nu)/\rho}{(N_m B_{mn} - N_n B_{nm})\, \phi(\nu)/\rho}. \tag{I.23}$$

Here, A_{nm}, B_{mn}, and B_{nm} are the transition-specific Einstein rate coefficients for spontaneous emission, absorption, and stimulated emission, respectively. Moreover, $\psi(\nu)$ and $\phi(\nu)$ are emission and absorption profiles in frequency space, which encode the likelihood of a photon of frequency ν being emitted, absorbed, or leading to stimulated emission. Inserting the relations

$$B_{nm} g_n = B_{mn} g_m \quad \text{and} \quad A_{nm} = \frac{2h\nu^3 B_{nm}}{c^2} \tag{I.24}$$

between the Einstein coefficients yields

$$S_l = \frac{2h\nu^3}{c^2} \frac{1}{(N_m/N_n)(g_n/g_m) - 1} \frac{\psi(\nu)}{\phi(\nu)}, \tag{I.25}$$

which under the LTE assumption (Equation I.20) and by using $\Delta\chi_{\mathrm{ex},nm} = h\nu_0$ evaluates to

$$S_l = B_\nu(\nu_0, T), \tag{I.26}$$

that is, the Planck curve from Equation I.2. Here, $\psi(\nu) = \phi(\nu)$ was assumed since the equilibrium state demands equal rates in emission and absorption.

Finally, the only missing ingredient for Equations I.18 and I.19 to be fully determined is a parametrization of the line absorption coefficient, κ_ν^l, which already appeared in the denominator of Equation I.23. A rearrangement of that denominator under consideration of Equations I.20 and I.24 leads to

$$\kappa_\nu^l = \frac{N_m B_{mn}}{\rho} \left(1 - e^{\Delta\chi_{\mathrm{ex},nm}/(k_\mathrm{B} T)}\right) \phi(\nu). \tag{I.27}$$

The Einstein B_{mn} coefficient are commonly tabulated as literature data (either theoretical or preferentially measured in the laboratory) in the form of the oscillator strength

$$gf = g_m f_{mn} = -g_n f_{nm} = \frac{g m_e c h \nu_0}{\pi e^2} B_{mn} \quad \text{(in the cgs system)}. \tag{I.28}$$

It is evident from Equation I.27 that κ_ν^{l} is directly proportional to the number of absorbers, which is the circumstance that is used when inferring chemical abundances by comparing models to observed spectra. The line shape function $\phi(\nu)$ is a convolution of a number of broadening profiles. These are the natural line broadening, which is a result of the energy levels having finite widths that are a consequence from the Heisenberg uncertainty principle, pressure broadening, collisional broadening, hyperfine structure, thermal broadening, and microturbulent broadening. A detailed description of each of these mechanisms is beyond the scope of this introduction and the reader is referred to, for example, Gray (2005) for further information. Nonetheless, microturbulence and hyperfine splitting shall be briefly discussed as they are relevant to some aspects of the discussed projects. The microturbulent velocity, v_{mic}, describes the velocity dispersion of the particles in the stellar atmosphere on length scales smaller than the mean free path length. The effect is the same as from thermal broadening – in other words it behaves in the same manner as a Gaussian convolution of dispersion $\sigma_\lambda = \lambda v_{\mathrm{mic}}/c$. The broadening by hyperfine structure (HFS), on the other hand, goes back to tiny shifts within the energy levels that are caused by the coupling of the nuclear angular momentum to the electron spin[21]. McWilliam et al. (1995) showcased that the HFS of species with nonzero nuclear spin can have a considerable impact on inferred abundances, reaching corrections as high as 0.7 dex for the important *r*-process tracer Eu.

4.5 A note on non-local thermodynamic equilibrium

The main prerequisite of LTE radiative transfer as it is outlined above is that the line source function S_l is independent from I_ν, in other words, that collisional excitation and de-excitation is the prevailing mechanism that keeps the populations of the energy levels at balance. However, in the general case the level population also depends on radiative processes like (stimulated) emission and absorption and thereby the statistical equilibrium couples to the radiation field. In fact, as demonstrated by, among others, Asplund (2005), in many real astrophysical applications the radiative rates are comparable to the collisional rates or even dominate the equilibrium state. Such conditions are met, for example, in the outer atmospheres of metal-poor giants, which are so dilute that it is more probable for a particle state to undergo radiative de-/excitation than for the particle to encounter another – most likely H – particle (see, e.g., Bergemann et al. 2012b; Lind et al. 2012, for the effect on Fe line formation).

In the above case, an appropriate physical description must involve the simultaneous

---

[21] A graphical example for HFS is provided in Section III.5.3.16 where the analysis of a line of the ^{175}Lu isotope is described.

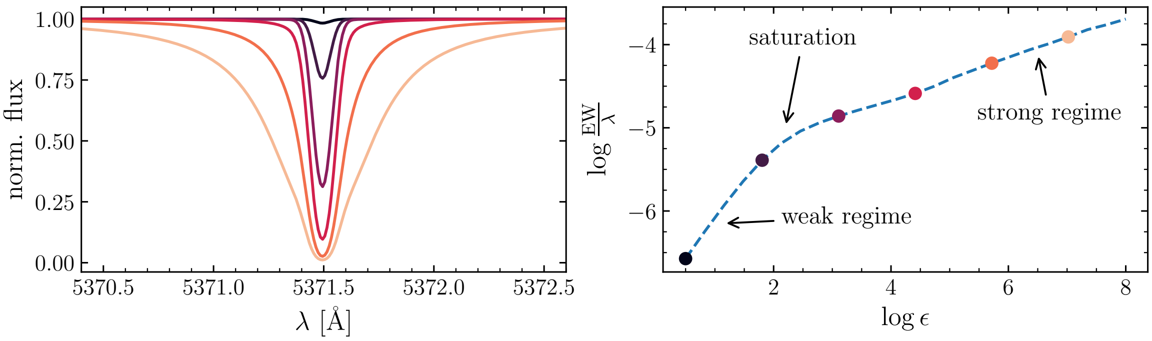

FIGURE I.18: Synthetic line profiles for the Fe I line at $\lambda = 5371.489$ Å with transition parameters $\chi_{\mathrm{ex}} = 0.958$ eV and $\log gf = -1.645$. The atmosphere model employed is the one for α Boo from Figure I.16. The profiles for Fe abundances between 0.5 dex and 7 dex are presented in the *left panel*, whereas the respective reduced equivalent widths, $\log \mathrm{EW}/\lambda$, which were obtained by profile integration, are marked on the *right* by circles of the same colors. In the same panel, the curve of growth – that is, the run of $\log \mathrm{EW}/\lambda$ with $\log \epsilon$ – is depicted by a blue-dashed line. Arrows annotate the weak regime, the region where the line core begins to saturate, and the strong-line domain.

solution of both the radiative transfer and the statistical equilibrium. Further complexity arises from the fact that individual levels within an atom are coupled radiatively, which consequently requires a model atom for which hundreds to thousands of transition populations need to be solved synchronously. Fortunately, computationally only moderately expensive codes have been developed for this purpose (e.g., Giddings 1981; Carlsson 1986; Hubeny 1988; Uitenbroek 1998). Departures from LTE that are mentioned in this study were mostly based on computations made within the `MULTI` framework (Carlsson 1986).

4.6 The inference of stellar chemical abundances

Many LTE radiative transfer solvers are in use to numerically solve Equation I.18 with the goal of generating synthetic line profiles or – more generally – stellar spectra (e.g., Sneden 1973; Kurucz 1993; Gray & Corbally 1994; Valenti & Piskunov 1996; Kochukhov 2007; Plez 2012). Throughout the projects presented here, `MOOG` by Sneden (1973) is employed in its 2017 version for LTE calculations with the inferred abundances being corrected for NLTE departures whenever possible.

As an example, the left-hand side of Figure I.18 shows `MOOG` syntheses of an Fe I feature in an α Boo-like atmosphere. With all other parameters kept fixed, the only varied quantity is the Fe abundance, $\log \epsilon$. A useful quantity to parametrize the strength of a spectral line is its equivalent width (EW), which is defined as

$$\mathrm{EW} = \int \frac{F_{\lambda,\mathrm{c}} - F_{\lambda,\mathrm{l}}}{F_{\lambda,\mathrm{c}}} \mathrm{d}\lambda \tag{I.29}$$

with $F_{\lambda,\mathrm{c}}$ and $F_{\lambda,\mathrm{l}}$ representing the continuum and line flux, respectively. Its reduced form $\log\left(\mathrm{EW}/\lambda\right)$ has a characteristic monotonic behavior with $\log\epsilon$, the so-called curve of growth (COG), which is also displayed in Figure I.18 for the exemplary line.

The COG has three characteristic parts: the weak, saturated, and strong regimes. For the weak regime of the COG an instructive relation can be approximated (e.g., Gray 2005):

$$\log\frac{\mathrm{EW}}{\lambda} = \log\epsilon + \log gf + \log\frac{\lambda}{\text{Å}} - \log\frac{5040\ \mathrm{K}}{T_{\mathrm{eff}}}\chi_{\mathrm{ex}} - \log\kappa_{\nu}^{\mathrm{c}} + \log C. \tag{I.30}$$

Here all quantities have their usual meanings as defined in the previous section and the constant C incorporates several physical constants and the fractional ionization of the ion/atom of interest. From Equation I.30 it becomes apparent why the weak regime is also referred to as the linear part where $\log\frac{\mathrm{EW}}{\lambda}$ is directly proportional to $\log\epsilon$. In this part the profile shape also behaves approximately Gaussian; hence it is easily parameterizable and the EW can be measured directly from the spectrum. The inference of abundances via measuring EWs and comparing to a COG is sometimes called EW method. Among the methods in use to compute EWs are the fully manual `IRAF` routines implemented in `splot`, the semi-automated code `EWCODE` (Hanke et al. 2017), and the fully automated tool `DAOSPEC` (Stetson & Pancino 2008).

Once the core of the line gets dimmer – that is, when its formation depth in the atmosphere becomes shallower at lower temperatures closer to the stellar exterior – the core of the line profile starts to saturate and a steadily increasing amount of absorption moves away from the central wavelength. With the formation of such extended profile wings the Gaussian approximation breaks down and a larger number of fit parameters is required to still accurately represent the profile by, for instance, a Voigt profile. Alternatively, the line profile can be fit directly using synthetic spectra as models with only the abundance itself as free parameter. The employment of the latter approach becomes mandatory particularly in those situations where blends become an issue and many lines occupy a rather confined wavelength interval, which inhibits the separation into individual line profiles. Such situations are encountered, for example, in spectra of metal-rich stars or in low-temperature stars that form strong molecular bands that are found almost everywhere in the spectrum. Yet, also in the metal-poor regime one may face strong bands in carbon-enhanced metal-poor stars (CEMP; e.g., Hansen et al. 2016).

4.7 Full spectrum fitting and data-driven approaches

Following the approaches above – that is, fitting or measuring individual spectral lines followed by the deduction of mean chemical abundances from the ensemble of lines for each species – is one way of obtaining a set of abundances for a star. The circumstance that uncertainties and systematics can be mapped on a line-by-line basis and thereby their impacts on the ensemble statistics can be traced in an unchallenged manner, certainly warrants the comparatively large time demand for both manpower and computational power. However, as larger and larger spectroscopic surveys emerged over the years, the careful analysis of individual spectra became infeasible and automated pipelines had to be – and still are in the process of being – developed.

Methods that are still rather computationally expensive but require little to no user interference are based on on-the-fly syntheses of large spectral domains that are fit to observed spectra. Examples for codes employing this method are `SME` (Valenti & Piskunov 1996) and `BACCHUS` (Masseron et al. 2016).

The canonical approach to parameterizing large datasets (i.e., thousands to millions of spectra) is the fitting of synthetic template grids. To this end, radiative transfer solvers are used to construct regular grids of spectra in stellar parameter space, which can either be rather low-dimensional (e.g., just T_{eff}, $\log g$, [M/H], and maybe [α/Fe]) or incorporate a high number of dimensions (e.g., T_{eff}, $\log g$, and [M/H], as well as a set of detailed abundances [X_1/H], [X_2/H], ..., [X_n/H]). Grids of this kind are employed by existing pipelines like the SEGUE Stellar Parameter Pipeline (Lee et al. 2008a), the `MATISSE` algorithm (Recio-Blanco et al. 2006), the APOGEE Stellar Parameter and Chemical Abundances Pipeline (García Pérez et al. 2016), or in some of the parametrization tools – the so-called nodes – of the *Gaia*-ESO survey (Smiljanic et al. 2014).

In recent years, modern computer science applications found their way into astronomical spectroscopic studies. Especially the predictive powers of spectral models that are constructed using highly flexible machine-learning (ML) techniques like artificial neural networks are seeing an increasingly widespread usage. The basic idea behind these approaches is to construct a spectroscopic training set, where the stellar parameters (structural parameters and chemical abundances) – or labels as they are frequently called in the ML context – are known. From this training set a model is constructed that has the labels as free parameters, which in turn can be tuned to predict and compare models to unseen data (i.e., observed spectra that are to be classified). Training sets either consist of observed spectra that were labeled using one of the classical techniques mentioned above, or are constructed via synthetic grids of predefined parameters. Either procedure comes with its own advantages and disadvantages. For instance, using real spectra bears the main benefit that a training spectrum and an observed spectrum of intrinsically the same labels look exactly the same, which is not necessarily the case for theoretical models with flaws in their assumptions or insufficient descriptions of physical processes (see, e.g., Section 4.5). Synthetic training grids, on the other hand, have the merit that they are very flexible in terms of parameter coverage and number statistics. Spectroscopic pipelines that use ML (or data-driven) methods have been introduced by, for example, Ness et al. (2015), Guiglion et al. (2016), Ting et al. (2019), and Guiglion et al. (2020).

Via the synergy of these revolutionary aspects of stellar spectroscopy with the theories based on classical physics outlined above, the present work establishes an advanced reliable parametrization technique. Together with the installation of a new benchmark star for nuclear astrophysics and novel insights into the missing link between globular clusters and the Galaxy, this thesis conveys advancements in the thriving field of Galactic archaeology as a whole.

Image/logo credit.
C. J. Hansen.

CHAPTER II

This chapter in brief

ATHOS: On-the-fly stellar parameter determination of FGK stars based on flux ratios from optical spectra

`ATHOS`, A Tool for HOmogenizing Stellar parameters, and its new flux-ratio (FR) based spectroscopic technique are introduced in this chapter. It is organized as follows:

- In Section 2, the set of training spectra used in this project together with a brief discussion of the stellar parameter derivation are presented.
- Section 3 introduces the concept of FRs and the identification of those FRs that carry information about stellar parameters.
- The computational implementation of the deduced analytical relations is outlined in Section 4.
- At the core of Section 5 is the comparison of `ATHOS`′ parameter scales to various existing spectroscopic surveys.
- Finally, a summary of the results is given in Section 6.

The chapter is based on a publication (Hanke et al. 2018) that was co-authored by C. J. Hansen, A. Koch, and E. K. Grebel.

1 Context

While spectroscopic campaigns aimed at dissecting the formation history of the Milky Way have a long-standing history (e.g., Beers et al. 1985b; Christlieb et al. 2001; Yanny et al. 2009), the astronomical landscape of the next decades will be governed by ever-larger spectroscopic surveys that aim at painting a complete chemo-dynamic map of our Galaxy. Amongst these are the surveys RAVE (Steinmetz et al. 2006), SEGUE (Yanny et al. 2009), APOGEE (Majewski et al. 2017), GALAH (De Silva et al. 2015), Gaia-RVS (Cropper et al. 2018), LAMOST (Zhao et al. 2012), *Gaia*-ESO (Gilmore et al. 2012), 4MOST (de Jong et al. 2012), and WEAVE (Dalton et al. 2012). All these build on the multiplexing capacities of present and future spectrographs and have the goal of expanding the six-dimensional phase space into a multidimensional information space by adding chemical abundance measurements of a large number of tracers of chemical evolution for several hundred thousands to millions of stars. Inevitably, this requires high spectral resolving power ($R =\gtrsim 20\,000$; Caffau et al. 2013), but also a precise and accurate knowledge of the stellar parameters[1] of the target stars.

As detailed in Section I.4.2, various methods for parameter determination are in use, ranging from photometric calibrations of a temperature scale (e.g., Alonso et al. 1996b, 1999b), excitation equilibrium using large numbers of Fe lines, Balmer-line scrutiny, to least-squares fitting of spectral templates or line indices over a broad parameter grid (Lee et al. 2008a). Systematic effects can, to first order, be decreased by using analysis techniques differentially to a standard star of known parameters (Fulbright et al. 2006; Koch & McWilliam 2008). To ensure success, all these methods, in turn, require accurate atomic data and stellar model atmospheres (Barklem et al. 2002), and yet, degeneracies and covariances, in particular between T_{eff} and $\log g$, are often inevitable (McWilliam et al. 1995; Hansen et al. 2011; Jofré et al. 2019; Blanco-Cuaresma 2019). Further problems arise with large data sets, where the homogenization of parameter scales (Venn et al. 2004; Smiljanic et al. 2014) and the sheer computational time for spectral analysis become an issue.

Here, we introduce a new, fast, and efficient algorithm for stellar parameter determination, named `ATHOS` (A Tool for HOmogenizing Stellar parameters). `ATHOS` relies on the measurement of flux ratios (FRs) between well-tested spectral regions that are sensitive to specific parameter combinations and that we optimize to reproduce a

---

[1] Here taken as effective temperature, $\mathrm{T}_{\mathrm{eff}}$, surface gravity, $\log g$, microturbulence, v_{mic}, and the overall metallicity, [M/H], which we will use synonymously with [Fe/H] in the following, though we are aware that the latter nomenclature is at odds with the formally correct definition. We chose, however, to follow the common usage in the literature. Higher order parameters such as stellar rotation will only be briefly discussed.

compilation of training spectra and their parameters, amongst which are the accurate and precise parameters of the *Gaia* benchmark stars (Jofré et al. 2014).

An extension to the LDR method explained in Section I.4.2.1 rather employs the ratios of flux points that do not necessarily coincide with the line cores, but with other parts of the lines that show empirical, strong sensitivities to the parameter of choice. Kovtyukh et al. (2003) provided a very precise calibration of LDRs to the temperatures of F to K dwarfs. However, their stellar sample restricted its applicability to a narrow metallicity window of $-0.5 <$[Fe/H]$< +0.5$ dex and the way of measuring line depths of the lines – that is, profile fits to the line – made this method prone to the uncertainties of continuum normalization, which is circumvented by using FRs with rather narrow wavelength spacing. By not relying on pairs of low- and high-excitation lines, `ATHOS` further allows for measurements of parameters down to much lower metallicities.

Notable features of `ATHOS` are its fast performance (~ 25 ms/< 10 ms for a high-/low-resolution spectrum), applicability over a wide range of resolving powers ($R \gtrsim 10\,000$ for all parameters; $R \gtrsim 2000$ for the T_{eff} scale), and validity over a broad range of stellar parameters ($T_{\mathrm{eff}} \approx 4000$ to 6500 K, [Fe/H] ≈ -4.5 to 0.3 dex, $\log g \approx 1$ to 5 dex). This makes it an ideal tool to provide precise and accurate stellar parameters for large samples within seconds – an important asset in the era of future spectroscopic missions.

This tool is meant to work for all optical spectra, not just for stars originating from one survey as most tailored pipelines do, but it offers a way to homogenize large samples from different surveys. It is by no means an attempt to supersede various survey pipelines, but a simple way to put the millions of stars to be observed on the same scale, so that these are homogeneously treated and not biased by the choices or methods adopted within individual surveys.

2 Training set

This project was originally meant to be model-driven. Therefore, we initially synthesized spectra of a homogeneous and dense coverage of the parameter space and conducted the analysis outlined in Section 3. Unfortunately, it turned out that the optimal FRs deduced from theory alone cannot be reproduced in real spectra, and vice versa. A possible explanation is the oversimplification made throughout the modeling by preferring LTE assumptions and plane-parallel, static atmospheres over a fully three-dimensional, hydrodynamic treatment under NLTE conditions.

This, in turn, would come with enormous computational costs. Further, we identify inaccurate line data as an additional caveat of the theoretical treatment. Due to these limitations, the decision was made to base this work entirely on observed spectra with accurately determined stellar parameters.

To this end, we have compiled a grid of in total 195 high-resolution, high S/N spectra of 124 stars covering the visual wavelength range including the regions around the strong features of the Hβ profile at 4861.3 Å, the Mg I b triplet at $\sim$ 5175 Å, the Na I D doublet at $\sim$ 5890 Å, and Hα at 6562.8 Å. A valuable part of the sample is the *Gaia* FGK benchmark star library of Blanco-Cuaresma et al. (2014, henceforth GBS) with attributed stellar parameters from Jofré et al. (2014) and Heiter et al. (2015) for the more metal-rich stars, and Hawkins et al. (2016) for the metal-poor targets. Their data were obtained with four different spectrometers and resolutions. These are the HARPS spectrograph (Mayor et al. 2003) at the ESO, La Silla 3.6 m telescope; UVES (Dekker et al. 2000) on the VLT/UT2 at Cerro Paranal, Chile; ESPaDOnS (Donati et al. 2006) on the Canada-France-Hawaii Telescope at the Mauna Kea observatory, Hawaii, and its twin NARVAL (Aurière 2003) mounted on the 2 m Telescope Bernard Lyot on Pic du Midi, France. Most of the stars in the library have data available from at least two of these instruments and the S/N is mostly well above 100 pixel^{-1}. Moreover, the GBS library includes high-quality spectra of the Sun and Arcturus observed by Hinkle et al. (2000) with the Echelle spectrograph at the Coudé Feed telescope on Kitt Peak, Arizona. We added UVES dwarf and giant spectra from Hansen et al. (2012, hereafter CJH12) to the grid. The metal-poor end (-4.5 dex to -1.0 dex) was additionally populated by stars characterized by Roederer et al. (2014, from now on R14). Unfortunately, their spectra are not publicly available. Consequently, we used the ESO Advanced Data Products (ADP) query to cross-check for publicly available data, yielding matches for 48 stars with mainly UVES and some HARPS observations. In order to fill the otherwise sparsely populated horizontal branch (HB), we once again employed the ADP to retrieve spectra for the cooler targets in the spectroscopic HB studies of For & Sneden (2010) and Afşar et al. (2012, red HB). A list of all the data including the respective stellar parameters and sources thereof can be found in Table II.2.

2.1 Stellar parameters

For the GBS sample, Heiter et al. (2015) and Hawkins et al. (2016) inferred $T_{\rm eff}$ and $\log g$ from angular diameters and bolometric fluxes, as well as from fitting stellar evolutionary tracks. The deduced errors for these procedures range from $\sim$ 20 to 100 K and from 0.01 to 0.15 dex for stars other than the Sun, which exhibits

TABLE II.1: Line list used in Section 2.1

λ [Å]	χ_{ex} [eV]	$\log gf$ [dex]	λ [Å]	χ_{ex} [eV]	$\log gf$ [dex]
Fe I			Fe II		
3536.556	2.880	0.115	3406.757	3.944	−2.747
3640.389	2.730	−0.107	3436.107	3.967	−2.216
3917.181	0.990	−2.155	3535.619	3.892	−2.968
4021.867	2.760	−0.729	4178.862	2.583	−2.535

Notes. Only a portion of the table is provided to indicate its form and content. The full dataset is available through the Centre de Données astronomiques de Strasbourg (CDS) via anonymous ftp to `cdsarc.u-strasbg.fr` (130.79.128.5) or via `http://cdsarc.u-strasbg.fr/viz-bin/qcat?J/A+A/619/A134`.

comparatively negligible errors. In light of the new interferometric temperature measurements for HD 140283, HD 122563, and HD 103095 by Karovicova et al. (2018), who found earlier measurements to have suffered from systematic effects much larger than the provided errors, we decided to use their more recent values and errors for these stars. For the metallicity, Jofré et al. (2014) averaged line-by-line abundances that stem from up to seven different analysis codes. These have been each corrected for departures from LTE. Uncertainties achieved in this way span 0.03 dex up to 0.40 dex.

CJH12 derived effective temperatures for their sample using photometric color–T_{eff} relations. The same study provides $\log g$ based on either parallaxes in conjunction with stellar structure equations, or by enforcing ionization balance, that is requiring deduced abundances from Fe I and Fe II to agree with each other. The provided [Fe/H] values originate from an LTE analysis of Fe I lines.

R14 employed a strictly spectroscopic determination of T_{eff} by balancing abundances of Fe I transitions at low and high excitation potentials. For stars cooler than the main sequence turnoff (MSTO), $\log g$ was based on fits to theoretical isochrones, while for the hotter stars it was inferred from ionization balance. [Fe/H] values for the R14 targets were calculated using LTE Fe II abundances, which ought to experience smaller corrections in an NLTE treatment (e.g., Bergemann et al. 2012b; Lind et al. 2012).

Due to the former two studies pursuing different approaches to obtain stellar parameters – notably T_{eff} from photometry or from excitation balance and [Fe/H] from

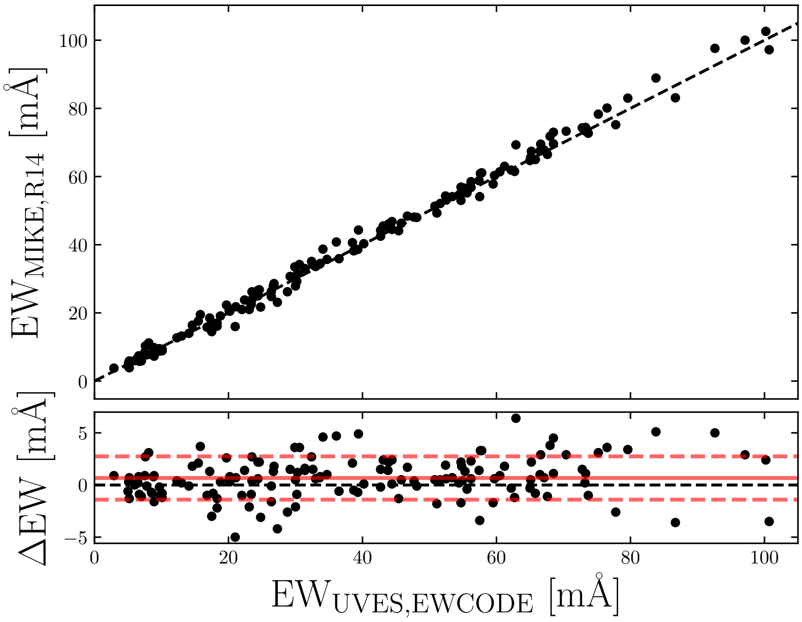

FIGURE II.1: *Upper panel*: comparison of our `EWCODE` runs on UVES spectra to the literature values determined from MIKE spectra by R14. The one-to-one trend is shown by the dashed black line. *Lower panel*: residual distribution. The solid and dashed red lines indicate the mean deviation of 0.67 mÅ and the rms scatter of 2.07 mÅ, respectively.

Fe I or from Fe II abundances – we decided to reanalyze both samples in a homogeneous investigation[2]. This was done by employing a common, carefully selected and inspected Fe line list, in conjunction with EWs. The Fe line list was compiled for CJH12 and used therein. The lines were chosen such that there was no trend with wavelength, and so that excitation and ionization trends were tight (little scatter). The Fe I lines are from the Vienna Atomic Line Database (VALD; Piskunov et al. 1995; Ryabchikova et al. 2015), the Oxford group (Blackwell et al. 1979a,b; Blackwell & Shallis 1979; Blackwell et al. 1982a,b,c), O'Brian et al. (1991), and Nissen et al. (2007). For Fe II the list was based on VALD, Blackwell et al. (1980), and Nissen et al. (2007). The line list is presented in Table II.1.

In case of the CJH12 spectra, EWs were computed from our library spectra (see next section) using our own, semi-automated EW tool `EWCODE` (Hanke et al. 2017). For spectra in the R14 sample, we relied on published EWs after cross-matching our line list with Roederer et al. (2014). Systematic differences in the methods to determine EWs and/or the spectrographs (UVES compared to MIKE) could be excluded by checking the EW results of Fe lines for the five stars in common between R14 and CJH12. At a mean deviation of 0.67 ± 2.07 mÅ (root mean square deviation, rms) no significant discrepancy was found (see Figure II.1). We note that not all of these EWs

---

[2] For further information on the discrepancy of photometric and spectroscopic parameter scales, see Section 5.4.

entered our subsequent analysis, because the stars in question were present in the GBS sample, which supersedes our parameters.

We used EWs to constrain T_{eff} by enforcing excitation equilibrium of Fe I lines adopting plane-parallel `ATLAS9` model atmospheres interpolated from the grid by Castelli & Kurucz (2004). Line-by-line abundances were computed using the LTE analysis code `MOOG` (Sneden 1973, July 2014 release). Typical temperature uncertainties are of order 100 K. In parallel to excitation equilibrium, the empirical atmospheric microturbulence parameter, v_{mic}, was tuned to satisfy agreement between weak and strong lines. For the majority of stars, where CJH12 and R14 used parallaxes and photometry to deduce $\log g$, we did not allow the model gravity to vary and used the literature values instead. For the other stars, ionization equilibrium was required to derive $\log g$ (labeled in Table II.2). Finally, our estimate for [Fe/H] is based on Fe II abundances derived from the optimal set of model atmosphere parameters. Following, for example, Roederer et al. (2014), here we preferred the ionized species over the neutral one at the expense of number statistics because it is less prone to NLTE effects. For the Fe abundance we adopted errors of 0.10 dex.

For & Sneden (2010) and Afşar et al. (2012) used only spectroscopic indicators for the red HB sample, that is, excitation equilibrium for T_{eff} and LTE ionization balance for $\log g$ and consequently [Fe/H] from Fe lines. The provided uncertainties are 150 K, 0.16 dex, and ~ 0.1 dex, respectively. Here, we adopted the literature parameters.

Since a few stars have been covered by more than one of the individual subsets discussed above, we had to homogenize the deduced stellar parameters from the different studies. For those stars that occur in the GBS, we chose the GBS parameters as reference. If this was not the case we averaged over the parameters we have derived from different EW sources and used the deviations and respective uncertainties for a new uncertainty estimate. In the present study we relied on the solar chemical composition by Asplund et al. (2009) stating $\log \epsilon(\mathrm{Fe})_{\odot} = 7.50$ dex. Hence, GBS metallicities, which are based on $\log \epsilon(\mathrm{Fe})_{\odot} = 7.45$ dex by Grevesse et al. (2007), had to be adjusted accordingly. The final training parameters of the spectra entering our analysis can be found in Table II.2.

The selected spectra cover stars in the most relevant parts of the Hertzsprung-Russel diagram (upper left panel of Figure II.2), viz. on the MS, the MSTO, the subgiant branch (SGB), the red giant branch (RGB), and the HB. In terms of stellar parameters, the training set spans a parameter space from $T_{\mathrm{eff}} \approx 4000$ to 6500 K, $\log g \approx 1$ to 5 dex, and $[\mathrm{Fe/H}] \approx -4.5$ to 0.30 dex. Figure II.2 illustrates the distribution of our training sample in stellar parameter space (T_{eff}, $\log g$, and [Fe/H]).

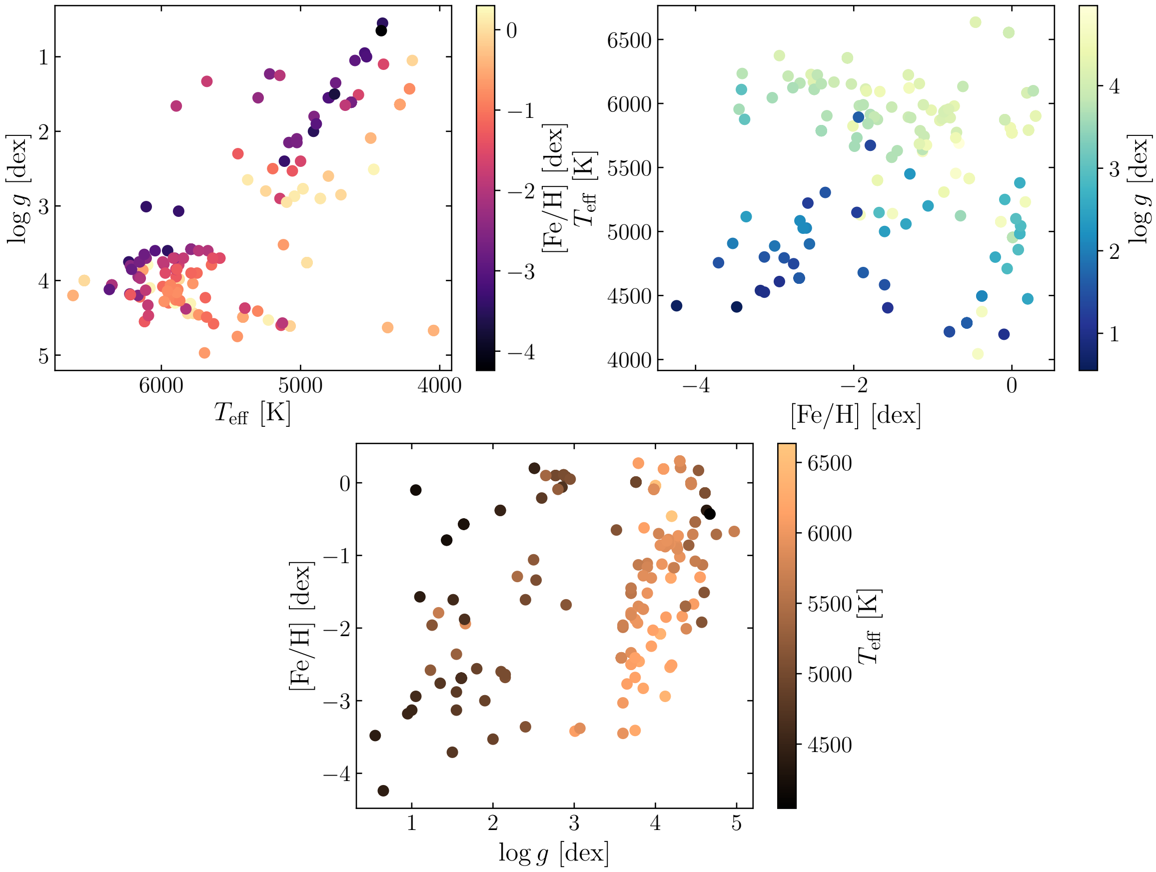

FIGURE II.2: Distribution of the training set in the parameters T_{eff}, [Fe/H], and $\log g$. The color coding in each panel indicates the respective missing dimension.

TABLE II.2: Training set information

Name	T_{eff} [K]	$\sigma_{T_{\mathrm{eff}}}$ [K]	$\log g$ [dex]	$\sigma_{\log g}$ [dex]	[Fe/H] [dex]	$\sigma_{\mathrm{[Fe/H]}}$ [dex]	Spectrograph	Source
α Boo	4286	35	1.64	0.09	-0.57	0.08	Coudé	GBS
ω^2 Sco	5380	150	2.65	0.16	0.10	0.10	HARPS	red HB
BD +20 571	5935$^{(a)}$	100	4.06$^{(b)}$	0.20	-0.86$^{(a)}$	0.10	UVES	CJH12
BD +24 1676	6110$^{(a)}$	71	3.70	0.05	-2.50$^{(a)}$	0.07	UVES	R14

Notes. The full table is available through the CDS via anonymous ftp to `cdsarc.u-strasbg.fr` (130.79.128.5) or via `http://cdsarc.u-strasbg.fr/viz-bin/qcat?J/A+A/619/A134`. $^{(a)}$ Parameters redetermined from excitation balance (T_{eff}) and Fe II abundances ([Fe/H]) using updated line data (see Section 2). $^{(b)}$ $\log g$ inferred from ionization equilibrium of Fe I and Fe II. Otherwise, the literature parameter was used.

2.2 Grid homogenization

For the purpose of spectral homogeneity and computationally efficient access, spectra from different sources and spectrographs were first shifted to rest-frame wavelengths.

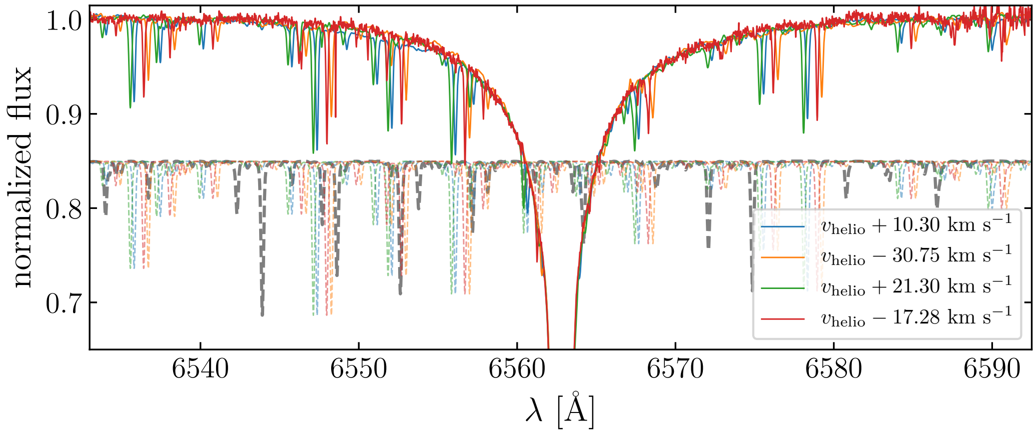

FIGURE II.3: Telluric contamination due to H_2O vapor in Earth's lower atmosphere. Shown as solid lines are rest-frame spectra of HD 140283 that were taken at different epochs and line-of-sight radial velocities. The apparent motion with respect to the heliocentric velocity $v_{\mathrm{helio}} = -169.00$ km s^{-1} is indicated in the legend. All dashed lines represent the same topocentric telluric absorption model (gray, see text for details) but being shifted in wavelength space to match the radial velocity of their observed counterpart (light-colored). For better visibility the models are shifted in flux direction as well.

This was achieved by using radial velocities determined from a cross-correlation, either with a template spectrum of the Sun or α Boo, depending on which of those is closer to the target in stellar parameter space. Imprecisions introduced by using these metal-rich templates for metal-poor targets are unproblematic for this investigation (effect of less than 1 km s^{-1}), which we validated by cross-correlating some of the v_r-shifted, metal-poor targets against each other. Next, the spectra were degraded to match a resolving power of $R = 45\,000$ by convolution with a Gaussian kernel of appropriate width. Some of the spectra in the R14 sample are originally at resolving powers slightly below the desired one, but still well above 40 000. We kept those at their original value and point out that this has negligible effects on this study (see Section 5.1). Finally, the data were rebinned to a common, linear wavelength scale with equidistant spacing of $\delta\lambda = 0.017$ Å pixel^{-1}, this configuration being representative for a typical UVES580 setup (Pasquini et al. 2000). We did not normalize the training spectra since the method introduced here (Section 3) considers relative fluxes and is consequently scale-free.

2.3 Telluric contamination

In the Hα region, telluric absorption plays a non-negligible role in the line shape of this feature. As briefly noted in, for example, Eaton (1995) and Cayrel et al. (2011), there is a wealth of absorption features caused by H_2O vapor in the Earth's lower atmosphere falling right in the spectral region around Hα. None of the archival spectra in our set has been corrected for telluric contamination. We address this issue in Figure II.3, where we plotted a portion around Hα of four out of the six available spectra of the metal-poor SGB star HD 140283 ($T_{\rm eff} = 5522$ K, $\log g = 3.58$ dex, [Fe/H] $= -2.41$ dex; Jofré et al. 2014; Heiter et al. 2015), which were acquired at different epochs. Being fairly metal-poor and hot, HD 140283 is not expected to show substantial stellar absorption in the presented region except for Hα itself. Yet, there is a clear indication of contamination from lines moving with the topocentric – that is the telescope's – rest frame. We retrieved a telluric absorption model using SkyCalc (Noll et al. 2012; Jones et al. 2013), a tool dedicated to compute sky models for the VLT observatory on Cerro Paranal at 2640 m above sea level. We did not attempt to match the ambient conditions of the observations of HD 140283, but used a global model for a zenith pointing and a seasonal averaged precipitable water vapor of 2.5 mm. A comparison of the models to the observed spectra reveals that the vast majority of the small-scale features originate from telluric absorbers. We note the variations of the depths of the real tellurics between observations and attribute them to varying observing conditions such as airmass and/or water vapor content in the lower atmosphere.

As we are aiming for stellar parameter determinations irrespective of the targets' relative motions, we have to take into account the fact that – depending on radial velocity – contamination can in principle prevail at any wavelength in the vicinity of Hα. In the training set with precisely known velocities, we achieve this by masking out tellurics in the individual spectra based on their velocity shifts. This was done by looking for flux minima with line depths above 3% in the telluric model described above and masking the neighboring wavelength ranges of one FHWM on either side. We favor this masking procedure over a detailed modeling and removal of telluric features because of missing information about ambient observing conditions for most of the spectra. In addition, we strived to avoid possible caveats coming from model uncertainties. Since many of the stars in the grid are represented by more than one spectrum at various topocentric velocities, a range masked in one spectrum may well be accessible in another one (as can be seen in Figure II.3). Keeping the tellurics in would increase the rms scatter in our Hα-based temperature scales to 280 K compared to the 122 K we find below.

3 Method

In our study we investigated how FRs are affected by stellar parameters and, vice versa, how they can be used to constrain them. We define an FR as the ratio of the two mean flux levels of a spectrum F in the open intervals of width w around the central wavelengths λ_1 and λ_2, that is,

$$\mathrm{FR}_{\lambda_1,\lambda_2} = \frac{\langle F_{\lambda_1} \rangle}{\langle F_{\lambda_2} \rangle} \tag{II.1}$$

with

$$\langle F_{\lambda_i} \rangle = \frac{1}{n} \sum_{j=1}^{n} F(\lambda_j), \quad \lambda_j \in (\lambda_i - w/2, \lambda_i + w/2). \tag{II.2}$$

Using FRs bears the main benefit that they are scale-free, meaning they circumvent the caveats of normalization procedures. These are heavily affected by, among others, S/N and resolution of the spectrum, as well as by intrinsic physical quantities such as metallicity and temperature. Provided that the two dispersion points from which an FR is computed are closely spaced in wavelength, the local continuum can be approximated to be constant. This holds true even for merged echelle spectra with clearly extrinsic large-scale continuum variation. Another advantage of measuring FRs over employing iterative minimization approaches such as profile fits or full spectrum fits – on which to our knowledge any other approach of determining stellar parameters relies – is the comparatively reduced computation time. Therefore, per spectrum, the demand for computational resources can be significantly lowered.

In order to quantify the information content of an FR of a set of two wavelength regions in the grid with respect to a stellar parameter x, we chose the Pearson product-moment correlation coefficient

$$r_{\mathrm{FR},x} = \frac{\sum_{i=1}^{N} (\mathrm{FR}_i - \langle \mathrm{FR} \rangle)(x_i - \langle x \rangle)}{\sqrt{\sum_{i=1}^{N} (\mathrm{FR}_i - \langle \mathrm{FR} \rangle)^2} \sqrt{\sum_{i=1}^{N} (x_i - \langle x \rangle)^2}}, \tag{II.3}$$

where N corresponds to the number of grid points that do not contain pixels masked as tellurics in either of the two wavelength bins, or which are not accessible for other reasons. Here, $\langle \mathrm{FR} \rangle$ represents the mean of the measured FR_i and $\langle x \rangle$ the mean of the investigated parameter values x_i. According to Equation II.3, both strong anticorrelations and correlations, that is, absolute values $|r_{\mathrm{FR},x}|$ close to unity, indicate a tight linear relation between the tested FR and the quantity x. The demand for monotonic and linear – in other words, with constant sensitivity – analytical functions describing the behavior of a parameter with an FR justifies the use of Pearson's correlation coefficient as test measure.

Looking for the strongest correlations for each of the parameters T_{eff}, [Fe/H], and $\log g$, we tested all possible wavelength combinations in a window of width 17 Å – or 1000 pixels in the grid – around each dispersion point in the training set and ranked them by decreasing absolute value of the correlation coefficient. The width of 1000 pixels was chosen so that the maximum spacing between two ranges was 8.5 Å, thus ensuring the aforementioned condition of a close-to-constant continuum. In a subsequent step we excluded those FRs containing a wavelength interval that overlaps with one of the other FRs of higher $|r_{\mathrm{FR},x}|$. In doing so we made sure that individually measured ratios are independent of each other, thus enabling linear combinations of observables. In the following, we comment on the individual stellar parameters and the relations derived from them.

3.1 Effective temperature

According to the method outlined above, the best spectral regions to derive T_{eff} labels irrespective of the other stellar parameters appear to be the lines of the Balmer series of neutral hydrogen, Hα and Hβ. This does not come by surprise, as in FGK stars – that is at temperatures below 8000 K – the wings of the Balmer lines are rather pressure insensitive (see Amarsi et al. 2018, and references therein) and have previously been fit to accurately constrain T_{eff} (e.g., Barklem et al. 2002). Indeed, only in the wings of Hβ and Hα, $\left|r_{\mathrm{FR},T_{\mathrm{eff}}}\right|$ reaches values > 0.97. Because these wings are potentially very wide, the general method was altered to allow for a maximum dispersion spacing of 2000 pixels instead of 500 (corresponding to 34 Å instead of 8.5 Å). Hence, the FRs are in principle more prone to continuum variations, which seem to play a subordinate role, because we could not identify significant differences in the FRs among training spectra of the same targets from different spectrographs and therefore blaze functions.

In order to describe the tightest relations analytically, we first deduced the individual linear trends. For this task we fitted the function

$$T_{\mathrm{eff}}(\mathrm{FR}) = a\mathrm{FR} + b \tag{II.4}$$

by performing an orthogonal distance regression (ODR), that is, a minimization of the sum of the squared normalized orthogonal distances

$$F = \frac{1}{2}\sum_{i=1}^{N} \frac{(a^2\sigma^2_{T_{\mathrm{eff}},i} + \sigma^2_{\mathrm{FR}_i})(T_{\mathrm{eff}}(\mathrm{FR}_i) - T_{\mathrm{eff,ref},i})^2}{((a^2+1)\sigma_{\mathrm{FR}_i}\sigma_{T_{\mathrm{eff,ref}},i})^2} \tag{II.5}$$

of the points $(\mathrm{FR}_i, T_{\mathrm{eff},i})$ to the model. Here a and b denote the slope and intercept to be fit, N is the number of FRs measured for the particular relation, while $\sigma_{T_{\mathrm{eff,ref}},i}$ and σ_{FR_i} represent the standard errors of the grid temperatures, $T_{\mathrm{eff,ref},i}$, and measured flux ratios, FR_i, respectively. In a subsequent step the T_{eff} fit residuals were checked in a visual inspection for trends with metallicity and/or surface gravity. Fits showing (anti-) correlations with either of the two were rejected. In addition, we omitted sets of FRs where the minimum FR does not deviate by more than 15% from the maximum FR. In doing so we reduced the influence of S/N. This decision was made because larger spreads of possibly measurable FRs across the temperature range for one relation imply less sensitivity to S/N for that particular relation.

The aforementioned cleaning procedures left us with nine FR-$T_{\rm eff}$ relations. The strongest for either of the two profiles Hβ and Hα is presented in Figure II.4. There, we show how $T_{\rm eff}$ behaves with the FRs that were measured using $w = 0.357$ Å at $(\lambda_1, \lambda_2) = (4860.279$ Å, 4854.482 Å$)$ and $(\lambda_1, \lambda_2) = (6564.478$ Å, 6585.898 Å$)$, respectively. These wavelengths correspond to the blue wing of Hβ and the red wing of Hα. We explored various realizations of w and found a bin width of 0.357 Å, that is, 21 pixels in the training grid's dispersion direction, to be the best trade-off value between noise and resolution dependence on the one hand and information content on the other hand. A visual inspection of Figure II.4 confirms the strong temperature trend with FR as already indicated by $r_{{\rm FR},T_{\rm eff}}$. The fit results along with their respective temperature residuals are indicated in the same figure. For the two extreme values in terms of $T_{\rm eff}$ we show how the profile shapes and consequently the FRs of the wavelength regions of interest differ. We point out that N is not the same in both panels and does not resemble the total number of stars in the training set but the number of spectra free of telluric absorption in the regions of interest. If a star has more than one available spectrum satisfying this condition, we averaged the deduced FRs to a single value for that star. This ensures that intrinsically identical spectra are not over-represented in the fit.

We found that optimal solutions converge toward sets of two ranges obeying the following necessary conditions: At low metallicities and/or high temperatures, the ratio should incorporate one region with low and one region with high temperature sensitivity. In this case the first acts as pseudo-continuum while the latter carries the temperature information. At high metallicities and/or low temperatures, the line depths at both wavelengths, λ_1 and λ_2, should be equally sensitive to metallicity (and, less importantly, gravity), hence assuring a constant FR at a given $T_{\rm eff}$. This behavior is similar to the one employed by the classical LDR approach of Kovtyukh et al. (2003).

The above statements are bolstered by Figure II.5, where we demonstrate how the profile shape changes with $T_{\rm eff}$ at low (< -2.0 dex) and high (> -0.1 dex) metallicities. We picked four representatives for each of the two [Fe/H] bins from the training set. While being clearly identifiable in the low-metallicity regime, the FR-$T_{\rm eff}$ trend is less obvious at high metallicities in combination with low temperatures. This is

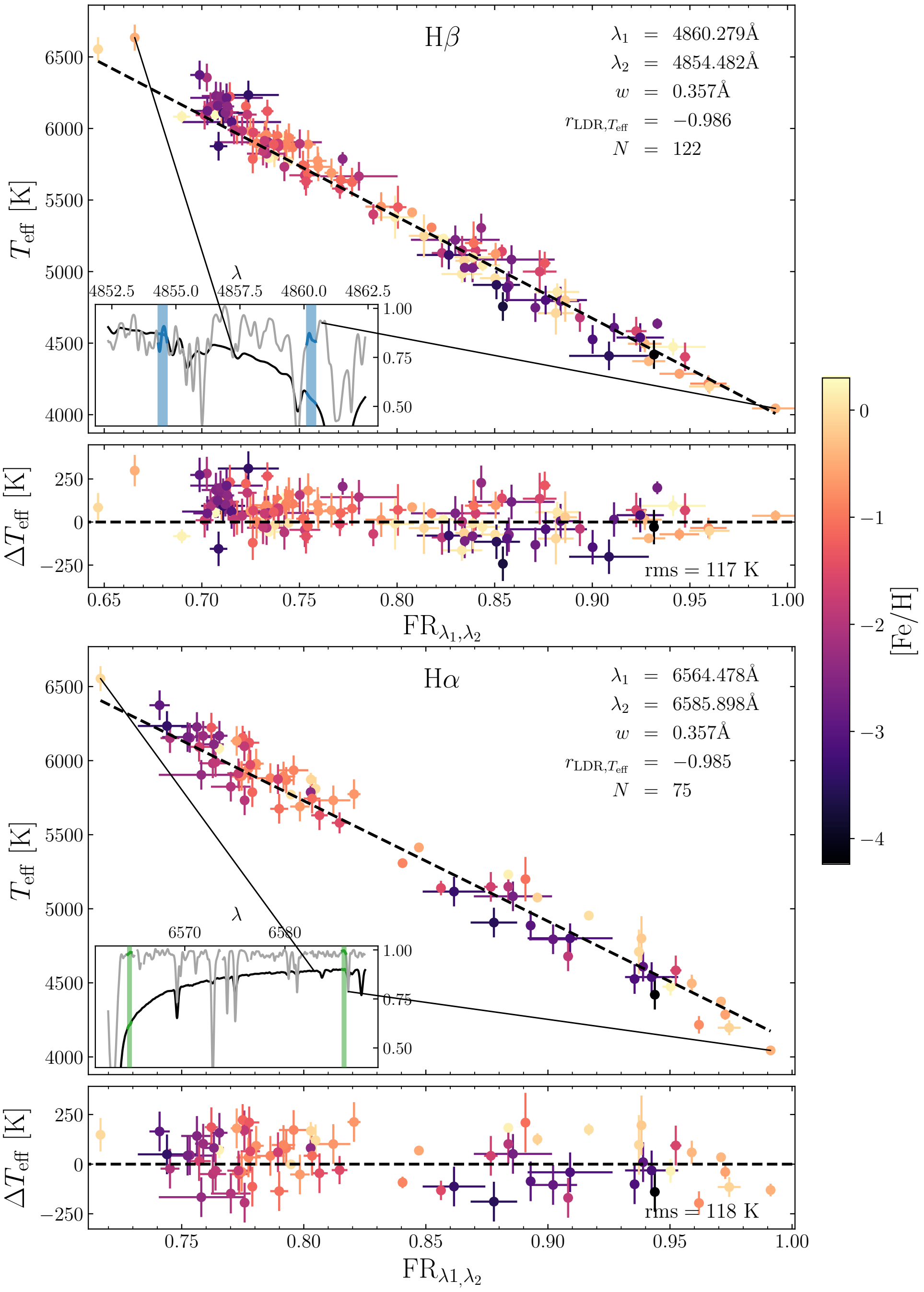

FIGURE II.4: *Large panels*: exemplary scatter plots for the FR-T_{eff} relations of the two strongest correlations in our test grid around Hβ (*top*) and Hα (*bottom*). The color coding is the same as in Figure II.2. Dashed black lines resemble the linear ODR fits to the data. The small inlays in the *lower left corners* show cut-out spectra that were normalized by their 99th percentile for the highest (black) and lowest (gray) corresponding T_{eff}, the former being offset by -0.1 in flux direction. Gaps in the spectra mark the expected positions of strong telluric contamination for the observed radial velocity (Section 2.3). The blue and green shaded regions in the inlays indicate the ranges from which the respective FRs were computed using Equations II.1 and II.2 with the characterizing values provided in the upper corner of each panel. *Small panels*: residual distributions.

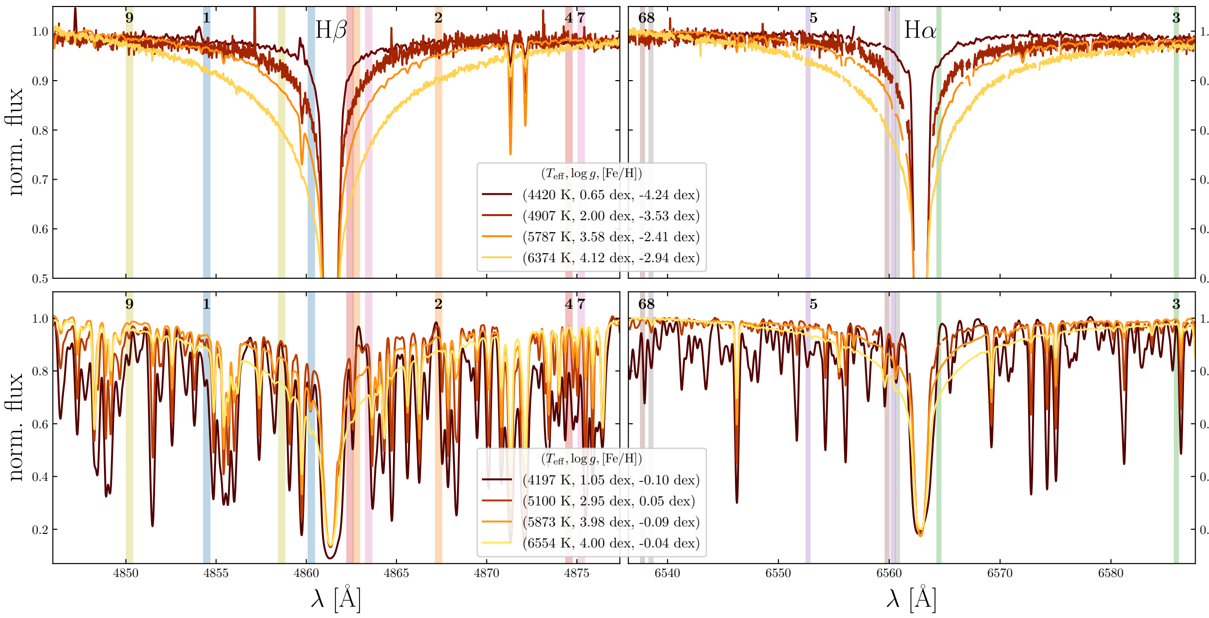

FIGURE II.5: Comparison of the shape changes with $T_{\rm eff}$ of the Hβ (*left*) and Hα (*right*) profiles at low (*top*) and high (*bottom*) metallicities. As for Figure II.4, the spectra were normalized by the 99th percentile of the flux in the shown wavelength intervals. Gaps in the spectra mark the positions of telluric lines. Blue and green colored ranges denote the same FRs as in the inlays of Figure II.4, while the additional colored regions show the remaining seven relations ranked by the number at the *top* of each panel.

due to the features of species other than H that dominate the wings of the Balmer lines, which means that both components of the FR vary and have to be taken into account simultaneously. The latter observation is more pronounced in the Hβ feature, because it lies in the blue part of the optical spectrum where metal absorption is much more frequent.

Typically, the rms scatter of $T_{\rm eff}$ around an individual relation is of order 110 K to 130 K. This is close to the median uncertainty of the training values of 100 K. It is not straightforward to linearly combine results from the nine individual measurements for each star to reduce $T_{\rm eff}$ uncertainties. It rather turned out that the fit residuals are correlated, as we show in Figure II.6. Ideally, this plot would consist of ellipses that are aligned with the coordinate axes, implying uncorrelated errors. Yet, the diagonal orientation of the ellipses indicates that the residuals are not purely noise-induced, but of systematic origin.

We discuss two possible reasons for this behavior, the first being the existence of hidden parameters. One or more additional parameters could affect the profile shape of Balmer lines and consequently lead to a correlation of the individual FRs and thus of the residuals of the linear FR-$T_{\rm eff}$ trends. Such parameters can either arise in the observations themselves or be of stellar origin. An observational bias could be

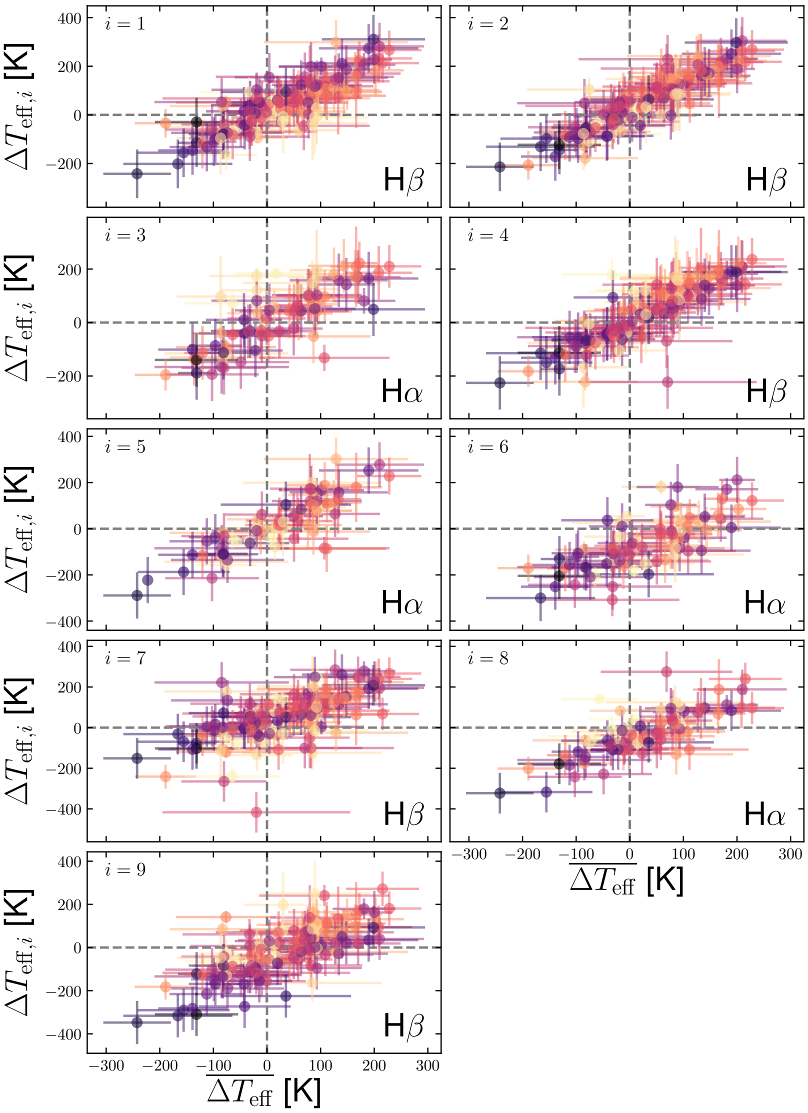

FIGURE II.6: Residuals between the inferred and the literature temperatures for our FR-T_{eff} relations versus the mean residuals. The color coding is the same as in Figure II.2. Spectra with telluric contamination in one of the regions were omitted. Errors on the abscissa were computed via the standard deviation of the $\Delta T_{\mathrm{eff},i}$ (see Equation II.8), while the ordinate errors only denote the claimed uncertainty in the literature data.

introduced by the continuum shape (i.e., the blaze function of the spectrograph) in the spectral order where the profiles appear. We tested this possibility on a normalized version of the training grid and found no significant improvement as compared to the unnormalized case. Moreover, due to their large wavelength spacing, Hα and Hβ are commonly not located in the same spectral order and hence not subject to the same part of the blaze function. Still, there is a non-negligible correlation of fit results from Hα with the ones from Hβ.

As far as stellar parameters are concerned, [Fe/H] and $\log g$ can be ruled out to be responsible since correlations of the temperature residuals with these two were explicitly omitted. Moreover, we could not find any trends with the microturbulent velocity. For the GBS sample, there are $v \sin i$ measurements available (ranging from 0 to 13 km s^{-1}), which enable us to eliminate rotation as driving mechanism for the deviations, too. The last parameter is chemical peculiarity. Depending on the chemical enrichment history of the star, elements other than iron do not necessarily have to scale with metallicity (here [Fe/H]). Most importantly, α-elements such as Mg are strong electron donors, so that their over- or under abundance can have effects on the electron pressure in the stellar atmosphere and accordingly the line formation. Using tabulated abundances for the GBS sample by Jofré et al. (2015), we could not find any trends of the T_{eff} residuals with abundances of any of the available chemical species.

The second plausible origin for the described systematics is the influence of inaccurate training values. So far, we have assumed that the training T_{eff} are of utmost accuracy, in other words the true individual temperatures should not deviate significantly from the training values when taking into account their uncertainties. If we dropped this hypothesis, correlations of the fit residuals to assumed uncorrelated FRs would indicate that either the error estimates in the sample temperatures are underestimated or that the procedures adopted to derive temperatures produce inaccurate temperatures. Considering the established accuracy of bolometric flux calibrations, which were used to determine T_{eff} for the GBS sample, this option seems unlikely. The spectroscopic determinations of T_{eff} for the remainder of the training set, however, might be subject to, for example, NLTE-, 3D-effects, or inaccurate atomic data. These can cause the true temperature of a star to expose non-zero slopes with excitation potential in an LTE treatment, which results in offset temperatures when enforcing excitation balance (e.g., Hanke et al. 2017).

For the above reasons we split the error budget on mean temperatures derived from our relations into a statistical and a systematic component. The latter is estimated by

$$\sigma_{T_{\text{eff}},sys} = \sqrt{\sigma_{\text{tot}}^2 - \sigma_{\text{stat}}^2}, \tag{II.6}$$

with

$$\sigma_{\text{tot}}^2 = \left\langle \left(T_{\text{eff}}(\text{FR}_i)_j - T_{\text{eff,ref},j} \right)^2 \right\rangle \tag{II.7}$$

and

$$\sigma_{\text{stat}}^2 = \left\langle \left(T_{\text{eff}}(\text{FR}_i)_j - \langle T_{\text{eff}}(\text{FR}_i) \rangle_j \right)^2 \right\rangle . \tag{II.8}$$

Here, for the jth star in the training sample, $T_{\text{eff}}(\text{FR}_i)_j$ is the measured temperature

TABLE II.3: Fit information on FR-T_{eff} relations (Eq. II.4) sorted by decreasing $|r_{\mathrm{FR},T_{\mathrm{eff}}}|$. The width, w, of the bands at central wavelengths λ_1 and λ_2 is 0.357 Å.

$r_{\mathrm{FR},T_{\mathrm{eff}}}$	$\sigma_{T_{\mathrm{eff}}}$ [K]	λ_1 [Å]	λ_2 [Å]	a [K]	b [K]
−0.986	117	4860.279	4854.482	−7095	11059
−0.986	129	4862.778	4867.334	−8586	12755
−0.985	118	6564.478	6585.898	−8131	12234
−0.985	116	4862.421	4874.559	−6405	10497
−0.983	123	6560.347	6552.680	−11576	15705
−0.982	131	6559.803	6537.737	−10724	15004
−0.981	132	4863.458	4875.239	−8602	12942
−0.981	122	6560.738	6538.502	−8741	12896
−0.979	124	4858.630	4850.198	−10689	15128

for the ith relation and $T_{\mathrm{eff,ref},j}$ is the corresponding literature value. We find a value of $\sigma_{T_{\mathrm{eff}},sys} \approx 97$ K. Our fit results are summarized in Table II.3.

3.2 Metallicity

Our method revealed that, using FRs, a star's metallicity can be estimated best by investigating low-excitation transitions of Fe I. The line strength (or depth) of these features is governed by the temperature and the abundance of Fe, while $\log g$ and v_{mic}, in comparison, play a rather subordinate role. Assuming LTE, higher temperatures shift the excitation-de-excitation equilibrium toward favoring higher occupation numbers at high-excitation levels and consequently lead to lower occupation in the lower levels. This results in a weakening of lines that are excited from these levels. The same effect would be observed at constant T_{eff} but at a lower [Fe/H], that is a lower number of atoms in the atmosphere column and thus less strong spectral features. We note that the former is a vastly simplified picture, which gets especially complicated by NLTE considerations, such as interactions between energy levels and over-ionization due to an enhanced UV-background (see, e.g., Lind et al. 2012, for a detailed discussion on NLTE effects on Fe lines). However, since this study concentrates on observables of real spectra and not the theoretical modeling thereof, these effects enter only to the extent that they affected the original determinations of the training values. Given that we can infer the effective temperature independently from other stellar quantities (see previous section), we can break the degeneracy between line strength (by means of FRs), [Fe/H], and T_{eff}, and hence constrain [Fe/H].

To this end, we first identified transitions that are readily described by FRs and furthermore detectable in all training sample spectra. We chose to pursue an empirical approach and only later consulted predictions from literature atomic data in order

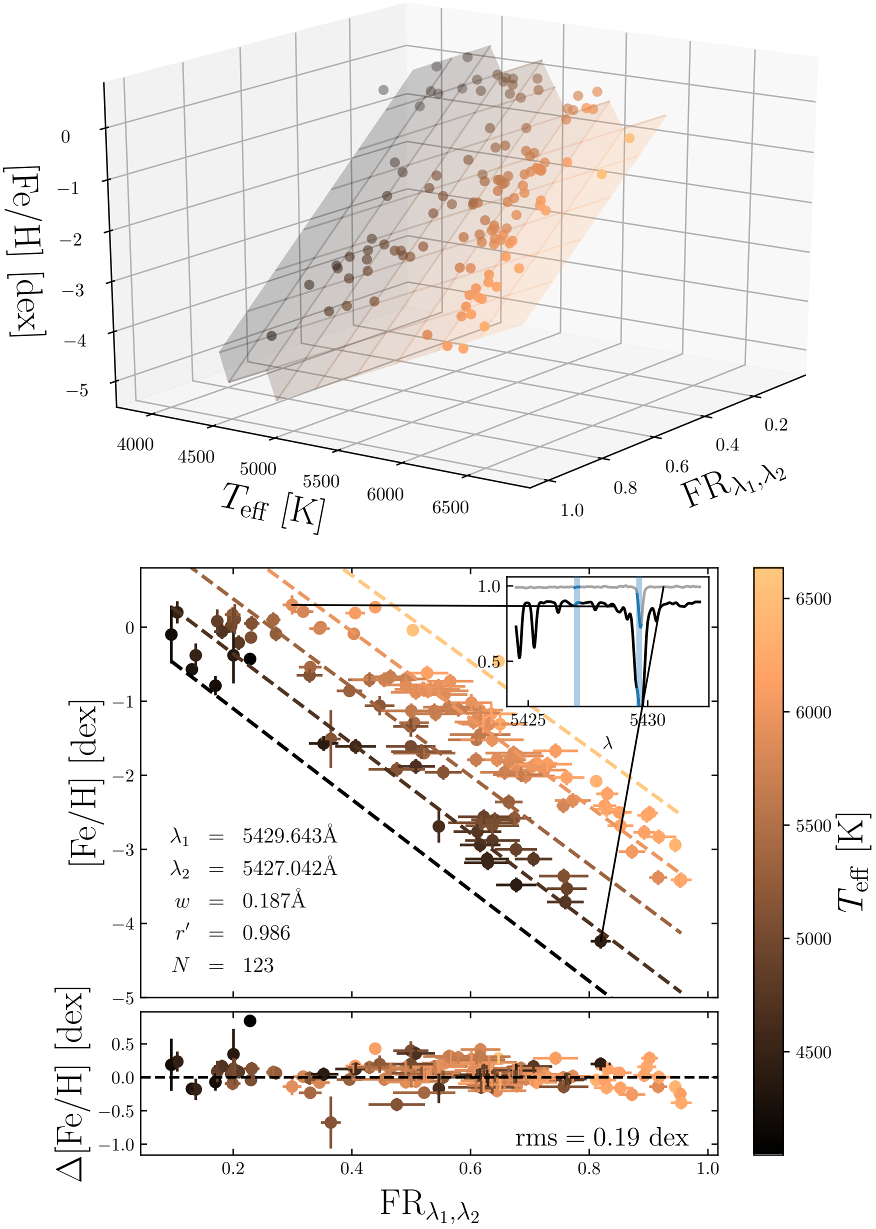

FIGURE II.7: Behavior of Metallicity with FR and T_{eff}. The *top panel* illustrates the distribution of points of the tightest relation in FR–T_{eff}–[Fe/H] space and the surface they span therein. To guide the eye, the best-fit surface according to Equation II.10 is overlaid as a light-colored, distorted grid, where the grid lines indicate the isothermal and iso-FR lines. The same distribution of points is shown in the *middle panel* but in a coordinate frame that is rotated such that it is aligned with the FR and [Fe/H] axes. Dashed lines indicate the track of the isothermal lines on the surface. In analogy to Figure II.4, the inlay shows the most extreme spectra in terms of metallicity, as well as the two wavelength regions the FR was computed from (blue). The fit residuals with respect to FR are presented in the *bottom frame*. All three scatter plots follow the same T_{eff} color coding as indicated by the bar on the *lower right*.

to be unbiased and not to miss features that are susceptible to stellar parameters in our FR approach. Due to the expected degeneracy between [Fe/H] and T_{eff}, the test statistic had to be modified to the multiple correlation coefficient

$$r' = \sqrt{\frac{r^2_{\text{FR},[\text{Fe/H}]} + r^2_{T_{\text{eff}},[\text{Fe/H}]} - 2r_{\text{FR},[\text{Fe/H}]}r_{\text{FR},T_{\text{eff}}}r_{T_{\text{eff}},[\text{Fe/H}]}}{1 - r^2_{\text{FR},T_{\text{eff}}}}}, \tag{II.9}$$

where the various r denote the correlation coefficients among the respective quantities as defined in Equation II.3. Here, once again, values of r' close to unity indicate that [Fe/H] is strongly correlated with the two independent variables T_{eff} and FR. If the latter is satisfied, points in FR-T_{eff}-[Fe/H] space generate a two-dimensional hypersurface. As opposed to the FR-T_{eff} relations, it is not sufficient to describe these using only first-order terms of the independent variables. We found that a significantly better description can be obtained by allowing a second-order interaction term. We use the modified algebraic hypersurface

$$[\text{Fe/H}]\,(\text{FR}, T_{\text{eff}}) = (a\text{FR} + bT_{\text{eff}} + c\text{FR}T_{\text{eff}} + d)\left(1 + e^{\beta(\text{FR}-\gamma)}\right) \tag{II.10}$$

to describe the behavior. The exponential cut-off term with coefficients β and γ was introduced since for some relations [Fe/H] asymptotically drops for FRs above ~ 0.9. This latter observation can be intuitively understood as the line depth of a profile inevitably approaching zero with decreasing metallicity. As a consequence, any FR will approach unity. This explains why for some relations the metallicity sensitivity sharply decreases for $[\text{Fe/H}] \leq -2.5$ dex. Given that those cases are still very sensitive indicators at higher metallicities, we decided to keep them and introduce the cut-off term. Neglecting the latter for those relations would lead to systematic overestimates of [Fe/H] by up to 0.5 dex in the regime of very low metallicities (i.e., $[\text{Fe/H}] \lesssim -2.5$ dex). Figure II.7 presents the closest resemblance ($r' = 0.986$) to a surface described by Equation II.10 that was identified. Here we are dealing with rather small-scale flux variations in contrast to the broad Balmer lines that were used before. Hence, the windows from which the mean flux levels were computed had to be decreased to 11 pixels (or 0.187 Å) at the expense of stability against S/N. The information carrier in this best case is an Fe I line at 5429.643 Å with its pseudo-continuum slightly further in the blue in a region that is devoid of substantial absorption. The distribution in the FR-[Fe/H] plane is shown next to its three-dimensional counterpart.

With in total 340 of these planes obeying $r' \geq 0.95$, we found surprisingly many tight relations. Following the same approach as in the previous section, we lowered this number to 41 by demanding non-significant correlations of the fit residuals with $\log g$ and v_{mic}. Hence, while the total amount of the absorbed flux in the line surely depends on pressure and turbulence, we empirically deduced ratios between smaller ranges in stellar spectra that are not significantly influenced by these two quantities.

Variations in the α-element abundances are amongst the most common departures from the solar-scaled abundance distribution. Therefore, in order to not bias our method against α-enhanced or α-depleted stars, we ensured that no strong feature of the species O, Mg, Si, Ca, or Ti was present in the wavelength ranges considered for the computation of FRs. VALD offers the extraction mode "extract stellar" to retrieve atomic data and estimates of the transition strengths in a given wavelength interval for a particular set of stellar parameters. We employed this tool to cross-match the literature wavelengths from a line list for a sun-like atmosphere ($T_{\mathrm{eff}} = 5750$ K, $\log g = 4.50$ dex, $[\mathrm{Fe/H}] = 0.00$ dex) and a solar-metallicity giant atmosphere ($T_{\mathrm{eff}} = 4500$ K, $\log g = 1.00$ dex, $[\mathrm{Fe/H}] = 0.00$ dex) with our 41 values for λ_1 and λ_2. The rejection threshold for unbroadened VALD estimates for the line depths was set to 0.2 for both hypothetical atmospheres. This way another ten FRs with nearby (± 0.5 Å) α-element features were excluded. Consequently, the final number of clean, metallicity-sensitive FRs is 31 .

The intra-relation rms metallicity scatter ranges from 0.16 up to 0.20 dex, while the inter-relation rms scatter for individual stars ranges from 0.01 to 0.31 dex. As fit residuals of individual hypersurfaces are correlated, in analogy to Equation II.6, we split the error into a statistical and a systematic part, that is $\sigma_{[\mathrm{Fe/H}],\mathrm{sys}} = 0.16$ dex. The systematic error budget of 0.16 dex can be explained by the uncertainties in the training metallicities, only. We tabulate the wavelengths together with the ODR fit results for the 31 most promising FRs in Table II.4.

The species of the closest and anticipated strongest (in terms of line depth provided by VALD) theoretical transition in the Sun are provided in separate columns in Table II.4. This information, however, has to be treated with caution because, first of all – apart from lines contaminated by α-elements – we did not restrict our analysis to blend-free lines but aimed for wavelength regions with a close to constant sensitivity to stellar parameters over a wide range of stellar parameters. Secondly, and more importantly, even if a line was isolated in the solar spectrum, this does not necessarily mean that it will be isolated in a different star with significantly different parameters. Fortunately, the interplay between these factors is intrinsically accounted for in our approach. In fact, our strongest correlation (see inlay of Figure II.7) incorporates not only the one Fe I transition listed, but several other possible Fe I blends on either side of the profile. We emphasize at this point that our method is prone to biases introduced

Table II.4: Information on the strongest FR-T_{eff}-[Fe/H] relations (Eq. II.10) sorted by decreasing r'. The width of the bands around the wavelengths λ_1 and λ_2 is 0.187 Å.

r'	$r_{\text{FR,[Fe/H]}}$	$\sigma_{\text{[Fe/H]}}$ [dex]	λ_1 [Å]	λ_2 [Å]	$\lambda_{\text{ref}}^{(a)}$ [Å]	Species$^{(a)}$	depth$_{\odot}^{(a)}$	a [dex]	b [10^{-4} dex K^{-1}]	c [10^{-5} dex K^{-1}]	d [dex]	β	γ
0.986	−0.819	0.19	5429.643	5427.042	5429.696	Fe I	0.88	−6.610	11.198	11.829	−4.402	∞	∞
0.985	−0.852	0.19	5227.122	5228.941	5227.189	Fe I	0.88	−6.379	10.285	5.500	−3.719	∞	∞
0.984	−0.803	0.20	5446.847	5443.974	5446.916	Fe I	0.87	−4.924	14.706	−31.008	−5.604	∞	∞
0.983	−0.904	0.16	5455.466	5459.801	5455.453	Fe I	0.70	−6.981	5.615	39.246	−1.442	37.220	1.0199
0.983	−0.902	0.19	4872.094	4879.234	4872.137	Fe I	0.83	−4.787	7.924	−4.738	−2.575	28.044	1.0428
0.982	−0.837	0.17	5328.476	5334.579	5328.531	Fe I	0.83	−4.723	11.695	−11.561	−4.524	82.200	0.9965
0.982	−0.837	0.20	5340.971	5347.703	5341.023	Fe I	0.81	−4.828	12.867	−21.451	−4.458	78.494	1.0090
0.980	−0.891	0.20	5266.494	5259.218	5266.554	Fe I	0.81	−4.553	9.122	−12.306	−3.004	23.424	1.0597
0.980	−0.931	0.19	5404.075	5408.087	5404.151	Fe I	0.71	−5.907	5.086	10.134	−0.351	32.793	1.0361
0.980	−0.900	0.19	5006.054	5011.409	5006.118	Fe I	0.82	−6.822	6.248	23.255	−1.100	58.534	1.0147
0.979	−0.934	0.19	5424.016	5415.839	5424.067	Fe I	0.72	−6.299	3.973	17.797	0.213	22.887	1.0530
0.979	−0.925	0.18	5133.639	5140.099	5133.688	Fe I	0.72	−5.537	6.529	−3.726	−0.763	53.246	1.0165
0.978	−0.858	0.19	5049.880	5046.854	5049.819	Fe I	0.81	−4.362	12.375	−31.623	−3.964	137.924	1.0021
0.977	−0.889	0.19	4903.255	4903.833	4903.310	Fe I	0.80	−5.014	8.576	−4.300	−2.399	50.381	1.0174
0.977	−0.929	0.18	5369.888	5367.763	5369.961	Fe I	0.72	−8.099	3.443	26.448	1.966	38.024	1.0275
0.977	−0.931	0.19	5369.922	5362.051	5369.961	Fe I	0.72	−6.822	3.292	27.035	0.739	29.052	1.0395
0.977	−0.932	0.20	5415.159	5414.462	5415.198	Fe I	0.73	−6.860	3.586	25.306	0.580	42.760	1.0199
0.976	−0.928	0.20	5415.227	5417.607	5415.198	Fe I	0.73	−6.287	4.085	21.904	−0.076	43.529	1.0146
0.976	−0.896	0.19	5281.726	5277.272	5281.789	Fe I	0.75	−5.972	7.677	1.553	−1.171	51.788	1.0255
0.976	−0.931	0.19	5162.216	5160.652	5162.272	Fe I	0.71	−7.568	3.086	31.213	1.384	36.542	1.0291
0.976	−0.802	0.19	5110.332	5117.285	5110.413	Fe I	0.85	−5.952	13.363	−6.359	−4.283	53.898	1.0178
0.974	−0.931	0.20	5162.335	5159.496	5162.272	Fe I	0.71	−8.036	2.606	38.862	1.703	45.191	1.0202
0.974	−0.838	0.20	6546.220	6550.045	6546.237	Fe I	0.61	−5.765	11.342	−8.249	−2.602	91.439	1.0184
0.972	−0.904	0.20	6400.071	6406.735	6400.000	Fe I	0.66	−6.359	6.320	11.849	−0.569	50.731	1.0214
0.972	−0.912	0.20	5014.877	5008.145	5014.942	Fe I	0.71	−7.053	6.110	6.324	0.638	83.241	1.0078
0.970	−0.844	0.19	5142.887	5143.363	5142.928	Fe I	0.80	−5.292	9.575	12.631	−3.506	70.293	1.0072
0.969	−0.919	0.19	5444.994	5440.931	5445.041	Fe I	0.64	−6.421	4.837	7.639	0.802	43.797	1.0184
0.968	−0.894	0.19	5215.137	5222.022	5215.180	Fe I	0.72	−6.704	6.178	20.460	−0.459	75.759	1.0123
0.966	−0.910	0.19	4983.189	4979.432	4983.250	Fe I	0.71	−7.336	5.430	11.336	1.220	88.469	1.0078
0.965	−0.912	0.20	5463.235	5467.587	5463.275	Fe I	0.65	−8.174	2.550	42.073	2.020	56.474	1.0105
0.962	−0.910	0.19	5078.967	5078.559	5078.974	Fe I	0.65	−6.356	5.470	8.597	0.422	76.379	1.0071

Notes. $^{(a)}$ Strongest line in the vicinity of λ_1 in a sun-like star according to VALD.

by chemical peculiarity to the extent that any non-regular chemical behavior of a target star could affect the relative strength of a blend in our wavelength regions and therefore cause the corresponding FRs to deviate from the ones expected at the star's metallicity. This effect can, for example, be expected to be encountered in spectra of CEMP stars, where absorption bands of carbonaceous molecules dominate the appearance of wide spectral bands.

3.3 Surface gravity

The derivation of stellar surface gravity using only dedicated FRs that are valid for the whole range of stellar parameters of our sample is less well defined. For dwarfs at moderately low to high metallicities, the wings of lines in the Mg I b triplet have proven to be good $\log g$ indicators (e.g., Ramírez et al. 2006). However, for certain combinations of stellar parameters like low gravities and metallicities pronounced wings do not form and cannot be used as universal gravity indicators. In fact, the largest correlation of surface gravity with FRs in the grid spectra is found to be only $r_{\mathrm{FR},\log g} = 0.89$. Unfortunately, strong $r_{\mathrm{FR},\log g}$ seem to be mainly explained by the spurious correlation of T_{eff} and $\log g$ in the grid ($r_{T_{\mathrm{eff}},\log g} = 0.66$, merely a consequence of stellar evolution). Hence, it was necessary to once again increase the dimensionality of the product-moment correlation coefficient to include T_{eff} and [Fe/H] as independent variables to end up with

$$R' = \sqrt{\begin{pmatrix} r_{x_1,\log g} \\ r_{x_2,\log g} \\ r_{x_3,\log g} \end{pmatrix}^{\mathrm{T}} \begin{pmatrix} 1 & r_{x_1,x_2} & r_{x_1,x_3} \\ r_{x_1,x_2} & 1 & r_{x_2,x_3} \\ r_{x_1,x_3} & r_{x_2,x_3} & 1 \end{pmatrix}^{-1} \begin{pmatrix} r_{x_1,\log g} \\ r_{x_2,\log g} \\ r_{x_3,\log g} \end{pmatrix}}, \qquad \text{(II.11)}$$

where

$$x_i \in \{\mathrm{FR}, T_{\mathrm{eff}}, [\mathrm{Fe/H}]\}\,. \qquad \text{(II.12)}$$

33 combinations of wavelength ranges of width 0.187 Å in the grid satisfy $R' \geq 0.95$. Our analytical description for these 33 FRs is the hyperplane

$$\log g(\mathrm{FR}) = a\mathrm{FR} + bT_{\mathrm{eff}} + c[\mathrm{Fe/H}] + d \qquad \text{(II.13)}$$

After carefully checking the residuals for small-scale structure and contamination by α-element transitions (see previous section), we ended up having 11 reliable relations. In Figure II.8 we visualize the four-dimensional plane in analogy to Figure II.7 for the strongest association at $R' = 0.977$. In the particular case of the shown relation, the blue wavelength region includes a strong Fe II line at 5316.508 Å, while the red range falls in a continuum window. Naturally, line strengths and therefore FRs involving

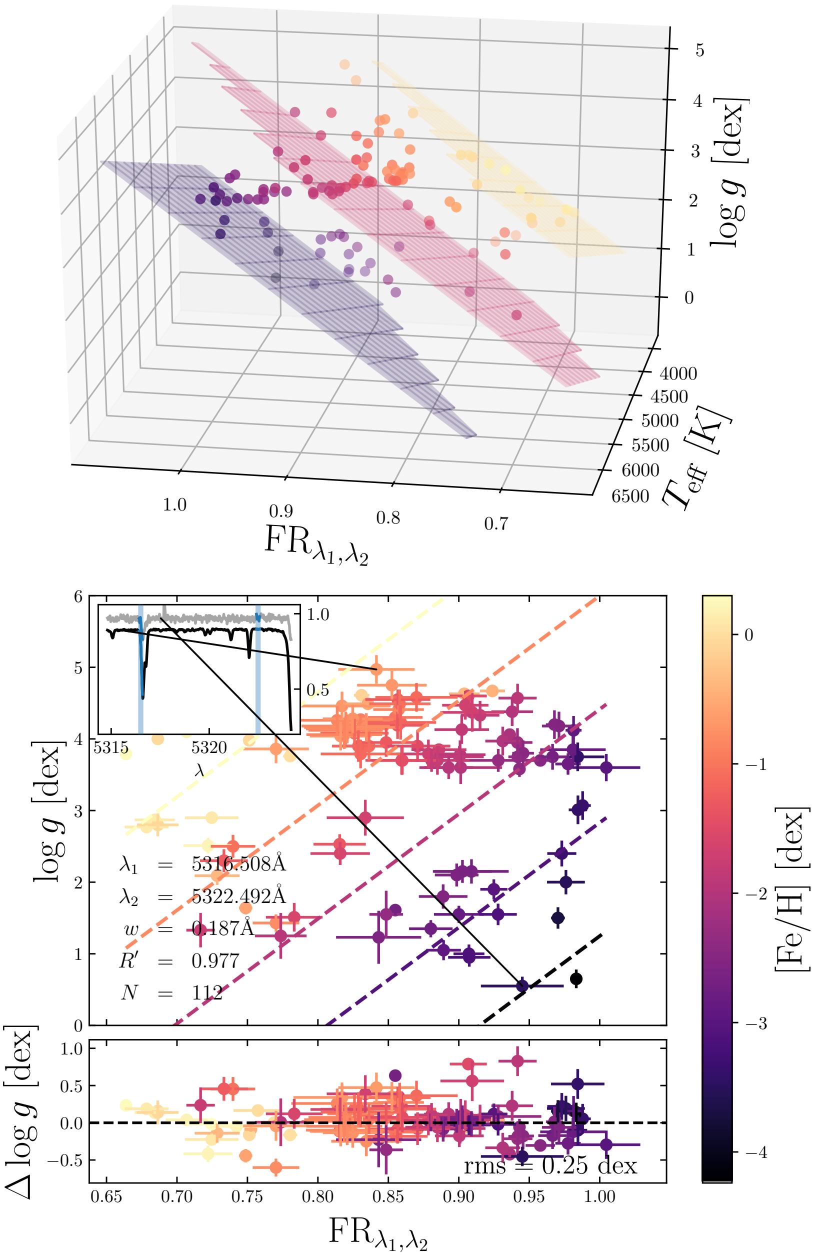

FIGURE II.8: log g dependence on FR, T_{eff}, and [Fe/H]. The *top panel* illustrates the distribution of points of the tightest relation in FR-T_{eff}–log g space, where the colors introduce metallicity as a fourth dimension. The fit solutions to Equation II.13 at fixed [Fe/H] values of −3.5 dex, −1.75 dex, and 0.00 dex are shown as three parallel hyperplanes. The *middle panel* resembles the distribution in FR-log g space, only. There, dashed lines indicate the track of the iso-metallicity lines on the surface at a fixed temperature of 5000 K. The inlay shows the most extreme spectra in terms of gravity, as well as the two wavelength regions the FR was computed from (blue). The fit residuals with respect to FR are presented in the *bottom frame*. All three scatter plots follow the same [Fe/H] color coding as indicated by the bar on the *lower right*.

Table II.5: Information on the strongest FR-T_{eff}-[Fe/H]-$\log g$ relations (Eq. II.13) sorted by decreasing R'. The width of the bands around the wavelengths λ_1 and λ_2 is 0.187 Å.

R'	$\sigma_{\log g}$ [dex]	λ_1 [Å]	λ_2 [Å]	$\lambda_{\mathrm{ref}}^{(a)}$ [Å]	Species$^{(a)}$	depth$_{\odot}^{(a)}$	a [dex]	b [dex K^{-1}]	c	d [dex]
0.977	0.25	5316.508	5322.492	5316.609	Fe II	0.68	14.635	8.522	1.395	−11.732
0.974	0.26	5197.474	5189.348	5197.568	Fe II	0.64	14.344	9.288	1.318	−12.549
0.973	0.27	5275.895	5273.022	5275.997	Fe II	0.66	13.314	9.859	1.173	−12.282
0.971	0.29	5234.500	5229.553	5234.623	Fe II	0.61	15.691	11.450	1.032	−15.961
0.969	0.30	5169.135	5170.291	5169.028	Fe II	0.80	8.678	7.940	1.372	−5.012
0.968	0.31	5018.549	5018.923	5018.436	Fe II	0.81	9.935	7.606	1.390	−6.053
0.967	0.30	5234.738	5229.366	5234.623	Fe II	0.61	14.429	9.649	1.319	−12.900
0.966	0.32	4924.046	4917.654	4923.921	Fe II	0.81	10.001	8.929	1.256	−7.585
0.966	0.32	5197.661	5199.191	5197.568	Fe II	0.64	15.213	7.582	1.557	−11.717
0.965	0.31	4923.791	4921.360	4923.921	Fe II	0.81	9.285	11.712	0.977	−9.534
0.961	0.33	5362.986	5369.310	5362.861	Fe II	0.53	18.580	10.704	1.151	−18.198

Notes. $^{(a)}$ Strongest participating ionized line in a sun-like star according to VALD.

Fe II lines have a strong [Fe/H] sensitivity. In fact, given gravity as prior, most FR combinations discussed here would offer a good metallicity indicator. Here, we use the fact that on top of their strong metallicity- and weak temperature-dependence profiles of ionized species expose a sensitivity to stellar surface gravity. Our 11 $\log g$ relations with the involved wavelength ranges and strongest contributing features in the Sun are listed in Table II.5.

Figure II.8 reveals the main weakness of our empirical approach to derive $\log g$. Ideally, an unbiased training sample would span a regularly spaced grid in parameter space. The sample used in this study, however, lacks coverage at the extreme values of almost all parameters (with the exception of high $\log g$ dwarfs; cf., Figure II.2). Even in an idealized homogeneously distributed case, our sample size of $124 \approx 5^3$ stars would only allow limited explanatory power in three dimensions of independent variables (FR, T_{eff}, and [Fe/H]). As a consequence, the low-number statistics prevents us from detecting subtle non-linearities causing systematic biases such as the ones seen in the high-FR regime in Section 3.2 at lower dimensionality (only two independent variables instead of three). A good example for potential non-linear behavior is the spectrum of the star β Ara. Its gravity is underestimated by ~ 1 dex in almost all relations, suggesting a breakdown of the linear relation towards β Ara's corner in the parameter space ($T_{\mathrm{eff}} = 4197$ K, $[\mathrm{Fe/H}] = -0.05$ dex, $\log g = 1.05$ dex). For the discussed reasons, one has to exercise caution when using the provided $\log g$ relations, especially for extreme cases corresponding to the edges of the parameter space studied here.

4 ATHOS

We implemented all the information provided in Tables II.3, II.4, and II.5, as well as the fit covariance matrices and systematic errors of Equations II.4, II.10, and II.13 in one stellar parameter tool, called `ATHOS`. `ATHOS` is a `Python`-based software capable of dealing with hundred thousands to millions of spectra within a short amount of time. In part, this is due to the incorporation of parallelization capabilities making use of modern multi-core CPU architectures. Using only FRs computed from input spectra and the dedicated analytical relations, the stellar parameters can be estimated in well under 30 ms. `ATHOS`' workflow for each spectrum is divided into four main phases:

The first step is the read phase. `ATHOS` operates on one-dimensional, v_r-corrected input spectra of various file structures. Among these are the standard FITS spectrum formats and binary tables, as well as `NumPy` arrays, comma-, tab-, and whitespace-separated ASCII files. A minimal input consists of spectral fluxes and the corresponding dispersion information. At least one of the Balmer lines Hβ and Hα should fall in the covered wavelength. Otherwise, an external estimate of T_{eff} has to be given. For a proper treatment of noise, the error spectrum should be provided. Alternatively, a global S/N value for the entire spectrum will be set (not recommended). On a state-of-the-art machine with solid-state drive, the required time to read a spectrum with $2 \cdot 10^5$ dispersion points into memory ranges from about 1 ms through 3 ms to 117 ms for `NumPy` arrays, FITS spectra, and ASCII files, respectively.

The second step masks out regions of potential telluric contamination. The correction is of utmost importance for the temperature determination from the heavily contaminated Hα profile. For this purpose `ATHOS` internally stores the strongest topocentric wavelengths of our telluric model (Section 2.3). In order to exclude these from consideration, the velocity of the stellar rest frame with respect to the topocenter has to be provided. If Hα is not included, or if the spectrum has been corrected for tellurics, this step can be omitted. The involved operations take about 0.5 ms per spectrum.

Next, the FRs are computed. To this end, the input spectrum is linearly interpolated between dispersion points in order to compute the mean fluxes in the interval $(\lambda - w/2, \lambda + w/2)$. The typical execution time required here for a spectrum with $2 \cdot 10^5$ dispersion points is ~ 13 ms. In case the resolving power of the input spectrum is less than 45 000, the FRs are corrected using the relations discussed in Section 5.1. Spectra at $R > 45\,000$ are internally degraded to match the requirements.

The final phase is the parameter cascade. Starting from the FRs measured in the previous step, this routine computes the stellar parameters according to Equations II.4, II.10, and II.13 in the order $T_{\rm eff}$, [Fe/H], and finally $\log g$. As any subsequent relation depends on the result of the former, this structure is mandatory. By default, each final parameter and its (internal) error are estimated as the median and the median absolute deviation (mad) of the distribution of results from the different relations. These two measures were chosen because they are more robust against outliers possibly arising from spectral artifacts compared to, for example, means or weighted means. In some situations, such as highly reddened stars, the S/N may strongly vary on larger scales from the blue to the red. To take this into account, we implemented the possibility of introducing wavelength-dependent weights for the individual FR-relations in the form of polynomials with user-defined degrees and coefficients. In these cases, the weighted median is used to compute the final set of parameters. Systematic errors are propagated throughout the whole cascade. The time demand of this computation step is ~ 0.6 ms.

5 Performance tests

5.1 Resolution dependencies

All the FR-parameter relations implemented in ATHOS have been trained on a spectral grid at a fixed resolving power of $R = 45\,000$. In order to be applicable to a variety of spectroscopic surveys conducted with different instruments and Rs, these relations have to be either insensitive to R, or exhibit predictable deviations with R. For this reason, we investigated R dependences by degrading our spectral grid to resolving powers of 40 000, 30 000, 20 000, 10 000, 7500, 5000, and 2500 followed by a re-computation of all FRs which were established at $R = 45\,000$.

Figure II.9 shows how the newly computed FRs for our nine $T_{\rm eff}$ indicators deviate from the originally derived ones. Since there is a simple linear relation between FR and $T_{\rm eff}$, the resulting temperature offset can be deduced by scaling the $\Delta{\rm FR}_i$ with the respective slope a_i. We found that down to $R \approx 20\,000$ there is generally no significant deviation in FR, meaning the temperature deviations remain well below 150 K. For even lower values of R the situation becomes non-trivial. Then, the absolute value and sign of the offset appears to not only depend on R, but on $T_{\rm eff}$ and [Fe/H], as well. For [Fe/H] $\lesssim -1$ dex and below, we found significant deviations only as "late" as $R \lesssim 10\,000$. At these low metallicities, the profile shapes of the Balmer lines are dominated by H I itself and consequently expose larger scale lengths than just the line spread function of the spectrograph. Hence, convolving with Gaussians of FWHMs shorter than the range width of $w = 0.357$ Å – the mathematical equivalent

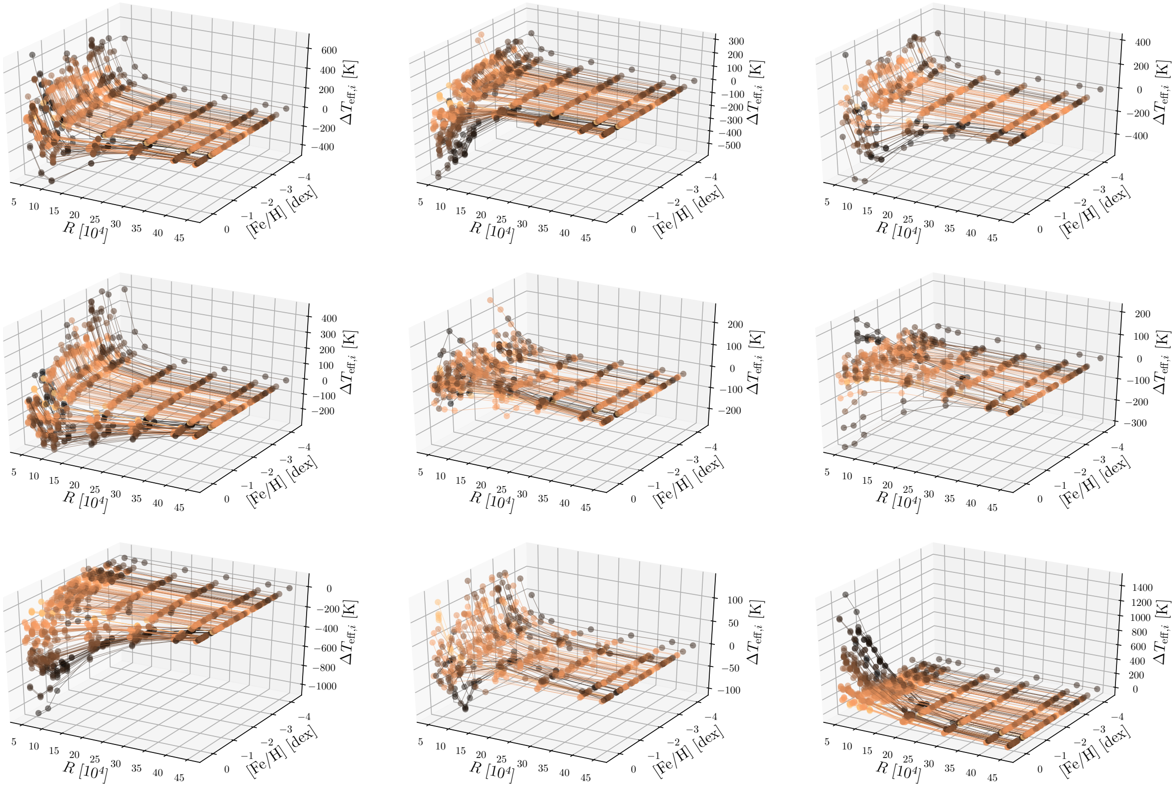

FIGURE II.9: T_{eff} deviations with respect to resolving power, R, and [Fe/H] ordered from the strongest to the weakest relation (see Table II.3 and Figure II.5) from *top left* to *bottom right*. The deviations were computed by scaling ΔFR with the slope of the respective relation. Points measured for the same star but at different Rs are connected by solid lines. The color coding is the same T_{eff} scale as in Figure II.7.

of employing a spectrograph of lower resolution – does not disperse large amounts of flux out of the wavelength ranges from which the FRs are measured. Accordingly, the FRs remain largely unaffected. For higher metallicities than -1 dex, a non-linear offset trend of the FRs with decreasing resolution and temperature manifests itself already for $R \lesssim 20\,000$. We suspect the driving mechanism for this behavior to be metal absorption from neighboring wavelengths being dispersed into the ranges of interest, or, vice versa, being dispersed out of the ranges. The strength of this additional (or lack of) absorption is mainly determined by T_{eff}, $\log g$, and – more importantly – [Fe/H]. Consequently, the T_{eff} relations are not clean anymore, but get susceptible to pressure and metallicity. Depending on the degree of isolation of the FR ranges from neighboring metal lines, this effect is more or less severe, which explains the large variety of absolute temperature deviations between relations in Figure II.9.

The same reasoning holds for the R dependence of the [Fe/H] relations, with the only difference being that optimal solutions usually consist of only one information carrier

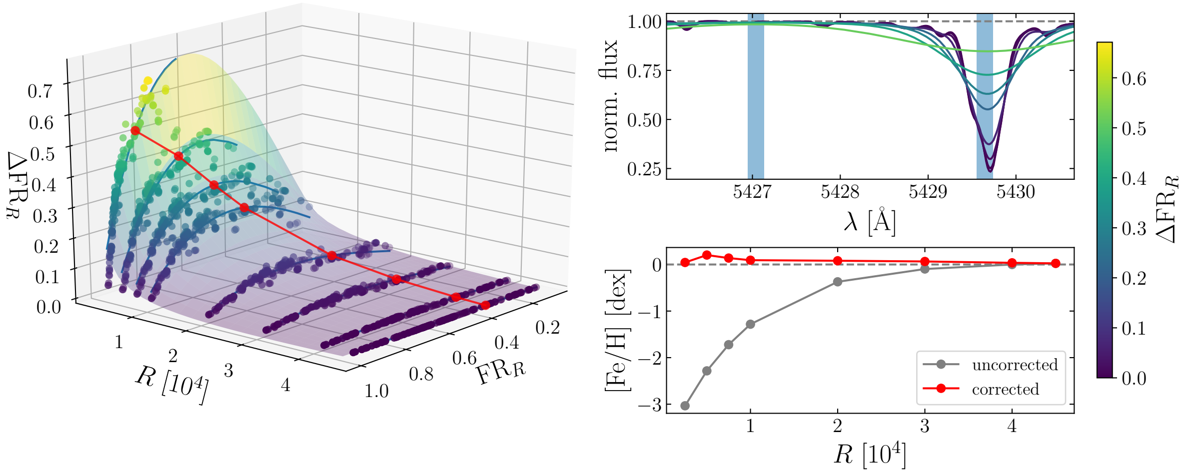

Figure II.10: *Left panel*: deviations of the FRs measured in all training spectra for the strongest metallicity relation (see Table II.4) at different resolutions with respect to the FRs computed at the original resolution of 45 000. In contrast to Figure II.9, we note that there is a non-linear relation between FR and [Fe/H], which is why we illustrate only the FR- and not the [Fe/H] deviations. The colored surface resembles the best-fit model to the data according to Equation II.14, where the color indicates the magnitude of the correction to be applied (see color bar on the *right*). Red points and their connecting line denote the track of the corrections to the FRs measured in the solar spectrum at different resolutions. *Upper right panel*: portion of the solar spectrum at resolutions of 45 000, 40 000, 30 000, 20 000, 10 000, 7500, 5000, and 2500 (dark- to light-colored). The color coding refers to the same FR corrections as in the *left panel*. Blue vertical bars indicate the wavelength ranges from which the FR is computed. *Lower right panel*: derived [Fe/H] for the Sun from uncorrected (gray) and corrected (red) FRs using Equation II.10 and only the strongest metallicity relation shown in the *upper right panel*.

and a normalization component. In the vast majority of cases, resolution deviations from the training value only affect the information carrier, since the regions of the pseudo-continuum tend to be free of absorption, or at least have a negligible absorption component with respect to the information carrier. This behavior can be seen in the upper right panel of Figure II.10, where we show how resolutions between 45 000 and 2500 affect the profiles in the solar spectrum in our strongest metallicity relation. Moreover, the FR deviations for all benchmark stars at their different metallicities and temperatures are presented in the left panel. It is obvious that higher metallicities, that is lower FRs, correspond to higher deviations in FR once the resolution is decreased. In general, low metallicities cause the line depths of the information carrier to be low and thus the FRs to reside close to unity. If the flux gets dispersed out of these profiles due to broader line spread functions, the FR is only marginally influenced. At higher metallicities, in turn, the FRs tend to be lower than unity and therefore the R-induced deviation can be much larger. Empirically,

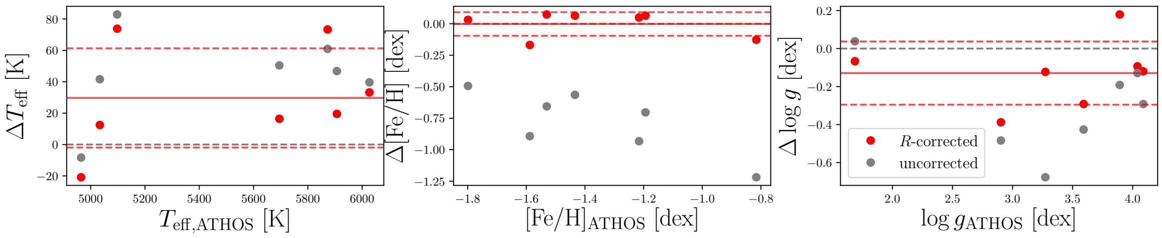

FIGURE II.11: Parameter deviations between `ATHOS` runs on X-shooter spectra and on high-resolution spectra of the same stars from our training sample. Here, gray circles indicate the values without any correction applied to the involved FRs, while red circles incorporate the corrections described by Equation II.14. The mean deviation and scatter for each stellar parameter are depicted by solid and dashed red lines, respectively.

we found that all corrections can be well described by the relation

$$\Delta \mathrm{FR}_R = \sum_{i=1}^{3} \left(\sum_{j=1}^{2} p_{ij} \ln \left(\frac{R}{45\,000} \right)^j \right) \mathrm{FR}_R^i \tag{II.14}$$

within an acceptable margin of error. Here, FR_R is the FR measured at the resolution R and p_{ij} is a coefficient matrix with six entries. The best-fit surface that is spanned by Equation II.14 for our strongest metallicity relation is illustrated in the left panel of Figure II.10. In the lower right panel of the same Figure we show the growing importance of the FR corrections with decreasing resolution by comparing the metallicity from the uncorrected FR with the one derived using the corrected FR. Similar to [Fe/H], our $\log g$ surfaces are based on small-scale flux variations. Hence, we see comparable trends of the corresponding FR residuals with R to the one shown in Figure II.10.

Despite the fact that Equation II.14 seems to hold down to the lowest resolutions, there are additional circumstances to be considered. First of all, a decrease in resolution shrinks the range of possible manifestations of FRs, which increases the noise sensitivity of Equations II.4, II.10, and II.13. Secondly, and more importantly, once the dispersion sampling of a real spectrum reaches the order of the width of the wavelength range we aim to measure – that is, $w = 0.187$ Å for the [Fe/H] and $\log g$ relations – the mean of the fluxes within that width might correspond to only a fraction of the flux in one pixel. If we considered, for example, the $0.7''$ slit configuration of the X-shooter spectrograph at the VLT with its moderate resolution of $\approx 10\,000$ and a sampling of ~ 5 pixels FWHM^{-1}, we would end up with only 1.87 pixels w^{-1} at a wavelength of $\lambda = 5000$ Å.

In testing `ATHOS`' sensitivity to spectral resolution under the aforementioned conditions, we retrieved and analyzed real spectra from the X-shooter spectral library

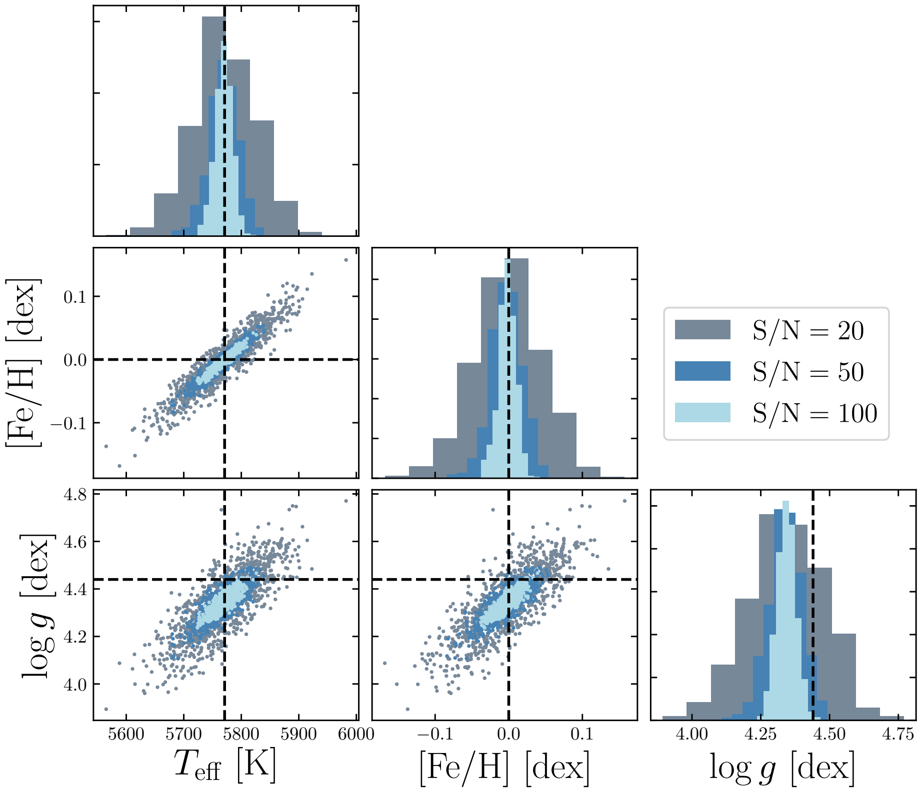

FIGURE II.12: `ATHOS` outputs from an MC simulation on the solar spectrum. Noise was artificially induced such that S/N values of 100 (gray), 50 (dark blue), and 20 (light blue) with 10^3 random initializations each were realized. The literature parameters (5771 K, 0.00 dex, 4.44 dex; Heiter et al. 2015) are indicated by black dashed lines.

(Chen et al. 2014) of the seven stars in common with our training sample. The results are presented in Figure II.11. There, we show the departures of the parameter values at moderate resolution (10 000) from the parameters obtained at high-resolution (45 000) for corrected and uncorrected FRs, respectively. From the diagnostic plot for $T_{\rm eff}$ and the mean deviation and scatter of 29 ± 32 K in the R-corrected case we conclude that our temperature relations are very stable against R – at least in the parameter space covered by the seven stars discussed here. This holds true even for the computed temperatures without any applied correction, where we found a marginally significant deviation of 45 ± 26 K (rms). The importance of introducing resolution corrections becomes apparent when looking at the [Fe/H] findings. By not accounting for resolution effects, `ATHOS` would underestimate the metallicity from the X-shooter spectra by on average -0.78 ± 0.23 dex, while the deviation vanishes for corrected FRs (0.00 ± 0.09 dex). Similarly, an uncorrected mean deviation of -0.31 ± 0.22 dex in the gravity results can be alleviated to -0.13 ± 0.17 dex.

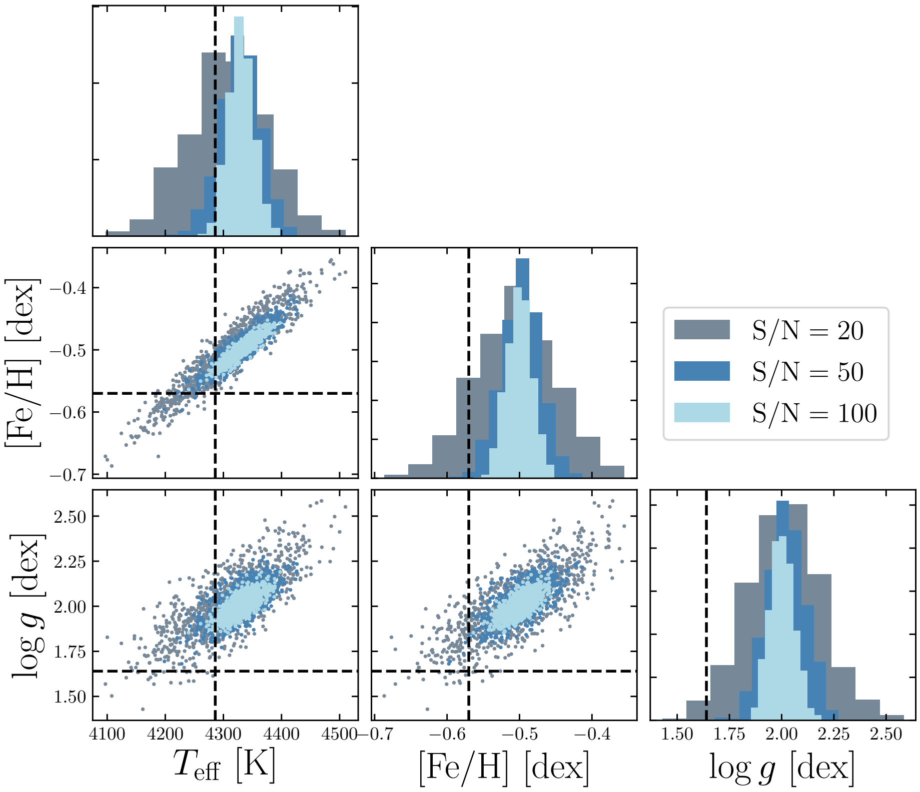

FIGURE II.13: Same as Figure II.12, but for α Boo (4286 K, −0.57 dex, 1.64 dex).

5.2 Spectrum noise and systematics

In order to test the stability of `ATHOS` against S/N we ran a series of Monte Carlo (MC) simulations by adding Poisson noise to high-S/N spectra of the Sun and α Boo as representatives of well studied and accurately parametrized dwarf and giant stars. The resulting spectra were fed to `ATHOS` to compute stellar parameters. This procedure was repeated 10^3 times for S/N values of 100, 50, and 20. Figures II.12 and II.13 show the distributions of the output. It is evident, for S/N = 100 and above, that `ATHOS` errors are not governed by random-noise effects in the input spectra, which can easily reach down to $\sigma_{T_{\mathrm{eff}}} = 50$ K, $\sigma_{[\mathrm{Fe/H}]} = 0.05$ dex, and $\sigma_{\log g} = 0.05$ dex. This has been discussed already in Sections 3.1, 3.2, and 3.3. The systematic errors provided there ($\sigma_{T_{\mathrm{eff}},\mathrm{sys}} = 97$ K, $\sigma_{[\mathrm{Fe/H}],\mathrm{sys}} = 0.16$ dex, $\sigma_{\log g,\mathrm{sys}} = 0.26$ dex) readily account for the deviations of non-stochastic origin found in the MC simulations.

Another implication of Figures II.12 and II.13 is the strong inter-dependence among the stellar parameters visualized by the inclination of the distribution ellipses. This does not come by surprise as the parameter cascade (phase 4) within `ATHOS` requires the output of all previous steps as input. The only truly independent quantity is

$T_{\rm eff}$, because we made sure that the respective relations are free of significant [Fe/H] or $\log g$ trends. Nevertheless, any deviation from the true value of $T_{\rm eff}$ enters the [Fe/H] relation (Equation II.10) as a constant and a (mild) additional slope with FR. Likewise, $T_{\rm eff}$ and [Fe/H] offsets propagate linearly onto the $\log g$ surfaces described by Equation II.13. We emphasize that this kind of behavior is also immanent to the established methods of using EWs or spectrum fitting to determine stellar parameters (see, e.g., the detailed discussion in the appendix of McWilliam et al. 1995). The inter-dependencies of the stellar parameters, however, tend to be neglected in most published studies; a practice that only started to change more recently (see, e.g., García Pérez et al. 2016). As our approach is capable of predicting temperature irrespective of the other two quantities, we can at least break the degeneracy with $T_{\rm eff}$ similar to studies employing spectrum fitting of Balmer lines (e.g., Barklem et al. 2002).

Ideally, an unbiased estimation of (in-)accuracies and precisions should be elaborated using data that have not been used for training, which was neither the case for the Sun nor α Boo. Hence, we decided to perform another test by employing the solar-type star 51 Peg. Being a famous exoplanet host (Mayor & Queloz 1995), there is a tremendous amount of high-quality (S/N > 300 pixel^{-1}, $R > 100\,000$) spectra in the ESO archive. From these, we retrieved 200 UVES and 91 HARPS spectra. Using two different spectrographs – one being operated in slit mode (UVES) and the other one being fiber-fed (HARPS) – offers the great advantage that the possibility of instrumental systematics can be investigated, whereas the considerable number statistics yield insights into the precision from real, high-quality spectra that may be obtained for dedicated abundance studies (e.g., Chapter III). Figure II.14 impressively demonstrates that – once fed with such high-quality data – `ATHOS` can reach precisions $\sim$ 10 K in temperature, $\sim$ 0.01 dex in [Fe/H], and $\sim$ 0.01-0.03 dex in gravity. Yet, the even more striking observation is that even at these extreme precisions we could not identify any systematic disagreements between two instruments that have very different positions of the spectral orders and therefore different blaze characteristics at the positions of the profiles of interest. Moreover there is a striking agreement with the reference parameters for 51 Peg by Sousa et al. (2018), which provides a first hint for the external accuracy of our new method. The latter can nonetheless only be properly investigated by means of larger comparison samples in excess of a single star. This is the goal of the following sections.

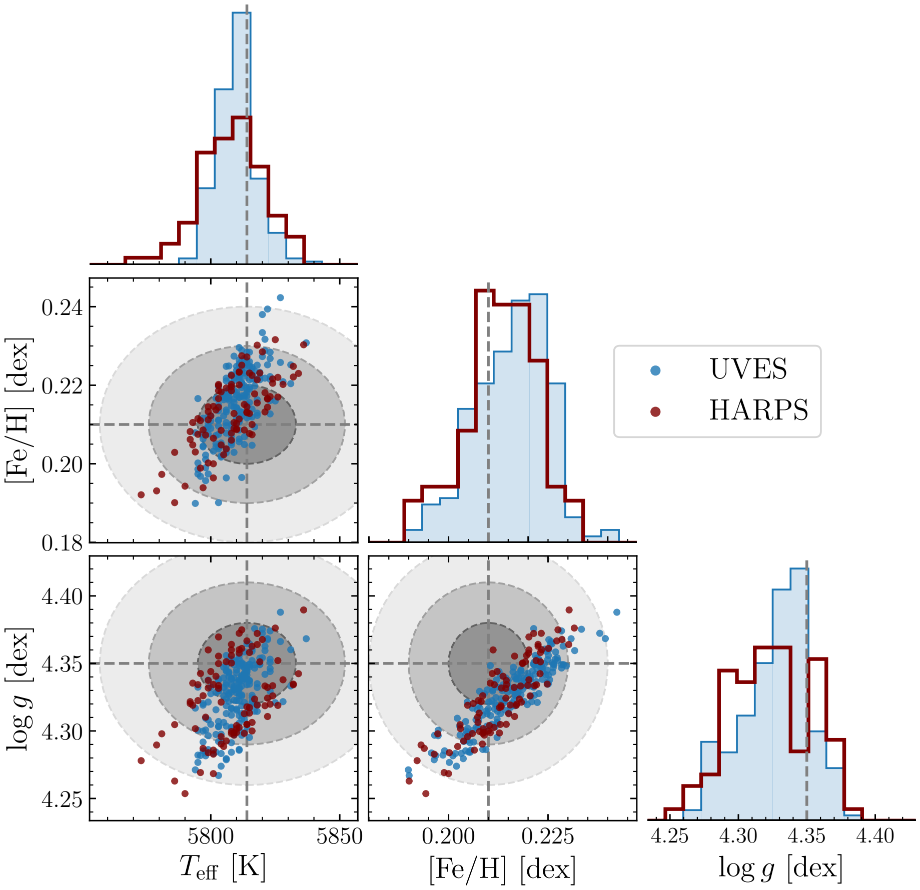

FIGURE II.14: `ATHOS` parameters for 51 Peg from a total of 291 real spectra that were obtained with UVES (200 spectra; blue) and HARPS (91 spectra; red). The marginalized distributions are represented by histograms in analogy to Figure II.12. We emphasize, however, that the axis limits are many times narrower compared to Figures II.12 and II.13. The sample means are 5810 ± 8 K/0.216 ± 0.009 dex/4.33 ± 0.02 dex and 5808 ± 12 K/0.213 ± 0.009 dex/4.32 ± 0.03 dex for UVES and HARPS, respectively. Literature parameters for 51 Peg by Sousa et al. (2018; 5814 ± 19 K/0.21 ± 0.01 dex/4.35 ± 0.03 dex) are indicated by dashed gray lines and ellipses marking 1σ, 2σ,and 3σ confidence intervals. Since no information about the covariances of the literature parameters was published, we do neglect them here and instead show ellipses that are aligned with the coordinate axes.

5.3 Comparison to spectroscopic surveys: ELODIE 3.1

The ELODIE library (Prugniel & Soubiran 2001) in its current version 3.1 (Prugniel et al. 2007) consists of 1959 spectra of 1389 stars obtained with the ELODIE spectrograph at the Observatoire de Haute-Provence. The spectra have a continuous coverage from 3900 to 6800 Å at a nominal resolving power of 42 000 and were released together with a catalog of stellar parameters compiled from literature data and with quality flags thereof. A restriction to the two best out of the four quality flags – i.e. maximum uncertainties in $T_{\rm eff}$ and [Fe/H] of 115 K and 0.09 dex – left us with 288 spectra of 201 stars. The median S/N of these spectra is 123 pixel^{-1} at

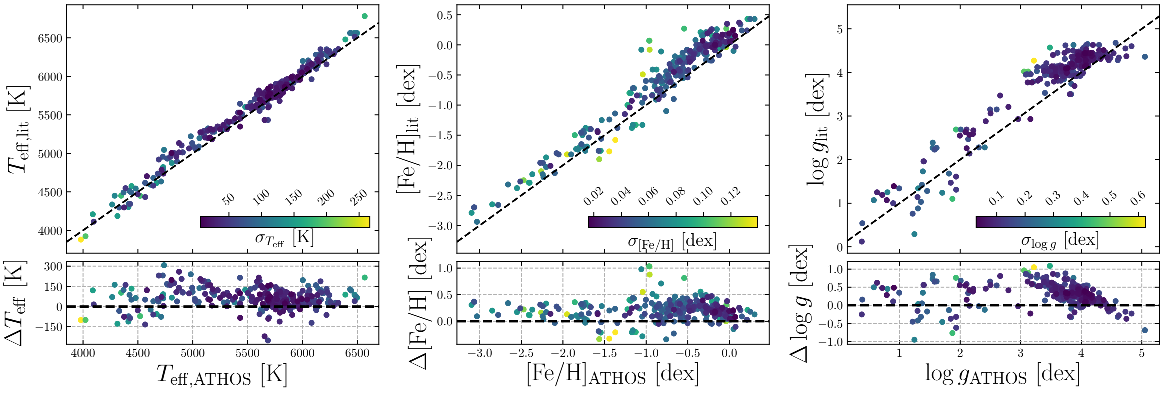

FIGURE II.15: *Upper panels*: comparison of the ATHOS output for $T_{\rm eff}$, [Fe/H], and $\log g$ with literature results for the ELODIE spectral library (version 3.1; Prugniel et al. 2007; see main text for quality cuts made here). In case a star occurs with multiple spectra in the library, it is represented by more than one point here. Dashed lines represent the one-to-one relation. The colors reflect the internal statistical uncertainties computed with ATHOS. *Lower panels*: residual distribution. All residuals are determined via $\Delta x = x_{\rm lit} - x_{\rm ATHOS}$.

5550 Å, while the minimum and maximum is 38 and 411 pixel^{-1}, respectively. The library is provided such that the spectra are already shifted to the stellar rest frame and tellurics were already masked, which enables an immediate analysis with ATHOS. The results of an ATHOS run on the 288 spectra and a comparison to the literature values are shown in Figure II.15.

We find an excellent agreement between ATHOS values for $T_{\rm eff}$ and the Elodie compilation. The mean deviation and scatter over the entire temperature range is 64 ± 76 K (rms). For 4750 K $< T_{\rm eff} <$ 5500 K, there seems to be a systematic offset of 105 K from unity. Cross-matching our training sample with the ELODIE library resulted in five overlaps in the temperature range in question (Table II.6). A possible source for the deviation could be the fact that our training $T_{\rm eff}$ are on average 71 K cooler. Two points in Figure II.15 around 5750 K are clearly off from the overall trend by more than 200 K. Both correspond to the star HD 245, which ATHOS consistently finds to be ~ 240 K warmer than the literature value of 5433 K. Comparing ELODIE spectra of the Sun with the two spectra of HD 245 shows a remarkable similarity of the Balmer profiles Hα and Hβ between the two stars. We conclude that both should have an almost identical temperature. Hence, the ATHOS result for HD 245 appears to be more reliable as it is closer to the solar value (5771 K). A visual inspection of the Balmer profiles in some of the ELODIE spectra revealed another possible explanation for $T_{\rm eff}$ differences to be bad pixel artifacts. We found several unphysical spikes with heights of a few 10% of the continuum level neighboring Hα and Hβ. These are neither masked nor flagged in the ELODIE library and can possibly falsify parameter measurements.

TABLE II.6: $T_{\rm eff}$ for overlapping stars between our training sample with interferometric temperatures and the ELODIE library in the range 4750 K to 5500 K.

Name	$T_{\rm eff,training}$ [K]	$T_{\rm eff,ELODIE}$ [K]	$\Delta T_{\rm eff}$ [K]
HD 103095	5140	5064	76
HD 175305	5059	5040	19
HD 188510	5400	5510	-110
HD 45282	5148	5273	-125
HD 108317	5027	5244	-217

The mean deviation in [Fe/H] is 0.21 ± 0.18 dex (rms). We investigated this behavior in the Sun. There are in total six solar spectra available through the ELODIE library, four of which satisfy $\mathrm{S/N} > 100\,\mathrm{pixel}^{-1}$. From those we derived $\mathrm{[Fe/H]} = -0.19$ dex with a negligibly small scatter. In Figure II.16, we compare a small wavelength portion to one of the solar spectra from our training grid. Here, the line cores in all ELODIE spectra do not reach as low as the ones in the reference spectrum. As a consequence, the overall line strength inferred from ELODIE is weaker, which translates into higher FRs and hence lower metallicities from `ATHOS`. Despite the fact that, compared to our training grid, ELODIE's resolution is slightly lower (42 000 versus 45 000), this finding cannot be attributed to resolution differences. If resolution were the sole reason, the missing line depth in the profile cores would be fully recovered in the wings, such that the total area of the profile (and hence the EW) stays constant and the integrated residuals evaluate to zero. This is not observed. We conclude that there must be an additive flux offset to ELODIE library spectra that leads to an unphysical weakening of absorption lines.

Looking at $\log g$, we computed a mean difference and scatter of 0.29 ± 0.30 dex (rms). The residual distribution for giants ($\log g \leq 2$ dex) is well described by random scatter, while for higher gravities there is a positive offset, which correlates strongly with Δ[Fe/H] and $\Delta T_{\rm eff}$. This is an expected behavior because – as discussed in Section 5.2 – our $\log g$ relations are sensitive to prior metallicity estimates.

5.4 Comparison with the S^{4}N library

S^{4}N is a high-resolution spectral library of 119 stars by Allende Prieto et al. (2004). The library encompasses a complete census of stars in the local volume (distances ≤ 15 pc) down to an absolute magnitude of $M_{\rm V} = 6.5$ mag. The spectra were obtained with either the 2dcoudé spectrograph ($R \approx 52\,000$) at McDonald Observatory or the FEROS spectrograph ($R \approx 45\,000$) at the ESO La Silla observatory. The S/N of the sample is very high (several 100s pixel^{-1}), so that noise-induced effects are uncritical.

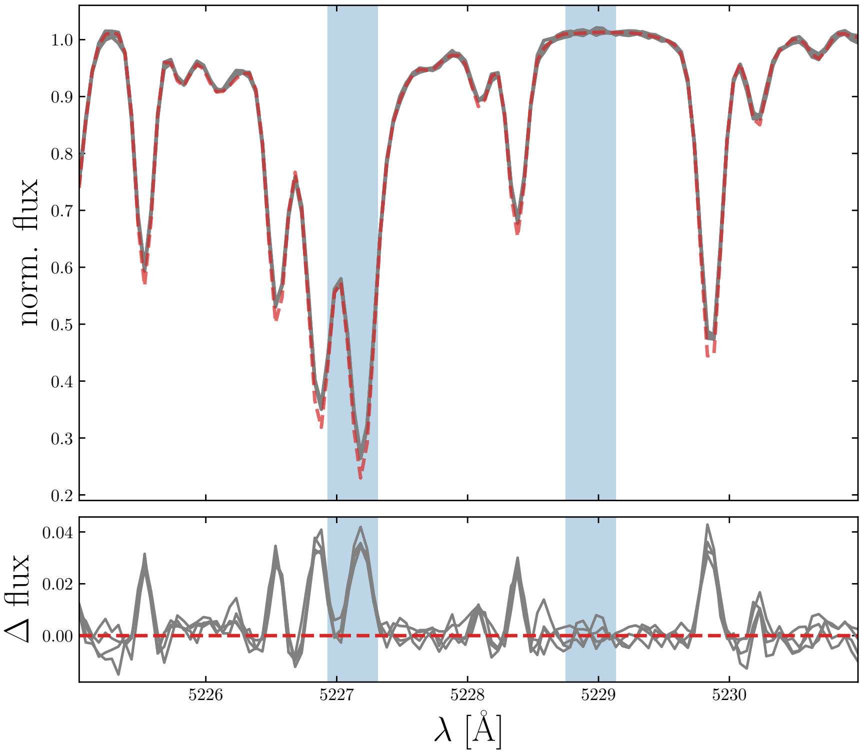

FIGURE II.16: *Upper panel*: comparison of the four ELODIE spectra for the Sun with S/N > 100 (gray) to the atlas spectrum by Hinkle et al. (2000) (red dashed). The latter was degraded to match the resolution of our training grid and resampled to the ELODIE dispersion scale. The blue regions show the fluxes used in one of our [Fe/H] relations. All spectra were normalized to the mean flux in the rightmost blue band. *Lower panel*: flux residuals.

The spectra cover all wavelengths of all of our parameter relations (3620 Å to at least 9210 Å). The provided T_{eff} was based on photometric colors assuming negligible reddening, while the metallicities were determined via full spectrum fitting of a 150 Å range around Hβ (see Allende Prieto 2003). S^{4}N gravities were inferred from fitting theoretical isochrones using HIPPARCOS parallaxes. We note that the sample may not be as homogeneous as wished since, for example, HD 82328 is a spectroscopic binary and HD 10780 is a BY Dra variable.

We computed stellar parameters for the S^{4}N library using `ATHOS`. To this end, we masked the Hα profiles of the FEROS spectra, because Allende Prieto et al. (2004) caution that those features have unreliable shapes due to fiber reflections within the spectrograph. Moreover, since the spectra are velocity-shifted but not corrected for tellurics, we had to cross-correlate our line list of tellurics with the library spectra in order to compute the respective velocities of the topocenter. This step was necessary to be able to include the Hα relations of the 2dcoudé spectra without being biased by telluric contamination. Three binaries (HD 110379, HD 188088, and HD 223778) were

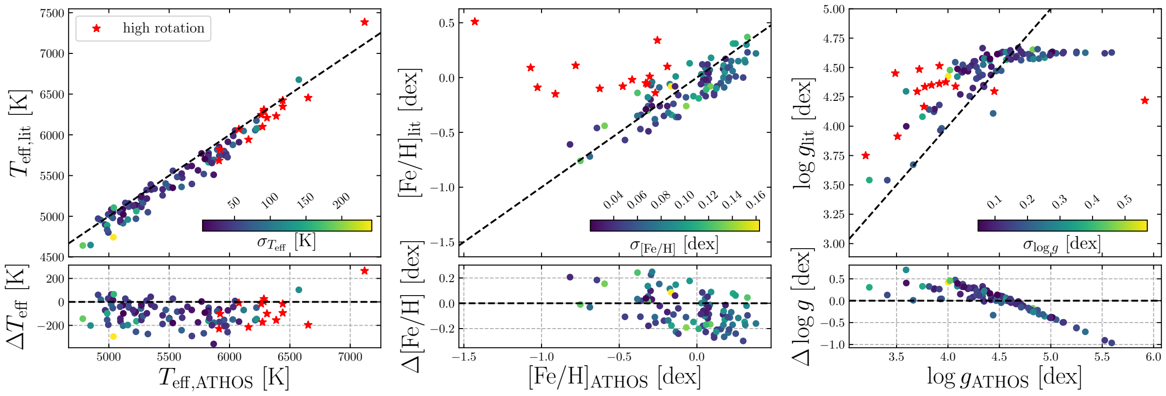

FIGURE II.17: Same as Figure II.15, but for the S^{4}N library (Allende Prieto et al. 2004). Red star symbols resemble stars with rotational velocities $v \sin i \geq 5$ km s^{-1}. For better visibility, we did not show these stars in the residual distributions of the *middle* and *right panel* as they are far off (see discussion in the main text).

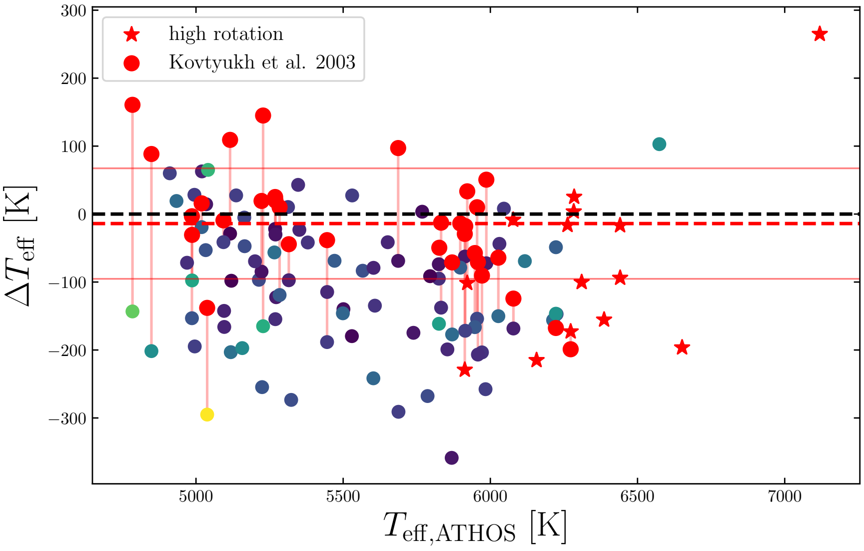

FIGURE II.18: Comparison of the residual temperature distribution of the S^{4}N literature temperatures (see *bottom left panel* of Figure II.17) with the ones in common with Kovtyukh et al. (2003) (red points). Vertical red lines connect points sharing the same spectrum and therefore `ATHOS` output. The red dashed line corresponds to the mean difference of 14 K when using the Kovtyukh et al. (2003) reference and the solid red lines indicate the $\pm 1\sigma$ scatter of 81 K.

excluded from consideration.

For T_{eff}, there seems to be a constant offset between the library parameters and `ATHOS`. Our temperatures are on average 105 ± 92 K (rms) warmer. We suspect that this is due to the literature values originating from photometric calibrations. The reader is referred, for example, to Lind et al. (2008) for a comparison of the Alonso et al. (1996b, 1999b) temperature scale with the one obtained from fitting Hα. Allende Prieto et al. (2004) cross-validated their photometric T_{eff} using the method of fitting

TABLE II.7: T_{eff} for overlapping stars between our training sample and the S^{4}N library.

Name	$T_{\text{eff,training}}$ [K]	$T_{\text{eff,S4N}}$ [K]	ΔT_{eff} [K]
α Boo	4286	4158	128
β Gem	4858	4666	192
δ Eri	4954	5023	-69
ϵ Eri	5076	5052	24
α Cen B	5231	4970	261
μ Cas	5308	5323	-15
τ Cet	5414	5328	86
α Cen A	5792	5519	273
18 Sco	5810	5693	117
β Hyi	5873	5772	101
β Vir	6083	6076	7
η Boo	6099	5942	157
α CMi	6554	6677	-123

Balmer lines by Barklem et al. (2002). Even though they have found almost negligibly warmer temperatures by on average 35 ± 84 K (rms), it seems that the small-scale trends in their figure 5 would – taken as correction for the literature values – improve our systematic discrepancies. Table II.7 shows a comparison of the temperatures of the stars in common between our sample and S^{4}N. All of them are also part of the GBS and therefore have highly reliable training temperatures, which are on average 88 K warmer. Another striking evidence showing that the photometric calibrations are systematically cooler than spectroscopic results can be seen when we compare our findings to those for the 32 stars in common with Kovtyukh et al. (2003). Their method for determining T_{eff} is based on spectroscopic line-depth ratios and has proven to have vanishingly small internal errors. In fact, as can be seen in Figure II.18, employing their published temperatures reduces the mean deviation and scatter of `ATHOS` results to 14 ± 81 K (rms), in other words the scatter approaches the order of the systematic uncertainty expected for our relations, $\sigma_{T_{\text{eff}},\text{sys}} = 97$ K.

In the middle panel of Figure II.17, there are several clear outliers (marked by red star symbols), which are predicted by `ATHOS` to have much lower metallicities than their tabulated reference values. Upon closer investigation, we found that the spectra expose significant rotational broadening. In fact, using $v \sin i$ values measured by Allende Prieto et al. (2004), there is a well defined behavior between Δ[Fe/H] and $v \sin i$ (see Figure II.19). To first order, rotational broadening looks similar to broadening by Gaussian line-spread functions. Thus the same reasoning as for the resolution dependencies in Section 5.1 holds: Rotation disperses flux out of the small-scale profiles used to determine [Fe/H]. Despite its implemented correction for R,

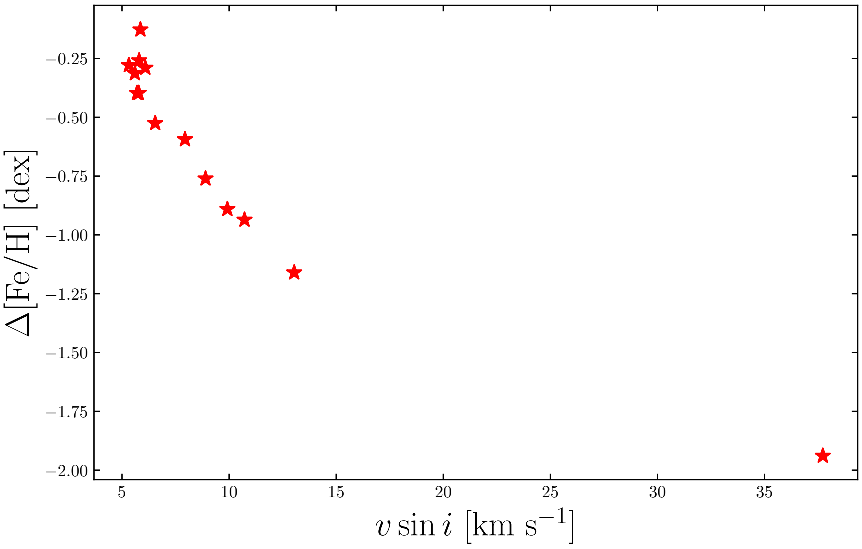

FIGURE II.19: Trend of Δ[Fe/H] with $v \sin i$ for the red stars in Figure II.17.

`ATHOS` is currently not capable of characterizing stars at rotational speeds $\gtrsim 5$ km s^{-1} unless provided with an approximate effective resolving power,

$$R_{\mathrm{eff}} = \frac{1}{1/R^2 + (v \sin i/c)^2}. \tag{II.15}$$

Overall, the [Fe/H] differences between S^{4}N literature values and `ATHOS` results are small, at an average of -0.06 ± 0.13 dex (rms). In the high-metallicity regime, we find higher metallicities by 0.14 ± 0.10 dex (rms). Assuming that the model temperatures for the full spectrum fitting of Allende Prieto et al. (2004) were systematically too cool, the majority of the synthesized (neutral) profiles would have been stronger at the true metallicity. As a consequence, [Fe/H] would have been underestimated to match the observed spectrum. This probably explains part of the `ATHOS` metallicities being slightly higher. Given that the quoted errors on S^{4}N gravities are very small, we can conclude from the linear $\Delta \log g$ trend with $\log g_{\mathrm{ATHOS}}$ (see right panels of Figure II.17) that our method's internal gravity error is relatively large. On average, however, the deviations do not exceed the $\sigma_{\log g,\mathrm{sys}} = 0.26$ dex provided for `ATHOS` (Section 3.3).

5.5 Comparison with the *Gaia*-ESO survey

The *Gaia*-ESO survey (henceforth GES, Gilmore et al. 2012) is a large-scale spectroscopic survey of $\sim 10^5$ stars in the Milky Way. Here, we studied how `ATHOS` performs on the high-resolution ($\sim$ 47 000) UVES spectra (4800 - 5800 Å) of field and cluster

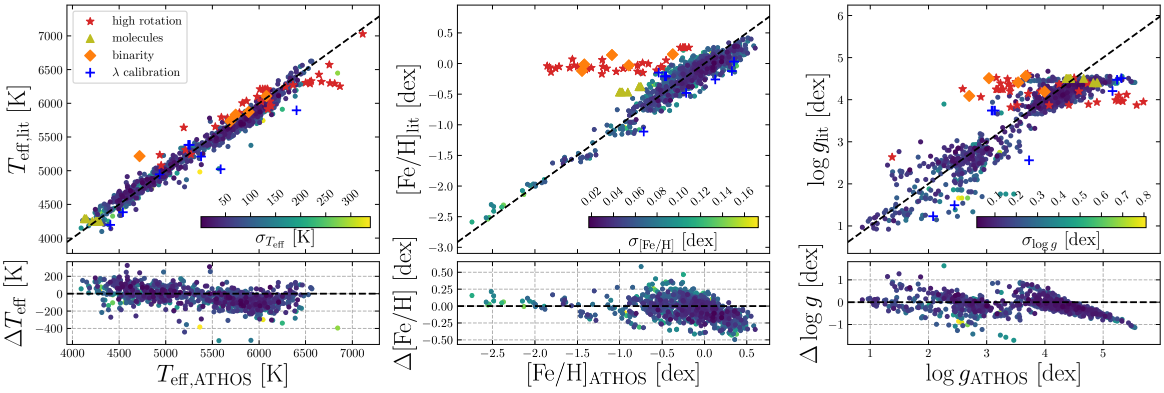

FIGURE II.20: Same as Figure II.15, but for the high-resolution spectra and recommended parameters from DR3 of the *Gaia*-ESO survey. Red stars, golden triangles, orange diamonds, and blue pluses indicate the peculiar spectra we found to show high rotational broadening, strong molecular blending, binary components, or erroneous wavelength calibrations, respectively. In the residual distributions (*lower panels*) we excluded those because they resemble extreme outliers (see text and Figure II.21).

stars that were released in data release 3.1 (DR3.1). GES published a catalog of recommended astrophysical parameters (Smiljanic et al. 2014). The spectra were analyzed by 13 different automated pipelines ("nodes"). Seven nodes measure EWs of Fe I and Fe II (see Section 2.1) via fully automated codes. The remaining six nodes fit either observed or synthetic spectra. All subgroups employed the same GES line list. The recommended, publicly available set of parameters are the weighted median results from all 13 nodes. In order to construct the respective weights, the nodes were applied to the GBS and the results split in three groups: metal-rich dwarfs, metal-rich giants, and metal-poor stars (here grouping dwarfs and giants). The average difference for each group was then used to estimate the weights for the respective nodes. We point out that, while vaguely accounting for changing systematic errors with gravity (at least for high-metallicity stars) and metallicity, this treatment does not consider varying systematics of individual nodes over the considerably large temperature range of the survey. If any such differential systematic deviation existed, it would bias the recommended temperature value. In order to be consistent with our reference solar Fe abundance $\log \epsilon(\mathrm{Fe})_{\odot} = 7.50$ dex by Asplund et al. (2009), we subtracted 0.05 dex from GES metallicities, which are based on Grevesse et al. (2007).

The spectra were shifted to their rest-wavelengths using v_rs provided in the GES parameter catalog. Spectra with $\mathrm{S/N} < 40\,\mathrm{pixel}^{-1}$ were omitted, as well as stars/spectra with GES peculiarity or technical flags including possible binarity, Balmer emission, strong molecular bands, strong rotation, radial velocity problems, or oversubtraction issues. The lower temperature limit was set to be 4000 K[3]. Moreover, in terms of parameter quality cuts, we set upper thresholds for the GES internal errors at 150 K

---

[3] Thereby, we lost six stars.

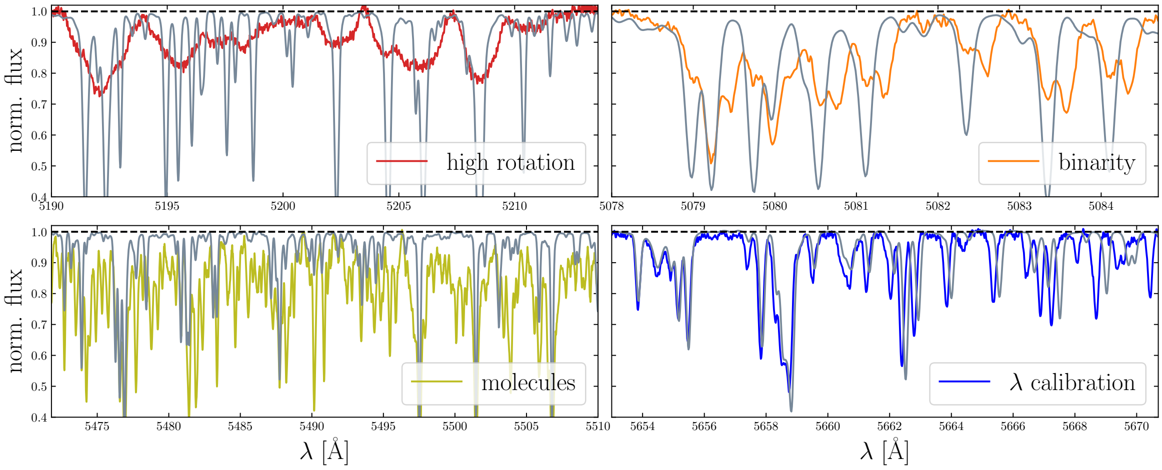

FIGURE II.21: Comparison of representative peculiar spectra (colored in the same way as in Figure II.20) to the solar spectrum (gray). An approximate normalization was performed by manually setting the continuum. The wavelength ranges were chosen such that the respective reason for peculiarity is illustrated best. The GES identifiers of the stars are (from *upper left* to *lower right*) 08100380-4901071, 18184436-4500066, 23001517-2231268, and 08090542-4740261.

and 0.2 dex for T_{eff} and [Fe/H], respectively. The final test sample comprised 1009 spectra of 912 stars. The median S/N is 67 pixel^{-1}, which is considerably lower compared to the ELODIE and S^{4}N libraries. The results are illustrated in Figure II.20.

The most striking feature is an apparent bifurcation in the [Fe/H] comparison (upper plot in the middle panel) very similar to the one in Figure II.17, which is induced by strong rotational broadening of the underlying spectra. We visually inspected the spectra of the stars with the strongest disagreement between GES and `ATHOS` metallicities and identified four distinct reasons (see Figure II.21). The most frequent reason for deviations is indeed rotational broadening. This is surprising, because the GES spectra that were flagged as exposing fast rotation were explicitly omitted. The same applies to stars flagged as showing binary signatures. Yet, we identified several spectra showing either pronounced double-lined or asymmetrically distorted single-lined profiles over the entire spectral range. The third intrinsic effect is strong blending by molecular features and was identified in eight spectra of two stars. These molecular features prevail in cool, metal-rich dwarfs and affect most of the otherwise blend-free components of the FRs used in the [Fe/H] relations (Equation II.10). `ATHOS` wrongly identifies the affected stars as being more metal-poor, because the portions of metal lines and their normalizing component are closer in flux than they would usually be at a given metallicity. The effect is 0.5 dex for the two stars studied here. For the remaining outliers, we found that there are severe inconsistencies in the wavelength calibration of the spectra. This can be seen in the lower right panel of Figure II.21: with increasing wavelength the blue spectrum appears compressed in comparison. We suspect that this is due to the wavelength solution diverging toward the edges of individual echelle orders. For some spectra the effect is so extreme that in the regions of overlapping orders, the order merging resulted in the spectrum appearing twice, spaced by up to 1.5 Å apart. We conclude that the observed disagreements are not caused by the method implemented in `ATHOS`, but by issues in the reduction pipelines and quality control of GES.

Over the entire $T_{\rm eff}$ range, `ATHOS` temperatures are marginally warmer by 39 ± 101 K (rms) compared to the recommended GES parameters. A closer look at the lower left panel of Figure II.20 showing the residual distribution reveals two subgroups. The dividing $T_{\rm eff}$ is at around 5500 K. Below this temperature, there is an excellent agreement at a mean difference and scatter of 14 ± 97 K. Above 5500 K, on the other hand, the mean deviation is -83 ± 82 K (rms), showing that GES is slightly cooler than our findings. Possible reasons are the potential systematics in the averaging process within GES on the one hand, or subtle non-linearities of $T_{\rm eff}$ with the FRs measured in the Balmer profiles, which were not detected. Nonetheless, given the rather low quality of the GES spectra in terms of S/N, it is remarkable that the scatter after removing the discussed biases of the two temperature groups is of order ~ 90 K.

`ATHOS` recovers the GES [Fe/H] with a mean deviation and scatter of -0.04 ± 0.15 dex. Again, considering the low S/N of the GES products and the fact that metallicities are computed from only a few pixels in the spectra, this is an extraordinary result. At super-solar metallicities there is a slight disagreement in that `ATHOS` metallicities are higher by ~ 0.15 dex. We argue that the trend arises due to the comparison sample (GES), which in Smiljanic et al. (2014), figure 18, shows the same trend. We point out that our method returns an rms of 0.15 dex for the entire sample, while they only show the GES stars for which the dispersion is less than 0.20 dex (so the trend may be even more pronounced). `ATHOS` accurately reproduces GES gravities at mean residuals of -0.18 ± 0.35 dex (rms).

5.6 Comparison with globular cluster studies

While the previous sections focused on an assessment of `ATHOS`' performance on surveys targeting heterogeneous stellar populations, we also aimed at testing results from the very homogeneous populations of RGB stars in GCs.

5.6.1 The Carretta et al. (2009) sample

We compare our method to the UVES study by Carretta et al. (2009, henceforth C09) of 202 stars of 17 GCs spanning a wide range of metallicities and masses. Out of

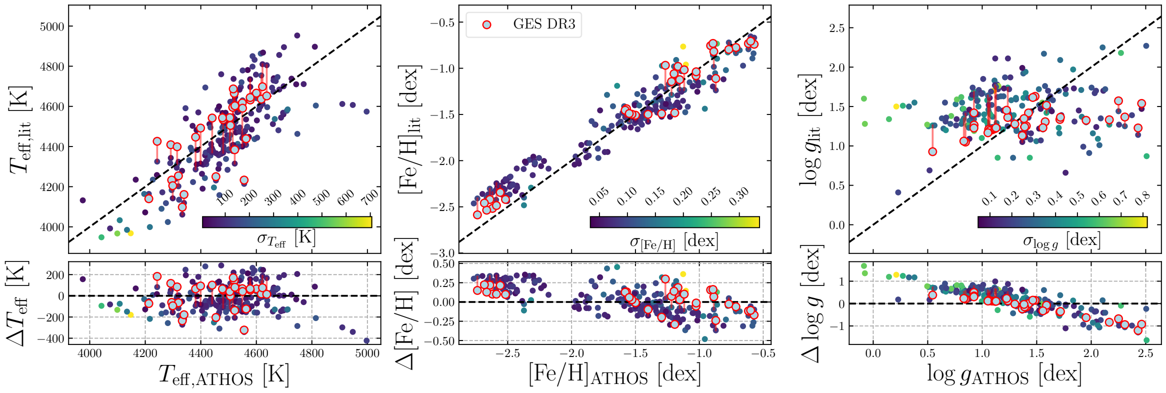

FIGURE II.22: Same as Figure II.15, but for the high-resolution UVES sample of GC stars from the study of C09. Points connected by a red line represent the same spectrum but have two different literature values. The additional red open circles indicate the recommended parameters for DR3 of GES.

the 17 GCs, four – NGC 104 (47 Tuc), NGC 2808, NGC 6752, and NGC 7078 (M 15) – were re-reduced from the C09 archival data by GES and made publicly available through DR3[4]. Reduced spectra for the remaining 13 clusters were kindly provided by E. Carretta (priv. comm.). For $T_{\rm eff}$, C09 relied on photometric calibrations and the assumption that the RGB of a GC is intrinsically narrow, which was used to infer $T_{\rm eff}$ from V magnitudes alone. Despite the lower star-to-star errors, we emphasize that the approach might still be subject to biases introduced by the photometric calibrations, $E(B-V)$, or differential reddening. C09 determined surface gravities from isochrone fitting and Fe abundances using EWs of both ionization stages[5].

We deduced a median S/N of 56 pixel^{-1} for the bluer spectral regions, where most of our FRs reside. Lacking information about the topocentric velocities by the time of the observations, Hα profiles were masked out entirely, so that tellurics would not hamper the analysis. Figure II.22 presents our results. On top of the C09 literature values, we show the recommended parameters by GES, which were based on a re-reduction and analysis of C09 raw data and make up a considerable fraction of the metal-poor stars discussed in the previous section.

`ATHOS` temperatures deviate on average by -30 ± 132 K (rms) from C09, hence there is an excellent agreement between the entirely photometry-based C09 $T_{\rm eff}$-scale and our purely spectroscopically constrained one. We note that the intra-cluster temperature deviations are less scattered than the global scatter of 132 K. There seems to be a systematic offset between individual clusters on the two scales. In Table II.8, we present the average temperature and [Fe/H] deviations between C09/GES and `ATHOS`.

---

[4] We note that compared to C09, two stars attributed to NGC 2808 are missing in DR3.

[5] We note that in the following we will refer to Fe II abundances whenever [Fe/H] is quoted in connection to C09.

TABLE II.8: Mean T_{eff} and [Fe/H] residuals of C09 and GES with respect to `ATHOS` for individual GCs, as well as the mean [Fe/H] and scatter determined in the three studies.

	C09					GES DR3					ATHOS		
GC ID	$\langle\Delta T_{\mathrm{eff}}\rangle$ [K]	$\sigma_{\Delta T_{\mathrm{eff}}}$ [K]	$\langle[\mathrm{Fe/H}]\rangle$ [dex]	$\sigma_{[\mathrm{Fe/H}]}$ [dex]	$\langle\Delta[\mathrm{Fe/H}]\rangle$ [dex]	$\langle\Delta T_{\mathrm{eff}}\rangle$ [K]	$\sigma_{\Delta T_{\mathrm{eff}}}$ [K]	$\langle[\mathrm{Fe/H}]\rangle$ [dex]	$\sigma_{[\mathrm{Fe/H}]}$ [dex]	$\langle\Delta[\mathrm{Fe/H}]\rangle$ [dex]	$\langle[\mathrm{Fe/H}]\rangle$ [dex]	$\sigma_{[\mathrm{Fe/H}]}$ [dex]	N_{stars}
NGC 104 (47 Tuc)	−175	84	−0.80	0.09	−0.05	−154	90	−0.76	0.03	−0.01	−0.75	0.12	11
NGC 288	−31	113	−1.35	0.08	−0.09	...	...	...	...	...	−1.26	0.14	10
NGC 1904 (M 79)	−107	82	−1.55	0.04	−0.01	...	...	...	...	...	−1.54	0.06	10
NGC 2808	−10	96	−1.17	0.09	−0.06	44	106	−1.06	0.06	0.06	−1.11	0.11	10
NGC 3201	−86	35	−1.46	0.07	−0.03	...	...	...	...	...	−1.44	0.13	13
NGC 4590 (M 68)	41	43	−2.27	0.09	0.22	...	...	...	...	...	−2.49	0.07	13
NGC 5904 (M 5)	−101	70	−1.34	0.06	0.05	...	...	...	...	...	−1.39	0.17	14
NGC 6121 (M 4)	−97	68	−1.17	0.05	−0.07	...	...	...	...	...	−1.10	0.16	14
NGC 6171 (M 107)	−300	80	−1.07	0.05	−0.11	...	...	...	...	...	−0.96	0.12	5
NGC 6218 (M 12)	−26	58	−1.37	0.05	−0.14	...	...	...	...	...	−1.22	0.09	11
NGC 6254 (M 10)	87	98	−1.60	0.07	0.07	...	...	...	...	...	−1.66	0.13	14
NGC 6397	204	42	−2.03	0.04	0.27	...	...	...	...	...	−2.30	0.07	13
NGC 6752	−99	42	−1.52	0.05	−0.06	84	38	−1.48	0.02	−0.03	−1.46	0.11	14
NGC 6809 (M 55)	−80	60	−1.92	0.07	−0.05	...	...	...	...	...	−1.87	0.08	14
NGC 6838 (M 71)	−103	122	−0.86	0.08	0.04	...	...	...	...	...	−0.90	0.23	11
NGC 7078 (M 15)	117	62	−2.35	0.07	0.23	52	24	−2.47	0.07	0.15	−2.59	0.13	13
NGC 7099 (M 30)	77	72	−2.34	0.06	0.15	...	...	...	...	...	−2.49	0.09	10

For example, the five stars of NGC 6171 constitute five of the six strongest deviating temperatures (lower left panel of Figure II.22). The mean deviation for this GC is −300 K with a scatter of only 80 K. Likewise, `ATHOS` predicts NGC 6397 stars to be cooler than the C09 findings by on average 204 ± 42 K (rms). Generally, the very low intra-cluster scatters confirm the high precision of the Balmer relations implemented in `ATHOS`. Systematic inter-cluster biases could either be founded in inaccuracies of the FR-relations for Balmer profiles in `ATHOS`, that is, linked to unresolved systematics connected to additional parameters, or in the already mentioned possible caveats of the photometric relations of C09. For NGC 6171, we suspect dereddening to be the main source causing the offset (cf., O'Connell et al. 2011) and for NGC 6397, assuming a too warm estimate of T_{eff} for all cluster members in C09 could explain the discrepant metallicities of C09 and Koch & McWilliam (2011).

Globally, our metallicity scale agrees within $\langle\Delta[\mathrm{Fe/H}]\rangle = 0.03 \pm 0.19$ dex (rms) with the one by C09. For the fairly large scatter, random uncertainties are likely to play a rather minor role. Figure II.22 implies a trend of $\Delta[\mathrm{Fe/H}]$ with metallicity, which is also reflected on the individual cluster scale (see Table II.8). Deviations of clusters are most likely caused by a drift in the T_{eff} scale. This is confirmed by Figure II.23, where we present a strong correlation between the mean temperature deviations and the mean metallicity residuals between C09 and `ATHOS` for individual GCs. In case of the strongest outlier in positive direction, NGC 6397, Koch & McWilliam (2011) found a metallicity of −2.10 dex compared to −2.03 dex. Adopting these values would reduce `ATHOS`' offset to 0.20 dex. At this point it is noteworthy that Lind et al. (2008) found much lower metallicities for NGC 6397 in better agreement with our findings for a stellar sample between the TO and the blue RGB. However, they showed that there is a significant trend of [Fe/H] with evolutionary stage (−2.41 dex

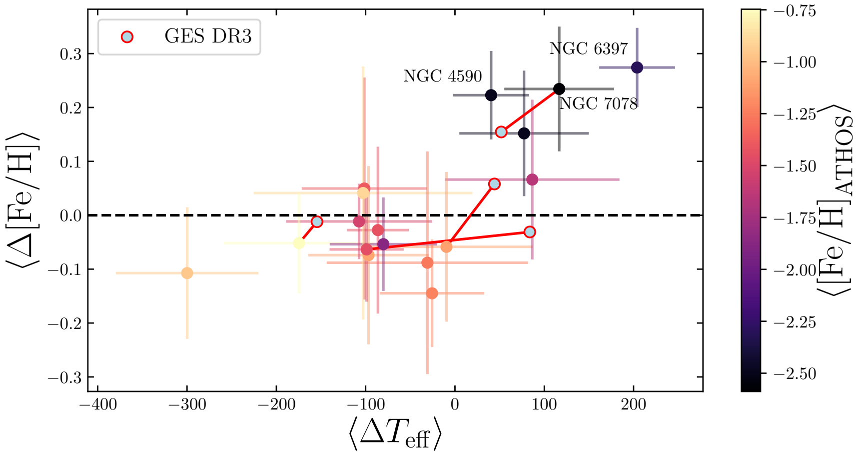

FIGURE II.23: [Fe/H] residuals averaged per GC versus mean temperature offset. The color coding resembles the cluster metallicity (see color bar on the *right*). Light-colored error bars indicate the respective $\sigma_{\Delta T_\mathrm{eff}}$ and $\sigma_{[\mathrm{Fe/H}]}$ from Table II.8. Red lines connect the same clusters corresponding to the same stars and spectra, but with stellar parameters either from C09, or GES DR3 (red circles).

TABLE II.9: Comparison of the literature stellar parameters of the MIKE GC sample to `ATHOS`.

GC ID	$\langle\Delta T_\mathrm{eff}\rangle$ [K]	$\sigma_{\Delta T_\mathrm{eff}}$ [K]	$\langle[\mathrm{Fe/H}]\rangle$ [dex]	$\sigma_{[\mathrm{Fe/H}]}$ [dex]	$\langle\Delta[\mathrm{Fe/H}]\rangle$ [dex]	Reference	`ATHOS` $\langle[\mathrm{Fe/H}]\rangle$ [dex]	`ATHOS` $\sigma_{[\mathrm{Fe/H}]}$ [dex]	N_stars
NGC 104 (47 Tuc)	14	65	−0.84	0.05	−0.07	Koch & McWilliam (2008)	−0.77	0.07	8
NGC 5897	−71	44	−1.92	0.08	−0.02	Koch & McWilliam (2014)	−1.89	0.13	7
NGC 5904 (M 5)	−39	89	−1.21	0.04	−0.17	Koch & McWilliam (2010)	−1.04	0.13	6
NGC 6397	22	289	−2.07	0.08	0.03	Koch & McWilliam (2011)	−2.10	0.38	5
NGC 6426	203	92	−2.37	0.04	0.21	Hanke et al. (2017)	−2.57	0.16	4
NGC 6864 (M 75)	−55	156	−0.98	0.13	−0.14	Kacharov et al. (2013)	−0.84	0.15	15

to −2.28 dex).

We found a marginal overall deviation of 0.17 ± 0.55 dex (rms) in the residual distribution of $\log g$ between C09 and `ATHOS`. Given that all stars considered here are giants clustering around $\log g \approx 1.3$ dex, the apparent trend in the residual distribution can be attributed to larger errors on individual `ATHOS` gravities leading to an increased star-to-star scatter with respect to C09. The difference between the two distributions produces the observed anticorrelation of $\log g_\mathrm{ATHOS}$ and $\Delta \log g$. Given that most of the information carried by the FRs is related to [Fe/H] (see Section 3.3), here the S/N of the giant spectra probably plays an important role for the large scatter in $\log g$.

5.6.2 The MIKE sample

During the last ten years, we have published a series of detailed spectroscopic studies of GC member stars. In total, 46 targets of six GCs (see Table II.9 for details and references) have been observed using the high-resolution ($R \approx 40\,000$) MIKE

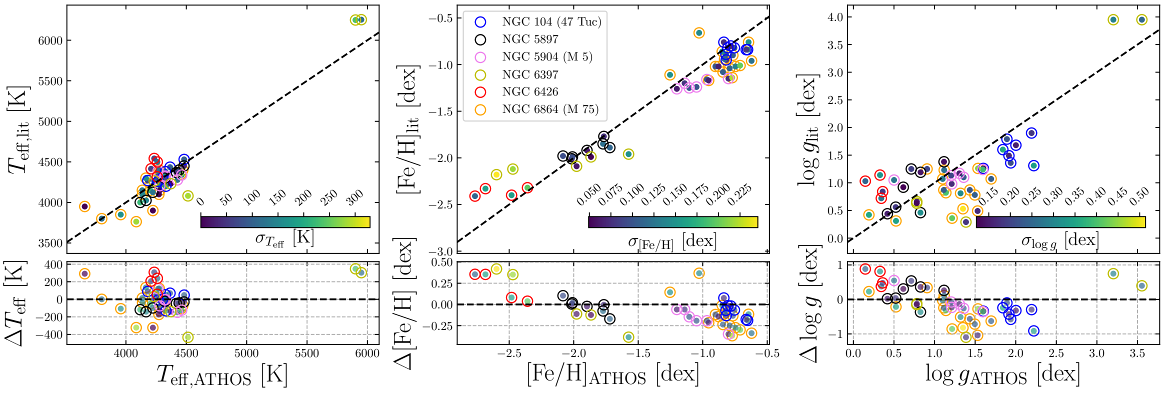

FIGURE II.24: Same as Figure II.15, but for a sample of MIKE spectra of GC stars. The colored open circles indicate the membership in either of the GCs 47 Tuc (blue, Koch & McWilliam 2008), M 5 (pink, Koch & McWilliam 2010), NGC 6397 (yellow, Koch & McWilliam 2011), M 75 (orange, Kacharov et al. 2013), NGC 5897 (black, Koch & McWilliam 2014), or NGC 6426 (red, Hanke et al. 2017).

spectrograph mounted at the 6.5 m Clay telescope at Las Campanas Observatory. The stellar sample of NGC 6397 contains two MSTO stars, for which Koch & McWilliam (2011) used profile fits to Hα to deduce T_{eff}. With the exception of stars belonging to NGC 5897 and NGC 6864, all temperatures of RGB stars were derived in a differential approach, that is, excitation balance was enforced differentially on abundances of Fe I lines with respect to the same lines in well understood standard stars with reliable reference parameters (see Koch & McWilliam 2008). These should be as close as possible to the stellar parameters of the stars to be analyzed. Then, the differential treatment cannot only forgo relying on uncertain oscillator strengths, but reduce the influence from NLTE-induced excitation imbalances as well (Hanke et al. 2017, and references therein). In all studies, $\log g$ was computed from basic stellar structure equations. Here, we refer to abundances of Fe II, which were computed from EWs as [Fe/H].

Figure II.24 together with Table II.9 show the comparison between the original works on the GCs and an ATHOS run. The mean T_{eff} difference is -12 ± 161 K (rms), with a scatter dominated by differences between individual clusters. In terms of temperature, we found one cluster to systematically deviate from the one-to-one trend.

While exposing a rather small star-to-star dispersion in the residuals, all four stars of NGC 6426 are predicted to be cooler by ~ 203 K compared to their respective reference values. One possible explanation for this observation is that none of the stars in Hanke et al. (2017) satisfy excitation equilibrium of Fe I in an absolute abundance treatment. In the differential approach pursued in that work the imbalances were compensated by the strong excitation imbalance (on the absolute scale) of the very

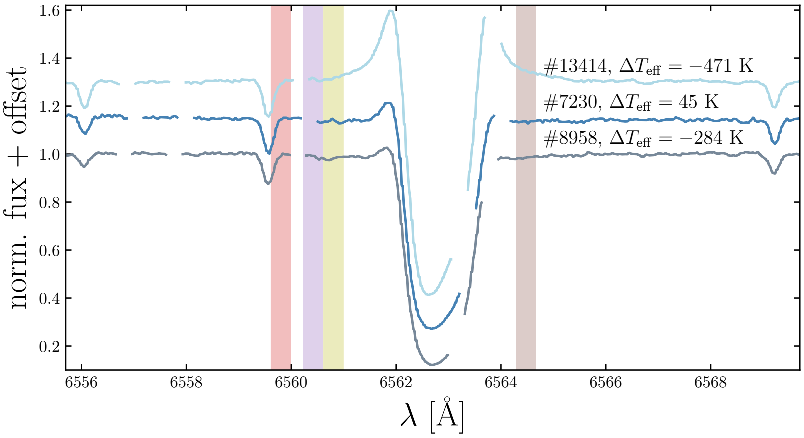

FIGURE II.25: Impact of wind-induced emission on `ATHOS` temperatures from Hα. Shown are the three red giant spectra of NGC 6397 by Koch & McWilliam (2008) in the Hα spectral region. The vertical colored ranges mark the close-by components of the four temperature FRs for Hα. The emission on either side of the profile core is especially pronounced for the star #13414 and it is evident that the irregular behavior has an impact on the wavelength windows of interest.

similar, metal-poor benchmark star HD 122563. The imbalance in this star is likely to originate from NLTE effects (Mashonkina et al. 2011). We showed that, in order to achieve excitation equilibrium, T_{eff} had to be lowered by 200 K compared to the differential case. As the majority of the temperatures of the metal-poor training stars in this study were determined using absolute abundances, the offset for NGC 6426 can be explained by `ATHOS`' temperature scale being tied to absolute rather than to differential methods. We point out that the other two metal-poor clusters, NGC 5897 and NGC 6397, do not show the same deviation. NGC 5897 was studied with an absolute treatment, hence the findings are accurately reproduced by `ATHOS`. For NGC 6397, the employed benchmark star was Arcturus, which does not show any excitation imbalances in an absolute LTE analysis (Koch & McWilliam 2008). Consequently, the differential temperature scale is essentially the same as the absolute one.

Two GCs, namely NGC 6397 and NGC 6864, exhibit a large scatter (285 K and 179 K, respectively) with respect to what we would expect given the high S/N of the spectra. This was partly due to Hβ not being covered by most of the MIKE spectra and additional loss of Hα relations due to telluric contamination. An important source for the strongest offset ($\sim$ 400 K), which is shown by the RGB star #13414 in NGC 6397, is its strong mass-loss that manifests in wind-induced emission spikes in the profile wings of Hα as showcased in Figure II.25. For the two MSTO stars in NGC 6397, we identify the treatment of different broadening mechanisms in the LTE Balmer synthesis of the original work as possible origin of deviations in the temperature scales. The large intra-cluster scatter of ΔT_{eff} for NGC 6864 (156 K) remains inexplicable.

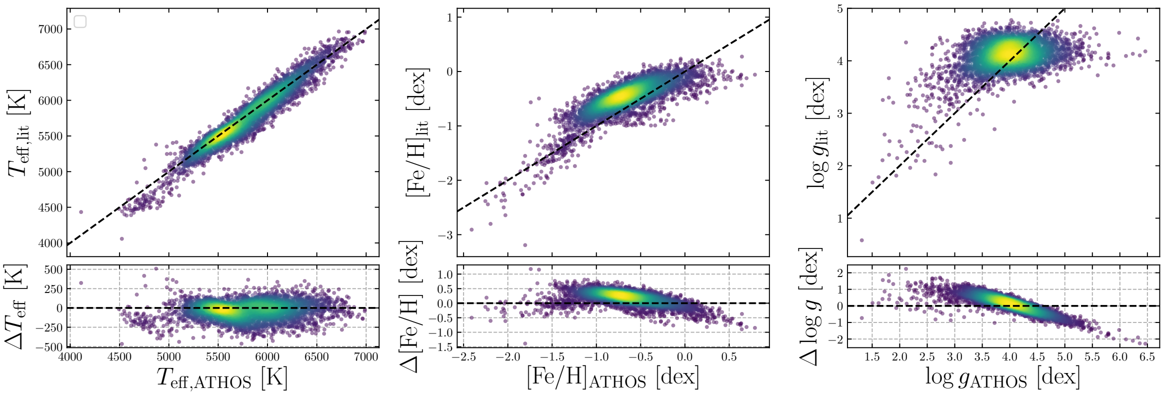

FIGURE II.26: Same as Figure II.15, but for 3966 SDSS low-resolution ($R \approx 1500$ to 2500) spectra. As opposed to earlier figures, here the color does not represent `ATHOS` errors but the local point density (arbitrary units) obtained via a Gaussian kernel-density estimate.

In terms of metallicity, the mean residual deviation and scatter is -0.06 ± 0.20 dex. Similar to before, neither mean nor scatter are representative for all the subsamples and differences can be linked to deviating temperatures of individual stars.

The comparison of the literature gravities with our results for $\log g$ confirms that especially for gravities well below 1 dex `ATHOS` can only provide a rough estimate. Partly, this is also related to rather low S/N values of the spectra, which increase the internal $\log g$ errors of `ATHOS` (see right panels of Figure II.24).

5.7 Comparison with SDSS

The SDSS released several hundred thousand optical spectra at low resolution ($R \approx 1500$ to 2500) with an accompanying catalog of stellar parameters for a subset thereof (Abolfathi et al. 2018). These parameters were determined using the SEGUE Stellar Parameter Pipeline (`SSPP`, Lee et al. 2008a), which obtains stellar parameters from several photometric and spectroscopic estimators. The final adopted `SSPP` parameters are averaged from the individual measurements using a decision tree that excludes certain results based on photometric quality cuts and S/N values of the analyzed spectra (see Lee et al. 2008a, for a detailed discussion).

We used the DR14 SSPP catalog – which has not changed since DR12 – to retrieve and analyze spectra obeying our own quality cuts. These were set such that only spectra without peculiar flags, maximum SSPP uncertainties on T_{eff}, [Fe/H], and $\log g$ of 50 K, 0.05 dex, and 0.1 dex, as well as with $\mathrm{S/N} > 80\ \mathrm{pixel}^{-1}$ were considered. The fact that we analyzed the resulting 3966 spectra within 16 s, that is 4 ms per spectrum, impressively shows that `ATHOS`′ execution time is merely limited by the size of the input spectra (in this case $\sim$ 3800 dispersion points). We illustrate the comparison between `ATHOS` and `SSPP` results in Figure II.26.

The mean offset and rms scatter in T_{eff} is -37 ± 115 K, which proves our new temperature indicator to be accurate (on the scale of SSPP) and precise even at resolutions as low as $\sim$ 2000. Further, despite not being covered by our benchmark sample, the temperature range between 6500 K and 7000 K appears to be described well by extrapolating our linear FR-trends.

In terms of metallicity, we found a bias of 0.20 ± 0.24 dex (rms) and additional substructure in the residual distribution. This is not further surprising, because the pixel spacing in SDSS spectra resides mostly well above 1 Å. Hence, `ATHOS` determines metallicities (and gravities) for the individual relations from wavelength ranges ($w = 0.187$ Å) that span less than a fifth of a pixel's width. Due to this, any inaccuracy in the wavelength solution or in the radial velocity determination of the input spectra adds a systematic contribution that potentially has a large influence on the deduced parameters. Nonetheless, it is tempting to argue that the residual trend shown in Figure II.26 shows a striking resemblance with the trend in the lower panel of figure A2 by Smolinski et al. (2011), where the authors compare SSPP parameters to literature values from high-quality (i.e., high-resolution and high S/N) spectra. This could be interpreted as hint that – despite being mainly designed for medium- to high-resolution instruments – `ATHOS` outperforms `SSPP` in the metallicity scale when compared to high-resolution studies.

Our $\log g$ estimate is accurate on the SSPP scale on a 0.01 dex level with a scatter of 0.50 dex. While its T_{eff} method is highly accurate and the metallicity scale reveals promising insights, `ATHOS`' gravity estimates at these low resolutions are rather vague. Nevertheless, they can still be used as means to distinguish dwarfs from giants, which is a challenge in itself when analyzing low-resolution spectra.

5.8 Comparison across surveys

A key goal of this project was to enable cross-validation and parameter homogenization across various survey pipelines. This main strength of `ATHOS` is illustrated in Figure II.27, where we show the combined results of all six data sets (ELODIE, S^{4}N, GES, C09, our MIKE GC studies, and SDSS/SEGUE) that have been described in detail before. It is noteworthy that all 1579 high-resolution spectra of different resolutions originating from six different instruments were analyzed within 43 s, corresponding to an average execution time of 27 ms per spectrum. For the 3966

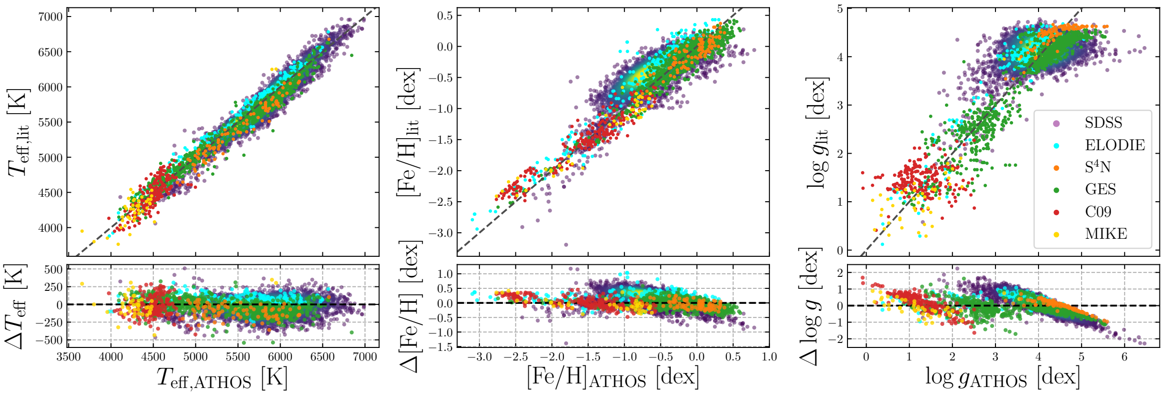

FIGURE II.27: Comparison of the results from all surveys discussed in Sections 5.3 to 5.7. The color coding is indicated by the legend in the *right panel*.

low-resolution spectra the average time demand was considerably lower at 4 ms. We emphasize that this was achieved using only one CPU core on a regular laptop.

From Figure II.27 we conclude that using `ATHOS`' homogeneous parameter scale together with its wide-ranging applicability enables the detection of discrepancies between the methods employed by the different surveys. Our in-depth investigations of the individual samples (see earlier sections) revealed that departures from the `ATHOS` scale – especially for $T_{\rm eff}$ – are likely to be founded either in erroneous spectroscopic data, or possible shortcomings of the various survey pipelines.

6 Summary and Conclusions

In this Chapter we presented a novel approach of deriving the fundamental stellar parameters $T_{\rm eff}$, $\log g$, and [Fe/H] by employing parameter-sensitive FRs of close-by wavelength windows in optical stellar spectra. Using a set of simple analytical relations, the FRs described here were tied to the well-calibrated parameters of a training set of 124 stars. The training sample comprised stars spanning a wide domain of stellar parameters, that is dwarfs and giants of spectral type F to K that range from very metal-poor ([Fe/H]≈ -4.5 dex) to super-solar metallicities. The introduced technique is non-iterative – that is computationally inexpensive – and depends on models only to the degree that the training parameters have been determined via model-dependent approaches.

Our method was implemented into a `Python`-based code we call `ATHOS`, which is made publicly available[6]. Being fairly simple, it is straightforward to implement the

---

[6] https://github.com/mihanke/athos

relations established here in any other piece of spectrum analysis code. We have shown that our method accurately recovers the atmospheric parameters of the large samples of the ELODIE and S^4N libraries, the high-resolution part of the *Gaia*-ESO survey, the GC studies by C09 and our own group comprising in total 20 clusters, and – at least in terms of $T_{\rm eff}$ – the SDSS/SEGUE survey. Thus, `ATHOS` temperatures have proven to be insensitive to spectral resolution over more than a magnitude of resolutions ($R \approx 2000$ to $52\,000$), while [Fe/H] and $\log g$ are reproduced accurately down to $R \approx 10\,000$.

Our machine-learned, optimal FRs converged toward determining a star's effective temperature from wavelength regions around the Balmer lines Hβ and Hα. As opposed to many other parameter-estimation methods, this can be done truly independent from any other stellar parameter, such as metallicity. We could show that our new temperature estimator agrees very well with the LDR-based scale of Kovtyukh et al. (2003) ($\Delta T_{\rm eff} = 14 \pm 81$ K, based on spectra of 32 stars). Our method, however, has a much more extended range of applicability, because it is also capable of analyzing giants and – due to relying on Balmer- instead of metal lines – metal-poor stars down to metallicities of ~ -4.5 dex.

Based on the determined temperature, we can use FRs involving spectral features of atomic and ionized species to deduce [Fe/H] and $\log g$, respectively. We have been more lenient with the gravity estimates, since we assume that *Gaia* parallaxes (Gaia Collaboration et al. 2018a) will – at least for the brighter and/or near-by stellar populations – oust any spectroscopic method in the future.

Provided the optical spectra include parameter sensitive wavelength regions like Hα, `ATHOS` can efficiently and fast (a few milliseconds per spectrum) determine the three key stellar parameters, $T_{\rm eff}$, [Fe/H], and $\log g$. Unlike previously established automated methods of determining stellar parameters such as EW-matching algorithms (e.g., Smiljanic et al. 2014, and references therein) or full spectrum fitting techniques (e.g., `The Cannon`, Ness et al. 2015), the approach introduced here is largely insensitive to continuum normalization and resolution of the spectra. Hence the strength of `ATHOS` is that it is not confined to a specific survey or spectrograph and that it does not require a separate training for each individual survey. Furthermore, it can deal with any spectral type (within the training sample's limitations) irrespective of a priori assumptions or priors. These aspects constitute `ATHOS`' main strength, which is the determination of homogeneous stellar parameters across surveys whilst, at the same time, proving highly reliable for detailed studies with a critical demand for high accuracies and precisions.

Our new tool is capable of parameterizing one million stars in just about eight hours on a single CPU core. Hence, in its current version, `ATHOS` can homogeneously and robustly analyze all high-resolution spectra ever to be observed with 4MOST and WEAVE in less than one day, without any manual interference or having to use extensive computational resources. In addition, it is a very useful tool for flagging outliers (binaries, fast rotators, chemically peculiar stars) which previous surveys like GES may have overlooked.

Future add-ons in `ATHOS` will focus on the investigation of peculiar stars like CEMP stars, fast rotators, and low-gravity ($\log g < 1$ dex) stars. Another class of peculiar stars we desire to explore is the collection of variable stars, such as RR-Lyrae or Cepheid variables, which can exhibit atmospheric shocks that might distort spectral profiles like Hα. Finally, we will examine the possibility to extend our FR-based method to near-infrared spectra in order to enlarge `ATHOS`' wavelength applicability.

CHAPTER III

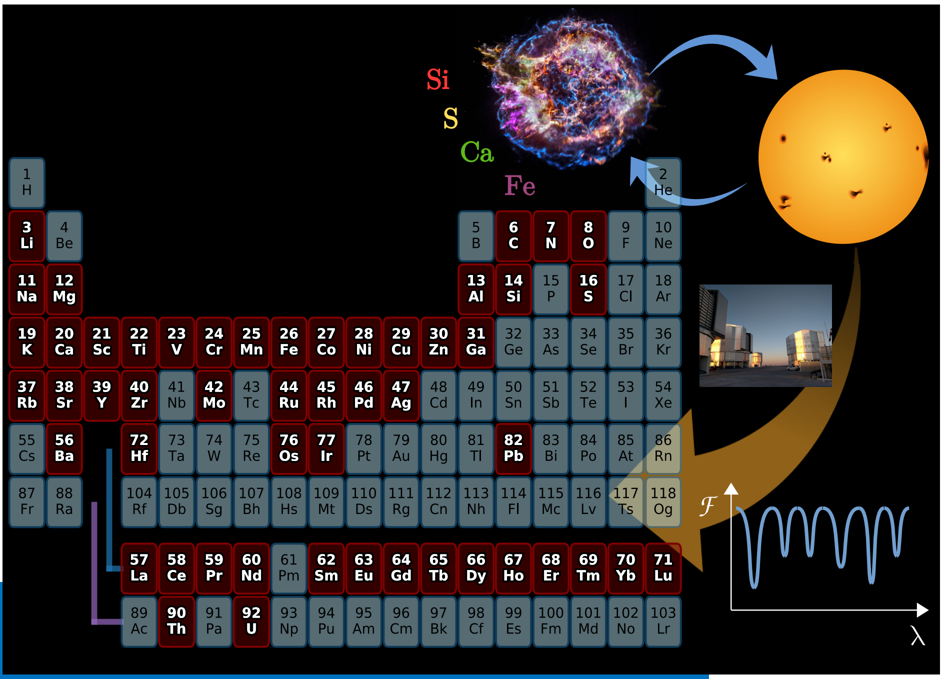

This image shows a periodic table where those elements that were investigated in the present study are highlighted in white. Furthermore shown is a composite false-color X-ray image of Cas A, a representative of Type II supernovae that produce chemical species up to and including the iron-peak elements (seen in X-ray emission lines and represented here by different colors). **Image credits.** Cas A: NASA/CXC/SAO. *VLT/UT2,UT3, and UT4*: M. Hanke.

A high-precision abundance analysis of the nuclear benchmark star HD 20

This chapter in brief

At the core of this chapter lies the detailed derivation and interpretation of chemical abundance distributions in the metal-poor halo star HD 20.

- In Section 2, the employed data sets and their reduction are outlined.
- Section 3 is dedicated to the inference of HD 20's fundamental structural parameters, which are independently corroborated in Section 4.
- A description of the abundance analysis and a critical assessment of statistical uncertainties and systematics are provided in Sections 5 and 6.
- The implications drawn from the abundance pattern with respect to contributing nucleosynthesis processes and sites are discussed in Section 7, whereas a summary of the project is given in Section 8.

This chapter was published in Hanke et al. (2020a) and has been co-authored by C. J. Hansen, H.-G. Ludwig, S. Cristallo, A. McWilliam, E. K. Grebel, and L. Piersanti.

1 Context

After having established FRs as highly reliable spectroscopic tools, the present chapter builds upon the solid foundation of reliable fundamental structural parameters and delves into detailed chemical abundance analyses and the scientific interpretation of deduced chemical patterns for a newly established metal-poor benchmark star. Studies of such metal-poor stars as bearers of fossil records of Galactic evolution are among the cornerstones of Galactic archaeology. In this respect, revealing the kinematics and chemistry of this relatively rare subclass of stars provides vital insights into the build-up of galaxy components, such as the Galactic halo and the origin of chemical elements. Nuclear benchmark stars with available robust and comprehensive chemical patterns allow for detailed studies of each of the nucleosynthetic processes that led to their enrichment.

From an observational point of view, there have been a number of spectroscopic campaigns that specifically targeted metal-poor stars to constrain the nucleosynthesis of heavy elements in the early Milky Way, among which are, to name a few, Christlieb et al. (2004), Hansen et al. (2012, 2014), and the works by the r-process alliance (e.g., Hansen et al. 2018b; Sakari et al. 2018, and follow-up investigations). Following Beers & Christlieb (2005), the rare class of r-process-rich stars is commonly subdivided by a somewhat arbitrary cut into groups of moderately enhanced r-I ($0.3 \leq$ [Eu/Fe]$\leq +1.0$ dex; [Ba/Eu] < 0 dex) and strongly enhanced r-II ([Eu/Fe] $> +1.0$ dex; [Ba/Eu] < 0 dex) stars. Recently, Gull et al. (2018) reported on the first finding of an r-I star with a combined "r+s" pattern, which was explained by postulating mass transfer from a companion that evolved through the AGB phase.

Here we present an in-depth spectroscopic abundance analysis of HD 20, an r-I star at the peak of the halo metallicity distribution function ([Fe/H] $= -1.60$ dex) with a heavy-element pattern that suggests pollution with s-process material.

Based on the full 6D phase-space information from *Gaia* DR2, Roederer et al. (2018a) concluded that HD 20 may be chemodynamically associated with two other metal-poor halo stars with observed r-process excess. Judging from its kinematics – characterized by a highly eccentric orbit ($e = 0.975^{+0.002}_{-0.004}$) and a close pericentric passage ($r_{\text{peri}} = 0.19^{+0.04}_{-0.02}$ kpc) – and its low metallicity, the authors speculate that HD 20 and its associates may have been accreted from a disrupted satellite.

Among others, HD 20 has been a subject of two previous abundance studies by Burris et al. (2000) and Barklem et al. (2005) who reported eight and ten abundances for elements with $Z \geq 30$, respectively. Both groups employed medium-resolution

TABLE III.1: Comparison of abundances for HD 20 in common between Burris et al. (2000) and Barklem et al. (2005). Typical errors are 0.20 to 0.25 dex.

X	$\log \epsilon(X)$ [dex] Burris et al. (2000)	 Barklem et al. (2005)	Δ [dex]
Fe	6.28	5.92	0.36
Sr	1.56	1.51	0.05
Y	0.80	0.62	0.18
Zr	1.67	1.40	0.27
Ba	1.32	0.86	0.46
La	0.22	−0.08	0.30
Nd	0.69	0.26	0.43
Eu	−0.11	−0.27	0.16

($R \approx 20\,000$) spectra at S/N slightly above 100 pixel^{-1}. Table III.1 lists the findings for the eight elements that are in common between both works and we note systematic disagreements – in a sense that the abundances by Burris et al. (2000) generally are above Barklem et al. (2005) – exceeding even the considerable quoted errors of about 0.2 dex. The authors adopted very similar effective temperatures for their analyses (5475 K versus 5445 K), while the employed stellar surface gravities and microturbulent velocities differ strongly by +0.41 dex and -0.30 km s^{-1}. Inconsistencies between the studies are likely to be tied to these discrepancies, as has already been recognized by Barklem et al. (2005; see also Section 6.2 for a detailed discussion of the impact of model parameters on individual stellar abundances).

Our work is aimed at painting a complete picture of the chemical pattern in HD 20 consisting of 58 species from the primordial light element Li to the heavy r-process element U. To this end, a compilation of high-quality, newly obtained and archival spectra was used, allowing for many elemental detections with high internal precisions. Furthermore, specific attention was devoted to the determination of accurate stellar parameters in order to mitigate the effect of systematic error contributions to the robustness of the deduced pattern. In this respect, an essential building block of our analysis is a highly accurate and precise stellar surface gravity from an asteroseismic analysis of the light curve that was obtained by NASA's TESS mission (Ricker et al. 2015). Hence, we established HD 20 as a new metal-poor benchmark star – both in terms of fundamental properties as well as complete abundance patterns – which, in light of its bright nature ($V \approx 9$ mag), provides an ideal calibrator for future spectroscopic surveys.

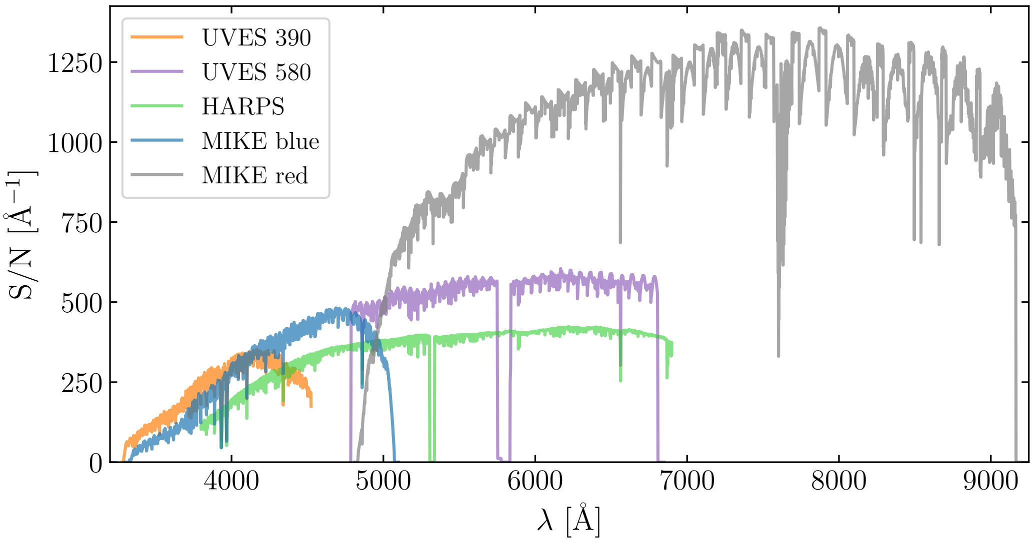

FIGURE III.1: S/N as a function of wavelength for the employed spectra of HD 20 from all three high-resolution spectrographs. Since the dispersion spacing between adjacent pixels varies among the instruments, we present the S/N per 1 Å.

2 Observations and data reduction

2.1 Spectroscopic observations

We obtained a spectrum of HD 20 in the night of August 15, 2013 using both arms of the *Magellan* Inamori Kyocera Echelle (MIKE) spectrograph (Bernstein et al. 2003). An exposure of 1093 s integration time was taken using a slit width of 0.5″and a 2x1 on-chip-binning readout mode. This setup allowed for a full wavelength coverage from 3325 to 9160 Å at $R \approx 45\,000$.

The raw science frame was reduced by means of the pipeline reduction package by Kelson (2003), which performs flat-field division, sky modeling and subtraction, order tracing, optimal extraction, and wavelength calibration based on frames obtained with the built-in ThAr lamp. For the MIKE red spectrum, the reduction routine combined 26 ten-second "milky flat" exposures, taken using a quartz lamp and diffuser, resulting in a S/N of approximately 100 per 2x1 binned CCD pixel near the middle of the array, per exposure. This gave a total S/N of about 500 pixel^{-1} in the combined flat. Due to lower flux in the blue quartz lamp, the milky flat exposure time was set to 20 s per frame. In addition, the 26 blue-side milky flat exposures were supplemented with seven ten-second exposures of a hot star, HR 7790, taken with the diffuser. The median seeing of 0.72″, corresponding to 5.4 CCD pixels FWHM, indicates that the flux for each wavelength point was taken from approximately 2 FWHM, or about 11 pixels. At the Hα wavelength the pixels are 0.047 Å wide, indicating roughly 21 pixels per Å. These details suggest that the S/N of the final, extracted, flat field flux is 5000 to 7000 Å^{-1}, significantly greater than the S/N of the stellar spectrum. The resulting S/N of the extracted object spectrum ranges from about 40 Å^{-1} at the blue-most edge to more than 1200 Å^{-1} redward of 7000 Å. We present the detailed distribution of S/N with wavelength in Figure III.1.

Our MIKE observation was complemented by data retrieved through the ESO ADP query form, with two additional, reduced high-resolution spectra for this star: The first is a 119 s, reduced exposure (ID 090.B-0605(A)) from the night of October 13, 2012 using the UVES spectrograph with a dichroic (Dekker et al. 2000) at the ESO/VLT Paranal Observatory. For the blue arm, a setup with an effective resolving power of $R \sim 58\,600$ centered at 390 nm (UVES 390) was chosen, whereas the red arm was operated at $R \sim 66\,300$ with a central wavelength of 580 nm (UVES 580). Especially the UVES 390 exposure poses an additional asset, since it supersedes our MIKE spectrum in the UV at higher S/N and – more importantly – bluer wavelength coverage and considerably higher resolution.

The second ESO spectrum was taken on December 29, 2006 (ID 60.A-9036(A)) employing the HARPS spectrograph (Mayor et al. 2003) at the 3.6 m Telescope at the ESO La Silla Observatory. With a similar wavelength coverage and at substantially lower S/N than the UVES spectra, this observation adds a very high resolution of 115 000 that was used to corroborate our findings for the intrinsic line broadening (Section 3.5). The S/N values reached with both ESO spectrographs are shown in Figure III.1 alongside the distribution for MIKE.

2.2 Radial velocities and binarity

All spectra were shifted to the stellar rest frame after determining radial velocities through cross correlation with a synthetic template spectrum of parameters that are representative for HD 20 (see Section 3 and Table III.2). For the HARPS and UVES spectra, we established the radial velocity zero point using standard stars that were observed in the same nights (HD 69830 and HD 7041, respectively, with reference values from Soubiran et al. 2018), whereas we used the telluric O_2 B-band at ~ 6900 Å to calibrate the MIKE spectrum. This way, we found $v_{\rm helio} = -57.16 \pm 0.15$, -57.04 ± 0.26, and -56.86 ± 0.44 km s^{-1} from the HARPS, UVES, and MIKE spectra of HD 20. These findings are consistent with the mean value -57.18 ± 0.11 km s^{-1} from the radial-velocity monitoring program by Carney et al. (2003) and considerably above the reported value by Hansen et al. (2015) of -57.914 ± 0.041 km s^{-1}. A

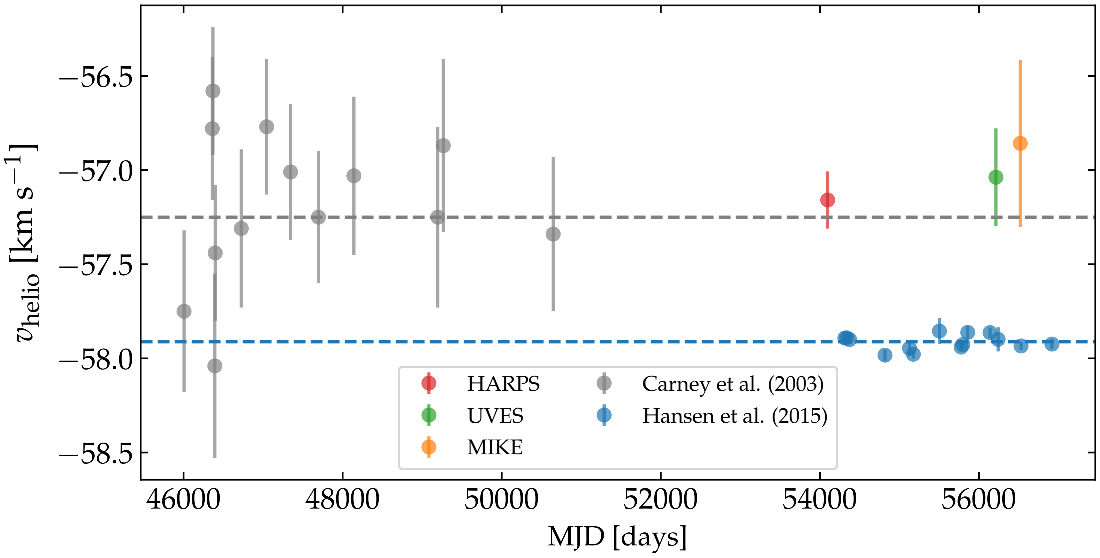

FIGURE III.2: Comparison of literature time series for v_{helio} by Carney et al. (2003, gray-filled circles) and Hansen et al. (2015, blue-filled circles) to measurements from the three spectra employed throughout this study (see legend). The gray and blue dashed lines resemble the median values for the two reference samples.

graphical juxtaposition is shown in Figure III.2. We note that – owing to the usage of different spectrographs and resolutions – our radial velocity analysis is by no means homogeneous and slight discrepancies are therefore to be expected. Nevertheless, the observed offset with respect to Hansen et al. (2015) is significant. The anomaly with respect to Carney et al. (2003) has already been noted by Hansen et al. (2015) and was linked to a difference in the applied scales. Apart from this systematic bias, over a time span of 10 011 days, there is no indication of real radial velocity variations. As a consequence, a binary nature of HD 20 can be ruled out with high confidence.

2.3 Photometry and astrometric information

Visual to near-infrared broadband photometric information for HD 20 was compiled from the literature and is listed in Table III.2 together with the respective errors and sources. $BVR_{\mathrm{C}}I_{\mathrm{C}}$ photometry was presented in Beers et al. (2007) in a program that was targeting specific stars such as HD 20. Their results were also employed by Barklem et al. (2005) and follow-up works by relying on the deduced parameters. The authors report $V = 9.236 \pm 0.001$ mag, which is in strong disagreement to other findings in the literature. For example, the HIPPARCOS catalog (ESA 1997) lists $V = 9.04$ mag (used for temperature estimates in the spectroscopic studies of Gratton et al. 2000; Fulbright & Johnson 2003), while Anthony-Twarog & Twarog (1994) provide a consistent value of $V = 9.059 \pm 0.013$ mag (used, e.g., by Carney et al.

TABLE III.2: Fundamental properties and stellar parameters entering this work.

Quantity	Value	Unit	Ref.	Note
(Astro-) physical constants				
L_0	$3.0128 \cdot 10^{28}$	W	1	
$L_\odot$	$3.828 \cdot 10^{26}$	W	1	
$M_{\mathrm{bol},\odot}$	4.74	mag	1	
$R_\odot$	$6.9577 \pm 0.0014 \cdot 10^8$	m	2	
$T_{\mathrm{eff},\odot}$	5771	K	2	
$\log g_\odot$	4.438	dex	3	
Observables				
B	9.65 ± 0.02	mag	4	
V	9.059 ± 0.013	mag	5	
J_{2MASS}	7.704 ± 0.030	mag	6	
H_{2MASS}	7.348 ± 0.029	mag	6	
$K_{\mathrm{s,2MASS}}$	7.249 ± 0.031	mag	6	
$b - y$	0.434 ± 0.003	mag	7	
$E(B - V)$	0.0149 ± 0.0005	mag	8	
G	8.849	mag	9	
$G_{\mathrm{BP}} - G_{\mathrm{RP}}$	0.886	mag	9	
ϖ	1.945 ± 0.053	mas	9	
$\mu_\alpha \cos\delta$	132.434 ± 0.066	mas yr^{-1}	9	
μ_δ	-39.917 ± 0.058	mas yr^{-1}	9	
v_{helio}	-57.914 ± 0.041	km s^{-1}	10	
f_{max}	$27.19^{+1.34}_{-1.17}$	μHz	11	Section 3.1
Deduced quantities				
d	507 ± 13	pc	11	Section 2.3
$\log g$	$2.366^{+0.020}_{-0.021}$	dex	11	Section 3.1
T_{eff}	5246^{+76}_{-50}	K	11	Section 3.4
v_{mic}	$1.95^{+0.09}_{-0.06}$	km s^{-1}	11	Section 3.4
[M/H]	-1.60 ± 0.03	dex	11	Section 3.4
[Fe/H]	-1.60 ± 0.03	dex	11	Section 3.3
v_{mac}	5.82 ± 0.03	km s^{-1}	11	Section 3.5
$L/L_\odot$	$60.9^{+4.6}_{-4.3}$		11	Section 3.6
$R/R_\odot$	$9.44^{+0.46}_{-0.43}$		11	Section 3.6
$M/M_\odot$	0.76 ± 0.08		11	Section 3.6
$^{12}\mathrm{C}/^{13}\mathrm{C}$	$3.92^{+1.68}_{-0.98}$		11	Section 5.3.2
$[\alpha/\mathrm{Fe}]^{(a)}$	0.45	dex	11	Section 7.3
age	11.0 ± 3.8	Gyr	11	Section 7.6

References. (1): Mamajek et al. (2015); (2): Heiter et al. (2015) and references therein; (3): Prša et al. (2016); (4): Høg et al. (2000); (5): Anthony-Twarog & Twarog (1994); (6): Skrutskie et al. (2006); (7): Hauck & Mermilliod (1998); (8): Schlafly & Finkbeiner (2011); (9): Gaia Collaboration et al. (2018a); (10): Hansen et al. (2015); (11): This study.

Notes. $^{(a)}$ $[\alpha/\mathrm{Fe}] = \frac{1}{5}[(\mathrm{Mg} + \mathrm{Si} + \mathrm{S} + \mathrm{Ca} + \mathrm{Ti})/\mathrm{Fe}]$.

2003). Furthermore, we estimate $V \approx 9.00 \pm 0.05$ mag from *Gaia* photometry and the analytical relation for $(G - V)$ as a function of G_{BP} and G_{RP}[1]. For completeness, we ought to mention the finding of $V = 9.40$ mag by Ducati (2002), which again poses a strong deviation. We point out that HD 20 does not exhibit any signs of photometric variability as revealed by time-resolved photometry over 6.6 yr from DR9 of the All-Sky Automated Survey for Supernovae (ASAS-SN, Jayasinghe et al. 2019) showing – which is again in agreement with most of the literature – $V = 9.01 \pm 0.08$ mag.

Despite the relatively low quoted internal uncertainties, we discard the photometry by Beers et al. (2007) and Ducati (2002) from consideration as we suspect inaccuracies in the calibration procedures. A disruptive factor might be a blend contribution by a star about 14″ to the southeast, although we deem this an unlikely option since *Gaia* DR2 reports it to be much fainter ($G = 8.849$ mag versus 14.675 mag). Consequently, we resorted to magnitudes for the B-band from the *Tycho*-2 catalog (Høg et al. 2000) and for V by Anthony-Twarog & Twarog (1994). For the near-infrared JHK_{s} photometry we queried the 2MASS catalog (Skrutskie et al. 2006) and the Strömgren color $b - y$ is taken from Hauck & Mermilliod (1998).

In terms of reddening we applied $E(B - V) = 0.0149 \pm 0.0005$ mag, which was extracted from the reddening maps by Schlafly & Finkbeiner (2011). Whenever dereddened colors or extinction-corrected magnitudes were employed, we adopted the optical extinction ratio $R_V = A(V)/E(B - V) = 3.1$ attributed to the low-density interstellar medium (ISM) together with the reddening ratios $E(\mathrm{color})/E(B - V)$ compiled in Table 1 of Ramírez & Meléndez (2005). Considering the overall very low reddening of HD 20, uncertainties in the latter ratios ought to have negligible impact on the quantities deduced from photometry.

A parallax of $\varpi = 1.945 \pm 0.053$ mas was retrieved from *Gaia* DR2 from which we computed a geometric distance to HD 20 of $d = 507 \pm 13$ pc[2]. Here we accounted for the quasar-based parallax zero point for *Gaia* DR2 of -0.029 mas (Lindegren et al. 2018). Our finding is fully in line with the distance 507^{+14}_{-13} pc derived in the Bayesian framework of Bailer-Jones et al. (2018).

3 Stellar parameters

A crucial part of any spectroscopic analysis which is aimed at high-accuracy chemical abundances is the careful determination of the stellar parameters entering the model

---

[1] Section 5.3.7 of the *Gaia* Data Release 2 Documentation release 1.2: `https://gea.esac.esa.int/archive/documentation/GDR2/`

[2] While it may prove mathematically incorrect, the error on the inverse parallax can be considered symmetric in light of the small relative parallax error.

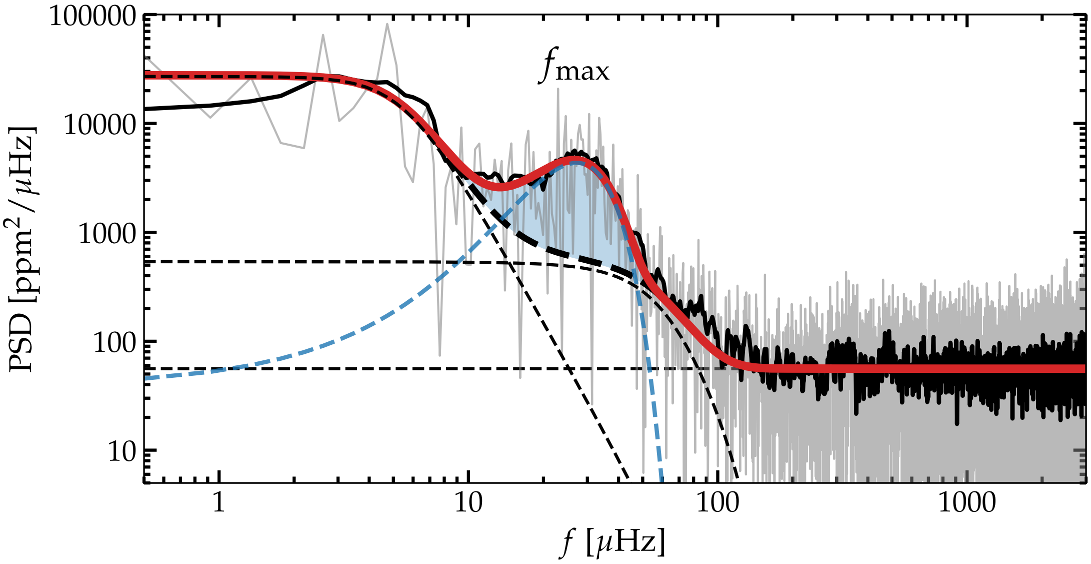

FIGURE III.3: Power spectral density (PSD) for HD 20 based on TESS light-curve data. The thick black line depicts a smoothed version of the PSD (thin gray line) and the best-fit model is shown in red. The blue shaded area indicates the power excess, whereas individual model components are represented by thin blue and black dashed lines.

atmospheres needed when solving for the radiative transfer equations. Here we outline the inference method applied for determining the parameters; effective temperature, surface gravity, microturbulence, metallicity, and line broadening.

Our adopted stellar parameters (Table III.2) are based on a spectroscopic analysis of Fe lines that were corrected for departures from the assumption of local thermodynamic equilibrium (LTE) together with asteroseismic information from the TESS mission, whereas several other techniques – both spectroscopic and photometric – including their caveats are discussed in Section 4.

3.1 Surface gravity from TESS asteroseismology

Recently, Creevey et al. (2019) showed in their time-resolved radial velocity analysis of the benchmark star HD 122563 that the asteroseismic scaling relation for solar-like oscillations (Equation I.13) holds even in the regime of metal-poor and evolved stars. This motivated the exploration of the feasibility of an asteroseismic gravity determination for HD 20.

Fortunately, TESS measured a 27.4 days light curve with a two-minute cadence for this star during Sector 2. We employed the `lightkurve` Python package (Lightkurve Collaboration et al. 2018) to retrieve and reduce the data in order to calculate the power spectrum seen in Figure III.3. A power excess is identifiable around the frequency $f_{\mathrm{max}} \approx 27\ \mu\mathrm{Hz}$, which we attribute to solar-like oscillations.

We performed a fit to the obtained power spectrum following the prescriptions by Campante et al. (2019). Therefore, we assumed a multi-component background model consisting of super-Lorentzian profiles that account for various granulation effects (see, e.g., Corsaro et al. 2017, for details) as well as a constant noise component. The decision on the number of super-Lorentzian components for the background was made based on Bayesian model comparison using Bayes factors from evidences that were estimated with the `Background`[3] extension to the high-DImensional And multi-MOdal NesteD Sampling (`DIAMONDS`[4], Corsaro & De Ridder 2014) algorithm. We found that a model with three super-Lorentzian components has an insignificantly stronger support compared to a two-component one. The latter observation indicates that – given the data – the meso-granulation around frequencies of $f_{\mathrm{max}}/3 \approx 9\ \mu\mathrm{Hz}$ is indistinguishable from the component due to super-granulation and/or other low-frequency signals since they occupy a similar frequency range in HD 20. Thus, we adopted only two super-Lorentzians for the background fit. Finally, a Gaussian profile was used to represent the power excess on top of the background model.

In order to sample and optimize the high-dimensional parameter space of all involved model coefficients, we again made use of `DIAMONDS`. The resulting best-fit model, as well as its individual components, are depicted in Figure III.3. We estimated $f_{\mathrm{max}} = 27.19^{+1.34}_{-1.17}\ \mu\mathrm{Hz}$ which translates into $\log g = 2.368^{+0.021}_{-0.019}$ dex from Equation I.13 using $f_{\mathrm{max},\odot} = 3050\ \mu\mathrm{HZ}$ (Kjeldsen & Bedding 1995) and our adopted T_{eff}. Owing to a weak coupling of the asteroseismic gravity to the temperature, we do not consider it in isolation, but refer the reader to Section 3.4, where we outline the procedure to reach simultaneous parameter convergence.

3.2 Iron lines

A list of suitable Fe I and Fe II lines for the purpose of deriving accurate stellar parameters was compiled using the Atomic Spectra Database (Kramida et al. 2018) of the National Institute of Standards and Technology (NIST). To this end, in order to mitigate biases by uncertain oscillator strengths ($\log gf$), only those lines were considered that are reported to have measured $\log gf$ values with accuracy levels $\leq 10\%$ (grade B or better in the NIST evaluation scheme) for Fe I and $\leq 25\%$ (grade C or better) for Fe II lines. The lines retrieved this way were checked to be isolated by means of spectrum synthesis (see Section 5.1) and their EW was measured by `EWCODE`

---

[3] https://github.com/EnricoCorsaro/Background

[4] https://github.com/EnricoCorsaro/DIAMONDS

(Section 5.2). From these, we added the ones that were measured with more than 5σ significance to the final list. Laboratory line strengths for the resulting 133 Fe I transitions were measured and reported by Fuhr et al. (1988), O'Brian et al. (1991), Bard et al. (1991), and Bard & Kock (1994). For the 13 Fe II lines that survived the cleaning procedure, the data are taken from Schnabel et al. (2004).

3.3 Spectroscopic model atmosphere parameters

Throughout our analyses, we employed the LTE radiation transfer code `MOOG` (Sneden 1973, July 2017 release) including an additional scattering term in the source function as described by Sobeck et al. (2011)[5]. Our atmosphere models are based on the grid of 1D, static, and plane-parallel `ATLAS9` atmospheres by Castelli & Kurucz (2003) with opacity distribution functions that account for α-enhancements ([α/Fe]=+0.4, Section 7.3). Models for parameters between the grid points were constructed via interpolation in the grid. Here we used the iron abundance [Fe/H] as proxy for the models' overall metallicities [M/H] since we assume that all elements other than the α-elements follow the solar elemental distribution scaled by [Fe/H]. We note that the fact that HD 20 shows enhancements in the neutron-capture elements (Section 7.4) does not prevent this assumption, as the elements in question are only detectable in trace amounts with negligible impact on atmospheric properties such as temperature, density, and gas or electron pressure.

Our T_{eff} estimate is based on the spectroscopic excitation balance of Fe I lines (Section I.4.2.1). In this respect it is important to account for the circumstance that Fe I transitions are prone to substantial NLTE effects in metal-poor stars, in a sense that not only the overall abundance is shifted toward higher values, but the magnitude of the effect varies with χ_{ex}, too. Hence, as pointed out by Lind et al. (2012), the T_{eff} for which the excitation trend is leveled is shifted to systematically offset temperatures from the LTE case (see Figure III.4). To overcome this problem, we computed NLTE abundance departures by interpolation in a close-meshed, precomputed grid of corrections that was created specifically for this project and parameter space (priv. comm.: M. Bergemann and M. Kovalev, see Bergemann et al. 2012b; Lind et al. 2012, for details).

The microturbulence parameter v_{mic} is an ad-hoc parameter that approximatively accounts for the effects of otherwise neglected turbulent motions in the atmosphere, which mainly affect the theoretical line strength of strong lines. Here we tuned v_{mic} in order to erase trends of the inferred, NLTE-corrected abundances for Fe I features with the reduced line strength, $\text{RW} = \log\left(\text{EW}/\lambda\right)$.

---

[5] `https://github.com/alexji/moog17scat` as of November 2018

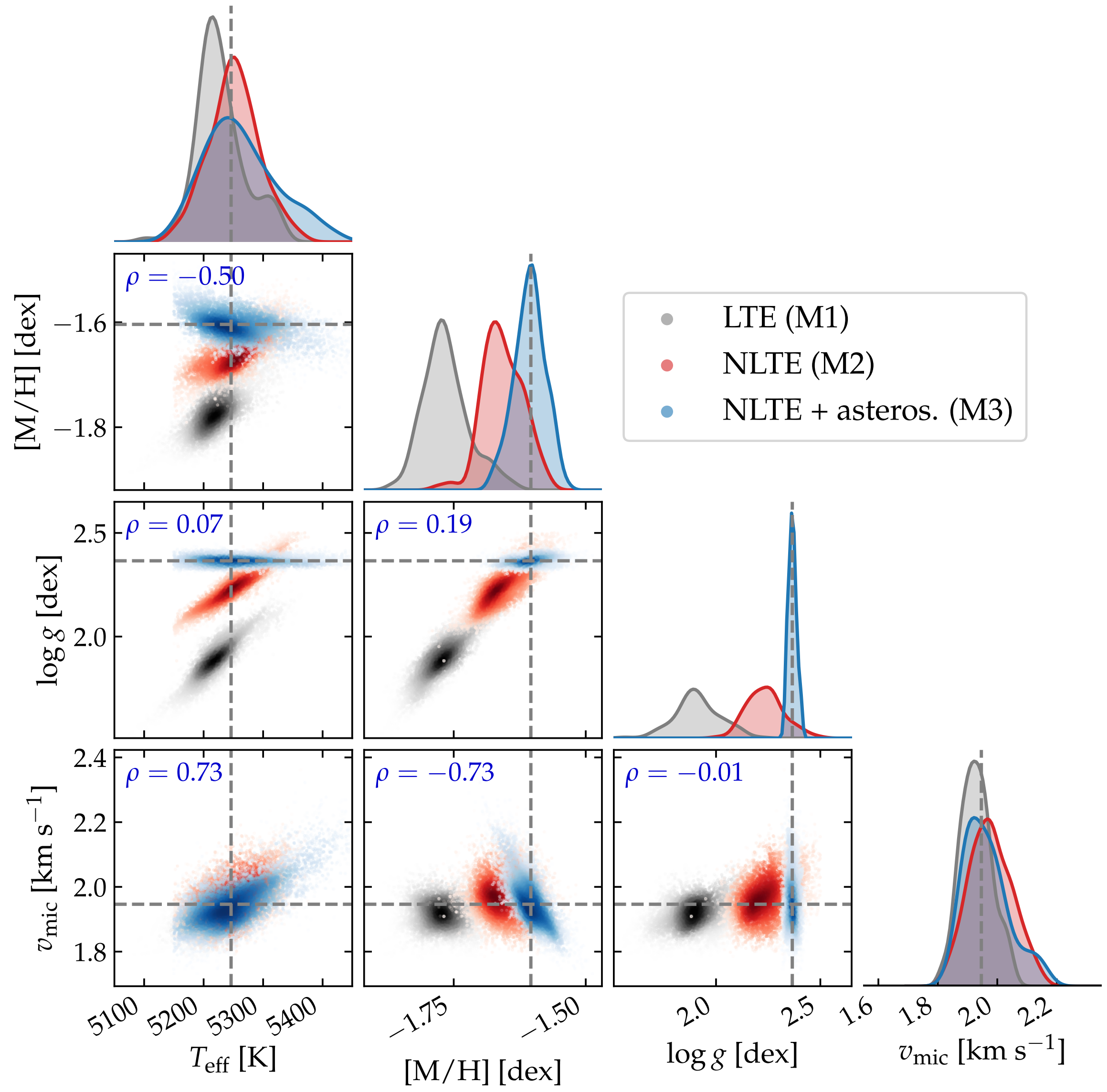

FIGURE III.4: Samples drawn from the posterior distribution of the stellar parameters (Equation III.1). Shown are the three different approaches M1 (gray), M2 (red), and M3 (blue) with the darkness of the colors illustrating the local density as estimated from a Gaussian kernel density estimate. The sample sizes are $2 \cdot 10^4$ and the adopted stellar parameters from method M3 (Tables III.2 and III.3) based on the median of the distributions are indicated using horizontal and vertical dashed lines. The correlation coefficients for pairs of two parameters in M3 are presented in the *top left corner* of each panel. The marginalized, one-dimensional distributions for the individual parameters are depicted by smoothed histograms at the top of each column.

Even though we prefer our highly accurate asteroseismic measurement over requiring spectroscopic ionization balance for determining $\log g$, we discuss this method here to compare our findings to more classical spectroscopic parameter estimation methods that are widely used throughout the literature. The procedure is based on balancing abundances of neutral lines and singly ionized lines that are sensitive to

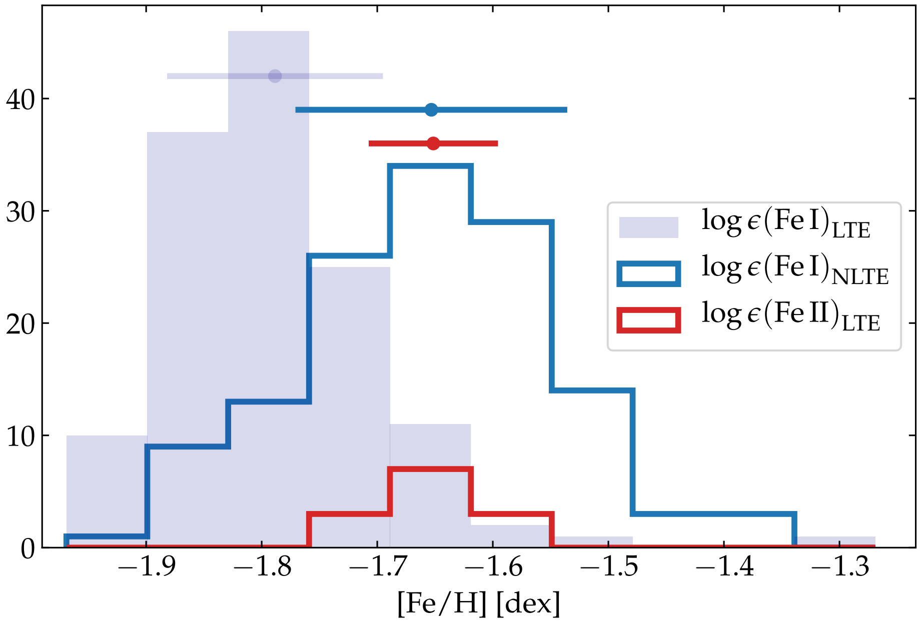

FIGURE III.5: Diagnostic plot for spectroscopic ionization balance. Shown are the histograms of the Fe abundance distributions ($[\mathrm{Fe/H}] = \log\epsilon(\mathrm{Fe}) - 7.50$ dex) at the adopted gravity ($\log g = 2.24$ dex from method M2, see Section 3.4) both in LTE (gray filled) and NLTE (blue) for Fe I and in LTE for Fe II (red). NLTE corrections for Fe II remain well below 0.01 dex and are therefore neglected here. Points with error bars and arbitrary ordinate offsets at the top of the panel denote the means and standard deviations for each of the distributions of the same color.

changes in gravity (see also Section 6.2). Hence, by tuning the model gravity to erase discrepancies between the abundances deduced from both ionization states of the same element, $\log g$ can be inferred. Commonly, especially for FGK stars, the high number of available Fe lines in both ionization stages qualifies this species as an ideal indicator. While the modeling of Fe II line strengths is insensitive to departures from LTE (<0.01 dex), trustworthy gravities from the ionization balance can only be obtained once departures from LTE are removed from the Fe I abundances (e.g., Lind et al. 2012). In particular, by neglecting NLTE influences, one would considerably underestimate $\log\epsilon(\mathrm{Fe\,I})$ and consequently $\log g$. This can be seen in Figure III.5, where we compare Fe I under the LTE assumption to NLTE-corrected Fe I. Illustrated is the best abundance agreement – that is, a perfect overlap of both the $\log\epsilon(\mathrm{Fe\,I})_{\mathrm{NLTE}}$ and $\log\epsilon(\mathrm{Fe\,II})_{\mathrm{LTE}}$[6] abundance distributions – obtained for $\log g = 2.24$ dex and $[\mathrm{M/H}] = -1.65$ dex.

When assessing the error budget on [Fe/H], we caution that in this study's realm of very high S/N spectra, random noise is not the prevailing origin for the line-by-line scatter of 0.10 dex and 0.03 dex for $\log\epsilon(\mathrm{Fe\,I})_{\mathrm{NLTE}}$ and $\log\epsilon(\mathrm{Fe\,II})_{\mathrm{LTE}}$, respectively. In fact, looking at the abundance errors for individual lines from EW errors only, the

---

[6] Since we find corrections for Fe II that amount to less than 0.01 dex, we can assume $\log\epsilon(\mathrm{Fe\,II})_{\mathrm{LTE}} = \log\epsilon(\mathrm{Fe\,II})_{\mathrm{NLTE}}$.

random component remains well below 0.03 dex in the majority of cases. We conclude that the scatter is mostly of non-stochastic nature – for example due to uncertain oscillator strengths and flaws in the 1D assumption – and hence a division of the rms scatter by the square root of the number of lines is not a statistically meaningful quantifier of the metallicity error (see Section 6.1 for more detailed discussions).

3.4 Bayesian inference

We emphasize that spectroscopic stellar parameters are strongly interdependent, that is, uncertainties and systematic errors of one quantity should not be considered in isolation. The usage of asteroseismic information mitigates this circumstance only to some degree as we show below. Hence, all model parameters need to be iterated until simultaneous convergence is reached. For this purpose, we used the `emcee` (Foreman-Mackey et al. 2013) Python implementation of a Markov chain Monte Carlo (MCMC) sampler in order to draw samples from the posterior probability distribution P of the four model parameters $T_{\rm eff}$, [M/H], $\log g$, and $v_{\rm mic}$,

$$P(\vec{x}|\vec{y}) \propto \mathcal{L}(\vec{y}|\vec{x}) \cdot p(\vec{x}), \tag{III.1}$$

with $\mathcal{L}$ being the likelihood function and p the prior. Here $\vec{y}$ denotes the measured EWs and $\vec{x}$ represents the set of model atmosphere parameters. A flat prior of unity was assumed within the parameter space covered by our grid of NLTE corrections, and zero otherwise. We explored three different likelihoods representing the purely spectroscopic LTE (M1) and NLTE (M2) methods, as well as a mixed "NLTE + asteroseismology" (M3) approach. The likelihoods take the form of

$$\mathcal{L} = \exp\left(-\frac{a_{\chi_{\rm ex}}^2}{2\sigma_a^2} - \frac{b_{\rm RW}^2}{2\sigma_b^2} - \frac{\Delta^2_{[{\rm M/H}],{\rm Fe\,II}}}{2\sigma^2_{\rm Fe\,II}} - \Gamma_i\right), \tag{III.2}$$

where $a_{\chi_{\rm ex}}$ and $b_{\rm RW}$ are the slopes of the deduced LTE (M1) or NLTE (M2 and M3) abundances, $\log\epsilon_{\rm Fe\,I}(\vec{y},\vec{x},\chi_{\rm ex})$, with $\chi_{\rm ex}$ and RW for any given set of parameters $\vec{x}$. The variances of the latter slopes were determined from repeated linear fits to bootstrapped samples by means of robust least squares involving a smooth L1 loss function. We prefer this non-parametric approach over ordinary least squares because of the systematically underestimated abundance errors from EW uncertainties alone (see previous section). The third term in Equation III.2 represents the difference between the model metallicity and Fe II abundance, whereas Γ_i introduces the gravity

TABLE III.3: Median values and 68.2% confidence intervals for the stellar parameters from the posterior distributions for the three different likelihood functions (see main text for details). The method adopted throughout this work is M3.

Method	T_{eff} [K]	[M/H] [dex]	$\log g$ [dex]	v_{mic} km s^{-1}
LTE (M1)	5220^{+35}_{-32}	$-1.78^{+0.04}_{-0.04}$	$1.894^{+0.115}_{-0.115}$	$1.92^{+0.05}_{-0.05}$
NLTE (M2)	5250^{+48}_{-43}	$-1.65^{+0.04}_{-0.04}$	$2.244^{+0.102}_{-0.095}$	$1.97^{+0.07}_{-0.06}$
NLTE + asteros. (M3)	5246^{+76}_{-50}	$-1.60^{+0.03}_{-0.03}$	$2.366^{+0.020}_{-0.021}$	$1.95^{+0.09}_{-0.06}$

sensitivity. For approaches M1 and M2, it represents the ionization (im-)balance,

$$\Gamma_{\mathrm{MI/MII}} = \frac{\Delta^2_{\mathrm{Fe\,I,Fe\,II}}}{2\sigma^2_{\Delta}}, \tag{III.3}$$

in the LTE and NLTE case, while we do not enforce ionization balance for M3, but use the asteroseismic information through

$$\Gamma_{\mathrm{M3}} = \frac{\log g - \log g_{\mathrm{seis.}}(T_{\mathrm{eff}}, f_{\mathrm{max}})}{2\sigma^2_{\log g_{\mathrm{seis.}}}}. \tag{III.4}$$

In this expression $\log g_{\mathrm{seis.}}$ is calculated from Equation I.13. We emphasize that, while being clearly subject to biases in LTE, a perfect ionization balance may not be desirable even in the 1D NLTE case (M2), because it still lacks proper descriptions of hydrodynamical and 3D conditions. These might pose other sources for differences between abundances from Fe I and Fe II at the true $\log g$. In fact, there is a remaining marginal ionization imbalance $\log \epsilon\mathrm{Fe\,II} - \log \epsilon\mathrm{Fe\,I} = 0.08 \pm 0.10$ when adopting the M3 approach.

Figure III.4 shows various representations of the multidimensional posterior distributions for M1, M2, and M3. As expected, we found strong correlations between T_{eff}, [M/H], and $\log g$ in the purely spectroscopically informed methods M1 and M2. Using approach M3, we can effectively lift the degeneracies with $\log g$ as quantified by insignificant Pearson correlation coefficients (Figure III.4). For each approach, we deduced the optimal parameters and error margins from the median, 15.9th, and 84.1th percentiles, respectively. These are listed in Table III.3. It is evident that M1 significantly underestimates both [M/H] and $\log g$ due to deducing lower Fe I abundances that have a direct impact on the ionization balance and therefore the inferred gravity. M2 and M3, however, yield results that are in good agreement with the strongest deviation amounting to just 1.2σ in $\log g$. This highlights the importance of considering NLTE effects already at the stage of stellar parameter inference and

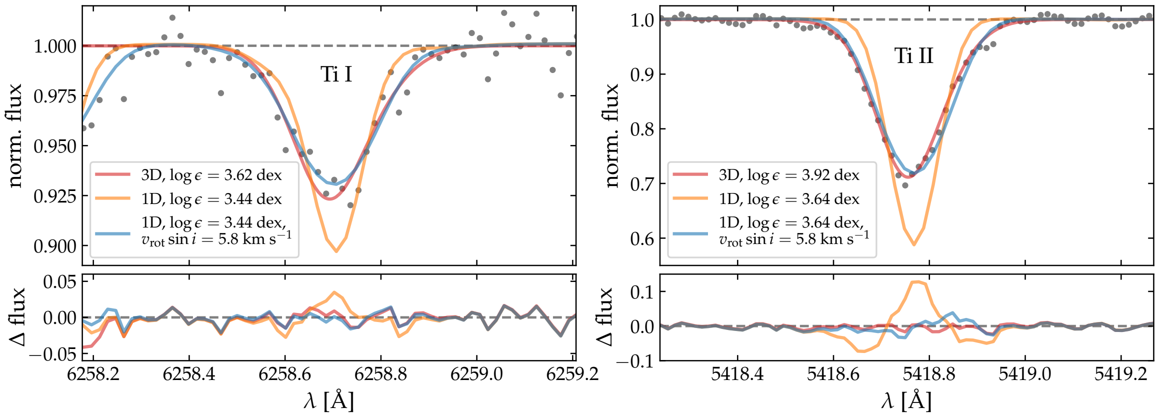

FIGURE III.6: Comparison of synthetic line shapes against the observed profiles in the UVES 580 spectrum for two representative Ti lines. Red spectra resemble 3D syntheses, while blue and orange colors indicate 1D syntheses with and without additional broadening. The instrumental profile ($R = 66\,230$) was mimicked by convolution with a Gaussian kernel for all three types of synthesis. No rotational broadening was applied to the 3D syntheses.

shows that 1D NLTE ionization balance is capable of producing gravities that are as accurate as the highly trustworthy asteroseismic scaling relations. Since the precision of the latter is better by about a factor of five, we adopt the parameters inferred from M3 throughout this work. We corroborated this set of fundamental stellar parameters using several independent techniques, including temperatures from the shapes of the Balmer lines in HD 20's spectrum. We refer the reader to Section 4 for a detailed outline and comparison.

3.5 Line broadening

Carney et al. (2003) report a rotational velocity of $v_{\rm rot}\sin i = 5.9$ km s^{-1} for HD 20, which is unexpectedly high given the evolutionary state of this star where any initial rotation is expected to be eliminated. The authors caution, however, that the face value just below their instrumental resolution of 8.5 km s^{-1} might be biased due to a number of systematic influences on their method, amongst which is turbulent broadening (see also, e.g., Preston et al. 2019). Turbulent and rotational broadening have almost identical impacts on the line shape, a degeneracy that can only be broken using spectra of very high resolution and S/N (Carney et al. 2008). Hence – despite the name – we consider $v_{\rm rot}\sin i$ a general broadening parameter.

Given that rotation or any other line broadening mechanism are key quantities that critically affect the precision and accuracy of abundances from spectrum synthesis (Section 5), we tackled this property from a theoretical point of view. To this end, a collection of isolated Ti I and Ti II features were simulated using LTE radiative transfer in a CO^{5}BOLD model atmosphere (Freytag et al. 2012), which realistically models the microphysics of stellar atmospheres under 3D, hydrodynamical conditions. We note that the chosen atmospheric parameters ($T_{\text{eff}} = 5500$ K, $\log g = 2.5$ dex, [M/H] $= -2.0$ dex) only roughly match our findings – hence deviations in the abundance scales can be expected. The overall line-shape, however, is expected to be reasonably accurately reproduced. Our synthetic profiles were compared to their observed counterparts in the UVES 580 spectrum, which offers the best trade-off between resolution and S/N in the considered wavelength regimes. The nominal velocity resolution is 4.5 km s^{-1}. Comparisons for two representative lines are presented in Figure III.6. The 3D profiles are shown next to rotationally broadened, 1D versions and we find that no additional rotational broadening is required in the 3D case as the line shape can be fully recovered by properly accounting for microphysics together with the instrumental resolution. Thus, we conclude that – if at all – HD 20 is rotating only slowly (i.e., $v \sin i \lesssim 1$ km s^{-1}). On top of the overall line broadening, slight profile asymmetries are correctly reproduced by the 3D models.

In order to improve our 1D spectrum syntheses beyond broadening by the instrumental line spread function, we analyzed the deviation of individual, isolated Fe features from their 1D LTE line shape. The comparison was performed against the UVES 580 and the HARPS spectrum. Based on 171 lines in common for both spectra, we found that a broadening velocity of $v_{\text{mac}} = 5.82 \pm 0.03$ km s^{-1} can successfully mimic the line shape from both spectrographs. The latter value is in good agreement with the value 5.9 km s^{-1} found by Carney et al. (2003), who do not list an error specific to HD 20 but quote general standard errors between 0.5 and 3 km s^{-1} for their entire sample of stars.

3.6 Other structural parameters

Given our spectroscopic temperature and metallicity, we can deduce HD 20's luminosity through

$$\frac{L}{L_\odot} = \left(\frac{d}{10\text{pc}}\right)^2 \frac{L_0}{L_\odot} \cdot 10^{-0.4(V - A(V) + BC_V(T_{\text{eff}}, [\text{Fe/H}]))} \tag{III.5}$$

with the zero-point luminosity L_0 (see Table III.2) and the bolometric correction BC_V from the calibration relation by Alonso et al. (1999b, henceforth AAM99), which itself depends on T_{eff} and [Fe/H]. We find $L/L_\odot = 60.9^{+4.6}_{-4.3}$, in line with the value 58.6 ± 2.2 reported in *Gaia* DR2. The error on L was computed through a Monte Carlo error propagation assuming Gaussian error distributions for the input variables and an additional uncertainty for BC_V of 0.05 mag. The asymmetric error limits stem from the 15.9th and 84.1th percentiles of the final parameter distributions, respectively.

We can furthermore infer the stellar radius using

$$\frac{R}{R_\odot} = \sqrt{\frac{L}{L_\odot}} \left(\frac{T_\mathrm{eff}}{T_{\mathrm{eff},\odot}} \right)^{-2}, \tag{III.6}$$

resulting in $9.44^{+0.46}_{-0.43}$. This compares to $8.69^{+0.19}_{-0.80}$ from *Gaia* DR2, where the slight discrepancy can be explained by a higher temperature estimate from *Gaia* (see discussion in Section 4.1.3).

Finally, it is possible to deduce a mass estimate by inversion of Equation I.14. The solar reference values involved can be found in Table III.2. As for Equation III.5, the bolometric magnitude M_bol can be computed from the V-band photometry and the BC_V relation by AAM99. We found a mass of $(0.76 \pm 0.08) M_\odot$.

4 Alternative methods for determining stellar parameters

4.1 Effective temperature

In order to put our adopted T_eff in context to other methods, we derived this parameter from several other spectroscopic and photometric techniques that are summarized and presented together with existing literature values in Figure III.7.

4.1.1 ATHOS – temperatures from Balmer lines

`ATHOS` was applied to all spectra containing Hα and Hβ, that is, the UVES 580, MIKE, and HARPS spectra. In order to account for the substantial line broadening present in HD 20 (see Section 3.5), we provided `ATHOS` with an effective resolution,

$$R_\mathrm{eff} = \left(\left(\frac{1}{R_0} \right)^2 + \left(\frac{v \sin i}{c} \right)^2 \right)^{-\frac{1}{2}}, \tag{III.7}$$

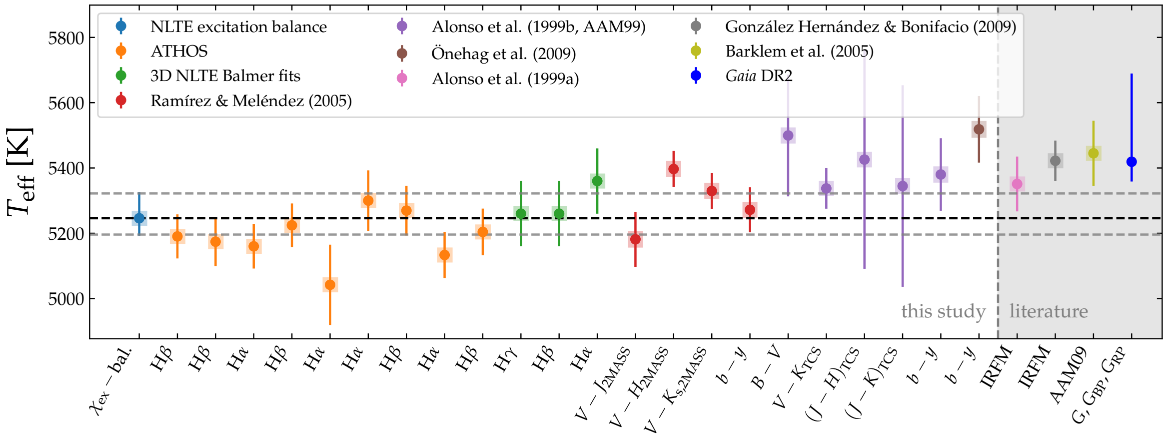

FIGURE III.7: Individual photometric and spectroscopic temperature measures for HD 20 obtained in this work. On the abscissa either the photometric color or the spectral region that was used to deduce T_{eff} is labeled. Different colors indicate the different scales and methods employed (see legend and main text for details). For each T_{eff} that was deduced from a color index, the negligible effect of no reddening and twice the applied reddening ($E(B-V) = 0.0149$ mag, Schlafly & Finkbeiner 2011) is denoted by light-colored ranges behind the circles that are barely visible. The IRFM findings for HD 20 by Alonso et al. (1999a) and González Hernández & Bonifacio (2009) are shown together with the literature values by Barklem et al. (2005) and *Gaia* DR2. The finally adopted temperature and its error (5246^{+76}_{-50} K) are shown by black- and gray-dashed lines, respectively.

under the assumption that rotational broadening behaves approximately Gaussian[7]. Here R_0 denotes the instrumental resolving power of the input spectra. The mean temperature and its error for each of the nine relations are depicted in Figure III.7, whereas the weighted mean T_{eff} from all `ATHOS` results is 5194 ± 25 K, a temperature in good agreement with our adopted value. The latter low uncertainty is typical for the very high internal precision of `ATHOS` temperatures from high-S/N data (as already indicated in the case of 51 Peg in Section II.5.2). Nevertheless, it is important to bear in mind that the initial temperatures of `ATHOS`' benchmark sample suffered from finite accuracy. Thus, we note the additional systematic error of 97 K.

4.1.2 3D NLTE modeling of Balmer lines

The classical spectroscopic approach of inferring T_{eff} from Balmer lines relies on their theoretical modeling and comparison of the profile wings to observed spectra (Barklem et al. 2002). As a consequence, the approach is strongly model-dependent and prone to inaccuracies or unknowns in the attempts to reproduce real physical processes. To date, Amarsi et al. (2018) presented the most complex and potentially most accurate calculations of Balmer line formation in late-type stars involving 3D hydrodynamic atmosphere models and NLTE radiative transfer. The authors showed

---

[7] We emphasize that this step is not utterly important at this point because the `ATHOS` implementation for T_{eff} is largely insensitive to rotational broadening (cf., Section II.5.1). Line broadening, however, does affect `ATHOS`' [Fe/H] estimators (Section 4.2).

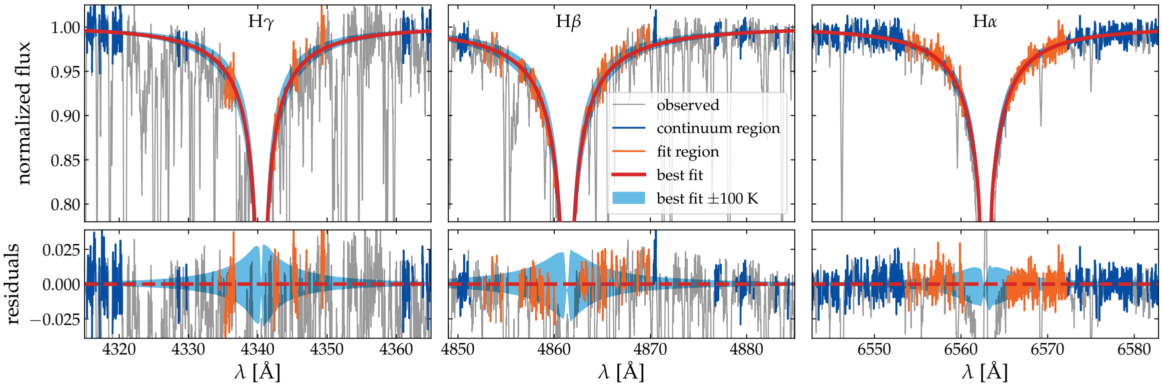

FIGURE III.8: T_{eff} fit results from fitting the wings of the Balmer lines Hγ (*left*), Hβ (*middle*), and Hα (*right*). *Upper panels*: Observed spectra (gray) with the best-fit 3D NLTE models (5260/5260/5360 K) by Amarsi et al. (2018) and their error margins of 100 K depicted by red lines and blue areas, respectively. The wavelength regions used to obtain the continuum level are marked in blue, whereas orange lines highlight the parts of the spectrum that entered the χ^2 minimization. *Lower panels*: Residual spectrum.

that departures from ordinary 1D LTE line formation can be substantial and their negligence could introduce temperature inaccuracies on the order of 100 K.

We took advantage of the extensive grid of 3D NLTE Balmer line models published by Amarsi et al. (2018) and closely followed their fitting scheme to deduce T_{eff} for HD 20 from Hγ, Hβ, and Hα in the UVES spectra. In brief, for each profile, two 1D LTE spectra – one including metal lines and one considering only the H lines – were modeled for the final parameters (Table III.2) and a line list including all transitions for the respective synthesis range found in VALD. We used these two artificial spectra to define "clean" wavelength regions free from substantial metal absorption by requesting the residual deviation to result in a change of less than 30 K in the derived temperature. Furthermore, for Hα, we employed SkyCalc (Noll et al. 2012; Jones et al. 2013) to obtain a representative, synthetic telluric spectrum for the average observing conditions on Cerro Paranal and excluded all features above a threshold of 1% in absorption. Any of the remaining wavelength ranges with fluxes above 98% of the continuum flux were used to fit a linear continuum, while ranges of $\leq$ 98% of the continuum flux entered a χ^2-minimization algorithm that interpolates between points of the Balmer model grid by employing cubic splines. For this purpose, all model parameters but T_{eff} were kept fixed at their recommended values (Table III.2). The resulting temperatures are 5260 K from Hγ, 5260 K from Hβ, and 5360 K from Hα. Here we caution against an over-interpretation of the deviation of the latter temperature because it amounts to less than one combined error margin and Hα is the least strong and least temperature-sensitive profile as can be seen in Figure III.8. There the best-fit results are illustrated for all three profiles together with margins amounting to ±100 K, which we adopt as error estimate for individual measures from this method. The straight average $T_{\text{eff}} = 5293 \pm 58$ K is in good agreement with our independently determined, adopted value of 5246 K.

We would like to stress that, apart from model uncertainties, the accuracy of the outlined procedure is affected by non-linearities in the global continuum shape due to the blaze function, as has already been pointed out for UVES spectra by Amarsi et al. (2018). In fact, we see an asymmetric substructure in the residuals of Hβ that cannot be explained by model deficiencies. For the same reason the Balmer profiles in the MIKE spectrum were not used as they show slightly stronger persistent distortions after performing the above simple normalization scheme. The HARPS spectra only cover Hβ and Hα (5190 K and 5300 K, respectively) with no apparent residual substructure after normalization. However, the noise level considerably exceeds the error margin of 100 K, which is why we also excluded the HARPS spectrum from our consideration.

The treatment of normalization is one of the key advantages of the technique implemented in `ATHOS` over Balmer modeling: `ATHOS` does not rely on one global continuum for each Balmer profile, but rather computes its individual FRs from two wavelength regions that are spaced much less than the overall extent of the line. Indeed, this is based on the premise that between the two involved ranges the continuum stays constant. The narrow spacing, however, justifies the latter assumption. Moreover, typically, `ATHOS` provides four to five measures of temperature per Balmer line, such that any persistent effect induced by small-scale continuum variations can effectively be averaged out. This, on the other hand, would manifest itself in an increased relation-to-relation scatter, which is not observed for any of our HD 20 spectra.

4.1.3 Color - [Fe/H] - T_{eff} calibrations

We further used the available photometry to compute T_{eff} from several empirical relations in the literature. The first one was introduced by AAM99, who calibrated their analytical functions against a large sample of known [Fe/H] and T_{eff}, which themselves were inferred from the infrared flux method (IRFM, e.g., Blackwell & Shallis 1977). Since HD 20 was part of their sample, we mention here their IRFM-based temperature of 5351 ± 84 K (Alonso et al. 1999a), which is slightly warmer compared to our adopted value. Unfortunately, most of the relations provided by AAM99 are not directly compatible with the photometry at hand, because AAM99 calibrated their relations for the infrared JHK bands in the Telescopio Carlos Sánchez (TCS) system instead of the 2MASS system. For this reason, we made use of a two-step conversion; first from the 2MASS to the CIT (California Institute of Technology) system as described in the supplemental material for the 2MASS mission[8], and secondly to the TCS system adopting the transformations given by Alonso et al. (1994). Errors were propagated through all conversion steps, which poses the dominant source of error in the derived individual temperatures. We find a weighted average temperature of 5362 ± 52 K.

Barklem et al. (2005) report a result of 5445 ± 100 K using $BVR_CI_CJHK_s$ photometry ($b - y$ was not considered) by Beers et al. (2007) as well as the same color transformations and calibration relations. Despite having rejected that photometry (see Section 2.3), we attempted to reproduce their value from their photometry. To this end, for the R and I bands we applied the transformations given in Bessell (1983) to convert the magnitudes by Beers et al. (2007) to the Johnson ones. Nonetheless, using exactly the same averaging scheme – that is, dropping the strongest outliers in either direction, not considering $b - y$, and taking an unweighted mean[9] – we cannot reproduce their rather hot value, but find 5270 K in accordance with our adopted estimate. Barklem et al. (2005) already noted generally warmer temperatures when comparing their sample to existing literature values and claimed the origin to be the usage of different reddening maps. Adopting their slightly higher extinction value of 0.017 only marginally increases our value by 5 K. We suspect two plausible reasons for the strong discrepancy, or a mixture thereof: If we neglected the erratum to AAM99 (Alonso et al. 2001) that cautions to invert the sign of the cross-term of colors and [Fe/H] in the calibrations, we would end up with temperatures that are on average higher by almost 200 K. Moreover, looking at Sivarani et al. (2004), who introduce the color transformations used by Barklem et al. (2005), we found that they transformed $V - K$ colors to the Johnson system, while the AAM99 requires this color in the TCS system.

Another empirical calibration was introduced by Ramírez & Meléndez (2005) who revisited the IRFM temperature scale by AAM99 and provided updated relations (here we are only considering the scales for giants) for the filter systems given in Table III.2. For the $B - V$ color we would in principle have the necessary photometry, but the colors lie outside of the validity range of the relations. The weighted mean T_{eff} from the remaining four colors involving the redder two 2MASS filters and Strömgren photometry is 5294 ± 79 K (rms), which is cooler (70 K) than the value obtained from AAM99 and hence more in line with the spectroscopic results.

The last photometric scale we consider is for the Strömgren color $b - y$, invented by Önehag et al. (2009). It is based on synthetic colors from MARCS model atmospheres.

---

[8] `http://www.astro.caltech.edu/~jmc/2mass/v3/transformations/`

[9] We note that a weighted average would result in a substantially lower T_{eff}, since the value from $(V - K)_{\mathrm{TCS}}$ is much less uncertain than all the others.

TABLE III.4: Stellar masses and $\log g$ from the core of Hα.

Spectrum	$W_{\mathrm{H}\alpha}$ [Å]	$\log_{10} M/M_\odot{}^{(a)}$ [dex]	$M/M_\odot$	$\log g^{(b)}$ [dex]
UVES 580	0.863	-0.282 ± 0.095	$0.52^{+0.12}_{-0.10}$	2.17 ± 0.10
MIKE	0.863	-0.282 ± 0.095	$0.52^{+0.13}_{-0.11}$	2.17 ± 0.10
HARPS	0.861	-0.277 ± 0.094	$0.53^{+0.14}_{-0.10}$	2.18 ± 0.09

Notes. (a) Calculated from equation (3) in Bergemann et al. (2016). (b) Derived from Equation I.14.

At 5518 ± 102 K, we find the derived temperature to be much hotter (~ 250 K) than our adopted value.

Gaia DR2 provides temperature estimates for millions of sources based on *Gaia* colors alone, as described in Andrae et al. (2018). Although the authors note that due to several limitations their temperatures are impractical for studies of individual stars, for completeness, we mention their value of 5419^{+267}_{-57} K. Considering the small lower error margin, this again represents an unfeasibly high T_{eff}.

4.2 ATHOS – [Fe/H] from flux ratios

In order to test the comparability of `ATHOS`' metallicity scale to the in-depth analysis of carefully vetted Fe lines under NLTE conditions performed in this project, we ran `ATHOS` on the MIKE spectrum of HD 20. The latter was chosen since it exposes the highest S/N and it was already proven in Section II.5.2 that cross-instrument systematics are negligible (at least in the tested high-resolution regime). We found $[\mathrm{Fe/H}] = -1.62 \pm 0.06$ dex from the median and rms scatter of all 31 FRs, respectively. This finding is in excellent agreement with our adopted [Fe/H] of -1.60 dex and therefore poses and independent validation.

4.3 The width of the Hα core as mass indicator

While the wings of the Balmer line Hα were used earlier to infer T_{eff}, we will now address the usage of its line core to derive the stellar mass. Bergemann et al. (2016) have shown that even in the face of current, state-of-the-art modeling techniques, it is not possible to reliably synthesize this part of the line. However, adopting an empirical approach, the authors discovered a connection between the Hα core width and the stellar mass. The latter originated from CoRoT and *Kepler* asteroseismology.

We pursued the strategy outlined in Bergemann et al. (2016) and fit the blue profile wing ($6562.0 < \lambda < 6562.8$) via the function

$$f(\lambda) = 1 - f_0 \exp\left(-\left(\frac{\lambda_0 - \lambda}{W_{\mathrm{H}\alpha}}\right)^3\right), \tag{III.8}$$

with free parameters f_0 and $W_{\mathrm{H}\alpha}$, and the central position of the line core $\lambda_0 = 6562.819$ Å. From the width $W_{\mathrm{H}\alpha}$, we then computed the mass parameter $\log_{10} M/M_\odot$ using the relation given in Bergemann et al. (2016) and subsequently the surface gravity through inversion of Equation I.14. The involved solar reference values can be found in Table III.2. As for Equation III.5, we computed the bolometric magnitude M_{bol} from the V-band photometry and BC_V by AAM99. The measurements and results for individual spectra covering Hα are presented in Table III.4. The error in $\log g$ is largely governed by the uncertainty in the mass and for the gravity from this method we obtained $\log g = 2.17 \pm 0.10$ dex in line with our measurements based on NLTE ionization equilibrium and about 2σ lower than our asteroseismic finding. A plausible reason for this discrepancy may be found in the circumstance that, strictly speaking, HD 20 is about 250 K warmer than the upper validity bound for T_{eff} in the calibration relation by Bergemann et al. (2016).

5 Abundance analysis

The abundances presented here were computed using either EWs (Section 5.2) or spectrum synthesis for such cases where blending was found to be substantial. For this purpose we employed the spectra providing the highest S/N at any given wavelength, that is, UVES 390 blueward of ~ 4300 Å, MIKE blue for $4300 \lesssim \lambda \lesssim 5000$ Å, and MIKE red in the regime $5000 \lesssim \lambda \lesssim 8000$ Å (cf. Figure III.1). Despite the circumstance that MIKE reaches substantially more redward, we do not consider it there because of considerable fringing. The radiation transfer was solved using `MOOG` and an `ATLAS9` model for our exact specifications (previous sections and Table III.2) that was constructed via interpolation. Our computations involved molecular equilibrium computations involving a network consisting of the species H_2, CH, NH, OH, C_2, CN, CO, N_2, NO, O_2, TiO, H_2O, and CO_2. Individual, line-by-line abundances can be found in Table III.5, while we summarize the adopted final abundances and their associated errors in Table III.6. In order to reduce the impact of outliers, abundances were averaged using the median. For ensembles of four and more lines, we computed the corresponding errors via the median absolute deviation (mad) which is scaled by the factor 1.48 in order to be conform with Gaussian standard

Table III.5: Atomic transition parameters and abundances for individual lines.

λ	X	χ_{ex}	$\log gf$	EW	$\log\epsilon(X)$		Δ	Reference
					LTE	NLTE		
[Å]		[eV]	[dex]	[mÅ]	[dex]	[dex]	[dex]	
6707.800$^{(a)}$	Li I	0.000	0.174	< 0.3	< -0.34	…	…	1
4300.000	C (CH)	…	…	syn	6.25 ± 0.05	…	…	2
3360.000	N (NH)	…	…	syn	6.21 ± 0.10	…	…	3
5577.339	O I	1.967	-8.204	2.8 ± 1.4	7.86 ± 0.31	7.86	0.00	4

Notes. The full table is available through CDS via `http://cdsarc.u-strasbg.fr/viz-bin/cat/J/A+A/635/A104`. $^{(a)}$ Additional HFS was considered.

References. (1): Hobbs et al. (1999); (2): Masseron et al. (2014); (3): Kurucz & Bell (1995); (4): Wiese et al. (1966); (5): Kramida et al. (2018); (6): Pehlivan Rhodin et al. (2017); (7): Smith & Liszt (1971); (8): Wiese et al. (1969); (9): Garz (1973); (10): Piskunov et al. (1995); (11): Biemont et al. (1993); (12): Smith & Raggett (1981); (13): Smith (1981); (14): Smith (1988); (15): Smith & O'Neill (1975); (16): Lawler & Dakin (1989); (17): Lawler et al. (2013); (18): Nitz et al. (1998); (19): Martin et al. (1988); (20): Wood et al. (2013); (21): Bizzarri et al. (1993); (22): Pickering et al. (2001); (23): Ryabchikova et al. (1994); (24): Lawler et al. (2014); (25): Wood et al. (2014a); (26): Sobeck et al. (2007); (27): Raassen & Uylings (1998); (28): Pinnington et al. (1993); (29): Sigut & Landstreet (1990); (30): Den Hartog et al. (2011); (31): Bard & Kock (1994); (32): O'Brian et al. (1991); (33): Fuhr et al. (1988); (34): Bard et al. (1991); (35): Schnabel et al. (2004); (36): Wood et al. (2014b); (37): Warner (1968b); (38): Shirai et al. (2007); (39): Warner (1968a); (40): Parkinson et al. (1976); (41): Hannaford et al. (1982); (42): Pitts & Newsom (1986); (43): Ljung et al. (2006); (44): Cowley & Corliss (1983); (45): Whaling & Brault (1988); (46): Wickliffe et al. (1994); (47): Kwiatkowski et al. (1982); (48): Biemont et al. (1984); (49): Migdalek (1978); (50): Hansen et al. (2012); (51): McWilliam (1998); (52): Lawler et al. (2001a); (53): Corliss & Bozman (1962); (54): Lawler et al. (2009); (55): Sneden et al. (2009); (56): Den Hartog et al. (2003); (57): Meggers et al. (1975); (58): Lawler et al. (2006); (59): Lawler et al. (2001c); (60): Den Hartog et al. (2006); (61): Lawler et al. (2001b); (62): Wickliffe et al. (2000); (63): Lawler et al. (2004); (64): Lawler et al. (2008); (65): Wickliffe & Lawler (1997); (66): Lawler et al. (2007); (67): Ivarsson et al. (2003); (68): Biémont et al. (2000); (69): Nilsson et al. (2002b); (70): Nilsson et al. (2002a)

errors. As noted already in Section 3.3, for the vast majority of species, the magnitude of the line-by-line scatter is inconsistent with merely the propagation of random spectrum noise, but accounts for additional – possibly systematic – sources of error further down in the abundance analysis. Consequently, we set a floor uncertainty of 0.10 dex for those species with less than four available lines, where the mad would not be a robust estimator for the scatter. For a discussion of this as well as of influences from uncertain stellar parameters, we refer the reader to Sections 6.1 and 6.2. For elements with only one line measured with the line abundance uncertainty alone exceeding the floor error, we adopted the error on the line abundance instead.

5.1 Line list

Suitable lines for an abundance analysis of HD 20 were compiled and identified using atomic data from the literature. We retrieved all line data that are available through VALD in the wavelength range from 3280 Å to 8000 Å, representing the combined wavelength coverage of the spectra at hand. In a first run, we synthesized

TABLE III.6: Final adopted abundances.

	LTE			NLTE			
X	$\langle \log \epsilon(X) \rangle^{(a)}$ [dex]	$[X/\mathrm{Fe}]^{(b)}$ [dex]	n	$\langle \log \epsilon(X) \rangle^{(a)}$ [dex]	$[X/\mathrm{Fe}]$ [dex]	n	$\log \epsilon(X)_{\odot}^{(c)}$ [dex]
Li I	< -0.34	< 0.41	1	…	…	…	1.05
C (CH)	6.25 ± 0.05	-0.38 ± 0.07	1	…	…	…	8.43
N (NH)	6.21 ± 0.10	0.18 ± 0.11	1	…	…	…	7.83
O I	7.79 ± 0.18	0.70 ± 0.18	2	7.79 ± 0.18	0.70 ± 0.18	2	8.69
Na I	4.50 ± 0.10	0.06 ± 0.11	2	4.42 ± 0.10	-0.14 ± 0.12	2	6.24
Mg I	6.25 ± 0.10	0.45 ± 0.11	3	6.24 ± 0.10	0.32 ± 0.12	3	7.60
Al I	4.54 ± 0.15	-0.11 ± 0.16	5	4.68 ± 0.06	-0.09 ± 0.09	5	6.45
Si I	6.21 ± 0.13	0.50 ± 0.14	16	6.23 ± 0.03	0.40 ± 0.08	5	7.51
Si II	6.49 ± 0.10	0.58 ± 0.10	2	…	…	…	7.51
S I	6.03 ± 0.04	0.71 ± 0.06	4	…	…	…	7.12
K I	4.15 ± 0.10	0.92 ± 0.11	2	3.60 ± 0.10	0.25 ± 0.12	2	5.03
Ca I	4.92 ± 0.06	0.38 ± 0.08	25	…	…	…	6.34
Sc II	1.66 ± 0.06	0.11 ± 0.06	11	…	…	…	3.15
Ti I	3.34 ± 0.10	0.19 ± 0.11	20	3.81 ± 0.10	0.54 ± 0.13	15	4.95
Ti II	3.67 ± 0.10	0.31 ± 0.10	28	…	…	…	4.95
V I	2.07 ± 0.12	-0.06 ± 0.13	4	…	…	…	3.93
V II	2.50 ± 0.10	0.16 ± 0.10	2	…	…	…	3.93
Cr I	3.67 ± 0.12	-0.17 ± 0.13	12	…	…	…	5.64
Cr II	4.25 ± 0.15	0.21 ± 0.15	15	…	…	…	5.64
Mn I	3.33 ± 0.08	-0.30 ± 0.10	4	3.73 ± 0.08	-0.02 ± 0.11	4	5.43
Fe I	5.70 ± 0.07	0.00 ± 0.09	133	5.82 ± 0.10	0.00 ± 0.13	133	7.50
Fe II	5.90 ± 0.03	0.00 ± 0.04	13	5.90 ± 0.03	0.00 ± 0.04	13	7.50
Co I	3.25 ± 0.11	0.06 ± 0.12	6	3.61 ± 0.10	0.30 ± 0.12	3	4.99
Ni I	4.43 ± 0.07	0.01 ± 0.09	32	…	…	…	6.22
Cu I	1.76 ± 0.10	-0.63 ± 0.11	3	…	…	…	4.19
Zn I	2.88 ± 0.10	0.12 ± 0.11	2	…	…	…	4.56
Ga I	1.03 ± 0.20	-0.21 ± 0.21	1	…	…	…	3.04
Rb I	< 1.52	< 0.45	1	…	…	…	2.87
Sr I	1.00 ± 0.10	-0.07 ± 0.11	1	1.40 ± 0.10	0.21 ± 0.12	1	2.87
Sr II	1.50 ± 0.26	0.23 ± 0.26	1	…	…	…	2.87
Y II	0.54 ± 0.09	-0.07 ± 0.09	7	…	…	…	2.21
Zr II	1.26 ± 0.09	0.28 ± 0.09	5	1.41 ± 0.10	0.42 ± 0.10	2	2.58
Mo I	0.48 ± 0.10	0.40 ± 0.11	1	…	…	…	1.88
Ru I	0.55 ± 0.10	0.60 ± 0.11	1	…	…	…	1.75
Rh I	-0.19 ± 0.40	0.70 ± 0.40	1	…	…	…	0.91
Pd I	-0.12 ± 0.20	0.11 ± 0.21	1	…	…	…	1.57
Ag I	-0.29 ± 0.20	0.57 ± 0.21	1	…	…	…	0.94
Ba II	0.93 ± 0.10	0.35 ± 0.10	2	0.74 ± 0.10	0.16 ± 0.10	2	2.18
La II	-0.09 ± 0.06	0.41 ± 0.06	6	…	…	…	1.10
Ce II	0.19 ± 0.03	0.21 ± 0.04	11	…	…	…	1.58
Pr II	-0.35 ± 0.10	0.53 ± 0.10	3	…	…	…	0.72
Nd II	0.21 ± 0.06	0.39 ± 0.06	22	…	…	…	1.42
Sm II	-0.06 ± 0.04	0.58 ± 0.05	12	…	…	…	0.96
Eu II	-0.35 ± 0.10	0.73 ± 0.10	3	…	…	…	0.52
Gd II	0.04 ± 0.15	0.56 ± 0.15	5	…	…	…	1.07
Tb II	-0.74 ± 0.10	0.55 ± 0.10	2	…	…	…	0.30
Dy II	0.21 ± 0.07	0.70 ± 0.07	4	…	…	…	1.10
Ho II	-0.49 ± 0.10	0.63 ± 0.10	2	…	…	…	0.48
Er II	-0.04 ± 0.09	0.64 ± 0.09	4	…	…	…	0.92
Tm II	-0.87 ± 0.00	0.63 ± 0.02	4	…	…	…	0.10
Yb II	-0.06 ± 0.20	0.70 ± 0.20	1	…	…	…	0.84
Lu II	-0.57 ± 0.10	0.93 ± 0.10	1	…	…	…	0.10
Hf II	-0.23 ± 0.10	0.52 ± 0.10	3	…	…	…	0.85
Os I	0.40 ± 0.10	0.80 ± 0.11	2	…	…	…	1.40
Ir I	0.42 ± 0.10	0.84 ± 0.11	1	…	…	…	1.38
Pb I	< 0.37	< 0.42	1	…	…	…	$1.75^{(d)}$
Th II	-0.85 ± 0.10	0.73 ± 0.10	1	…	…	…	0.02
U II	< -1.21	< 0.93	1	…	…	…	-0.54

Notes. (a) For $n \geq 4$, the error is considered as the mad of the line-by-line abundance distribution scaled by the factor 1.48 to be concordant with a normal distribution. Otherwise, a floor error of 0.10 dex is assumed (see main text for details). (b) With the exception of O I, $[X/\mathrm{Fe}]_{\mathrm{LTE}}$ is given relative to the LTE abundance of the Fe species at the same ionization stage. (c) The solar reference abundances are from Asplund et al. (2009). (d) The Pb abundance was taken from meteoroids.

a spectrum from this line list and discarded all profiles that did not exceed a line depth of 0.1% of the continuum level. The remaining features were visually checked for their degree of isolation and usability by comparing the observed spectra with syntheses with varying elemental abundances. The resulting list with the adopted line parameters and original sources thereof can be found in Table III.5. Additional hyperfine structure line lists were considered for the elements Li (Hobbs et al. 1999), Sc (Kurucz & Bell 1995), V (Lawler et al. 2014), Mn (Den Hartog et al. 2011), Co (Kurucz & Bell 1995), Cu (Kurucz & Bell 1995), Ag (Hansen et al. 2012), Ba (McWilliam 1998), La (Lawler et al. 2001a), Pr (Sneden et al. 2009), Eu (Lawler et al. 2001c), Tb (Lawler et al. 2001d), Ho (Lawler et al. 2004), Yb (Sneden et al. 2009), and Lu (Lawler et al. 2009).

5.2 Equivalent widths

The majority of the spectral features identified to be suitable for our analysis are sufficiently isolated so that an EW analysis could be pursued. We measured EWs from the spectra of all three spectrographs using our own semi-automated Python tool `EWCODE` (Hanke et al. 2017). In brief, `EWCODE` places a local, linear continuum estimate that is based on the neighboring wavelength ranges next to the profile of interest and fits Gaussian profiles. The user is prompted with the fit and can interactively improve the fit by, for example, introducing additional blends or refining the widths of the continuum ranges. Our measurements for individual lines along with `EWCODE`'s error estimates are listed in Table III.5.

5.3 Notes on individual elements

In the following, we comment in detail on the analysis of abundances from several features that needed special attention exceeding the standard EW or spectrum synthesis analysis. Furthermore, whenever available, we comment on NLTE corrections that were applied to the LTE abundances.

5.3.1 Lithium (Z = 3)

The expected strongest feature of Li I is the resonance transition at 6707.8 Å. Despite our high-quality data, within the noise boundaries, the spectrum of HD 20 appears perfectly flat with no feature identifiable whatsoever. For the region in question we estimate from our MIKE spectrum $S/N \approx 1050$ pixel^{-1}, which would allow for 3σ detections of Gaussian-like features with EWs of at least 0.3 mÅ as deduced from the

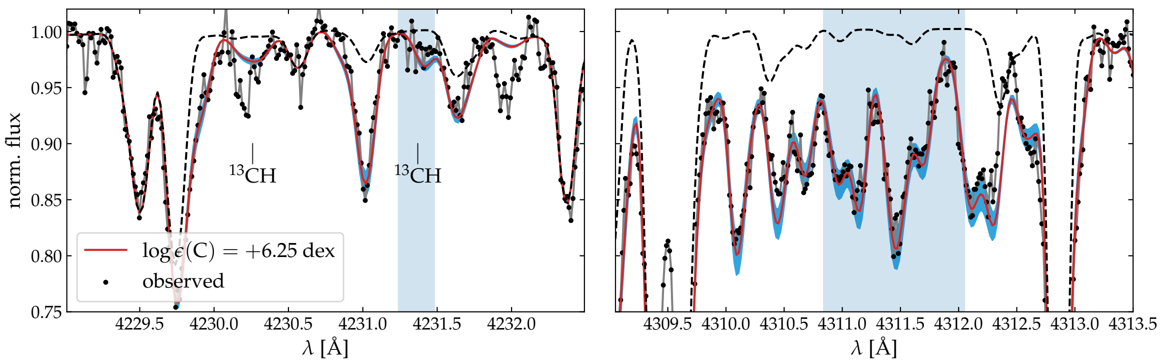

FIGURE III.9: C abundance and $^{12}\mathrm{C}/^{13}\mathrm{C}$ from the CH *G*-band in the UVES 390 spectrum. *Left panel*: region around the two features that are dominated by ^{13}CH, one of which is used to pinpoint $^{12}\mathrm{C}/^{13}\mathrm{C}$ (blue rectangle). The bluer feature at ~ 4230 Å was not considered due to an unidentified blend (see main text). The observed spectrum is represented by black dots connected by gray lines and the best-fit synthesis (red) and its abundance error margin of 0.05 dex are depicted in blue, respectively. The dashed spectrum shows a synthesis without any C. *Right panel*: same as *left panel* but in the range used to constrain the C (CH) abundance.

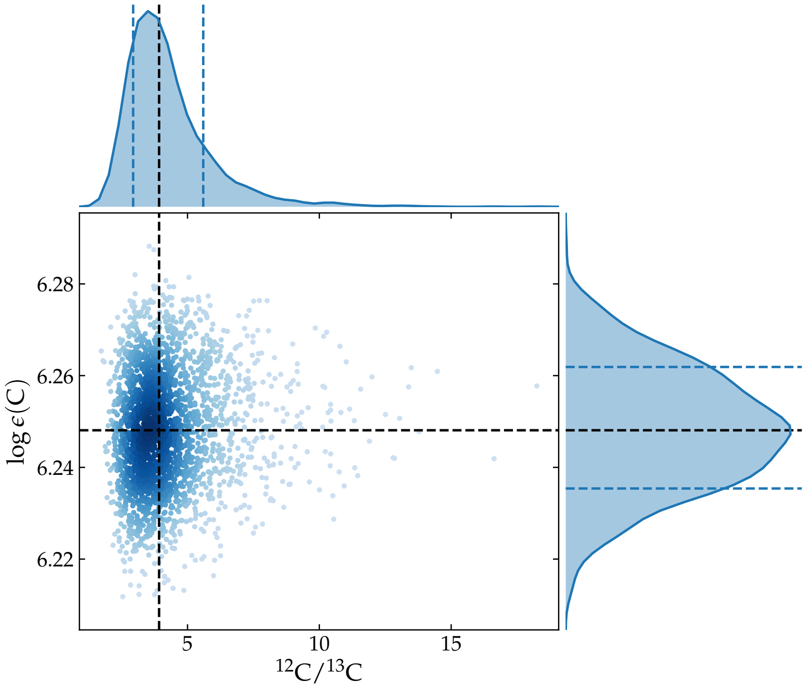

FIGURE III.10: Two-dimensional representation of the MCMC sample used to fit $\log\epsilon(\mathrm{C})$ and $^{12}\mathrm{C}/^{13}\mathrm{C}$ simultaneously including the marginal distributions. Median values and asymmetric limits are displayed by dashed lines.

formalism provided in Battaglia et al. (2008). The latter EW translates into an upper limit $\log\epsilon(\mathrm{Li}) < -0.34$ dex.

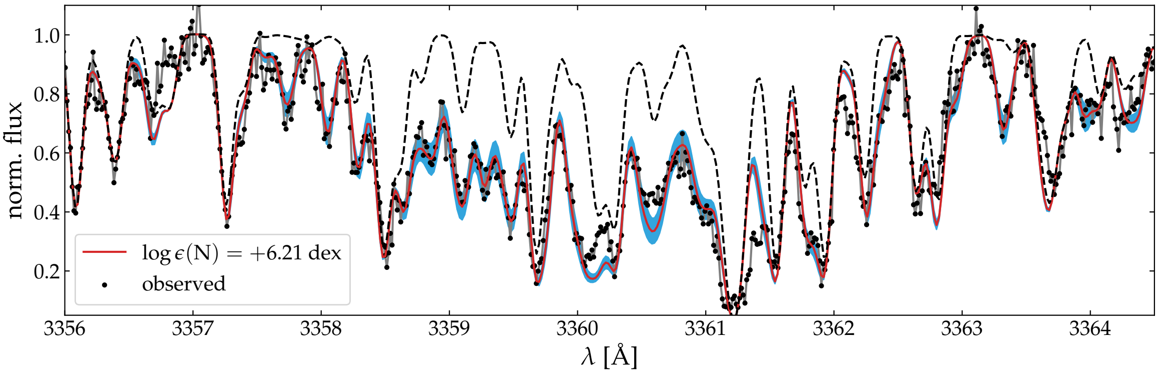

FIGURE III.11: Same as *right panel* of Figure III.9, but for a synthesis of the NH-band at ∼ 3360 Å. A synthesis without any N is indicated by the black dashed curve. The blue error range corresponds to an abundance variation of ±0.10 dex.

5.3.2 Carbon, nitrogen, and oxygen (Z = 6, 7, and 8)

Our C abundances are based on synthesis of the region around the CH *G*-band at ∼ 4300 Å with molecular line data for ^{12}CH and ^{13}CH from Masseron et al. (2014). We identified a range between 4310.8 Å and 4312.1 Å that in HD 20 is almost devoid of atomic absorption and hence is ideal for CH synthesis irrespective of other elemental abundances. We show this range in Figure III.9. Only very substantial changes in the model isotopic ratio $^{12}\mathrm{C}/^{13}\mathrm{C}$ have a notable effect on this region, manifesting mostly in an effective blue- or redshift of the molecular features. In contrast, the two ^{13}CH profiles near ∼ 4230 Å (left panel of Figure III.9) are rather sensitive to the isotopic ratio. As cautioned by Spite et al. (2006), the blueward profile has a dominant blend they attribute to an unidentified transition from an *r*-process element. Given the *r*-process-rich nature of our star, we do not consider this feature here. Employing both ranges, one for the C abundance and one for $^{12}\mathrm{C}/^{13}\mathrm{C}$, the two measures can be effectively decoupled as can be seen in Figure III.10, where we present the results of an MCMC sampling run used to draw from the posterior distribution of the fitted parameters in the regions indicated in Figure III.9. From this distribution we determine $^{12}\mathrm{C}/^{13}\mathrm{C} = 3.92^{+1.68}_{-0.98}$. Though nominally less, an error of 0.05 dex was adopted for $\log\epsilon(\mathrm{C}) = 6.25$ dex in order to account for the circumstance that the continuum level in the right-hand spectrum had to be established from a region more than one Å away on either side, thus introducing a slight normalization uncertainty.

We determined the N abundance in a similar fashion employing the NH-band at ∼ 3360 Å (see Figure III.11). From our synthesis we inferred $\log\epsilon(\mathrm{N}) = 6.21 \pm 0.10$ dex. The present data do not permit the determination of the isotopic ratio $^{14}\mathrm{N}/^{15}\mathrm{N}$.

Unfortunately, the frequently used [O I] line at 6300.3 Å is strongly blended with telluric absorption features in all available spectra and hence rendered useless for precise abundance studies. Nonetheless, the high S/N of the MIKE spectra allowed for the measurement of the much weaker [O I] transitions at 5577.3 Å and 6363.8 Å, from which we deduced a mean abundance of $\log\epsilon(\mathrm{O\,I})_{\mathrm{LTE}} = 7.79 \pm 0.18$ dex, or $[\mathrm{O/Fe}] = 0.70$ dex. The forbidden lines ought to have negligible LTE corrections, because they have metastable upper levels. Hence, the collisional rate is higher than the radiative rate and LTE is obtained, in other words $\log\epsilon(\mathrm{O\,I})_{\mathrm{NLTE}} = \log\epsilon(\mathrm{O\,I})_{\mathrm{LTE}}$. Severe changes in the O abundance result in non-negligible effects on the molecular equilibrium, in particular through their impact on the formation of CO. For this reason, the overabundance found here was considered in all syntheses, including the ones for CH and NH outlined above.

We note here that abundances from the O triplet at ~ 7773 Å could be firmly detected and are listed in Table III.5. However, we discard them ($\log\epsilon(\mathrm{O\,I})_{\mathrm{LTE}} \approx 8.22$ dex) from consideration in this work, since they are in strong disagreement to the abundances from the forbidden lines. The formation of the lines in question is subject to considerable NLTE effects as shown by, for example, Sitnova et al. (2013). Using the MPIA NLTE spectrum tools[10] to retrieve corrections for individual line abundances, we found an average 1D NLTE bias of -0.14 dex, which is not enough to erase the discrepancy. We therefore suspect much stronger effects when considering line formation in NLTE using 3D dynamical models (e.g., Amarsi et al. 2019).

5.3.3 Sodium (Z = 11)

Equivalent widths from the two weak Na lines at 5682 Å and 5688 Å were employed to compute an abundance of $\log\epsilon(\mathrm{Na})_{\mathrm{LTE}} = 4.50 \pm 0.10$ dex. We emphasize the artificial increase of the latter uncertainty to 0.10 dex as discussed earlier. According to the INSPECT database[11] (Lind et al. 2011), for these lines and HD 20's parameters a mean NLTE correction of -0.08 dex should be applied, leading to $\log\epsilon(\mathrm{Na})_{\mathrm{NLTE}} = 4.42$ dex and consequently $[\mathrm{Na/Fe}] = -0.14$ dex. The frequently used Na I transitions at 6154 Å and 6160 Å could not be firmly detected in any of our spectra owing to HD 20's rather high temperature, which strongly reduces the strength of these lines.

5.3.4 Magnesium (Z = 12)

The three Mg I lines employed for abundance determinations in this work were corrected for departures from the LTE assumptions by means of the MPIA NLTE

---

[10] `http://nlte.mpia.de/gui-siuAC_secE.php`

[11] `www.inspect-stars.com`

spectrum tools, which is based on Bergemann et al. (2017a,b). The mean correction is only +0.04 dex, indicating that the effects are not severe for the selected lines.

5.3.5 Aluminum (Z = 13)

Our Al abundance for HD 20 is based on five neutral transitions. While spectrum syntheses revealed the 3944 Å profile to be severely blended, the other strong UV resonance feature at 3961 Å was found to be sufficiently isolated for getting a robust abundance. In addition, the high S/N of our MIKE spectrum allowed for the detection of two pairs of weak, high-excitation lines at ∼ 6697 Å and ∼ 7835 Å, respectively. In LTE, there is a considerable difference of almost 1 dex between the abundances from the resonance line ($\log\epsilon(\mathrm{Al})_{\mathrm{LTE}} = 3.58$ dex), and the four weak lines ($\log\epsilon(\mathrm{Al})_{\mathrm{LTE}} = 4.54$ dex). As shown by Nordlander & Lind (2017), this can be explained by substantial NLTE effects on Al line formation in metal-poor giants like HD 20. Indeed, by interpolation in their pre-computed grid, we found corrections of 1.02 dex for the strong line and 0.14 to 0.20 dex for the weak lines, which alleviates the observed discrepancy. We emphasize that [Al/Fe] (Table III.6) remains unaltered by going from LTE to NLTE, because both the Fe I transitions and the majority of our Al I lines experience the same direction and magnitude of corrections. We note here that Barklem et al. (2005) report on a strong depletion in LTE of $[\mathrm{Al/Fe}] = -0.80$ dex (on the scale of Asplund et al. 2009) based on the UV resonance line, only. Hence, that finding at face value should be treated with caution since severe NLTE biases can be expected.

5.3.6 Silicon (Z = 14)

Five of our 16 Si I lines with measured EWs have a correspondence in the MPIA NLTE database (Bergemann et al. 2013). The deduced corrections for HD 20's stellar parameters are marginal at a level of −0.01 to −0.04 dex. As a consequence, the ionization imbalance of −0.28 dex between Si I and Si II that prevails in LTE cannot be compensated this way. Lacking NLTE corrections for our two Si II transitions, however, we cannot draw definite conclusions at this point.

5.3.7 Sulfur (Z = 16)

We detected in total four S features that are spread over two wavelength windows at ∼ 4695 Å and ∼ 6757 Å, corresponding to the second and eighth S I multiplet. Using spectrum synthesis, we found a mean abundance $\log\epsilon(\mathrm{S\,I})_{\mathrm{LTE}} = 6.03 \pm 0.04$ dex that is mainly driven by the strongest profile at 4694.1 Å. Concerning influences of NLTE on S I, in the literature there is no study dealing with the second multiplet. For the eighth multiplet, however, Korotin (2008, 2009) and Korotin et al. (2017) showed that the expected corrections for HD 20 are minor and remain well below 0.10 dex. Since we detected no considerable difference in our LTE analysis between the eighth and second multiplet, we conclude that the correction – if any – for the second multiplet is probably small, too.

5.3.8 Potassium (Z = 19)

The K abundance presented here is based on the EWs of two red resonance lines at 7665 Å and 7699 Å, respectively. These lines are expected to be subject to severe departures from LTE. Mucciarelli et al. (2017) showed for giants in four globular clusters that the magnitude of the NLTE correction strongly increases with increasing T_{eff}, $\log g$, and $\log \epsilon(\mathrm{K})_{\mathrm{LTE}}$. One of their clusters, NGC 6752, exhibits a similar metallicity (-1.55 dex) as HD 20 and we estimate from their Figure 3 a correction of our LTE abundance of at least -0.5 to -0.6 dex. For our adopted NLTE abundance (Table III.6) we assume a shift by -0.55 dex.

5.3.9 Titanium (Z = 22)

At $(\log \epsilon(\mathrm{Ti\,I}) - \log \epsilon(\mathrm{Ti\,II}))_{\mathrm{LTE}} = -0.33$ dex, our LTE analysis of Ti lines shows an ionization imbalance. We have determined line-by-line NLTE corrections for our Ti I abundances from the grid by Bergemann (2011) amounting to values ranging from $+0.4$ to $+0.6$ dex. It is noteworthy that corrections to Ti II are insignificant in the present regime of stellar parameters (cf., Bergemann 2011). The newly derived NLTE abundances switch the sign of the ionization imbalance with a reduced amplitude ($(\log \epsilon(\mathrm{Ti\,I}) - \log \epsilon(\mathrm{Ti\,II}))_{\mathrm{NLTE}} = +0.14$ dex). Inconsistencies in other metal-poor stars manifesting themselves in ionization imbalances even in NLTE have already been noted by Bergemann (2011) and were explained by inaccurate or missing atomic data. More recently, Sitnova et al. (2016) found lower NLTE corrections and therefore weaker – but still non-zero – ionization imbalances for stars in common with Bergemann (2011), which they mainly attributed to the inclusion of high-excitation levels of Ti I in their model atom. In light of prevailing uncertainties of Ti I NLTE calculations, we do not believe that the ionization imbalance of Ti contradicts our results from Section 3.3.

5.3.10 Manganese (Z = 25)

Following Bergemann & Gehren (2008), our four abundances from Mn I lines should experience a considerable mean NLTE adjustment of $+0.40$ dex and thus are consistent with a solar [Mn/Fe]. More recently, Mishenina et al. (2015) casted some doubt on the robustness of the aforementioned NLTE calculations by showing the absence of systematic discrepancies in LTE between multiplets that according to Bergemann & Gehren (2008) ought to have different NLTE corrections. Nonetheless, Bergemann et al. (2019) corroborated the strong NLTE corrections found in the earlier study. Moreover, the authors remark that Mn I transitions at a lower excitation potential of more than 2 eV are not strongly affected by convection – that is 3D effects – and are recommended as 1D NLTE estimator. Since the latter is satisfied for all of our four used Mn lines, our 1D NLTE abundance ought to be an accurate estimate.

5.3.11 Cobalt (Z = 27)

The Co NLTE corrections were obtained from Bergemann et al. (2010). For three out of the six measured lines corrections are available and amount to +0.46 dex on average.

5.3.12 Copper (Z = 29)

We measured three profiles of Cu I in our spectra, two of which originate from low-excitation ($\sim$ 1.5 eV) states. Albeit for dwarfs, at [Fe/H] ~ -1.5 dex, Yan et al. (2015) predicted for these two transitions at 5105.5 Å and 5782.2 Å stronger NLTE corrections compared to the ones for our high-excitation ($\sim$ 3.8 eV) line. This is somewhat reflected in our LTE abundances where the lower-excitation lines yield a lower value by about 0.3 dex. Lacking a published pre-computed grid, it is hard to predict the exact amount of NLTE departures for our giant star and its temperature. Yet, Shi et al. (2018) and Korotin et al. (2018) showed that the corrections correlate much stronger with [Fe/H] than they do with $\log g$ or T_{eff}. We make no attempt to rectify our Cu abundances at this point, but judging from the literature we note that the corrections are probably on the order of +0.2 dex for the low-excitation- and +0.1 dex for the high-excitation lines.

5.3.13 Strontium (Z = 38)

In principle, our spectra cover the UV resonance lines of Sr II at 4077 Å and 4215 Å, although we found those to be strongly saturated and we could not reproduce the line shape through LTE synthesis. Furthermore, the lines in question are subject to a substantial degree of blending by several atomic and molecular transitions (see also Andrievsky et al. 2011). Fortunately, it was possible to measure EWs of the much weaker lines at 4607 Å (Sr I) and at 4161 Å (Sr II). For these we deduced abundances of 1.00 dex and 1.50 dex, respectively, which indicates a substantial discrepancy between the two ionization stages. The latter can be attributed to considerable NLTE

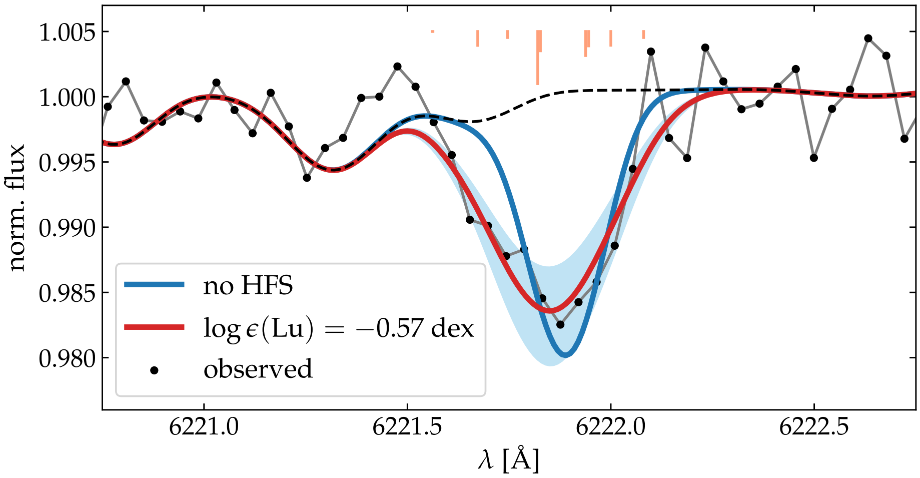

FIGURE III.12: Synthesis of the Lu II line at 6221.9 Å. The red line represents the best abundance match with an error of 0.1 dex (blue shaded region). The broad range of HFS components for ^{175}Lu from Lawler et al. (2009) are indicated by vertical orange lines at the top and have been taken into account for this synthesis. The impact of the negligence of HFS on the line shape is indicated by the blue line.

departures for the neutral transition. Bergemann et al. (2012a)[12] and Hansen et al. (2013) performed extensive NLTE calculations for this line from which we extract a correction of +0.4 dex for HD 20's stellar parameters. Thus, the observed difference is effectively erased, although we emphasize the lack of published Sr II corrections for the line and stellar parameters in question, which, in turn, may re-introduce a slight disagreement.

5.3.14 Zirconium (Z = 40)

Two out of our five measured Zr II lines were investigated for NLTE effects by Velichko et al. (2010). The authors note that departures mainly depend on metallicity and gravity, whereas there is only a weak coupling to T_{eff}. From their published grid of corrections we extrapolate corrections of 0.15 dex and 0.18 dex for our abundances from the lines at 4209.0 Å and 5112.3 Å, respectively.

5.3.15 Barium (Z = 56)

In HD 20, the Ba II profile at 4554 Å is strongly saturated and thus largely insensitive to abundance. We further excluded the 6141 Å line because of blending by an Fe feature. Our abundance hence is based on synthesis of the two clean and only moderately strong transitions at 5853 Å and 6496 Å, yielding $\log\epsilon(\text{Ba II}))_{\text{LTE}} =$ 0.77 dex and 1.09 dex, respectively. In light of the recent work on NLTE line formation

---

[12] Bergemann et al. (2012a) mention a Sr II line at 4167.8 Å in their Table 1. However the line parameters provided are for the line at 4161.8 Å. NLTE corrections are not provided for this transition.

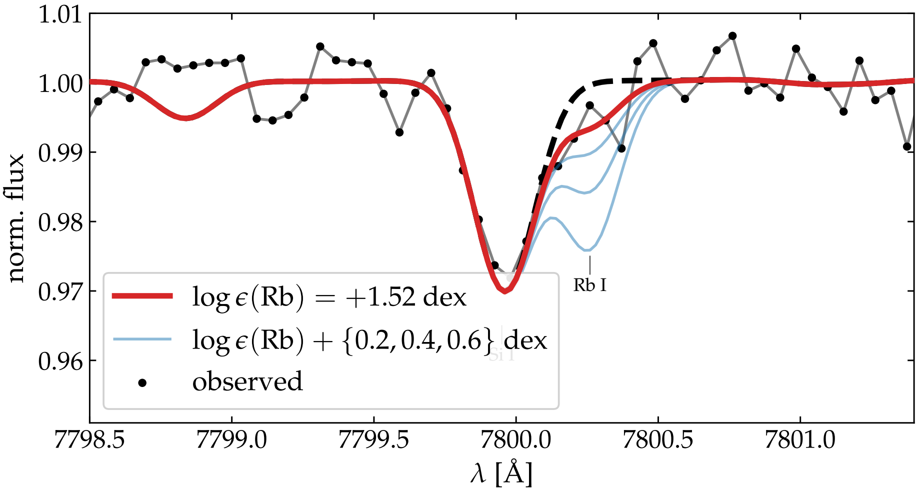

FIGURE III.13: Upper limit on Rb from the Rb I line at 7800.3 Å. The red model denotes the adopted upper limit of +1.52 dex, whereas blue lines are syntheses with Rb abundances successively increased by 0.2 dex.

by Mashonkina & Belyaev (2019), the presented disagreement can be expected in LTE, as in our parameter regime NLTE corrections for the two lines differ. Indeed, interpolation in their published grid[13] resulted in corrections of −0.10 dex and −0.27 dex, hence reducing the gap to 0.15 dex, which can be explained by the combined statistical uncertainties.

5.3.16 Lutetium (Z = 71)

The very high S/N of about 1000 pixel^{-1} in the MIKE spectrum together with an overall high Lu abundance ([Lu/Fe] = 0.93 dex) allowed for a solid detection (4.7 mÅ) of the otherwise very weak Lu II profile at 6221.9 Å. We mention the line here explicitly because it was found to have an exceptionally pronounced HFS structure, as we show in Figure III.12 where two syntheses are compared; one including HFS and one neglecting it. The line components were taken from Lawler et al. (2009). We note that we consider only the ^{175}Lu isotope here, because the only other stable isotope, ^{176}Lu, is expected to be a minority component judging from its solar fractional abundance (2.59%, Lawler et al. 2009). Despite the considerable additional line broadening due to atmospheric effects (Section 3.5), hyperfine splitting is still the dominant source of broadening, thus highlighting the importance of including it in our analysis.

---

[13] The grid does not reach down to $\log g = 2.37$ dex, but instead ends at $\log g = 3.0$ dex. Consequently, a linear extrapolation was performed. We note, however, that this seems uncritical since gravity is not a governing parameter in the considered regime.

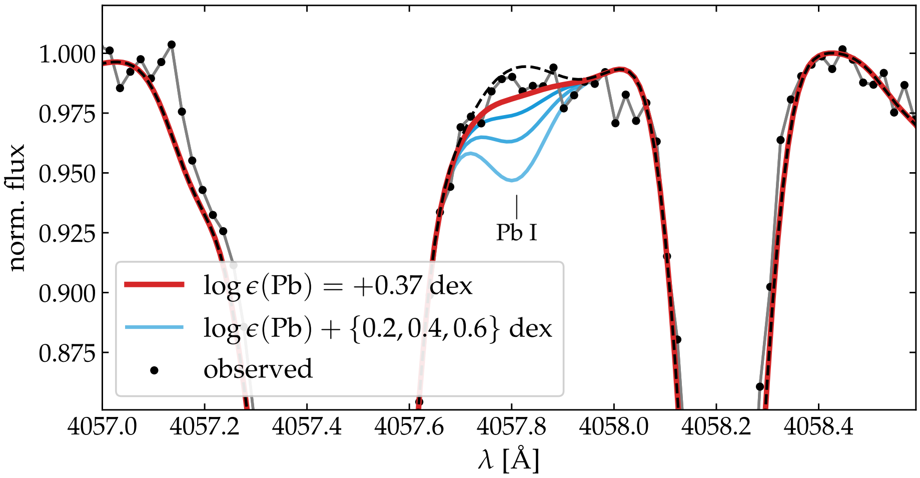

FIGURE III.14: Same as Figure III.13 but for the Pb I transition at 4057.8 Å and an upper limit of $+0.37$ dex.

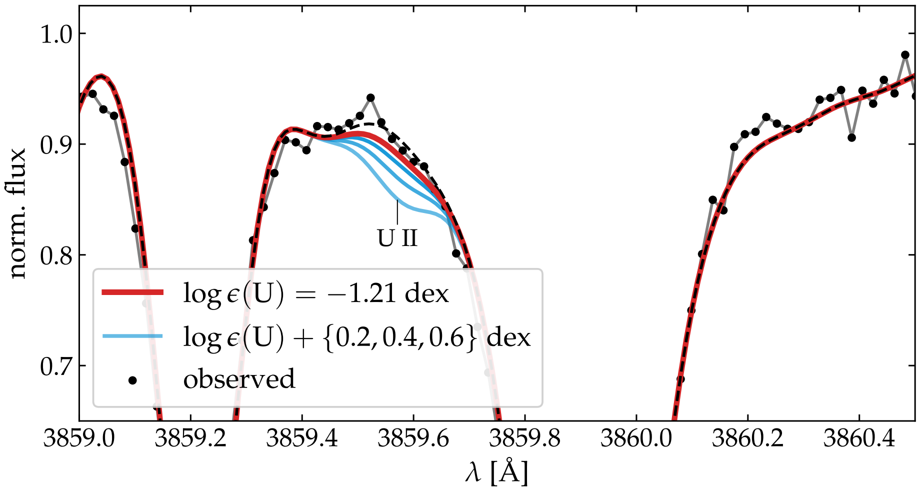

FIGURE III.15: Same as Figure III.13 but for the U II feature at 3859.6 Å and an upper limit of -1.21 dex.

5.3.17 Upper limits on rubidium, lead, and uranium (Z = 37, 82, and 92)

For Rb, Pb, and U, it was not possible to obtain solid detections despite the high-quality spectra at hand. Nonetheless, we could estimate reasonable upper limits based on the lines at 7800.3 Å (Rb I), 4057.8 Å (Pb I), and 3859.6 Å (U II). Since there is a considerable amount of blending by a variety of species involved in shaping the spectrum in the three wavelength regimes, we cannot estimate the upper limit in the same way as for Li (Section 5.3.1). Thus, we used synthesis at varying abundances of the target elements in order to establish the highest abundance that is still consistent

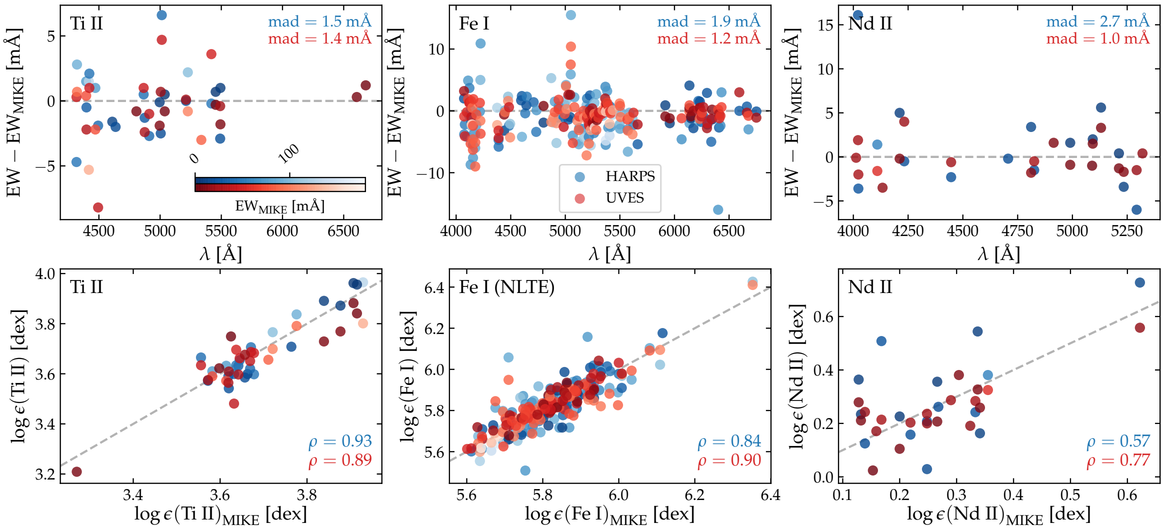

FIGURE III.16: Comparison of EWs (*upper panels*) and deduced abundances (*lower panels*) obtained from the same lines that were measured with three different instruments. Panels are horizontally separated by the three representative chemical species (from *left* to *right*: Ti II, Fe I, and Nd II). *Upper panels*: residual EWs between HARPS (blue) and UVES (red) measurements with respect to the corresponding MIKE EWs as a function of wavelength. The lightness of the color stands for the measured EW in the MIKE spectrum as indicated by the color bars in the *upper left panel*. *Lower panels*: abundances from the MIKE spectrum are shown on the abscissas, whereas HARPS and UVES findings are given along the ordinates. In each panel the perfect one-to-one correlation is represented by gray dashed lines and the correlation coefficients computed for the samples are presented on the *lower right*.

with the noise level present in the spectral regions (Figures III.13, III.14, and III.15). This way, we found $\log\epsilon(\mathrm{Rb}) < 1.52$ dex, $\log\epsilon(\mathrm{Pb}) < 0.37$ dex, and $\log\epsilon(\mathrm{U}) < -1.21$ dex, respectively.

6 Abundance systematics

6.1 Instrument-induced versus other systematics

Given our high-quality spectra gathered with three different instruments, we were in the fortunate situation to be able to investigate the presence of systematics originating from the choice of different resolving powers and fiber-fed (in case of HARPS) versus slit spectrographs (MIKE and UVES). To this end, we performed tests using lines of the species Ti II, Fe I, and Nd II that are distributed between 4000 Å and 6800 Å, which renders them accessible by all three instruments with only a few exceptions in the chip gaps. These three elements were chosen because they are, on the one hand, representatives for the main groups of α, iron-peak, and neutron-capture elements and, on the other hand, they allow for measurements of a sufficient number of lines

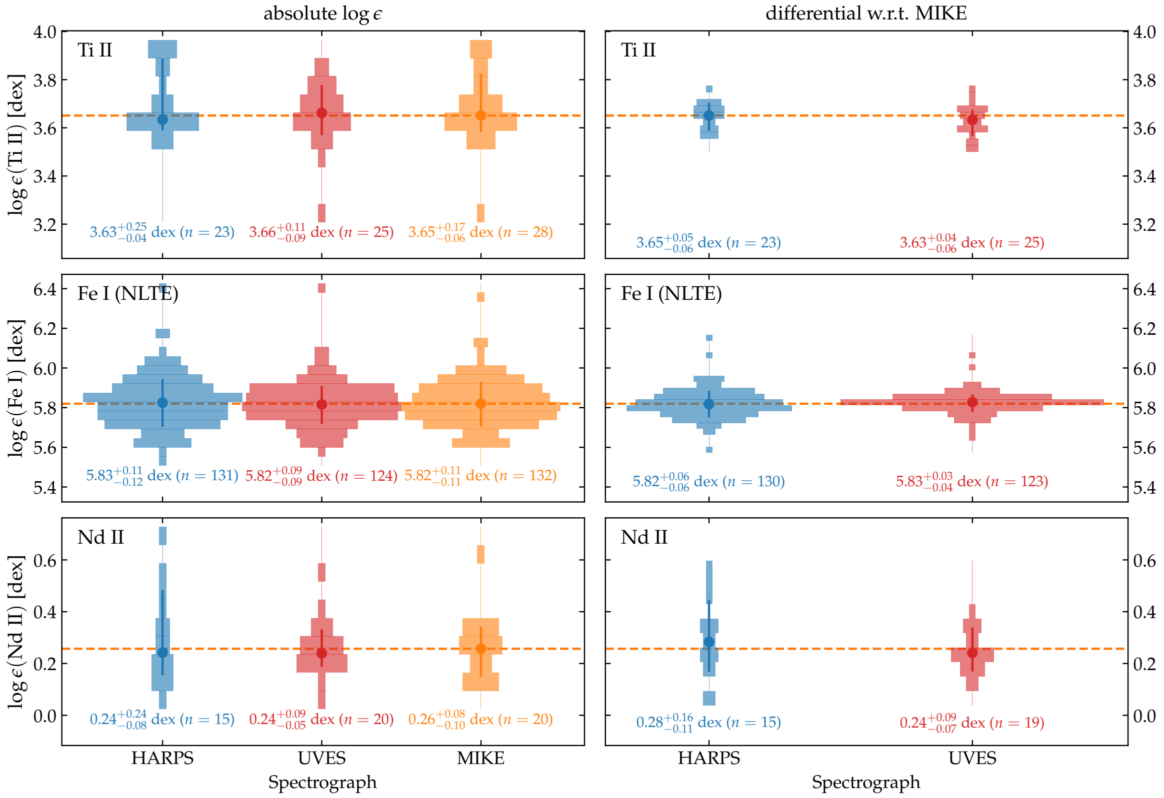

FIGURE III.17: Violin plots of absolute (*left*) and line-by-line differential abundances (*right*) for the same representative elements as in Figure III.16. Colors indicate spectrographs in the same way as in that figure with MIKE additionally being depicted in orange. Circles and vertical lines represent the median abundances, 15.9th, and 84.1th percentiles, respectively. The latter are furthermore printed at the *bottom* of each panel together with the number of involved lines, *n*.

(in this case more than 20) that permit meaningful number statistics.

EWs for the sample of lines described above were measured in all three spectra using `EWCODE`. In the upper panels of Figure III.16 we present the difference between measurements employing HARPS and UVES with respect to MIKE EWs. It is noteworthy that in principle the spread in this quantity is a convolution of both noise-induced errors from HARPS (UVES) and MIKE. However, in light of the substantially higher S/N of the MIKE spectrum at almost any wavelength, it appears safe to assume only a minor contribution due to noise in the MIKE spectrum. There are no obvious systematic trends or biases in the residuals, which leads us to the conclusion that for our analysis procedures of the star HD 20 the three spectrographs are entirely interchangeable without having to worry about introducing (additional) abundance systematics. The only notable difference is of a pure stochastic nature in the sense that HARPS EW residuals show larger spreads than UVES, which can be tied to the significantly lower S/N (see Figure III.1).

Once the EWs are propagated through the abundance analysis, it becomes obvious that noise is not the dominant source of error for the vast majority of lines when employing any of the tested instruments and their attributed S/N levels. This is illustrated in the lower panels of Figure III.16, where individual abundances from lines measured in the HARPS and UVES spectra are depicted as a function of their MIKE counterpart. NLTE corrections were applied to Fe I and are expected to be negligible for the other two species. If spectrum noise were the sole reason for abundance errors the distributions would be completely uncorrelated and show ellipses that are aligned with the coordinate axes. Instead, we found strong correlations that imply governing systematic error components. We mention here possible origins for this observation to be uncertain oscillator strengths and/or shortcomings in the assumptions of one-dimensional and static atmospheres.

For Figure III.17 we decoupled the systematic from the statistical component by performing line-by-line differential comparisons to the MIKE abundances. It is evident that the scatter in absolute abundances is hardly lower than 0.1 dex, while it is as low as 0.03 dex in the differential case for Fe I and the UVES-MIKE combination. The spread in absolute abundances motivates the floor abundance error of 0.1 dex employed throughout this work in those cases ($n < 4$) where the scatter could not be rigidly determined from the sample of lines themselves.

6.2 Impacts of model atmosphere errors

Here we present a detailed investigation of the propagation of errors on the key atmospheric parameters T_{eff}, $\log g$, [Fe/H], and v_{mic} into the inferred individual stellar abundances (or upper limits) in LTE. To this end, eight model atmospheres were interpolated from the `ATLAS9` grid, each denoting the departure of a stellar parameter from its optimal value by an amount dictated by our adopted errors (Table III.2). These altered atmospheres were used to redetermine the abundances from all transitions measured in this work based on their EW. In those cases where spectrum synthesis was used, a converted EW corresponding to the determined abundance was initially calculated through the `MOOG` driver *ewfind* and the set of optimal atmospheric parameters. New average abundances were then derived using the median of all findings for one species. The resulting departures from the abundances listed in Table III.6 can be found in Figure III.18.

While the model metallicity can certainly be neglected as a factor of uncertainty, for the vast majority of elements, the model temperature appears to be the most critical parameter, in that changes induce the largest abundance deviations. Generally, the neutral species are more susceptible to T_{eff} than their ionized counterparts.

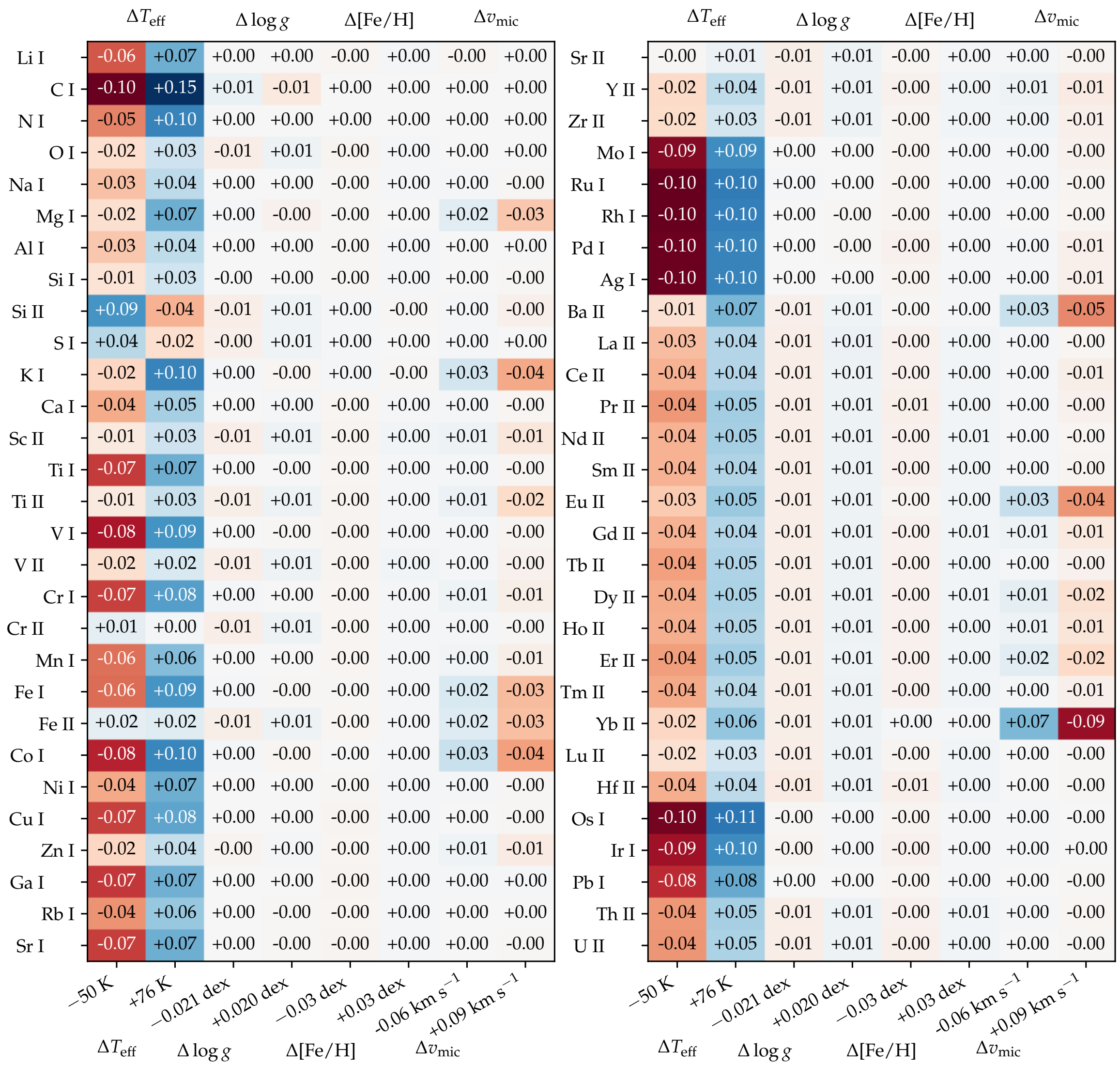

	ΔT_{eff}		$\Delta\log g$		Δ[Fe/H]		Δv_{mic}	
	−50 K	+76 K	−0.021 dex	+0.020 dex	−0.03 dex	+0.03 dex	-0.06 km s^{-1}	+0.09 km s^{-1}
Li I	-0.06	+0.07	+0.00	+0.00	-0.00	+0.00	-0.00	+0.00
C I	-0.10	+0.15	+0.01	-0.01	+0.00	+0.00	+0.00	+0.00
N I	-0.05	+0.10	+0.00	+0.00	+0.00	+0.00	+0.00	+0.00
O I	-0.02	+0.03	-0.01	+0.01	-0.00	+0.00	+0.00	+0.00
Na I	-0.03	+0.04	+0.00	+0.00	-0.00	+0.00	+0.00	-0.00
Mg I	-0.02	+0.07	+0.00	-0.00	-0.00	+0.00	+0.02	-0.03
Al I	-0.03	+0.04	+0.00	+0.00	-0.00	+0.00	+0.00	+0.00
Si I	-0.01	+0.03	-0.00	+0.00	-0.00	+0.00	+0.00	-0.00
Si II	+0.09	-0.04	-0.01	+0.01	+0.00	-0.00	+0.00	-0.00
S I	+0.04	-0.02	-0.00	+0.01	+0.00	+0.00	+0.00	+0.00
K I	-0.02	+0.10	+0.00	-0.00	+0.00	-0.00	+0.03	-0.04
Ca I	-0.04	+0.05	+0.00	+0.00	-0.00	+0.00	+0.00	-0.00
Sc II	-0.01	+0.03	-0.01	+0.01	-0.00	+0.00	+0.01	-0.01
Ti I	-0.07	+0.07	+0.00	-0.00	-0.00	+0.00	+0.00	-0.00
Ti II	-0.01	+0.03	-0.01	+0.01	-0.00	+0.00	+0.01	-0.02
V I	-0.08	+0.09	+0.00	-0.00	-0.00	+0.00	+0.00	-0.00
V II	-0.02	+0.02	-0.01	+0.01	-0.00	+0.00	+0.00	-0.00
Cr I	-0.07	+0.08	+0.00	+0.00	-0.00	+0.00	+0.01	-0.01
Cr II	+0.01	+0.00	-0.01	+0.01	-0.00	+0.00	+0.00	-0.00
Mn I	-0.06	+0.06	+0.00	+0.00	-0.00	+0.00	+0.00	-0.01
Fe I	-0.06	+0.09	+0.00	-0.00	-0.00	+0.00	+0.02	-0.03
Fe II	+0.02	+0.02	-0.01	+0.01	-0.00	+0.00	+0.02	-0.03
Co I	-0.08	+0.10	+0.00	-0.00	-0.00	+0.00	+0.03	-0.04
Ni I	-0.04	+0.07	+0.00	+0.00	-0.00	+0.00	+0.00	-0.00
Cu I	-0.07	+0.08	+0.00	+0.00	-0.00	+0.00	+0.00	-0.00
Zn I	-0.02	+0.04	-0.00	+0.00	-0.00	+0.00	+0.01	-0.01
Ga I	-0.07	+0.07	+0.00	+0.00	-0.00	+0.00	+0.00	+0.00
Rb I	-0.04	+0.06	+0.00	-0.00	-0.00	+0.00	+0.00	+0.00
Sr I	-0.07	+0.07	+0.00	-0.00	-0.00	+0.00	+0.00	-0.00

	ΔT_{eff}		$\Delta\log g$		Δ[Fe/H]		Δv_{mic}	
	−50 K	+76 K	−0.021 dex	+0.020 dex	−0.03 dex	+0.03 dex	-0.06 km s^{-1}	+0.09 km s^{-1}
Sr II	-0.00	+0.01	-0.01	+0.01	-0.00	+0.00	+0.00	-0.00
Y II	-0.02	+0.04	-0.01	+0.01	-0.00	+0.00	+0.01	-0.01
Zr II	-0.02	+0.03	-0.01	+0.01	-0.00	+0.00	+0.00	-0.01
Mo I	-0.09	+0.09	+0.00	+0.00	-0.00	+0.00	+0.00	-0.00
Ru I	-0.10	+0.10	+0.00	+0.00	-0.00	+0.00	+0.00	-0.00
Rh I	-0.10	+0.10	+0.00	-0.00	-0.00	+0.00	+0.00	-0.00
Pd I	-0.10	+0.10	+0.00	-0.00	-0.00	+0.00	+0.00	-0.01
Ag I	-0.10	+0.10	+0.00	+0.00	-0.00	+0.00	+0.00	-0.01
Ba II	-0.01	+0.07	-0.01	+0.01	-0.00	+0.00	+0.03	-0.05
La II	-0.03	+0.04	-0.01	+0.01	-0.00	+0.00	+0.00	-0.00
Ce II	-0.04	+0.04	-0.01	+0.01	-0.00	+0.00	+0.00	-0.01
Pr II	-0.04	+0.05	-0.01	+0.01	-0.01	+0.00	+0.00	-0.00
Nd II	-0.04	+0.05	-0.01	+0.01	-0.00	+0.01	+0.00	-0.00
Sm II	-0.04	+0.04	-0.01	+0.01	-0.00	+0.00	+0.00	-0.00
Eu II	-0.03	+0.05	-0.01	+0.01	-0.00	+0.00	+0.03	-0.04
Gd II	-0.04	+0.04	-0.01	+0.01	-0.00	+0.01	+0.01	-0.01
Tb II	-0.04	+0.05	-0.01	+0.01	-0.00	+0.00	+0.00	-0.00
Dy II	-0.04	+0.05	-0.01	+0.01	-0.00	+0.01	+0.01	-0.02
Ho II	-0.04	+0.05	-0.01	+0.01	-0.00	+0.00	+0.01	-0.01
Er II	-0.04	+0.05	-0.01	+0.01	-0.00	+0.00	+0.02	-0.02
Tm II	-0.04	+0.04	-0.01	+0.01	-0.00	+0.00	+0.00	-0.01
Yb II	-0.02	+0.06	-0.01	+0.01	+0.00	+0.00	+0.07	-0.09
Lu II	-0.02	+0.03	-0.01	+0.01	-0.00	+0.00	+0.00	-0.00
Hf II	-0.04	+0.04	-0.01	+0.01	-0.01	+0.00	+0.00	-0.00
Os I	-0.10	+0.11	-0.00	+0.00	-0.00	+0.00	+0.00	-0.00
Ir I	-0.09	+0.10	-0.00	+0.00	-0.00	+0.00	+0.00	+0.00
Pb I	-0.08	+0.08	+0.00	+0.00	-0.00	+0.00	+0.00	-0.00
Th II	-0.04	+0.05	-0.01	+0.01	-0.00	+0.01	+0.00	-0.00
U II	-0.04	+0.05	-0.01	+0.01	-0.00	+0.00	+0.00	-0.00

FIGURE III.18: Change in elemental abundances $\log\epsilon$ from individually varying the input model parameters by their error margins. Red and blue colors denote negative and positive residuals, respectively. The strength of the impact of an altered parameter (abscissa) on the elemental abundance (ordinate) is highlighted by the lightness of the color, where dark colors indicate strong departures.

Abundance deviations of the ionized species of the neutron-capture elements do not exceed the 0.05 dex level, therefore highlighting the robustness of the resulting pattern against model uncertainties.

Interestingly, the overall trend of abundances correlating with temperature is reversed for Si II and S I, where an anti-correlation is seen. We further note that considerable departures reaching or even exceeding the 0.10 dex level were found for C (CH), Mo I to Ag I, Os I, and Ir I. Both effects can be linked to the lower energy level of the transitions as we show in Figure III.19. At the extreme end of temperature-related departures the lower level exclusively resides close to or at the ground

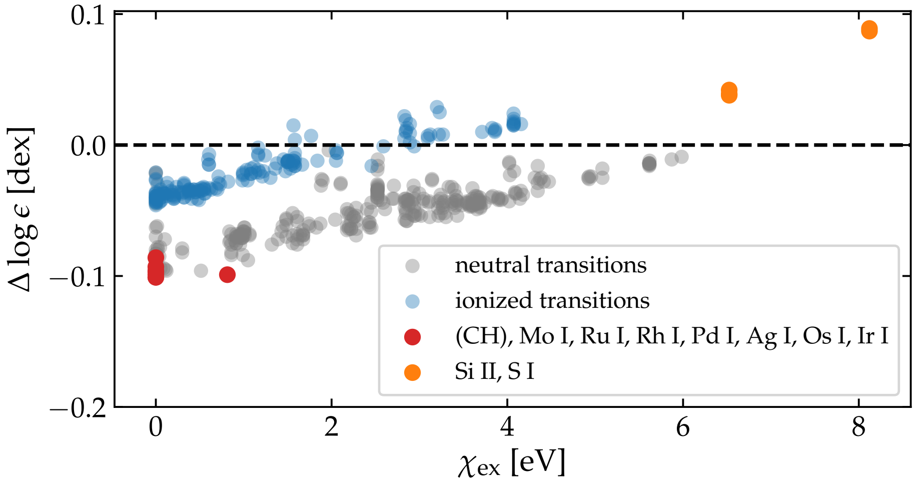

FIGURE III.19: Individual abundance changes from lowering the model $T_{\rm eff}$ by 50 K. Features from neutral species are shown in gray, whereas blue circles indicate ionized species. Highlighted in red and orange are the elements explicitly mentioned in the text. The manifold of CH lines used for synthesis and hence determination of the C abundance are not shown here. Their $\chi_{\rm ex}$ commonly resides around 0 eV.

level. In that regime, the occupation is largely independent of temperature and the $T_{\rm eff}$ affects exclusively the H^{-} continuous opacity with its strong temperature gradient. This leads to a strengthening of lines and, in turn, lower abundances at fixed line strengths. With increasing $\chi_{\rm ex}$ the occupation becomes susceptible to the $T_{\rm eff}$ change and increasingly counteracts the effect of the lower H^{-} opacity. Hence, the abundance departures are reduced. For the high-$\chi_{\rm ex}$ lines, the impact of the change in level occupation exceeds the opacity effect, which leads to the inverse temperature dependence seen in Figure III.19.

Variations in the stellar surface gravity have their strongest effect on abundances of ionized species, although the overall magnitude remains low at $\sim \pm 0.01$ dex. This can be understood in terms of gravity having a direct impact on the electron pressure which, in turn, determines the degree of ionization (Saha; Equation I.21). Here our O I and S I transitions behave as if they were ionized.

Deviations from changing $v_{\rm mic}$ exceed the 0.03 dex level in the mean abundances only for K I, Co I, Ba II, Eu II, and Yb II. The effect is limited to these species, as they show moderately strong lines with EWs of more than 80 mÅ and effects from microturbulence are limited to the higher line strength regime.

7 Results and Discussion

7.1 Light elements (Z $\leq$ 8)

Our Li, C, and N abundances show evidence of a pattern that is commonly attributed to internal mixing occuring when a star reaches the RGB bump where processed material from the H-burning shell gets dredged up to the convective layer. Observationally, the effect can be seen in the stellar surface abundances of bright giants (brighter than the RGB-bump at $\log L/L_\odot \sim 1.8$; e.g., Gratton et al. 2000) and horizontal branch stars that show non-detections of Li and depletions of [C/Fe] in lockstep with low ^{12}C/^{13}C ratios and enhancements in [N/Fe]. Indeed, for HD 20 we could not detect Li and found [C/Fe] $= -0.38$ dex, a value that is representative for the samples of mixed stars by Gratton et al. (2000) and Spite et al. (2006). On the other hand, as can be seen in Figure III.20, the marginal enhancement in [N/Fe] (0.18 ± 0.11 dex) and as a consequence the comparatively high [C/N] (-0.56 dex) render HD 20 at rather extreme positions among the mixed populations. A further puzzling observation is the strong O overabundance of [O/Fe] $= 0.70$ dex that places HD 20 slightly below the general trend of [N/O] with [O/H] by Spite et al. (2005) that appears generic for mixed stars (lower panel of Figure III.20). We lack a suitable explanation for a mechanism that could produce such large O excesses. Deep mixing with O-N cycle material can be ruled out as origin, as the O-N cycle would produce N at the expense of O and therefore show depletions – which is exactly the opposite of the observed O enhancement.

7.2 HD 20's evolutionary state

Earlier works on HD 20 assumed it to be a red horizontal branch star (e.g., Gratton et al. 2000; Carney et al. 2003). Given our newly derived set of fundamental parameters, we can neither reject nor confirm this hypothesis. In Figure III.21, we illustrate HD 20's position in the space of the structural parameters T_{eff}, $\log L/L_\odot$, and $\log g$ together with an isochrone from the Dartmouth Stellar Evolution Database (Dotter et al. 2008). The model parameters were selected to resemble the findings in the present work, that is, an age of 11 Gyr (Section 7.6), [Fe/H] $= -1.60$ dex, as well as [α/Fe] $= 0.40$ dex (Section 7.3). The impacts from uncertainties in the two input parameters that affect the isochrone most – the stellar age and [Fe/H] – are indicated by representative error margins. While we adopted a standard scaling for the He mass fraction ($Y = 0.245 + 1.5 \cdot Z$) for the latter model, we furthermore show the case

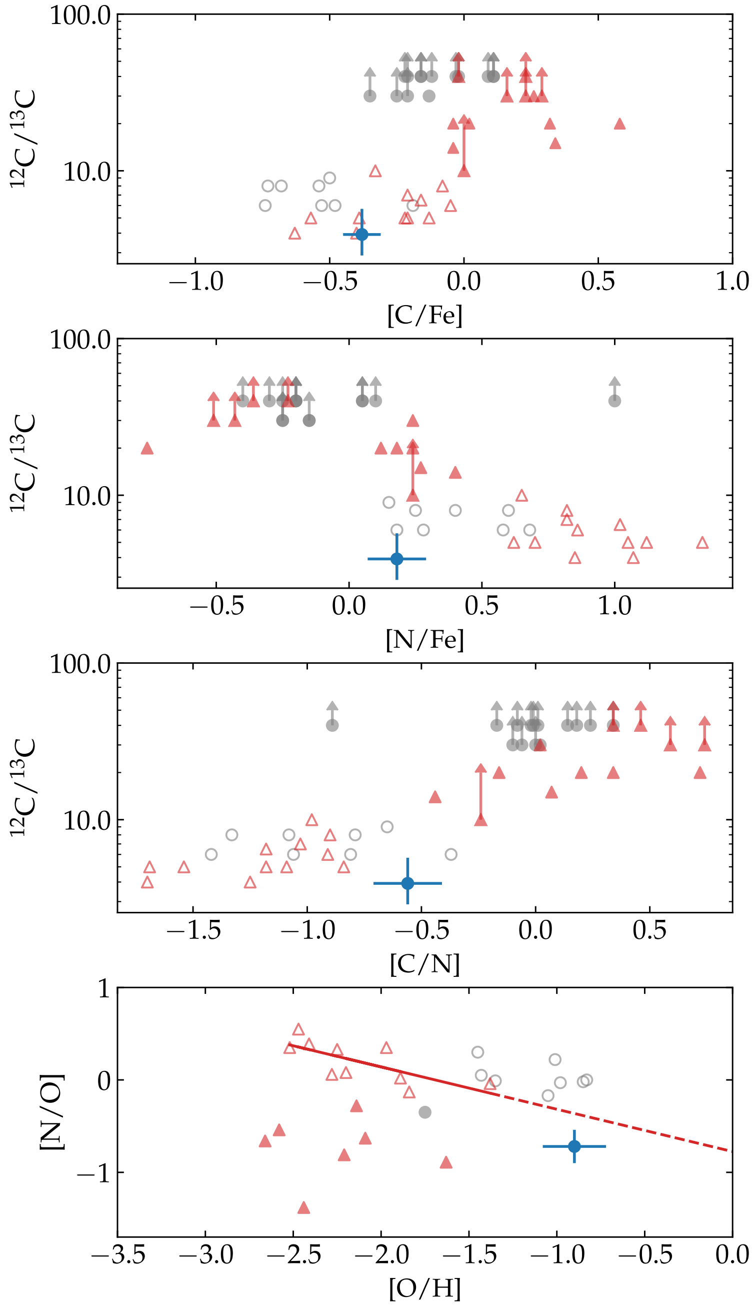

FIGURE III.20: Comparison of CNO elemental abundances of mixed and unmixed stars with HD 20, which is shown in blue for comparison. Gray circles resemble the study by Gratton et al. (2000) while red triangles indicate the stars published in Spite et al. (2005, 2006). Two C-rich stars were excluded from the latter sample. Lower limits on $^{12}C/^{13}C$ are indicated by upward pointing arrows and the classification into mixed and unmixed stars according to the authors are represented by open and filled symbols, respectively. The red line in the *lower panel* mimics the linear relation between [N/O] and [O/H] for mixed stars as reported by Spite et al. (2005), whereas the dashed line extrapolates the same relation to higher values of [O/H].

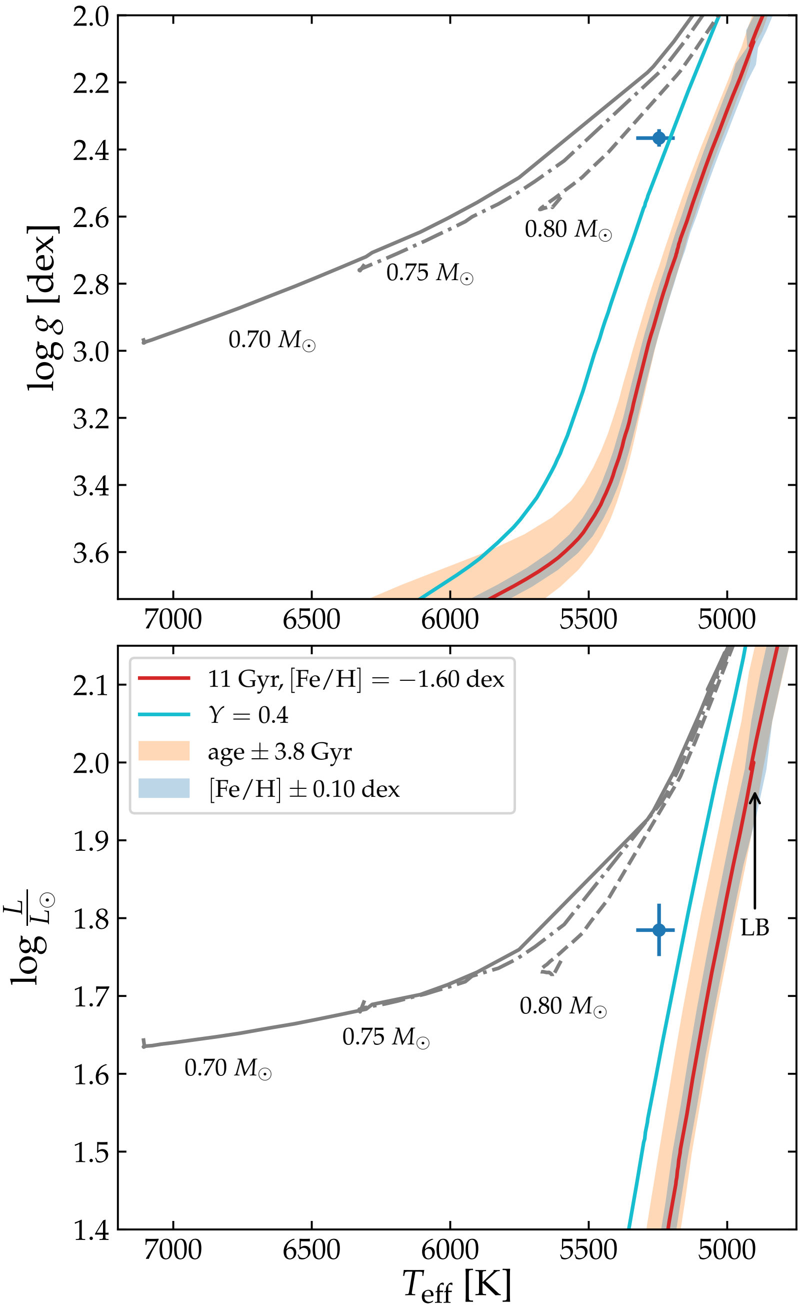

FIGURE III.21: Kiel diagram (*upper panel*) and Hertzsprung-Russell diagram (*lower panel*) with isochrones and helium burning tracks. HD 20's position is depicted by a blue filled circle with error bars. In the *upper panel* the error on the gravity is smaller than the circle size. The red line represents a He-normal 11 Gyr isochrone at [Fe/H] = −1.60 dex, and [α/Fe] = +0.4 dex with age and metallicity error margins shown by orange and blue ranges. The RGB luminosity bump for this particular model at $\log L/L_\odot \sim 2.0$ is highlighted in the *lower panel* by an arrow and the label "LB". The light blue curve is a model with the same parameters except for $Y = 0.4$. He-burning tracks for three different masses are shown by gray lines of different line styles with the stellar masses being indicated next to the respective tracks.

of an extreme He enhancement of $Y = 0.4$. In addition, a set of He-burning tracks for three different stellar masses (0.70, 0.85, and $0.9 M_\odot$) from the Dartmouth database are depicted in the same plot.

Given its luminosity and gravity ($\log L/L_\odot = 1.78$ and $\log g = 2.366$), HD 20 appears too warm for a $\sim$ 11 Gyr old classical red giant, though the implied mass from the isochrone of $0.84 M_\odot$ resides within one standard deviation of our mass estimate ($0.76 \pm 0.08 M_\odot$). On the other hand, taking our asteroseismic mass and L for granted, HD 20 would be between 250 K and 350 K too cool to be consistent with the models for the horizontal branch, depending on whether a one-sigma or spot-on agreement is desired. This appears unfeasible even for slightly warmer photometric temperature scales (Section 4.1.3). Still, the circumstance that sets our star as significantly fainter than the luminosity bump of the presented isochrone at $\log L/L_\odot \sim 2.0$ while nonetheless exhibiting mixing signatures (see the previous section) points towards a scenario where HD 20 has already evolved all the way through the red giant phase and is, in fact, now a horizontal branch star.

An alternative hypothesis for explaining HD 20's position in the Hertzsprung-Russell diagram would be a non-standard He content as the model with strongly increased Y poses a considerably better fit to the observations. Such extreme levels of He have been found for second-generation stars in the most massive globular clusters (Milone et al. 2018; Zennaro et al. 2019). Nevertheless, characteristic chemical signatures of these peculiar stars are strong enhancements in light elements such as N, Na, and Al in lockstep with depletions of O and Mg (e.g., Bastian & Lardo 2018); none of which were found here (see Sections 7.1 and 7.3). As a consequence, it is unlikely that HD 20 is a classical red giant star with high Y.

Unfortunately, our TESS light curve of HD 20 cannot be used to analyze the period spacing of the $l = 1$ mixed gravity and pressure modes to distinguish between helium-burning and non-helium-burning evolutionary stages as described by, for instance, Bedding et al. (2011) and Mosser et al. (2012b). To achieve this, a much longer time baseline than the available 27 days would be required in order to allow for a finer scanning of the frequencies around $f_{\max}$ and the identification of subordinate peaks in the power spectrum.

7.3 Abundances up to Zn ($11 \leq Z \leq 30$)

We could deduce abundances for 22 species of 17 chemical elements in the range $8 \leq Z \leq 30$. For the α-elements Mg, Si, S, Ca, and Ti, we report a mean enhancement of $[\alpha/\mathrm{Fe}] = 0.45$ dex in LTE, which is in disagreement with the finding by

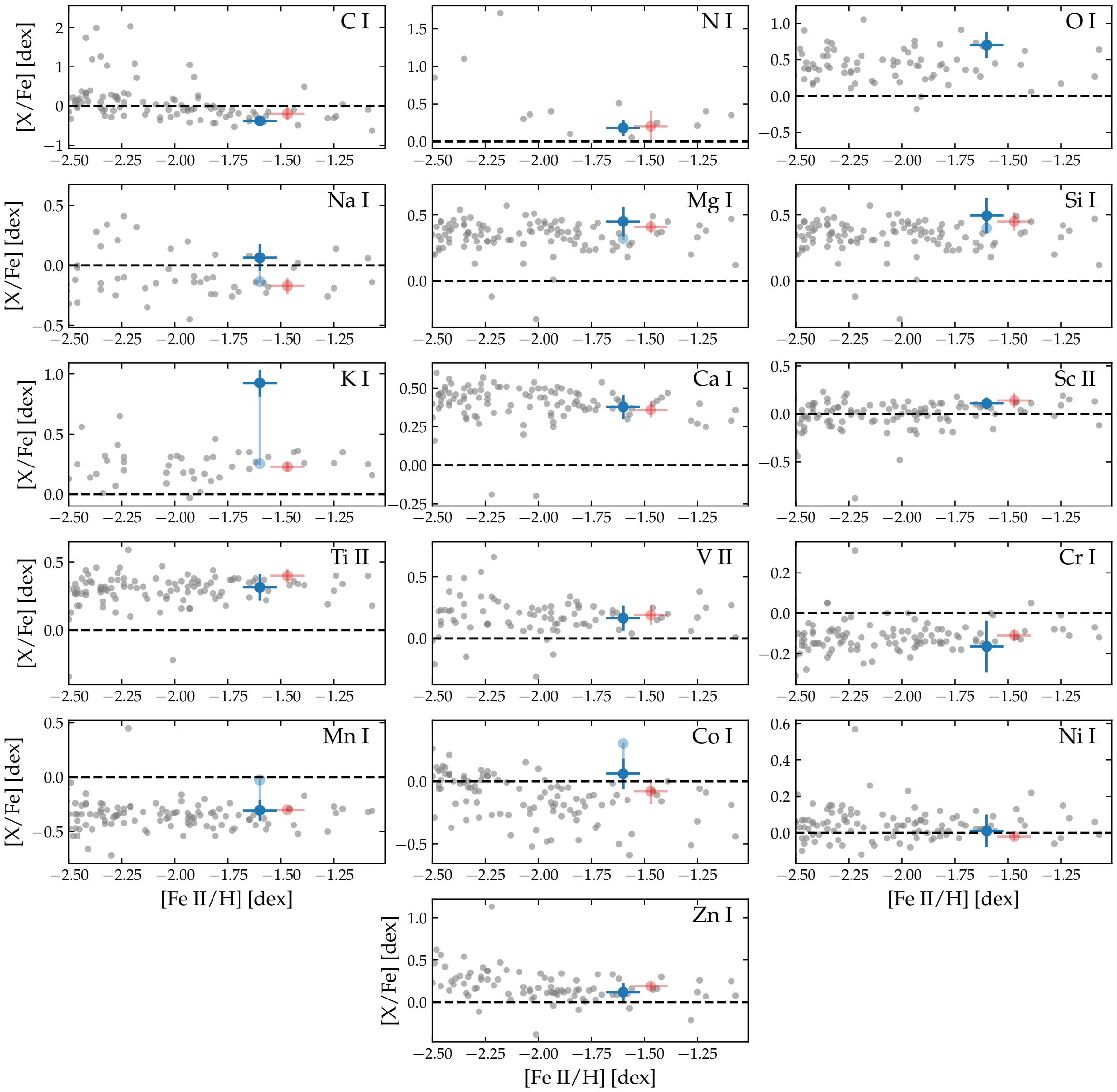

FIGURE III.22: Comparison of HD 20 (blue circle) to the metal-poor field star compilation (gray dots) by Roederer et al. (2014) and the red horizontal branch star HD 222925 (Roederer et al. 2018b, red circle). Dark blue circles and error bars indicate the result in LTE while the light blue circles indicate the NLTE-corrected ones. In the reference samples, corrections have been applied to O I, Na I, and K I. On the abscissa we show abundances from Fe II since these are less prone to departures from the LTE assumption (Section 3.3).

Barklem et al. (2005), where a conversion to the Asplund et al. (2009) scale yields $\frac{1}{3}[(\mathrm{Mg}+\mathrm{Ti}+\mathrm{Ca})/\mathrm{Fe}] \approx 0.23$ dex. The discrepancy is alleviated when using the same elements for comparison, that is, $\frac{1}{3}[(\mathrm{Mg}+\mathrm{Ti\,I}+\mathrm{Ca})/\mathrm{Fe}] = 0.34 \pm 0.13$ dex or $\frac{1}{3}[(\mathrm{Mg}+\mathrm{Ti\,II}+\mathrm{Ca})/\mathrm{Fe}] = 0.38 \pm 0.07$ dex. In light of Section 6.2, the origin for the observed difference is likely to be tied to their substantially hotter T_{eff} (see discussion in Section 4.1.3). Our value is typical for MW field stars at this [Fe/H] where nucleosynthetic processes in massive stars have played a dominant role in the enrichment

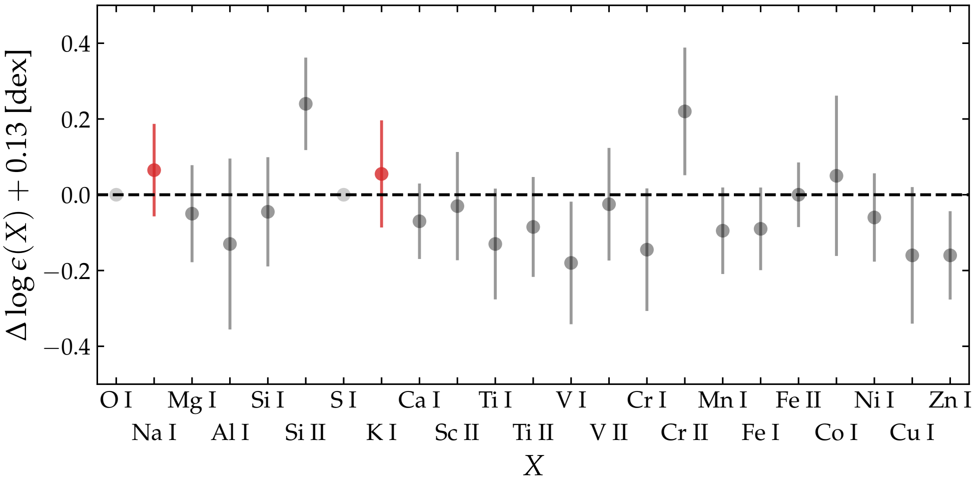

FIGURE III.23: Residual abundance pattern from O to Zn between HD 20 and HD 222925 after scaling by the difference in $\log \epsilon(\text{Fe II})$ of 0.13 dex. NLTE abundances were used for both stars for Na I and K I (red filled circles).

of the ISM and supernovae of type Ia (mostly Fe-peak yields) have not yet started to contribute (e.g., McWilliam 1997). A minimum χ^2 fit to the SN yields from Heger & Woosley (2010) using `StarFit`[14] (see Placco et al. 2016; Chan & Heger 2017; Fraser et al. 2017, for detailed discussions) shows that the lighter elements of HD 20 – in NLTE – can be well reproduced by a star of mass $\sim 11.6 M_\odot$ that undergoes a faint CCSN with an explosion energy of $0.6 \cdot 10^{51}$ erg. We stress that at HD 20's metallicity we are likely not dealing with a single SN enrichment. Nevertheless, we are looking for a dominant contribution, which might survive even if it is highly integrated over time.

Overall, we find an excellent agreement of the deduced abundances with the field population at similar metallicities as demonstrated in Figure III.22, where our findings are overlayed on top of the sample of metal-poor stars by Roederer et al. (2014). For elements with two available species we only present one representative. There are only two departures from the general trends: O and Co, which both are enhanced in comparison. However, as already noted in Roederer et al. (2014), the reference sample shows trends with stellar parameters – most notably T_{eff} – and thus evolutionary state. For elements heavier than N, mixing (Section 7.1) cannot be responsible for these trends, hence indicating contributions from systematic error sources in the abundance analyses. We therefore compare HD 20 to HD 222925, a star that was recently studied in great detail by Roederer et al. (2018b) and found to occupy a similar parameter space ($T_{\text{eff}} = 5636$ K, $\log g = 2.54$ dex, and $[\text{Fe}/\text{H}] = -1.47$ dex). Its light-element abundances are also indicated in Figure III.22 and we present

---

[14] `http://starfit.org/`

a differential comparison in Figure III.23. After correcting for the difference in metallicity (0.13 dex), we find a remarkable match between the two stars in the considered range (reduced χ^2 of 0.49). Similarities between the two stars have already been reported in the literature from a kinematical point of view (Roederer et al. 2018a) and based on their metallicity (Barklem et al. 2005; Roederer et al. 2018b). We emphasize, however, that the similarities do not extend to the neutron-capture regime, since HD 222925 is an r-II and HD 20 an r-I star with possible s-process contamination, as outlined in the following section.

7.4 Neutron-capture elements (Z > 30)

In order to delineate the nucleosynthetic processes that contributed to the observed abundances of heavy elements ($Z > 30$) in HD 20, we compare to a set of observed and predicted patterns. Following the classification scheme by Beers & Christlieb (2005), our findings of $[\mathrm{Eu}/\mathrm{Fe}] = +0.73$ dex and $[\mathrm{Ba}/\mathrm{Eu}] = -0.38$ dex place HD 20 in the regime of a typical r-I star. As indicated by the comparison in the top and middle panels of Figure III.24, HD 20's heavy-element pattern from Nd to Ir ($60 \leq Z \leq 77$) is consistent with the scaled solar r-process by Sneden et al. (2008) when considering observational errors. In the light neutron-capture regime from Sr to Ag ($38 \leq Z \leq 47$), however, the agreement is poor. This behavior is archetypal for r-process rich stars (e.g., Roederer et al. 2018b) and led to the postulation of the existence of an additional, low-metallicity primary production channel of yet to be identified origin (the so-called weak r or lighter element primary process, McWilliam 1998; Travaglio et al. 2004; Hansen et al. 2012, 2014).

In Figure III.24, we conduct a further comparison with the well-studied benchmark r-II and r-I stars CS 22892-052 (Sneden et al. 2003) and BD +17 3248 (Cowan et al. 2002, 2005; Roederer et al. 2010). The latter is a red horizontal branch star that is reasonably close to HD 20 in stellar parameter space ($T_{\mathrm{eff}} = 5200$ K, $\log g = 1.80$ dex, $[\mathrm{M}/\mathrm{H}] = -2.0$ dex, $v_{\mathrm{mic}} = 1.9$ km s^{-1}) – a circumstance that effectively reduces the impact of systematics (e.g., due to NLTE effects, see also Section 6.2) on differential comparisons. In our analyses, we omitted the Lu abundance for BD +17 3248 from the UV Lu II line reported by Roederer et al. (2010), because – regardless of the substantial quoted error of 0.3 dex – it appears to represent a strong, likely unphysical outlier. We stress that neither of the abundance patterns attributed to the two stars is necessarily a tracer of a pure nuclear process. In contrast, they are likely to represent integrated signatures with different contributions from both the main and weak primary r-components (cf., Li et al. 2013; Hansen et al. 2014). The abundances in the range of $38 \leq Z \leq 90$ for the two reference stars were scaled such that the

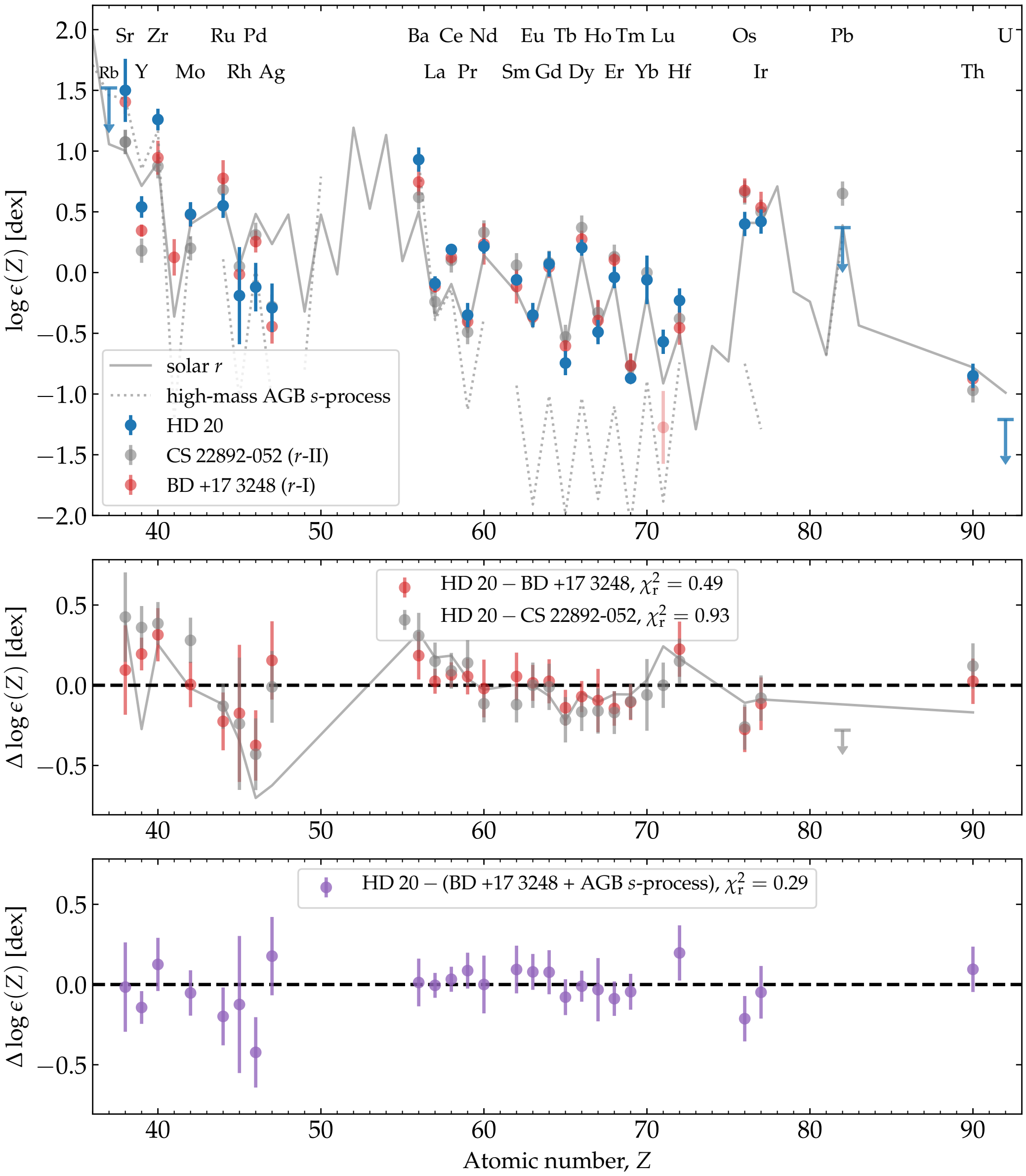

FIGURE III.24: Neutron-capture abundance pattern in LTE. *Upper panel*: HD 20's heavy element abundances are indicated in blue. Shown in gray and red are abundances of the *r*-II star CS 22892-052 by Sneden et al. (2003) and the *r*-I star BD +17 3248 by Cowan et al. (2002) with updates from Cowan et al. (2005) and Roederer et al. (2010). The omitted Lu abundance for BD +17 3248 (see main text) is depicted in light red. Both patterns were scaled to achieve the overall best match to HD 20 in the entire considered range. The gray solid line denotes the solar-scaled *r* pattern from Sneden et al. (2008) and the best-fit AGB model (see text) is represented by dotted lines. *Middle panel*: residual pattern between HD 20 and the solar *r* pattern (gray line), CS 22892-052 (gray), and BD +17 3248 (red). *Lower panel*: Residual pattern after mixing a contribution from BD +17 3248 with *s*-process material from the AGB yield model.

reduced sum of the normalized quadratic deviations, χ^2_r, was minimized (see middle panel of Figure III.24). Both patterns reproduce the depression of Y between Sr and Zr ([Y/<(Sr,Zr)>] $= -0.33$ dex) and the deviation of Ag from the solar *r*-process.

This points towards an enrichment contribution to HD 20 by the weak r-process as postulated earlier.

Nevertheless, the overall residual abundances from Sr to Zr as well as from Ba to Pr appear enhanced with respect to the heavy r-nuclei ($Z \geq 60$). Another particularly outstanding residual feature is a statistically significant downward trend from Ba to Yb, which seems slightly less pronounced in the comparison involving BD +17 3248. In Solar system material, the lighter elements in question have dominant contributions from the s-process (Bisterzo et al. 2014; Prantzos et al. 2019), leading to the intriguing conclusion that, despite its moderately low metallicity, HD 20's natal cloud might have been polluted with s-process material. In order to test this hypothesis, we mixed the pattern of BD +17 3248 as proxy for an integrated r-process pattern with main s-process yield models for thermally pulsing AGB stars with a standard ^{13}C pocket from the FUll-Network Repository of Updated Isotopic Tables & Yields (F.R.U.I.T.Y. Cristallo et al. 2011). An upper metallicity limit was placed at $[\mathrm{Fe/H}] = -1.6$ ($Z = 0.0003$), since it is infeasible for AGB polluters to have had higher [Fe/H] than HD 20 itself. We retrieved models for all remaining metallicities, stellar masses, and rotational velocities available through F.R.U.I.T.Y.. In addition, a set of newly computed models with initial rotational speeds of 30 and 60 km s^{-1} for stellar masses of 2 and $5M_\odot$ was included.

In the past, rotation has been considered as a potential process able to reproduce the observed spread in s-process elements at various metallicities (see Piersanti et al. 2013, and references therein). However, depending on the adopted physical prescriptions, different results have been obtained (see, e.g., Langer et al. 1999; Siess et al. 2004; den Hartogh et al. 2019). Moreover, it has to be taken into account that recent asteroseismic measurements of low-mass stars in the Galactic disk (see, e.g., Mosser et al. 2012a) demonstrated that stars belonging to the red clump region are characterized by slowly rotating cores. This latter feature tends to exclude the possibility to have fast-rotating cores for low-mass AGB stars in the solar neighborhood (which is an essential condition in order to have sizeable effects lead by rotation-induced mixing). However, the same has not yet been confirmed for stars with larger masses ($M > 3M_\odot$) and/or at low metallicities ($[\mathrm{Fe/H}] < -1$ dex).

The optimal mixture of integrated r- and main s-contributions to the overall neutron-capture budget of HD 20 was obtained by minimizing the expression

$$\chi^2 = \sum_i (\log(a \cdot \epsilon_{r,i} + b \cdot \epsilon_{s,i}) - \log \epsilon_{\mathrm{HD20,i}})^2 / \sigma_i^2, \tag{III.9}$$

with a and b being the weight coefficients for the two r and s template patterns

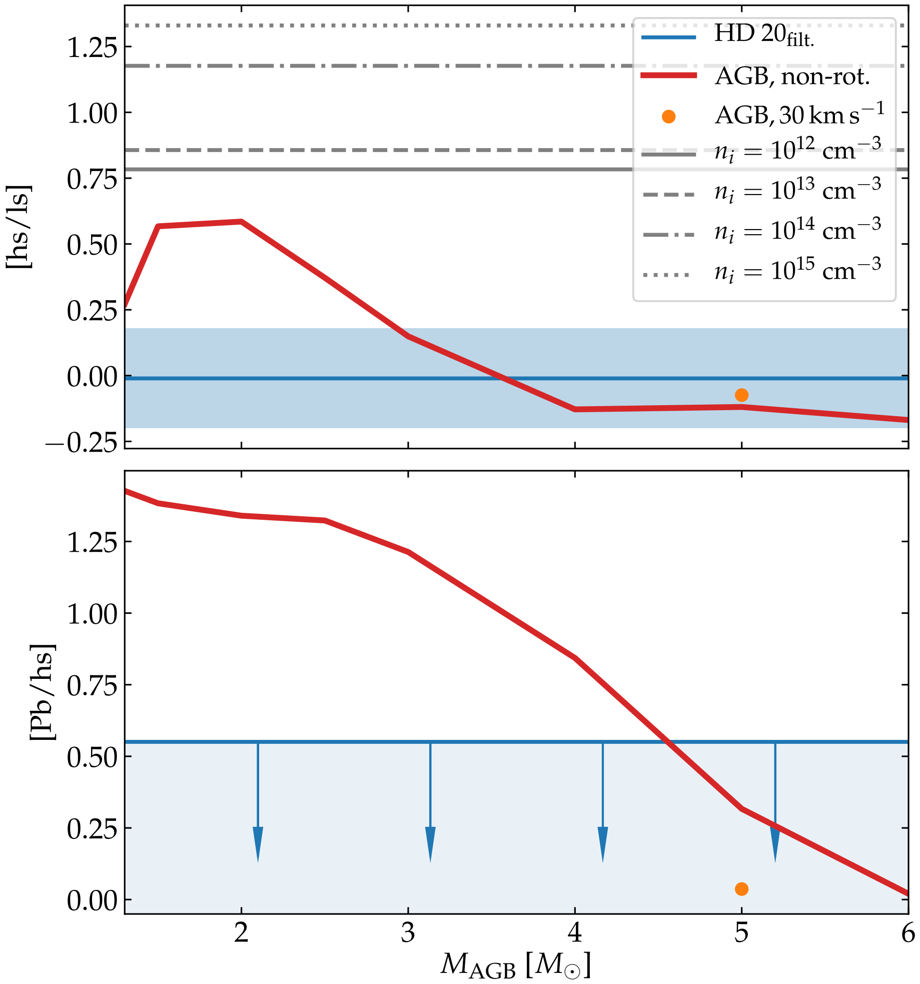

FIGURE III.25: Comparison of [hs/ls] and upper limit on [Pb/hs] for HD 20 against AGB *s*-process models of different initial masses. The value determined for HD 20 is indicated by blue horizontal lines and error margins, while models of $Z = 0.0001$ without rotation are shown in red. The adopted best-fit model with a rotation of 30 km s^{-1} is depicted in orange. For juxtaposition, we show *i*-process predictions for [hs/ls] from Hampel et al. (2016) for four different neutron densities, n_i, in the *upper panel* using black dotted, dash-dotted, dashed, and solid lines (see legend).

and the index i denoting those individual elements in the range $38 \leq Z \leq 90$ with available entries for the HD 20 pattern, the BD +17 3248 pattern, and the AGB yield tables.

A decisive observational quantity for pinpointing the AGB model mass is the ratio [hs/ls] of mean abundances for the heavy-*s* (hs, represented by Ba, La, and Ce) and light-*s* (ls, represented by Sr, Y, and Zr) elements. The models predict supersolar [hs/ls] at low masses ($\lesssim 3M_\odot$) with a decreasing trend with increasing model mass. Close-to Solar ratios are found in the region between $3M_\odot$ and $5M_\odot$. This behavior is demonstrated in Figure III.25, where we also indicate the Solar [hs/ls] measured

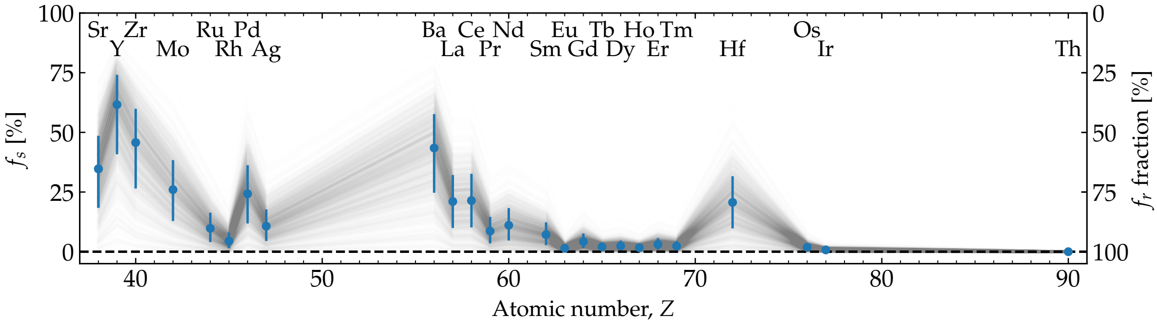

FIGURE III.26: Estimated r (*right-hand scale*) and s fractions (*left-hand scale*) in HD 20 based on Equation III.10 with BD +17 3248 as proxy for an r pattern and the best-fit AGB model representing the s-enrichment site. Shown are only those elements that have a measured abundance in BD +17 3248.

for HD 20 (0.00 dex[15]). We conclude that main s-process contributions are likely to originate from high-mass ($> 3M_\odot$) AGB stars. This is bolstered by only being able to deduce an upper limit for HD 20's Pb abundance – an element that is predicted to have strong contributions from models with masses $< 5M_\odot$ (e.g., Bisterzo et al. 2012; Cristallo et al. 2015). The large contribution to Pb comes from the radiative burning of the ^{13}C(α,n)^{16}O reaction (see Straniero et al. 1995), which is the dominant source in low-mass AGB stars. On the other hand, in more massive AGBs major neutron bursts come from the ^{22}Ne(α,n)^{25}Mg reaction, which is efficiently activated at the bottom of the convective shells during thermal pulses. These episodes commonly lead to minor Pb production[16]. At the same time, it is expected to find large Rb excesses from these massive AGB stars and their ^{22}Ne(α,n)^{25}Mg neutron source, manifesting in, for example, supersolar [Rb/Zr] (García-Hernández et al. 2009; Pérez-Mesa et al. 2017). For HD 20, we found $[\text{Rb}/\text{Zr}] < 0.55$ dex from the upper limit on the Rb abundance and after filtering our Zr finding from its dominant r-process contribution (see later in this section). This upper limit is $\sim$ 0.2 dex higher than the largest predictions from our employed, massive (i.e., 4-5$M_\odot$) AGB models. A robust measurement of Rb could be used to place further constraints on the exact initial mass of the polluting AGB star. In order to achieve this, spectra with an even higher S/N in the region around 7800 Å are required.

By minimizing Equation III.9, we found the best-fit ($\chi^2_\mathrm{r} = 0.29$) AGB model to be the one with $5M_\odot$, $Z = 0.0001$ ($[\text{Fe}/\text{H}] \approx -2.15$ dex), and a rotational velocity of 30 km s^{-1}. Here the model with non-zero angular momentum poses a slightly better fit than its non-rotating counterpart with all other parameters kept fixed (see also Figure III.25, top panel). The adopted mixture can successfully reproduce the entire

---

[15] Here we mention a ratio that was filtered for the r-process contribution (see later in this section) as compared to the unfiltered value of 0.18 dex.

[16] Telling the whole truth, also massive AGBs can produce large amounts of Pb, but this occurs at very low metallicities only (i.e., $[\text{Fe}/\text{H}] < -2$ dex).

TABLE III.7: Estimated fractional contributions from the r- and s-process for elements with $Z \geq 38$ in HD 20.

Z	Element	f_r [%]	f_s [%]	Z	Element	f_r [%]	f_s [%]
38	Sr	$67.0^{+15.6}_{-15.7}$	$33.0^{+15.7}_{-15.6}$	62	Sm	$93.4^{+3.7}_{-5.4}$	$6.6^{+5.4}_{-3.7}$
39	Y	$40.2^{+21.0}_{-14.4}$	$59.8^{+14.4}_{-21.0}$	63	Eu	$98.7^{+0.7}_{-1.2}$	$1.3^{+1.2}_{-0.7}$
40	Zr	$56.2^{+18.9}_{-16.3}$	$43.8^{+16.3}_{-18.9}$	64	Gd	$96.1^{+2.2}_{-3.4}$	$3.9^{+3.4}_{-2.2}$
42	Mo	$75.5^{+12.4}_{-14.0}$	$24.5^{+14.0}_{-12.4}$	65	Tb	$98.1^{+1.1}_{-1.7}$	$1.9^{+1.7}_{-1.1}$
44	Ru	$90.9^{+5.0}_{-7.1}$	$9.1^{+7.1}_{-5.0}$	66	Dy	$97.8^{+1.3}_{-2.0}$	$2.2^{+2.0}_{-1.3}$
45	Rh	$95.8^{+2.3}_{-3.6}$	$4.2^{+3.6}_{-2.3}$	67	Ho	$98.5^{+0.9}_{-1.4}$	$1.5^{+1.4}_{-0.9}$
46	Pd	$77.1^{+11.6}_{-13.5}$	$22.9^{+13.5}_{-11.6}$	68	Er	$97.2^{+1.6}_{-2.5}$	$2.8^{+2.5}_{-1.6}$
47	Ag	$90.0^{+5.5}_{-7.6}$	$10.0^{+7.6}_{-5.5}$	69	Tm	$97.8^{+1.2}_{-1.9}$	$2.2^{+1.9}_{-1.2}$
56	Ba	$58.4^{+18.3}_{-16.3}$	$41.6^{+16.3}_{-18.3}$	72	Hf	$80.6^{+10.1}_{-12.3}$	$19.4^{+12.3}_{-10.1}$
57	La	$80.2^{+10.3}_{-12.5}$	$19.8^{+12.5}_{-10.3}$	76	Os	$98.3^{+1.0}_{-1.5}$	$1.7^{+1.5}_{-1.0}$
58	Ce	$79.8^{+10.4}_{-12.6}$	$20.2^{+12.6}_{-10.4}$	77	Ir	$99.3^{+0.4}_{-0.6}$	$0.7^{+0.6}_{-0.4}$
59	Pr	$92.0^{+4.4}_{-6.4}$	$8.0^{+6.4}_{-4.4}$	90	Th	$100.0^{+0.0}_{-0.0}$	$0.0^{+0.0}_{-0.0}$
60	Nd	$89.7^{+5.7}_{-7.9}$	$10.3^{+7.9}_{-5.7}$				

neutron-capture pattern in HD 20. This includes the observations for the commonly employed tracers [hs/ls] and [Ba/Eu], as well as the downward trend from Ba to Yb that persists when assuming an r-only enrichment.

Using yields from the aforementioned s-process model and the BD +17 3248 pattern together with the best-fit model parameters for Equation III.9, we can estimate the fractional (integrated) r- and s-process contributions to individual elements in HD 20 through

$$f_{r,i} = \frac{a \cdot \epsilon_{r,i}}{a \cdot \epsilon_{r,i} + b \cdot \epsilon_{s,i}}; \quad f_{s,i} = 1 - f_{r,i}. \tag{III.10}$$

In order to properly account for fit uncertainties, we sampled the posterior distribution of the parameters a and b with `emcee` using the abundance errors. In Figure III.26 we show 800 individual realizations of the samples. From these, the fractions and asymmetric limits were estimated from the median, the 15.9th, and the 84.1th percentiles, respectively. These are listed in Table III.7. We find significant s-process fractions above 30% for the elements Sr, Y, Zr, and Ba, whereas only Y might have had a dominant ($f_s > 50\%$) enrichment contribution from the s-process. This could be corroborated by measuring isotopic fractions for selected elements from spectra at very high resolution (e.g., Mashonkina & Belyaev 2019), though we note that HD 20 shows considerable intrinsic line broadening signatures (Section 3.5) that may exceed the hyperfine splitting effect.

An important question that should be answered with respect to our proposed *s*-process imprint is whether the finding is caused by mixing in the ISM prior to the formation of HD 20 or whether it is a result of surface pollution via mass transfer in a binary system (e.g., Gull et al. 2018). The latter option was ruled out with high confidence in Section 2.2, where we showed a lack of radial velocity variation. Therefore, a binary signal could only be hidden if the orbit would be seen almost perfectly face-on. Consequently, we strongly prefer the scenario where HD 20 had its chemical pattern composition mixed in the ISM.

7.5 *i*-process considerations

Another metal-poor star with signatures of simultaneous overabundances in both *s*- and *r*-process material is HD 94028. Among others, this star has been studied spectroscopically by Roederer (2012) and Roederer et al. (2016), who complemented the abundance pattern from elements typically found in the optical with more exotic species (e.g., Ge, As, Se) that are only measurable in ultraviolet spectra gathered with the *Hubble* Space Telescope (HST). The authors concluded that several abundance ratios – most notably supersolar [As/Ge], [Mo/Fe], and [Ru/Fe] – are poorly described by combinations of *s*- and *r*-process patterns and therefore suggested an additional contribution by the *i*-process. However, more recently, Han et al. (2018) indicated that both [As/Ge] and [Mo/Ru] may be well explained by weak *r*-nucleosynthesis without the need for an additional *i*-process. The *i*-process was also proposed by Koch et al. (2019) as a candidate to reproduce their observed pattern for a metal-poor bulge star (labeled #10464, following the naming convention in Koch et al. 2016). The authors find that either a mixture of an *i*-pattern with a main *s*-pattern or an *i*-process with two proton ingestion events reproduces their observations best.

Based on Figure III.25, the residual [hs/ls] of HD 20 is seen to be well described by a $5M_\odot$ rotating AGB star, while the *i*-process of intermediate neutron densities predicts much too high [hs/ls] ratios. In any case, we compare HD 20 to the two supposedly *i*-enriched stars to search for *i*-process indications in the patterns. By comparing to the filtered patterns of HD 94028 $-(r+s)$ and #10464 $-s$ (Figure III.27), no clear *i*-process features stand out, and we cannot claim any *i*-process contribution in HD 20. However, some weak *r*-enrichment might have taken place. Until further *i*-process indications, such as elemental ratios [As/Ge] or strong pattern trends can robustly be associated with the *i*-process, it is hard to observationally investigate such contaminations. In order to test [As/Ge] we would need HST data.

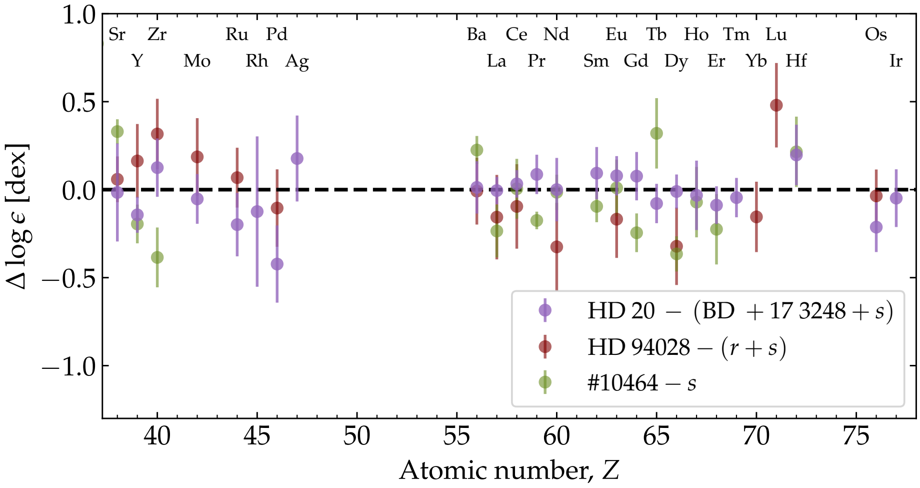

FIGURE III.27: Comparison of the residual HD 20 pattern (purple, same as *lower panel* of Figure III.24) to the patterns of HD 94028 (red) and #10464 (green) after subtracting $r + s$ and s contributions, respectively. The residual pattern for HD 94028 was determined following the procedure outlined in Section 5.2. in Roederer et al. (2016), whereas a $Z = 0.0001$, $2M_\odot$ AGB model was assumed for the s-enrichment in #10464.

TABLE III.8: Age estimates from different radioactive chronometers.

Ratio	$\log\epsilon(\mathrm{Th}/r)_0^{(a)}$ [dex]	$\log\epsilon(\mathrm{Th}/r)$ [dex]	Age [Gyr]
Th/Eu	−0.276	-0.50 ± 0.14	10.0 ± 6.5
Th/Hf	−0.063	-0.62 ± 0.14	26.0 ± 6.5
Th/Os	−1.009	-1.25 ± 0.14	11.3 ± 6.5
Th/Ir	−1.022	-1.27 ± 0.14	11.6 ± 6.5
Th/U	0.192	> 0.36	$> 7.8^{(b)}$

Notes. (a) Production ratios from method *"fit1"* in Table 2 of Kratz et al. (2007). (b) Calculated using equation (2) in Cayrel et al. (2001).

7.6 Cosmochronological age

Measuring a reliable abundance for the radioactive element Th enables an estimation of HD 20's age from nuclear cosmochronology. The only isotope of Th with a lifetime that is relevant on cosmological timescales is ^{232}Th ($\tau_{1/2} = 14.05$ Gyr). The currently observed ratio $\log\epsilon(\mathrm{Th}/r)$ of Th and other, stable r-elements can be related to a decay time using a theoretical initial production ratio, $\log\epsilon(\mathrm{Th}/r)_0$, together with the age relation,

$$\Delta t = 46.7\,\mathrm{Gyr} \cdot \left(\log\epsilon(\mathrm{Th}/r)_0 - \log\epsilon(\mathrm{Th}/r)\right), \tag{III.11}$$

as outlined by Cayrel et al. (2001). For Table III.8, we considered the reference elements Eu and Hf as well as the third-peak elements Os and Ir. Moreover, we obtained a lower-limit age of 7.8 Gyr from our upper limit on the U abundance. Despite considerable ambiguities in theoretical production ratios (e.g., Schatz et al. 2002; Cowan et al. 1999), the dominant source of error for the inferred ages is the combined uncertainty of the abundances for each pair, which amounts to $\sqrt{2} \cdot 0.1$ dex $= 0.14$ dex. The latter uncertainty is linearly propagated into an age error of 6.5 Gyr (see also Ludwig et al. 2010, for a detailed discussion of other error sources). According to Cayrel et al. (2001), the observational and theoretical uncertainties are minimized by using Os and Ir as baseline for the chronometers, since they are closest to Th in atomic number. However, we note that both Os and Ir were determined from the neutral species while our Th abundance was deduced from the singly ionized state, which potentially introduces biases due to NLTE effects[17]. As indicated by Hansen et al. (2018a), NLTE effects on Th II abundances may be alleviated by introducing a full, 3D NLTE treatment. Hence the obtained abundance would be close to our 1D LTE estimate.

The age of 26.0 Gyr from Th/Hf appears unreasonably high and we note that Roederer et al. (2009) reported a similar behavior for this chronometer. We thus suspect that the initial production rates are overestimated, which might be connected to a breakdown of the robustness of the heavy *r*-pattern in the region around Hf (M. Eichler, priv. comm.). Removing our estimated high *s*-process contribution (19.4%) for Hf only decreases the deduced age slightly, by about 4 Gyr. In any case, we exclude the corresponding age from consideration and calculate a mean age of 11.0 ± 3.8 Gyr from the remaining three actual detections (10.0, 11.3, and 11.6 Gyr, thereby excluding the lower limit involving U).

8 Summary and Conclusions

We present a detailed investigation of the chemical composition of the metal-poor ([Fe/H] $= -1.60$ dex), *r*-process enhanced (*r*-I) Galactic halo star HD 20. Using newly obtained and archival very high signal-to-noise and high-resolution spectra in concert with extensive photometry and astrometry from the *Gaia* and TESS missions, we carefully investigate the key fundamental stellar parameters, which are independently confirmed by a number of alternative approaches. These allow for a high-precision spectroscopic chemical analysis, yielding abundances for 25 species of

---

[17] Furthermore, as demonstrated in Section 6.2, among all relevant elements the two referred ones are most sensitive to uncertainties in the model temperature.

20 elements with $Z \leq 30$, as well as for 29 species of 28 neutron-capture elements. Hence, we report on abundances for in total 48 elements, thereby adding 26 elements to the largest existing study of this star by Barklem et al. (2005). Moreover, we deduce meaningful upper limits for Li, Rb, Pb, and U. Our presented abundance pattern is one of the most complete available to date and therefore establishes HD 20 amongst the short list of benchmark stars for nuclear astrophysics.

Regarding the light elements up to Zn, we find a behavior typical for the Galactic halo at comparable metallicities indicative of an enrichment history dominated by CCSNe prior to the onset of contributions by supernovae of type Ia. Using yield models, we could show that faint CCSNe of progenitor masses around $\sim 11.6 M_{\odot}$ and explosion energies $\sim 0.6 \cdot 10^{51}$ erg can explain the light-element pattern in HD 20. While the heavy neutron-capture elements are found to closely follow the solar *r*-process distribution, strong deviations are found with respect to the first-peak elements, primarily due to depletions in Y and Ag. We attribute this observation to the additional primary (weak) *r*-process acting at low metallicity that was postulated based on observations of other metal-poor stars (e.g., Hansen et al. 2012). This emphasizes that the Solar-scaled *r*-pattern cannot pose as a universal proxy for the *r*-process, particularly in the lighter neutron-capture regime.

In comparing our observed neutron-capture abundances to the benchmark *r*-I star BD +17 3248 – which was chosen in order to lessen the gravity of systematic abundance errors – we find that several elements (Sr, Y, Zr, Ba, La) that are commonly associated with the *s*-process appear to be enhanced in HD 20 with respect to a pure *r*-process pattern. We obtain a considerably better fit of the overall distribution by introducing a dilution with material from main *s*-process yield predictions of a low-metallicity, massive, and rotating AGB star. Based on this model, we estimate a dominant *s*-process fraction for Y ($59.8^{+14.4}_{-21.0}$%), whereas several other elements may still have a significant contribution from this production channel (Table III.7, Figure III.26). Given the abundance pattern for HD 20 presented here, we prefer an *r*+*s* mixing scenario and refute *i*-process contributions until more robust abundance ratios or patterns will be proposed. Based on the lack of evidence of HD 20 being part of a binary system, we propose that the mixing happened in the ISM prior to the star's formation as opposed to surface pollution due to mass transfer from a companion.

HD 20's age is estimated at 11.0 ± 3.8 Gyr based on nuclear cosmochronology from abundance ratios involving the radioactive element Th. We caution, however, that there are statistical and systematic error sources of both observational and theoretical nature that may bias this measure. Nonetheless, it appears safe to assume that the star is a representative of the old Galactic halo.

A future perspective for work on HD 20 is to complement our abundance pattern with UV spectra from HST. Deriving abundances from UV lines is extremely important in order to obtain more complete patterns. Key elements like As and Au carry important information on the neutron-capture environment and can only be assessed in HST data. Arsenic could contain crucial clues on the *i*-process, which we cannot explore in the ground-based, spectroscopically derived abundances, and Au is a good *r*-process indicator. An additional element that is more easily measured in the UV is Pb, which is an important *s*-process tracer for which we could only deduce an upper limit abundance in this study. Furthermore, understanding how and if the neutron-capture processes are formed and incorporated into later generations of stars is crucial to understand the need for an *i*-process versus efficient and fast mixing of *r*+*s*-process material in the ISM. Here HD 20 offers promising insights into the neutron-capture processes as it is slightly enhanced and we detect clear traces of both *r* and *s*.

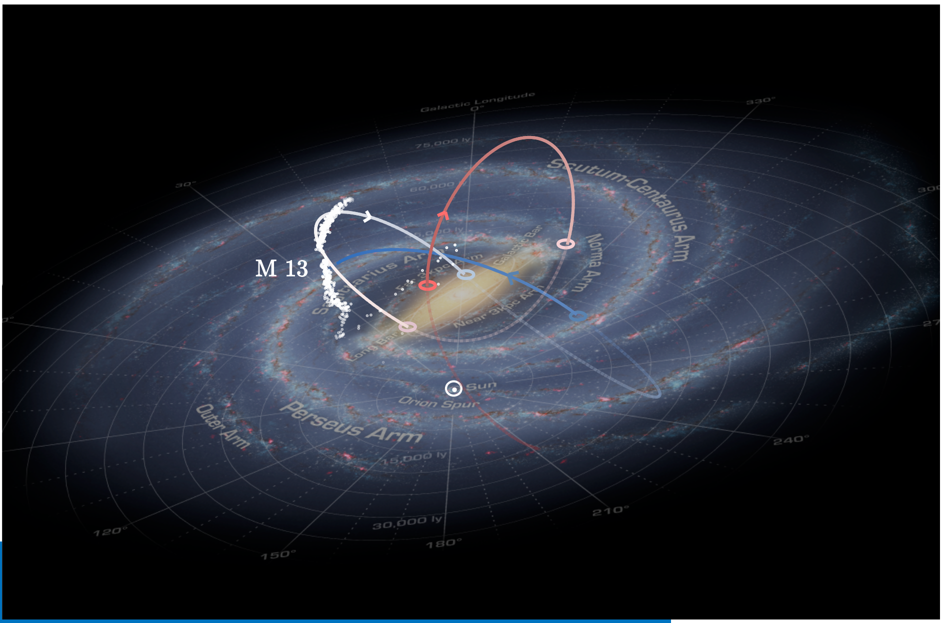

This image shows a 3D representation of the modeled orbit of the globular cluster M 13 both 200 Myr into the past (red colors) and into the future (blue colors). White dots indicate stars from simulated, dynamically cold tidal debris that is lost from the cluster to the Galactic halo. For orientation, an artist's impression of the Milky Way is shown in the background, whereas the location of the Sun is labeled "$\odot$". **Image credit.** The Milky Way Galaxy: NASA/JPL-Caltech/R. Hurt (SSC/Caltech). The original depiction of the Galaxy was rotated, tilted, and cropped.

CHAPTER IV

This chapter in brief

Chemodynamical association of halo stars with Milky Way globular clusters

In this chapter, we investigate chemodynamical links between globular cluster stellar populations and the Milky Way halo in order to further the knowledge about cluster contributions to the buildup of the halo. The chapter is organized as follows:

- In Section 2, we introduce the data sets employed throughout this work and discuss the involved statistical uncertainties and systematic errors.
- Next, in Section 3, the three employed tagging techniques are outlined.
- The associated findings and a discussion thereof is provided in Section 4.
- Finally, we summarize our main conclusions in Section 5.

The work this chapter is based on was accepted for publication in Astronomy & Astrophysics (Hanke et al. 2020b) and was co-authored by A. Koch, Z. Prudil, E. K. Grebel, and U. Bastian.

1 Context

Whether or not a sizable fraction of the Milky Way halo originated from disrupted globular clusters is a long-standing question that remains to be elucidated. One promising approach lies in chemical tagging of halo field stars that show unique chemical signatures in their light-element abundances that are otherwise only found in the enhanced stellar population (2P) of GCs (Sections I.2.4 and I.3.5). While the unenriched GC stars (1P) are chemically indistinguishable from the general field star population, discoveries of chemical fingerprints in the halo that are reminiscent of 2P stars are in strong favor of a GC origin.

A number of theoretical studies investigated aspects of GC formation and evolution by focusing on the amount of mass loss that eventually leads to a direct inference of the fraction of GC stars that contributed to the present-day observed stellar halo (D'Ercole et al. 2008; Bastian et al. 2013; Baumgardt & Sollima 2017; Reina-Campos et al. 2020). Such models ultimately have to be informed by observations of stars from both 1P and 2P, the latter of which can be unambiguously tied to GCs. In this respect, Martell & Grebel (2010) and Martell et al. (2011) used low-resolution spectra of the Sloan Extension for Galactic Understanding and Exploration (SEGUE-1 and SEGUE-2, Yanny et al. 2009; Eisenstein et al. 2011) as part of the SDSS (York et al. 2000) to identify 2P candidates in the halo from a combination of CN and CH bandstrengths in red giant branch stars. From their finding that 2.5% of their halo sample is CN-strong, these latter authors concluded that between 17% and 50% of the halo may have originated from GCs. Similar arguments hold for an identification of GC-like stars, enabled by the infrared APOGEE survey (Majewski et al. 2016), through their Mg and Al patterns as a product of hotter proton-burning cycles. Respective studies have been successfully carried out for the Galactic halo (Martell et al. 2016; Fernández-Trincado et al. 2019a,b), and others also detected N-enriched stars in the Milky Way bulge (Schiavon et al. 2017), hinting at a similarly (in-)effective formation channel of this old Galactic component.

Using the recent DR14 of SDSS-IV (Abolfathi et al. 2018) we doubled the number of known CN-strong stars by Martell & Grebel (2010) and Martell et al. (2011) to 118 (Koch et al. 2019, hereafter Paper I). From these, we estimated a fraction of 2.6 ± 0.2% 2P stars among all considered halo field giants, which led to a halo contribution from disrupted GCs of 11 ± 1%.

This project continues the publication series "Purveyors of fine halos", where we aim to explicitly tie halo field stars – both of enriched and unenriched nature – to a potential GC origin and to observationally test the fraction of bona fide 2P stars among the entire population of GC escapees. To this end, we combined radial velocities (v_r) and metallicities ([Fe/H]) from SDSS/SEGUE with *Gaia* DR2 astrometry to expand the previous chemical data used in Paper I into a seven-dimensional, chemodynamical information space (i.e., a three-component space vector, a three-component motion vector, and metallicty, [Fe/H]). This was achieved using three methods: First, we searched the immediate vicinity around GCs for extratidal stars that share the space motion and [Fe/H] of the clusters. Next, we used the conservation of action-angle coordinates to identify potential former host clusters for the sample of CN-strong stars from Paper I among the GCs that still exist in the MW. The third method is a modification of the first, and aims at finding stars that share the same portion of phase space as the CN-strong stars, which may indicate a common GC progenitor.

2 Data

For the present analysis, we employed the latest data release of SDSS (DR14, Abolfathi et al. 2018), which contains optical stellar spectra at low resolving power ($R \sim 2000$) that were obtained throughout the two phases of the SEGUE (Yanny et al. 2009; Eisenstein et al. 2011) survey and during the Extended Baryon Oscillation Spectroscopic Survey (eBOSS, Dawson et al. 2016). Of particular interest are the large samples of stellar metallicities and heliocentric radial velocities deduced using the SEGUE stellar parameter pipeline (`SSPP`, Allende Prieto et al. 2008; Lee et al. 2008a,b, 2011; Smolinski et al. 2011).

A large fraction of this study builds upon the compilation of CN-strong giants that were identified in Paper I. There, SDSS spectra of 4649 bona fide halo red giants in the metallicity regime $-1.8\,\mathrm{dex} < \mathrm{[Fe/H]} < -1.3\,\mathrm{dex}$ were examined for a combination of spectral indices involving carbonaceous molecules that are indicative of an unusually strong CN enrichment that is atypical for the general halo population.

In order to make use of the full 6D phase-space information, we complemented SDSS data with proper motions ($\mu_\alpha \cos\delta$ and μ_δ) and parallaxes (ϖ) from *Gaia* DR2 (Gaia Collaboration et al. 2018a; Lindegren et al. 2018). In addition, the mean phase-space vectors of clusters were retrieved from the published collection by Vasiliev (2019), which itself is based on the compilation of coordinates and distances in the Harris catalog of GC parameters (Harris 1996, 2010 edition) and on line-of-sight velocities from Baumgardt et al. (2019). Other properties used throughout this paper are cluster core radii (r_c), King-model central concentrations (c), and half-light radii (r_h), which were taken from the Harris catalog.

It is important to bear in mind that incorporating both realistic precisions and accuracies is essential for obtaining realistic probabilities in our Bayesian framework (Section 3). This latter is used to compare quantities from different sources and is therefore affected by potential systematic discrepancies. Below, we discuss the two main sources of error that were singled out throughout our analysis, namely inaccurate metallicities with additionally underestimated precisions, and underestimated errors for *Gaia* proper motions.

2.1 SSPP parameters

In light of the low-resolution ($R \sim 2000$) nature of the SEGUE/eBOSS surveys and possible systematic trends among the parameter scales involved in the `SSPP`, caution must be taken when using the quoted internal uncertainties on the adopted parameters. A realistic assessment of the error budget should incorporate both systematic error contributions such as wavelength calibration errors or calibration inaccuracies of the `SSPP` parameter scales, as well as random errors caused by the finite signal-to-noise ratios of the underlying spectra. Substantial metallicity- and temperature-dependent departures of the `SSPP` stellar parameter scales with respect to high-resolution reference samples have already been pointed out by Smolinski et al. (2011; see, in particular, their Figure A2). The authors further compared `SSPP` results for [Fe/H] and v_r for several GCs with literature values and claim overall "good internal and external consistency" despite the evidence they provide for a wealth of residual substructure. However, the independent analysis of SEGUE spectra using `ATHOS` in Section II.5.7 revealed hints for similar inconsistencies in the metallicity scale, thus contradicting the favored explanation by Smolinski et al. (2011), who speculate that deviations may originate from inhomogeneities among the high-resolution studies that were used as reference.

While performing an in-depth evaluation of different error sources, we compiled a sample of stars with a high probability of being associated with the GC M 13. This cluster was chosen because it is well-studied and, due to its proximity, has been targeted with many SDSS fibers. Only SDSS targets that fall within a projected separation of one tidal radius from the cluster center were considered. Furthermore, we employed *Gaia* parallaxes and v_r from SDSS as a means to reject fore- and background stars by selecting only those with insignificant ($< 5\sigma$) deviations from the mean values of the cluster. We note that at this point neither information about the chemical composition from SDSS nor *Gaia* proper motions entered the selection procedure.

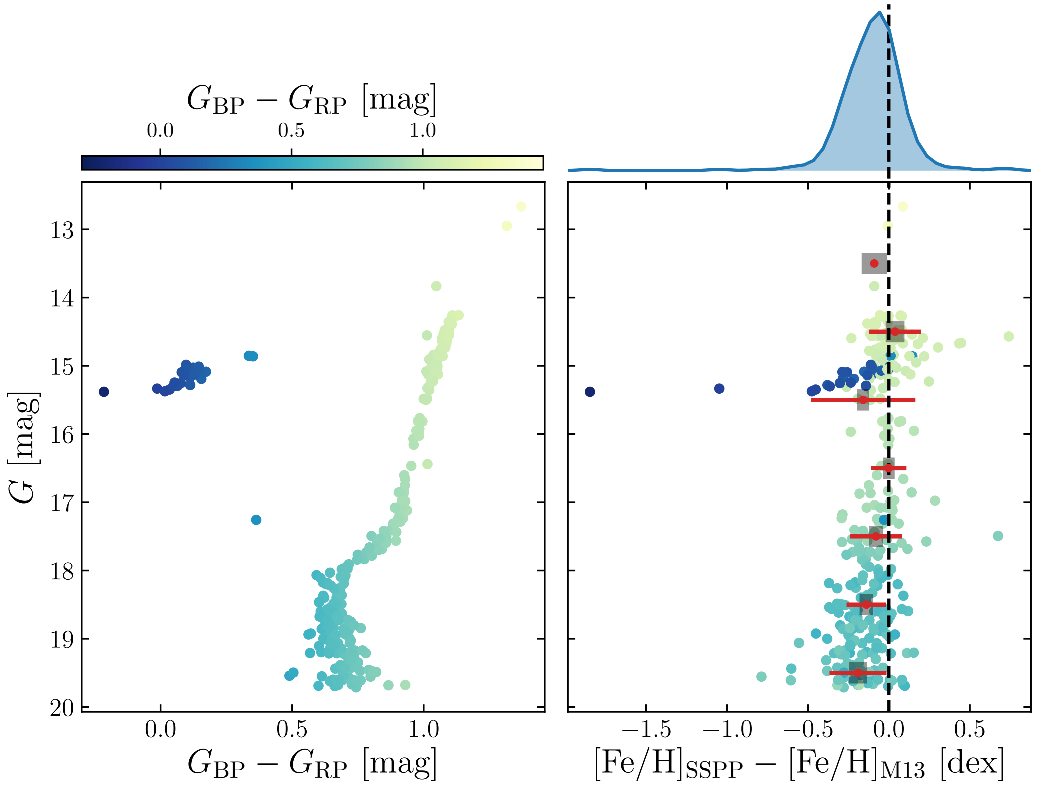

FIGURE IV.1: Precision and accuracy validation of [Fe/H]$_{\mathrm{SSPP}}$ for M 13 member stars. *Lower left panel*: proper-motion-cleaned CMD in the *Gaia* G, G_{BP}, and G_{RP} passbands. For reference to the *lower right panel*, $G_{\mathrm{BP}} - G_{\mathrm{RP}}$ is additionally indicated by colored symbols. *Right panels*: marginalized distribution of deviations (*top*) and behavior with evolutionary state (*bottom*) of SSPP metallicities with respect to the literature value [Fe/H]$_{\mathrm{M13}} = -1.53$ dex. Red points and error bars denote the means and standard deviations in bins of width 1 mag in G, whereas underlying gray bars represent the median of the SSPP uncertainties on [Fe/H].

Nevertheless, as can be seen in Figure IV.1, the resulting color–magnitude diagram (CMD) based on *Gaia* DR2 G and $G_{\mathrm{BP}} - G_{\mathrm{RP}}$ photometry appears clean with a low degree of contamination (likely less than five stars out of 283). On this account, the vast majority of the sample can be assumed to be cluster members. When comparing SSPP results for [Fe/H] with the literature value (−1.53 dex, Harris 1996), systematic discrepancies as a function of the evolutionary state of the individual stars (Figure IV.1) become apparent. Specifically, stars on the upper MS deviate by −0.18 dex with a decreasing trend toward the subgiant branch (Δ[Fe/H] ≈ -0.10 dex), while the RGB is consistent with a zero difference. Stars on the horizontal branch (HB) on the other hand differ by about −0.20 dex. Given the fact that M 13 shows no signs of intrinsic metallicity spread (e.g., Johnson & Pilachowski 2012), any such difference can be attributed to SSPP inaccuracies.

Again taking advantage of the fact that there are effectively no detectable metallicity spreads in M 13, we can estimate the internal `SSPP` precisions for [Fe/H] at different evolutionary states from the observed scatter. Typically, this scatter is larger by a factor of three compared to the provided `SSPP` uncertainties. The latter comparison is illustrated in the right panel of Figure IV.1.

Given the caveats discussed above, we quadratically added a global systematic error of 0.15 dex to individual errors on [Fe/H] measurements[1] throughout this work. This drastically increases the majority of the quoted (internal) `SSPP` uncertainties. We further caution that the total error budget on v_r cannot be less than 5 km s^{-1} (see the comparison of `SSPP` radial velocities to high-resolution results by Smolinski et al. 2011), which we accordingly adopted as another systematic error that is added in quadrature.

2.2 *Gaia* astrometric solution

For stars with an available five-parameter astrometric solution

$$\vec{x} = (\alpha, \delta, \varpi, \mu_\alpha \cos\delta, \mu_\delta)^T \,, \tag{IV.1}$$

the *Gaia* DR2 data tables enable the computation of the full covariance matrix, $\mathrm{Cov}(\vec{x})$, for the solution of each individual star. Incorporating its off-diagonal entries is crucial for this work, in that the measurements of ϖ, $\mu_\alpha \cos\delta$, and μ_δ may be correlated to varying degrees and thus must not be considered independent. Furthermore, we follow the technical note GAIA-C3-TN-LU-LL-124-01[2] and scale the covariance matrices by the squared re-normalized unit weight error (RUWE),

$$\mathrm{RUWE}^2 = \frac{\chi^2}{(N-5)\cdot u_0^2(G, G_{\mathrm{BP}} - G_{\mathrm{RP}})}, \tag{IV.2}$$

where χ^2 is the chi-square value of the astrometric fit to all N *Gaia* measurements in the direction along the scan that are considered “good”. The factor u_0 is an empirically calibrated quantity that can be extracted from dedicated lookup tables as a function of G and $G_{\mathrm{BP}} - G_{\mathrm{RP}}$[3]. We emphasize that all employed covariance matrices involving *Gaia* data were scaled by RUWE^2. In this work we moreover corrected for the quasar-based ϖ zero point of -0.029 mas (Lindegren et al. 2018) and assumed an additional global systematic error for proper motions of 0.035 mas yr^{-1} (Gaia Collaboration et al. 2018b).

---

[1] We emphasize that in doing so we are, strictly speaking, mixing a statistical source of error with an unrelated systematic component. Nonetheless, we treat this combined error as if it were of an entirely stochastic nature.

[2] `http://www.rssd.esa.int/doc_fetch.php?id=3757412`

[3] `https://www.cosmos.esa.int/web/gaia/dr2-known-issues`

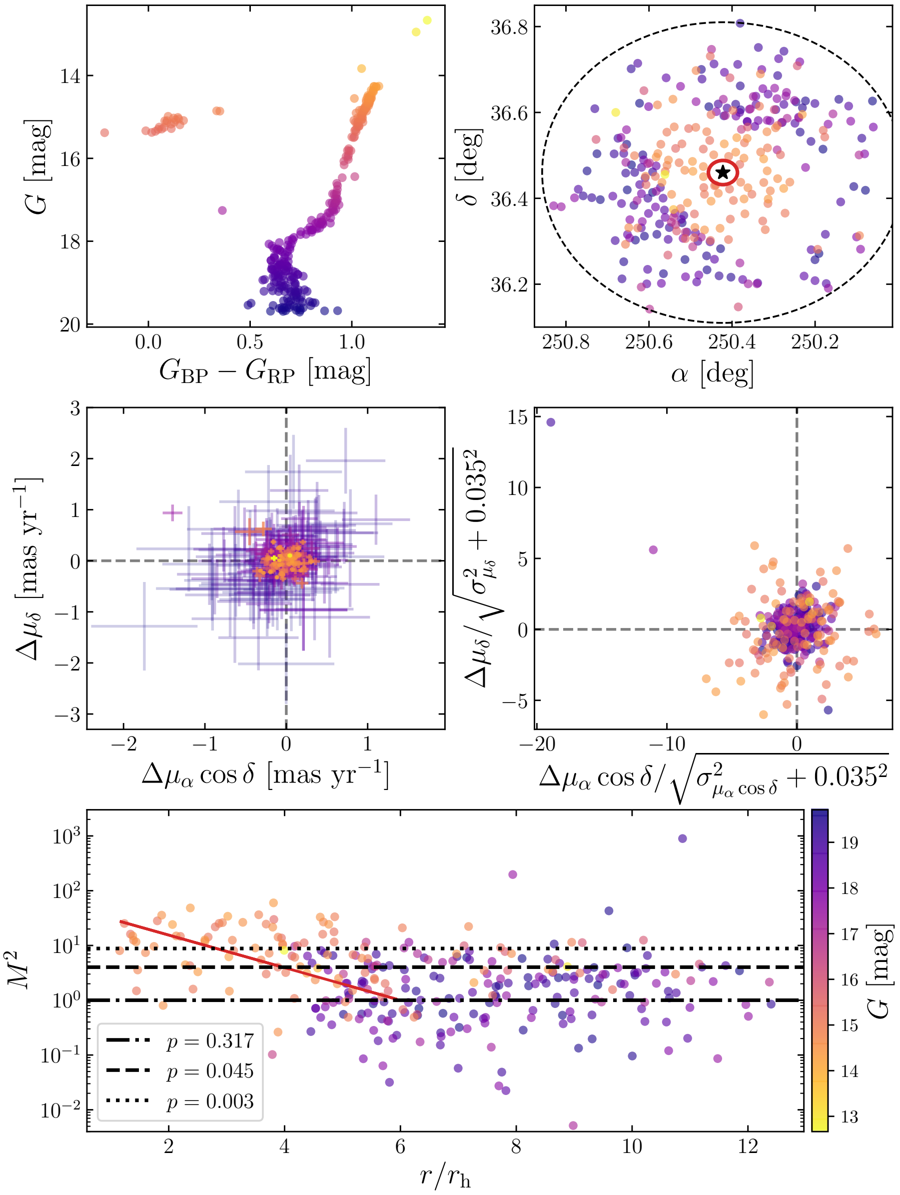

FIGURE IV.2: *Gaia* proper motion systematics. *Upper left*: same CMD as in Figure IV.1, but with the color coding indicating the brightness (see *lower right* color bar) and being the same as in all other panels. *Upper right*: spatial distribution of the M 13 validation sample. The cluster core, half-light radius (1.69 arcmin), and tidal radius (21 arcmin) are represented by a black star, red circle, and a dashed black line, respectively. We emphasize that the tidal radius together with ϖ and v_r were the only selection criteria applied to investigate proper motion systematics (main text). *Middle panels*: absolute (*left*) and relative (*right*) deviation in proper motion of the sample from the cluster mean value. *Lower panel*: squared Mahalanobis distance, $\mathcal{M}^2$, from proper motions only versus projected distance from the cluster center. In analogy to the 1σ, 2σ, and 3σ significances of a normal distribution, dash-dotted, dashed, and dotted lines resemble the corresponding p-values (see legend). The red line denotes the scaling relation introduced in Equation IV.4.

In elaborating on the formal DR2 proper-motion errors we again employ the sample of M 13 stars introduced earlier in this chapter. Their spatial distribution is presented in Figure IV.2 next to the corresponding CMD. We further show the distribution of the selection in absolute and relative (i.e., scaled by standard errors) proper-motion differences with respect to the mean values for M 13. While bright stars are highly clustered in an absolute sense, from Figure IV.2 it becomes apparent that there is an inversion of the relative distribution widths of bright and faint targets when going from absolute to relative proper motion differences. It is noteworthy that the RUWE remains below 1.5 for all but nine targets in the selection, four of which are fainter than $G = 17$ mag. Hence, for the vast majority of our bright stars, inseparable blends at the edge of the detection limit can be excluded with high confidence. We therefore attribute our observation to an additional, hitherto unexplained systematic error component of the proper motions in excess of the already applied 0.035 mas yr^{-1}.

Although we neglected covariances for the middle panels of Figure IV.2 for illustrative purposes, owing to the discussed correlations among the components of $\vec{y} = (\mu_\alpha \cos\delta,\ \mu_\delta)^T$, it is not straightforward to estimate the statistical significance of the deviation from the cluster mean, $\vec{y}_{\rm GC}$. Hence, for each star, we computed the squared Mahalanobis distance

$$\mathcal{M}^2 = (\vec{y} - \vec{y}_{\rm GC})^T \mathrm{Cov}(\vec{y} - \vec{y}_{\rm GC})^{-1} (\vec{y} - \vec{y}_{\rm GC}), \tag{IV.3}$$

which respects the combined covariance. Under the assumption of normally distributed errors, the latter quantity is chi-square distributed. Therefore, the p-value – that is, the probability of finding a value of $\mathcal{M}^2$ or more extreme under the null hypothesis that the star is not kinematically distinct from the cluster – can be computed from a chi-square distribution with one degree of freedom. In Figure IV.2, $\mathcal{M}^2$ is plotted against the projected angular distance to the cluster center, r, normalized by the half-light radius, $r_{\rm h}$. We identify two distinct groups of highly significant outliers that would be rejected in Section 4.1 based on their proper motions alone. First, starting from $r/r_{\rm h} \approx 6$, there is a trend of increasingly significant deviation with decreasing r. Secondly, irrespective of the separation from the cluster core, bright stars ($G \lesssim 16$ mag) tend to deviate more significantly than fainter ones. Based on the clean CMD and the $v_{\rm r}$-based association, we exclude the possibility that the majority of the strong proper motion outliers do not in fact belong to the cluster and conclude that the origin is genuinely to be found in underestimated *Gaia* errors. We compensate for the latter by introducing a distance-dependent factor

$$\alpha(r/r_{\rm h}) = \begin{cases} 10^{-0.3(r/r_{\rm h}-6)}, & \text{if } r/r_{\rm h} \leq 6 \\ 1, & \text{otherwise,} \end{cases} \tag{IV.4}$$

to be applied to the covariances. Though optimized for the M 13 stars, we note that we found the relation to hold true for several other GCs from our sample within an acceptable amount of variance.

3 Methods

In the following sections, we introduce the three approaches that were used to identify potential former GC members. The first method is tailored to test for stellar associations in the immediate cluster surroundings and does not require all of the three space motions and positions to be measured with the same precision. The second approach ties field CN-strong stars to clusters and bears the advantage of not being limited to a comparatively small patch of the sky, though at the expense of obtaining results that are strongly impacted by the lowest-precision entry in the phase-space vector. The third and last method is an adaptation of the first method, where we search for chemically normal stellar populations that share the same metallicity and kinematic properties as CN-strong stars in the halo field, possibly indicating a common origin.

In all three approaches we employed variations of the Bayesian approach described in Anderson et al. (2013). In brief, the association probability (posterior) of a star being attributable to a reference object (be it a CN-strong star or a GC) is given by

$$P(A|B) = \frac{P(B|A) \times P(A)}{P(B)} \propto P(B|A) \times P(A). \tag{IV.5}$$

Here, $P(B|A)$ is the conditional probability (likelihood) of encountering the star at its observed position in information space assuming it is indeed associated with (or used to be an intratidal member of) the reference. Further, $P(B)$ is the probability of observing the data and $P(A)$ is the initial degree of belief in association (prior).

3.1 Method I: Stars in the neighborhood of clusters

The potential GC origin of individual stars in the cluster vicinity (out to a few degrees separation) was evaluated on a cluster-by-cluster basis. Stars that escaped the GC potential and show a significant spatial separation from their previous host – while conserving their metallicity – no longer necessarily share the same space-motion vector as the cluster. We instead presume that their currently observed motion should show a stream-like behavior and thus be similar (though not exactly identical; see Sections 4.2 and 4.4) to the closest point along the hypothesized stream.

To implement this behavior, we extrapolated the orbits of all GCs in the list by Vasiliev (2019) to 2 Gyr in the past and future by performing point-particle integrations employing the python library `galpy` (Bovy 2015) and its standard Galactic potential `MWPotential2014`. As a means to track the behavior of stars lost from the clusters, we further used `galpy` for the modeling of dynamically cold ($\sigma_v = 1\ \mathrm{km\,s^{-1}}$) leading and trailing tidal streams. We introduced tracer particles along the streams with parameter covariances that account for the simulated distribution functions of the streams. From these, the likelihood terms in Equation IV.5 were calculated individually for each star based on the difference $\vec{\Delta z}$ between the five-component vector $\vec{z} = ([\mathrm{Fe/H}], v_\mathrm{r}, \varpi, \mu_\alpha \cos\delta, \mu_\delta)^T$ and the corresponding closest stream anchor point, $\vec{z}_\mathrm{s}$. Again following Anderson et al. (2013), in analogy to Equation IV.3, we computed the squared Mahalanobis distance, $\mathcal{M}^2$. Here we used the *Gaia* covariance entries for ϖ, $\mu_\alpha \cos\delta$, and μ_δ and assumed no correlation between SDSS and *Gaia* quantities. Furthermore, covariances between cluster mean proper motions were taken from Vasiliev (2019). Complete independence of the cluster quantities from the stellar quantities was presumed, such that the cross-covariances between $\vec{z}$ and $\vec{z}_\mathrm{s}$ are zero. With respect to the second assumption, while our potential extratidal candidates were not used by Vasiliev (2019) to constrain mean cluster parallaxes and proper motions, this does not necessarily hold for our supposedly bound cluster members. Vasiliev (2019) on the other hand commonly employed several orders of magnitude more stars from the *Gaia* tables than there are counterparts in the SDSS catalog. As a consequence, the overlap and therefore cross-covariances are minor. Interdependencies between ϖ, [Fe/H], v_r, and their respective mean cluster values can be excluded, as the cluster parallaxes (by means of inverse distances) and [Fe/H] are based on the Harris catalog of GC parameters (Harris 1996), and v_r stems from the collection of ground-based measurements compiled by Baumgardt et al. (2019). None of the former are in any way connected to SDSS or *Gaia*.

Finally, the likelihood can be expressed as

$$P(B|A) = 1 - p(\mathcal{M}^2), \tag{IV.6}$$

where $p(\mathcal{M}^2)$ is the p-value of a χ^2 distribution with five degrees of freedom. Anderson et al. (2013) emphasize that large errors – translating into low-significance values – cannot rigidly exclude a large portion of their corresponding phase-space dimensions and thus do not limit the high-likelihood regime to a confined range. A prime example of this behavior is ϖ, which – in light of typically large heliocentric cluster distances – hardly exceeds the 2σ significance level for most of the stars that are deemed cluster members below. Nonetheless, ϖ is a powerful means to reject the large number of foreground stars, exposing significant parallaxes that are inconsistent with cluster association.

In contrast to Anderson et al. (2013), who demanded their targets be gravitationally bound to the clusters, we cannot use this criterion for extratidal stars and hence assume a loose prior of the form

$$P(A) = \exp\left(-\frac{1}{2}\left(\frac{d_{\mathrm{s}}}{7r_{\mathrm{t}}}\right)^2\right), \tag{IV.7}$$

with d_{s} being the projected distance of a star to the closest tracer stream particle and r_{t} being the tidal radius of the cluster. This prior formulates the initial belief that former members at arbitrarily large angular separation will not share the same $\vec{z}$.

Figure IV.3 illustrates a graphical representation of the multivariate association procedure for the exemplary case of the cluster M 13. Candidates are reported if their associated $P(A|B)$ exceeds the threshold of 0.05. Both intra- and extratidal stars are treated in the same way.

3.2 Method II: Integrals of motion

It is possible that GC escapees that did not recently become unbound from their host cluster may no longer be found in the immediate cluster vicinity; such GCs would not be recovered by the approach in the previous section. Thus, for the manageably small sample of CN-strong stars used here, we resort to the fact that for most orbits in axisymmetric potentials there exists a set of three conservative integrals of motion (e.g., Henon & Heiles 1964); in other words, despite being spatially separated, escapees almost completely retain the integrals of motion[4] of their host (e.g., Savino & Posti 2019). We used the `galpy` implementation of the Stäckel approximation by Binney (2012) in order to integrate the axisymmetric `MWPotential2014` for the radial and vertical actions, J_r and J_z, as well as the azimuthal component of the angular momentum, L_z. With respect to the previous approach, such integrations bear the main disadvantage of relying on the full six-component phase-space vector to initialize an orbit, such that uncertainties are strongly driven by the least constrained observational quantity. While the latter restriction is not a major concern for our sample of GCs, the lack of highly significant measurements for the heliocentric distance, D, to the CN-strong stars ultimately drives the confidence for rejecting or accepting a potential cluster association. *Gaia* parallax significances $\varpi/\sigma_{\varpi} < 1$ have been attributed to 61% (68 stars) of our sample whereas only three measurements exceed the 4σ level. It is

---

[4] We emphasize that this is only approximatively true, because for a star to become unbound its phase-space position already has to be distinct from the main body of the cluster.

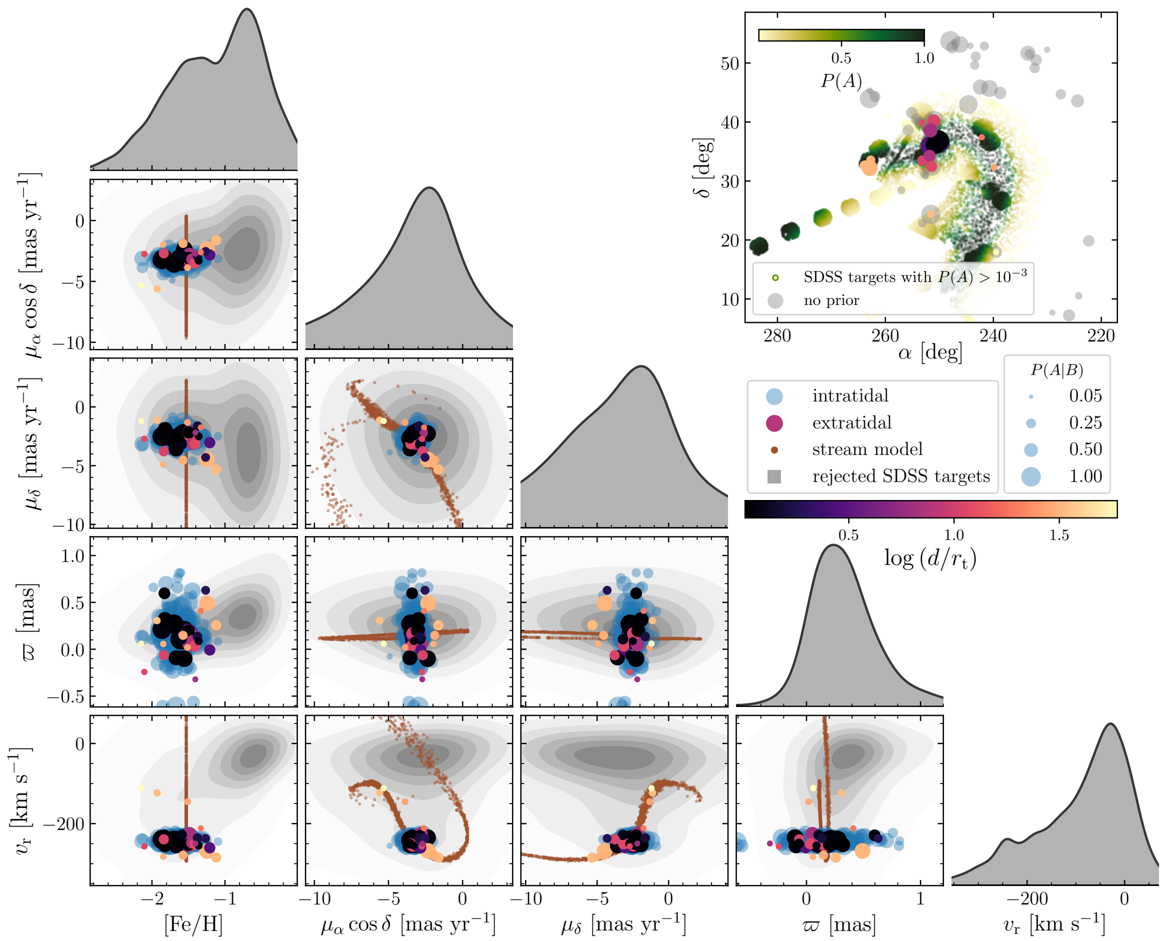

FIGURE IV.3: Five-parameter chemodynamical association criteria used to constrain the association with the GC M 13. The rejected back- and foreground population of stars with SSPP parameters and *Gaia* DR2 motions is indicated by gray density contours. Brown dots indicate the simulated stream (see main text). Intratidal and extratidal stars are depicted by blue and colored circles (see also Figure IV.7), respectively. Circle sizes indicate the association probability and colors resemble the projected distance to the cluster center (see legend and color bar). The marginalized distributions of each coordinate on the abscissa are shown on top of the two-dimensional representations. The adopted spatial prior as well as the stars that are rejected due to its usage (gray circles with no colored counterpart) are illustrated on the *upper right*.

evident that any distance inferred from ϖ alone (e.g., Bailer-Jones et al. 2018) will result in critical errors in the actions.

In order to obtain more precise estimates for D, we refined the spectrophotometric formalism from Paper I by adopting the Bayesian inference method for stellar distances by Burnett & Binney (2010) using photometry and stellar parameters from SDSS and ϖ as an additional constraint (cf., e.g., Savino & Posti 2019). Therefore, a likelihood was computed from the residuals between the observed quantities (color, apparent magnitude, T_{eff}, [Fe/H], $\log g$, and ϖ) and their theoretical counterparts

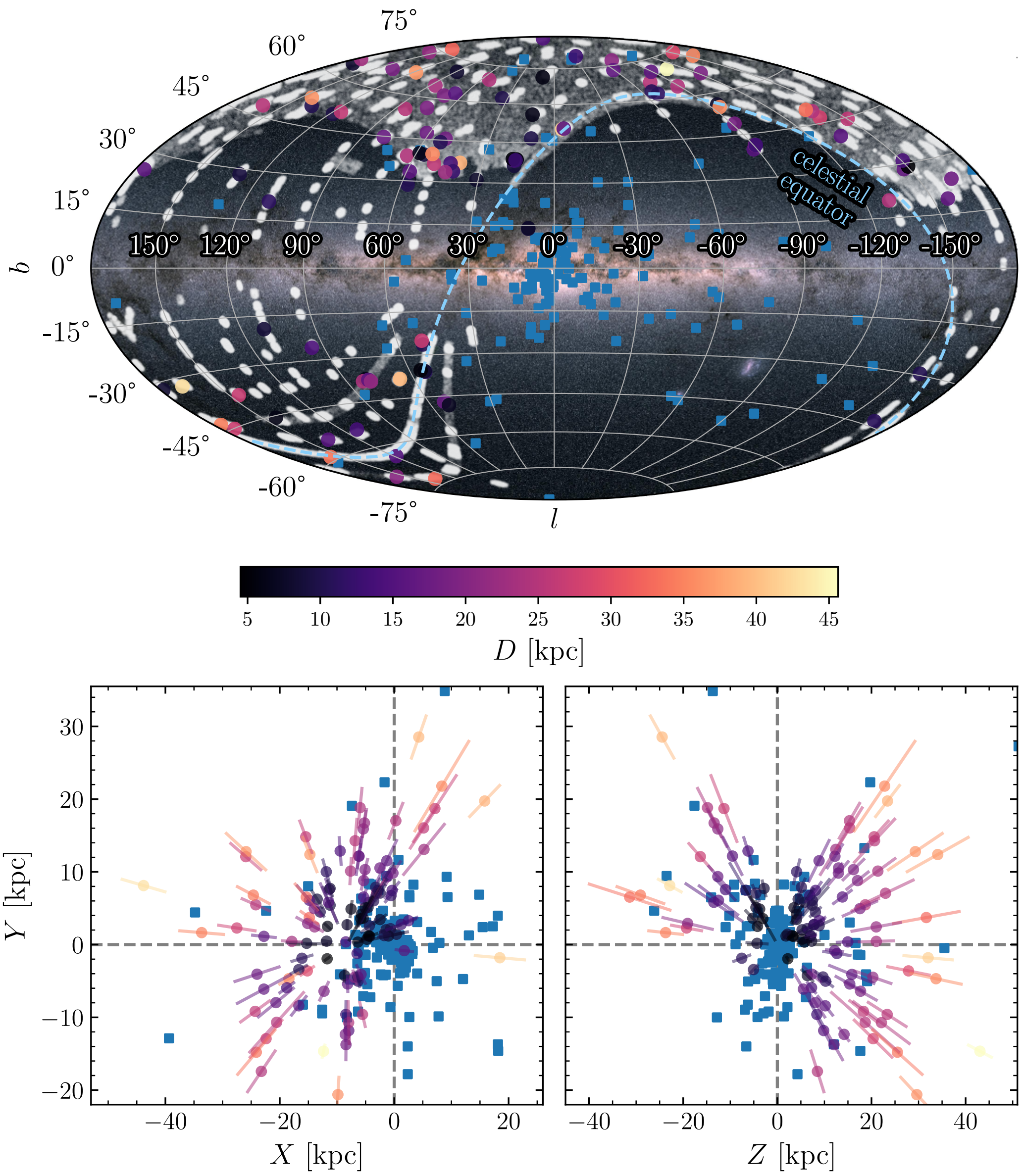

FIGURE IV.4: Spatial distribution of GCs (blue squares) and CN-strong halo giants (colored according to their distance) in Galactic coordinates (*top*) and the Cartesian Galactocentric frame (*bottom*). The dashed line in the *top panel* denotes the celestial equator. The SDSS footprint area is depicted in white while the *Gaia* all-sky map is illustrated in the background for orientation. **Image credit.** Milky Way all-sky map: Gaia Data Processing and Analysis Consortium (DPAC); A. Moitinho / A. F. Silva / M. Barros / C. Barata, University of Lisbon, Portugal; H. Savietto, Fork Research, Portugal; licensed under CC BY-SA 3.0 IGO.

from a grid of PARSEC (Marigo et al. 2017) isochrones. As prior, we used the three-component Galactic model adopted by Burnett & Binney (2010) for the thin and thick disks and the stellar halo, the latter being constructed from the parameters stellar age, [Fe/H], and mass. The magnitude and variance of D were deduced by means of the first and second moments of the star's posterior probability density function (pdf)

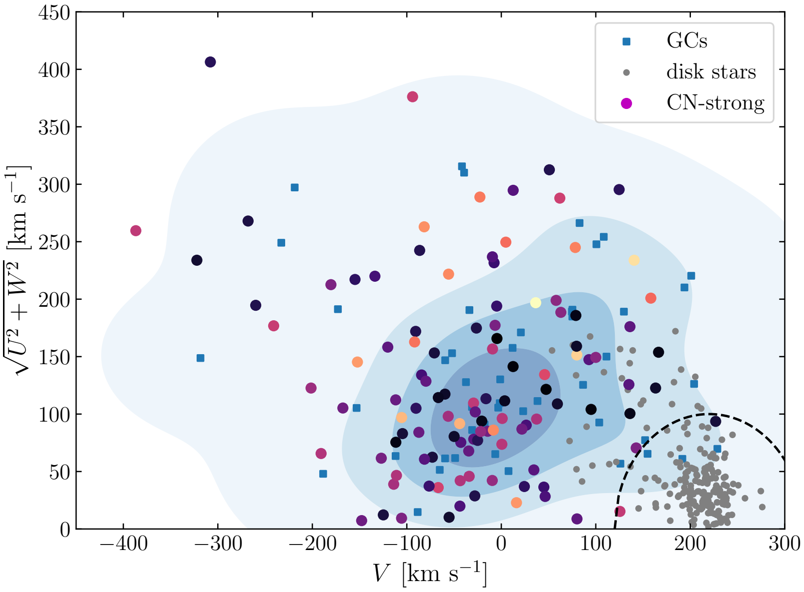

FIGURE IV.5: Toomre diagram for our CN-strong giants (colored circles) and the Galactic GC population (blue squares). The latter is only shown in the regime $-1.8 < \mathrm{[Fe/H]} < -1.3$ dex, representing the coverage of the analyzed stars. The color coding of the CN-strong stars is the same as in Figure IV.4. For better comparability, an additional Gaussian kernel density estimate of the GC sample is provided where increasing color darkness resembles increasing density. To show the clear contrast to the Galactic disk population, we also indicate all targets from our *Gaia* - SDSS crossmatch that obey $-5° < b < 5°$ and have a spectrophotometric distance as determined by SDSS of less than 1 kpc (gray dots). Moreover, the dashed line encircles the region of absolute velocities less than 100 km s^{-1} with respect to the local standard of rest.

marginalized in all other dimensions (cf., e.g., Savino & Posti 2019). Even though the nominal errors on the inferred distances are small and consequently the statistical significances are high (nearly 50% reside above $D/\sigma_D = 10$), we caution that there is ample room for various systematic errors that are not captured by the mentioned treatment. One example is the `SSPP` surface gravity – a quantity that is notoriously hard to obtain with any accuracy from low-resolution spectra – which may strongly favor much larger distances in cases where a star was erroneously classified as a low-gravity giant whilst in fact being a giant of intrinsically higher gravity or even a dwarf star.

Adopting the former distances, we present the resulting spatial distribution of our CN-strong giants in the Galactocentric frame in the upper part of of Figure IV.4, while a Hammer projection in the Galactic frame is shown on the lower part. Furthermore, in Figure IV.5, we show a Toomre diagram of our CN-strong stars and GCs of the same [Fe/H], from which, qualitatively, a remarkable distribution overlap can be seen. Nonetheless, we envision a more quantitative approach, exploiting the kinematic memory of our targets.

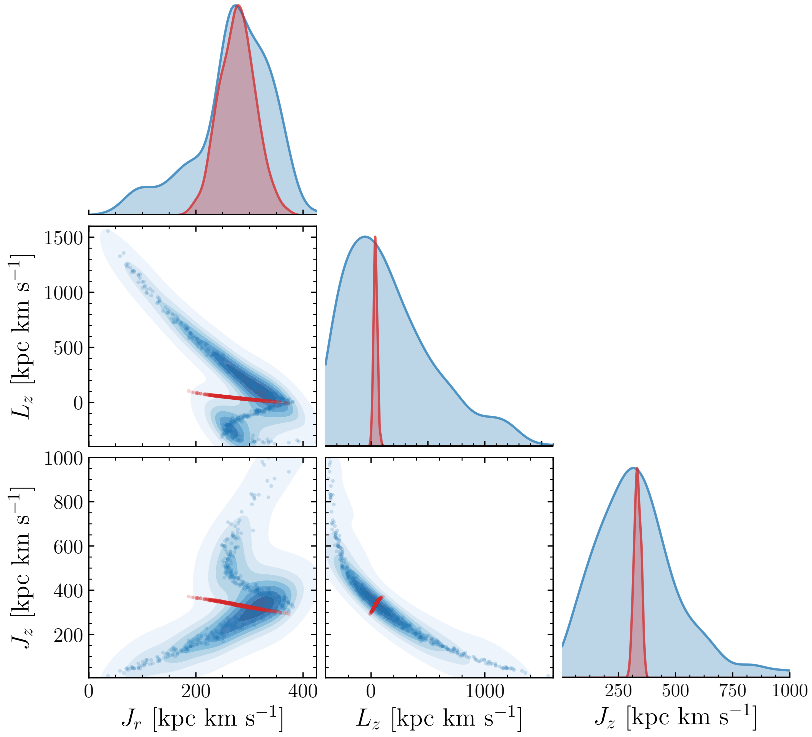

FIGURE IV.6: Distribution of Monte Carlo samples for the integrals of motion for M 70 (red) and the star *Gaia* DR2 3833963854548409344 (blue). The marginalized two-dimensional and one-dimensional kernel density estimates are indicated as contours in the frames and histograms at the top, respectively. For illustrating purposes, the histograms were normalized by their maxima.

To this end, all a priori known statistical error sources on the phase space vectors for both GCs and CN-strong stars were propagated in the action integration by means of a Monte Carlo analysis. Each orbit was initialized 500 times with values randomly drawn from a multivariate normal distribution respecting the covariance matrix, where we assumed cross-covariances between α, δ, D, and v_r to be negligible while maintaining the covariances for *Gaia* proper motions. As shown by the exemplary comparison in Figure IV.6, the obtained distributions in action space are highly coupled and non-normal, that is, the relations between action coordinates show a strong nonlinear behavior. It is apparent that, whilst cluster (M 70) and star (*Gaia* DR2 3833963854548409344) indicate a perfect match in the marginalized, one-dimensional distributions, in the multidimensional representation there is only a much smaller distribution overlap. If not properly accounted for, this effect would overestimate the association probability in most cases.

To test the possibility of former membership of a CN-strong halo star to a cluster, we required both the actions and [Fe/H] to be consistent. Hence, we compared the cluster vector $(J_r, J_z, L_z, [\mathrm{Fe/H}])^T_\mathrm{GC}$ to the corresponding vector for the star. Due to the non-normality of the MC samples mentioned above, we cannot simply compute the covariance matrices of the samples and proceed with the Mahalanobis distance employed in Section 4.1. Therefore, we approximated the four-dimensional probability density function, $\psi(\vec{v})$, of the difference vector, $\vec{v}$, using a nonparametric Gaussian kernel density estimate. We note that this is the main difference between our approach and that of Savino & Posti (2019), who did not account for nonlinear correlations between actions. As a means to accept or reject association, we obtained

$$p = \int_{\psi(\vec{v}') < \psi(\vec{0})} \psi(\vec{v}') d\vec{v}' \tag{IV.8}$$

through Monte Carlo integration.

3.3 Method III: Chemodynamical matches in the fields surrounding CN-strong stars

Following the predictions made by evolutionary GC models (e.g., D'Ercole et al. 2008; Bastian et al. 2013), a substantial number of first-generation stars are lost early on in the cluster formation phase. This unenriched population is chemically no different from the standard collection of halo stars and thus remains unidentifiable for classical tagging methods (e.g., Paper I). Yet, by exploring chemodynamical similarities between the enriched, bona fide second-generation cluster stars in the Galactic halo and their surrounding field, we can search for links that could indicate a common origin. Therefore, we once again employed the formalism of Section 3.1 with CN-strong stars taking over the role of the GCs. The main difference between this latter method and the one described here is that we did not attempt to integrate the orbit of the CN-strong stars because the much larger errors on the astrometry of these individual stars do not allow for the computation of the tightly constrained orbits required to confidently reject field interlopers. As a spatial prior, in analogy to Equation IV.7, we adopted a Gaussian centered on the CN-strong star with a standard deviation of seven degrees in projected distance.

Table IV.1: Clusters for which extratidal associations were singled out by method I

Name	$\alpha^{(a)}$ [deg]	$\delta^{(a)}$ [deg]	$r_{\mathrm{h}}^{(b)}$ [arcmin]	$r_{\mathrm{t}}^{(b)}$ [arcmin]	$D^{(b)}$ [kpc]	$v_{\mathrm{r}}^{(a)}$ [km s^{-1}]	$\mu_\alpha \cos\delta^{(a)}$ [mas yr^{-1}]	$\mu_\delta^{(a)}$ [mas yr^{-1}]	$r_\mu^{(a)}$	[Fe/H]$^{(b)}$ [dex]	$N_{<r_t}^{(c)}$	$N_{>r_t}^{(c)}$
NGC 4147	182.526	18.543	0.5	6.1	19.3	179.1 ± 0.3	-1.702 ± 0.016	-2.108 ± 0.010	-0.147	-1.80	3	19
NGC 5024 (M 53)	198.230	18.168	1.3	18.4	17.9	-63.1 ± 0.2	-0.151 ± 0.006	-1.350 ± 0.004	-0.261	-2.10	36	7
NGC 5053	199.113	17.700	2.6	11.4	17.4	42.5 ± 0.2	-0.353 ± 0.009	-1.257 ± 0.007	-0.334	-2.27	26	24
NGC 5272 (M 3)	205.548	28.377	2.3	28.7	10.2	-147.2 ± 0.2	-0.094 ± 0.004	-2.626 ± 0.003	-0.064	-1.50	181	18
NGC 6205 (M 13)	250.422	36.460	1.7	21.0	7.1	-244.4 ± 0.3	-3.172 ± 0.004	-2.586 ± 0.005	0.152	-1.53	260	32
NGC 6341 (M 92)	259.281	43.136	1.0	12.4	8.3	-120.7 ± 0.3	-4.923 ± 0.005	-0.556 ± 0.006	0.085	-2.31	75	35
NGC 7078 (M 15)	322.493	12.167	1.0	27.3	10.4	-106.5 ± 0.2	-0.622 ± 0.006	-3.782 ± 0.006	-0.037	-2.37	91	5
NGC 7089 (M 2)	323.363	-0.823	1.1	12.4	11.5	-3.6 ± 0.3	3.531 ± 0.007	-2.139 ± 0.007	0.027	-1.65	66	11

References. (a) Vasiliev (2019); (b) Harris (1996), 2010 version; (c) This study.

4 Results and Discussion

4.1 Extratidal escapee candidates around clusters

In this section, we present the discovery of new candidates for extratidal stars around GCs in the halo field based on their position in multi-dimensional information space. We started by cleaning the `SSPP` catalog for stars lacking a [Fe/H] or v_r detection. The remaining list was subsequently cross-matched with the *Gaia* DR2 source catalog. This vetting process – due to the SDSS sky coverage being limited to the northern sky (cf., Figure IV.4) – naturally rejected the southern GCs and left us with about $3.7 \cdot 10^5$ stars for further analysis. The relevant cluster properties entering the analysis can be found in Table IV.1.

We consider those stars with $P(A|B) > 0.05$ as bona fide cluster associates. A further sub-classification into extra- and intratidal candidates is performed based on whether the projected distances of the stars do or do not exceed the tidal radius of the cluster, r_{t}. We note the major caveat of this distinction to be the potential exclusion of truly extratidal stars that, owing to their line-of-sight position, happen to be projected into the tidal radius of the cluster. Unfortunately, the already mentioned low significance of ϖ for these distant objects cannot yield additional constraints and prohibits their identification.

In the following sections, we comment on our 151 extratidal candidates with likely associations with eight GCs. The discussion is separated by individual host clusters. A summary of the properties of all halo stars with potential GC origin is provided in Table IV.2.

TABLE IV.2: Candidate cluster escapees in the near-field of clusters (method I)

Gaia DR2 source ID	$\alpha^{(a)}$ [deg]	$\delta^{(a)}$ [deg]	r/r_t	ϖ [mas]	$\mu_\alpha \cos\delta$ [mas yr^{-1}]	μ_δ [mas yr^{-1}]	v_r [km s^{-1}]	[Fe/H] [dex]	$P(A/B)$	G [mag]	$G_{\rm BP} - G_{\rm RP}$ [mag]	Rem.$^{(b)}$
NGC 4147												
3950157700750904064	182.459	18.773	2.4	0.06 ± 0.15	-1.9 ± 0.2	-2.1 ± 0.2	184.8 ± 5.7	-1.53 ± 0.16	0.87	17.69	1.01	
3950527823852135808	183.537	19.185	11.4	-0.57 ± 0.38	-3.8 ± 1.0	-1.7 ± 0.4	188.1 ± 10.9	-1.90 ± 0.17	0.06	19.22	0.77	
3950992882911234944	182.416	19.691	11.4	-0.48 ± 0.46	-3.2 ± 0.9	-1.7 ± 0.4	160.6 ± 10.5	-1.91 ± 0.15	0.05	19.41	0.72	

Notes. Only a small portion of the data is shown to indicate the form and content of the table. The full table will be made available through the CDS upon publication of the paper. $^{(a)}$ Coordinates are in the *Gaia* DR2 reference epoch J2015.5. $^{(b)}$ Remarks: (1): Classified as being a CN-strong giant in Paper I. (2): Identified as RR Lyrae star.

4.1.1 M 13 (NGC 6205)

M 13 is an old (12.3 Gyr, VandenBerg et al. 2013), intermediately metal-poor (−1.5 dex, Johnson & Pilachowski 2012) GC known to host extreme light-element abundance variations (e.g., Sneden et al. 2004; Johnson & Pilachowski 2012). It has been shown by Cordero et al. (2017) that the most strongly enriched population of stars possesses a stronger degree of rotation with respect to the other samples, while Savino et al. (2018) were not able to find significant display of spatial segregations. Jordi & Grebel (2010) reported on an extratidal stellar halo in the immediate vicinity of this GC with a slight elongation aligned with its motion that was later extended to even larger distances out to 13.8 $r_{\rm t}$ by Navin et al. (2016; however, we note the reevaluation of these associations later in this section).

For M 13, we identified a total of 292 candidates that – according to our classification scheme – are candidate cluster associates. Out of those, 260 are still bound to the cluster and 32 are most likely extratidal. A multi-parametric representation of the chemodynamical associations against the rejected background population is presented in Figure IV.3. The clustering of the associates around the mean values for M 13 and the simulated stream is evident. Interestingly, M 92 (Section 4.1.2) can be identified as a slight background overdensity. Nonetheless, considering the full five-dimensional information space, M 13 can be discerned from M 92 stars with high confidence.

An independent and powerful constraint for the validity of our method can be obtained from the color–magnitude information for our candidates, which is presented in Figure IV.7 along with the spatial distribution. Though they are not part of the initial analysis, the distributions in the *Gaia* and SDSS passbands constitute well-behaved structures, which – with few exceptions and considering observational uncertainties – are consistent with a single ∼ 12 Gyr PARSEC isochrone that matches the age, [Fe/H], and distance modulus of M 13 (see Table IV.1). We note that the

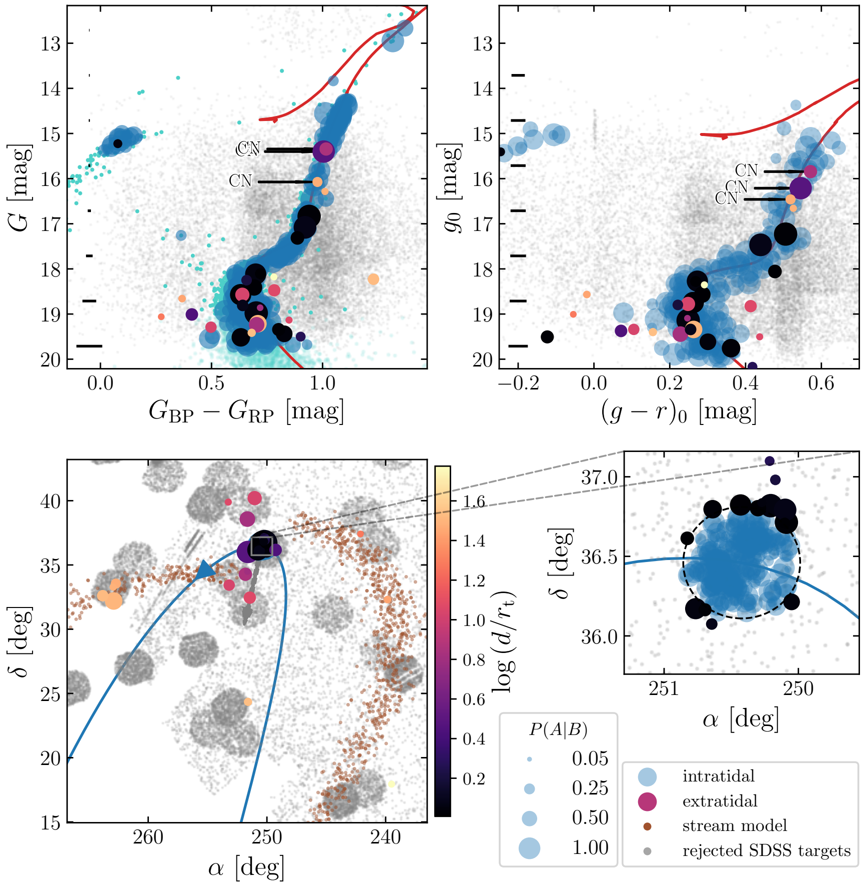

FIGURE IV.7: Parameter distributions of intra- (blue) and extratidal (black to light yellow) stars associated with M 13 on top of the field star population covered by the SDSS footprint (gray dots). Sizes of the colored circles resemble the membership probability $P(A|B)$ as indicated in the legend, while the color of the extratidal candidates denotes the projected distance from the cluster core in units of r_t (see color bar). *Upper panels*: CMDs from *Gaia* (*left*) and dereddened SDSS (*right*) bands. Cyan dots indicate proper motion and ϖ-selected *Gaia* sources without spectroscopic SDSS counterparts (see main text for details). Typical photometric errors are specified in each case by error bars on the left-hand side. For a subset of bright intratidal stars, reliable color information from SDSS is not available, which is why those targets were omitted in the *right* CMD. Red lines are 12 Gyr PARSEC isochrones (Marigo et al. 2017) matching the parameters from Table IV.1 with an applied manual shift in color for the *Gaia* CMD. The CN-strong giants classified in Paper I are labeled "CN" in both panels. *Lower panels*: distribution on the sky (*left*) and a zoomed-in view of the immediate cluster vicinity (*right*). The dashed black ellipse indicates the tidal radius, r_t, and the direction to the Galactic center is marked by a gray arrow. Properties for the integrated cluster orbit and the simulated stream are indicated by the blue curve and brown dots, respectively.

reddening value for the *Gaia* isochrone displayed in Figure IV.7 had to be manually adjusted to achieve a better fit. When using reddening coefficients provided in Yuan et al. (2013) for SDSS colors and from Casagrande & VandenBerg (2018) for *Gaia* colors, this reddening is not consistently described by the same visual extinction $A(V)$ as the SDSS colors. A detailed investigation of this behavior is beyond the scope of the present study. Due to this and the effects of varying extinction throughout the substantial sky coverage of more than 10 deg away from the cluster center, we do not attempt to incorporate the photometry in our mathematical treatment, but use it to qualitatively assess membership likelihoods. To guide the eye in the *Gaia* CMD, we furthermore show all *Gaia* targets – not just the ones with a counterpart in SDSS – that lie within the tidal radius and that do not deviate by more than 3σ in ϖ, $\mu_\alpha \cos\delta$, and μ_δ. Additionally, in order to overcome contamination by stars that might be affected by crowding and therefore might be blueshifted from the MS, the MSTO, and the RGB, we required the *Gaia* color excess factor[5] to remain below 1.4.

The projected angular distances of 13 out of the 32 extratidal candidates are only slightly larger than the tidal radius ($d < 1.2\,r_\mathrm{t}$) and thus may still be considered loosely bound to M 13. Their distribution qualitatively matches the photometrically determined contours by Jordi & Grebel (2010). At $d = 1.6\,r_\mathrm{t}$ and above, the remaining 19 candidates can safely be denoted extratidal. Looking at their spatial distribution (Figure IV.7), it is tempting to claim evidence for an overdensity towards the leading portion of the cluster orbit and/or stream. However, owing to the nonisotropic coverage of the SDSS footprint around the cluster, this observation should be treated with caution.

Apart from one star on the blue HB, the three brightest extratidal associations are affiliated with the RGB and were classified as CN-strong in Paper I. Furthermore, the stars are also attributable to M 13 by the method outlined in Section 4.2. Therefore, it appears very likely that the three stars in question are escapees that can be attributed to the second – or enhanced – population of M 13 stars. We emphasize that among all 32 candidates presented here, only four giants were studied in Paper I due to strict parameter limitations of the method therein. In other words, 75% of the stars in the region of parameter overlap are CN-strong. This being the case, it is intriguing to argue that a substantial fraction of all M 13 escapees might be second-generation stars, but due to low-number statistics, this remains rather speculative (see Section 4.5 for further discussion).

Navin et al. (2016) performed a pre-*Gaia*-era search for cluster associations both within and outside of the tidal radius of M 13. The study was based solely on space motions and photometry. The authors obtained initial membership estimates relying on radial velocities from the first data release of the LAMOST spectroscopic survey (Luo et al. 2015) and subsequently refined the selection criteria using cuts in color–magnitude and stellar-parameter space in order to end up with probable cluster giants and to exclude foreground dwarf stars. A further constraint was established by employing

---

[5] The color excess factor encodes the comparison of the summed BP and RP fluxes in a fixed $3.5'' \times 2.1''$ area to the G flux, which itself is estimated from spatially much more stringently confined PSF photometry. Hence, a high color excess indicates that blending sources affect the colors (see section 5.5.2 of the *Gaia* DR2 documentation).

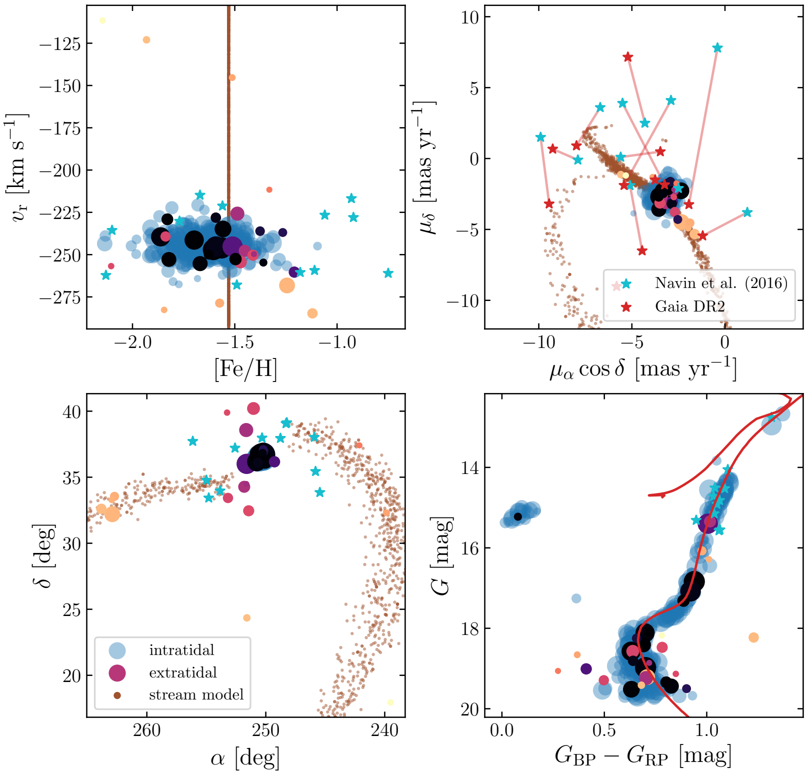

FIGURE IV.8: Comparison of the chemodynamical (*left two panels*) and spatial (*third panel*) distributions and the CMD (*right*) for M 13 between Navin et al. (2016, cyan stars) and the present study (same color and size scheme as in Figure IV.7). In the proper motion diagram, the values from the original study are connected by red lines with their *Gaia* DR2 counterparts (red stars).

UCAC4 (Zacharias et al. 2013) proper motions and demanding deviations from the cluster means of less than 10 mas yr^{-1}. We note that the proper motions used in this latter study are barely significant in any of the cases. Due to large uncertainties in LAMOST DR1, [Fe/H] was not used by the authors to further eliminate candidates.

Here, we cross-matched the 12 candidate extratidal halo stars for M 13 from Navin et al. (2016) with the *Gaia* DR2 catalog (see Figure IV.8). Given the bright nature of the stars in question, corresponding *Gaia* proper motions are highly significant[6] and from a visual inspection of the proper motion comparison in Figure IV.8 it is already evident that most claimed candidates can be excluded with high confidence. Moreover, our membership formalism (Equations IV.5 and IV.6) provides a zero probability and thus rejects all 12 candidates. Here, we assumed the sample mean and median errors quoted by Navin et al. (2016) on the LAMOST quantities of 17.1 km s^{-1} and 0.86 dex for v_r and [Fe/H], respectively. The latter values are relatively conservative, such that our strong exclusion confidence is almost entirely

---

[6] Here, the effects of crowding that were discussed in Section 2.2 should not play a role, as the stars in question are far from the cluster center.

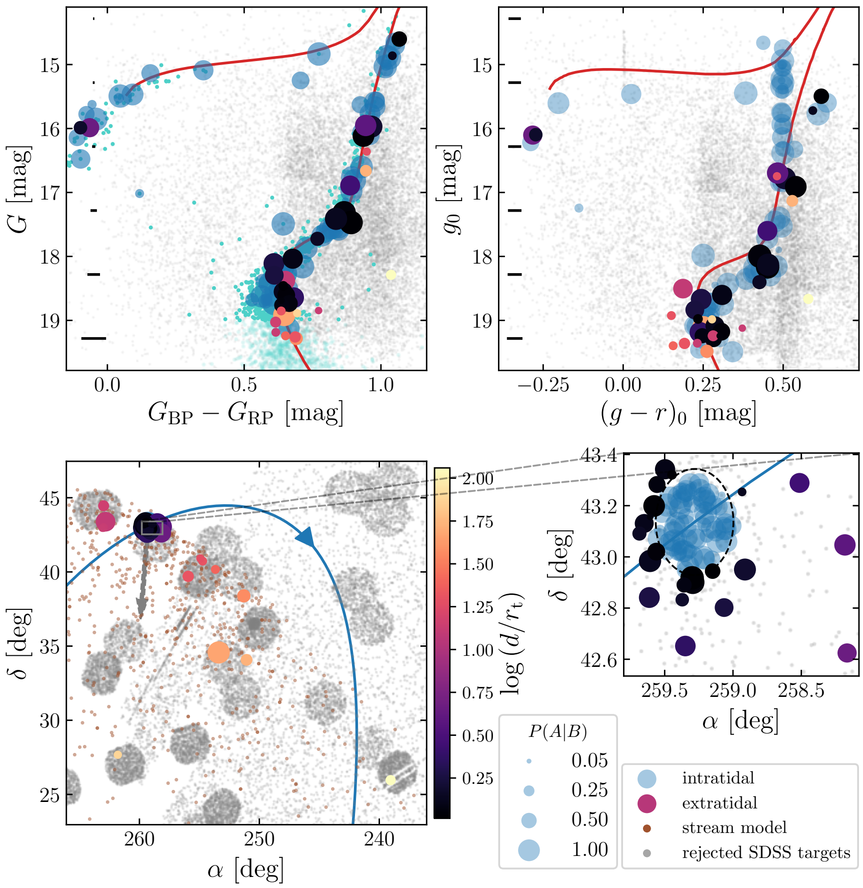

FIGURE IV.9: Same as Figure IV.7, but for M 92.

driven by the high-precision *Gaia* proper motions, which could not even remotely be equalled by available catalogs at the time of publication of the original study. At statistically significant parallax-based radial distances of 4.1 kpc and 4.7 kpc – as opposed to a cluster distance of 7.1 kpc – two stars can be ascribed to the foreground population and are excluded by this parameter alone.

4.1.2 M 92 (NGC 6341)

At [Fe/H] $= -2.35$ dex (Carretta et al. 2009), the GC M 92 is amongst the most metal-poor Galactic clusters known. Using photometric data, Testa et al. (2000) and Jordi & Grebel (2010) consistently reported on an extratidal halo for M 92. It is noteworthy that our debris model for this cluster is exceptionally scattered because of its rather close pericentric passages ($R_{\mathrm{peri}} \approx 0.17$ kpc) that result in a strong tidal field.

Figure IV.9 indicates the distribution in parameter space of our 110 potential M 92 associates, of which 35 are likely to be extratidal. Due to the low metallicity of the cluster, and its considerable proper motion in $\alpha \cos \delta$ direction (-4.9 mas yr^{-1}), it is straightforward to chemodynamically discern bona fide cluster associates from the fore- and background field stars and hence effectively diminish the false-positive detection probability. From the CMDs we find that – with the exception of one low-probability case at large angular separation – our candidates are consistent with the cluster isochrone and that they are distributed between the upper MS ($G \sim 19$ mag) and the upper RGB ($G \sim 14.5$ mag). Two stars fall on top of the blue HB of M 92. While nine candidates are borderline cases in terms of their distance to the cluster core ($d < 1.30\,r_\mathrm{t}$), 26 stars, mostly positioned south of the cluster, are clearly unbound at core separations of more than 1.3 tidal radii. Unfortunately, M 92 was placed on the northern edge of the SDSS plate such that any potential extratidal candidates in the immediate surroundings north of the cluster are missed by our analysis. The eastward elongation of the distribution of chemodynamically associated stars in the near-field surrounding the cluster shows a striking similarity to the photometric overdensity reported by Jordi & Grebel (2010).

Since our approach is density-insensitive and merely limited by the SDSS selection function, we can expand the search for cluster members out to larger separations. Moreover, omitting the clear contaminant from the CMD inspection, we associate 12 targets at $12.5 < d/r_\mathrm{t} < 75.2$ with M 92, thus expanding the previously known extension of the tidal debris from this GC.

4.1.3 M 3 (NGC 5272)

Of the 199 associates for M 3, we report on 17 probable candidates in the surrounding field star population that coincide with evolutionary stages between the cluster's upper MS, base of the RGB, and HB. The brightest extratidal star ($G = 15.8$ mag) shares the same region as the locus of intratidal HB stars. In fact, both Abbas et al. (2014) and Clementini et al. (2019) list this star as being a pulsating RR Lyrae star of type ab. The former authors provide a distance estimate of 10.99 kpc, which – lacking a proper attached error margin on that value – is hard to compare with the cluster distance of 10.2 kpc, although an association seems feasible. We performed our own analysis of the photometric time series available in the literature and furthermore corrected for the fact that, due to their pulsating nature, RR Lyrae do not straightforwardly reveal their systemic velocity from single-epoch spectra alone. A detailed description can be found in Appendix A.1. Our inferred value of 10.9 ± 2.6 kpc is in excellent agreement with the cluster distance. Kundu et al. (2019) present another two RR Lyrae stars that they associate with M 3. However, the search radius of these latter authors was restricted to $2/3 < d/r_\mathrm{t} < 3$, a circumstance that prohibited them from finding the variable presented here at $d = 9.4\,r_\mathrm{t}$.

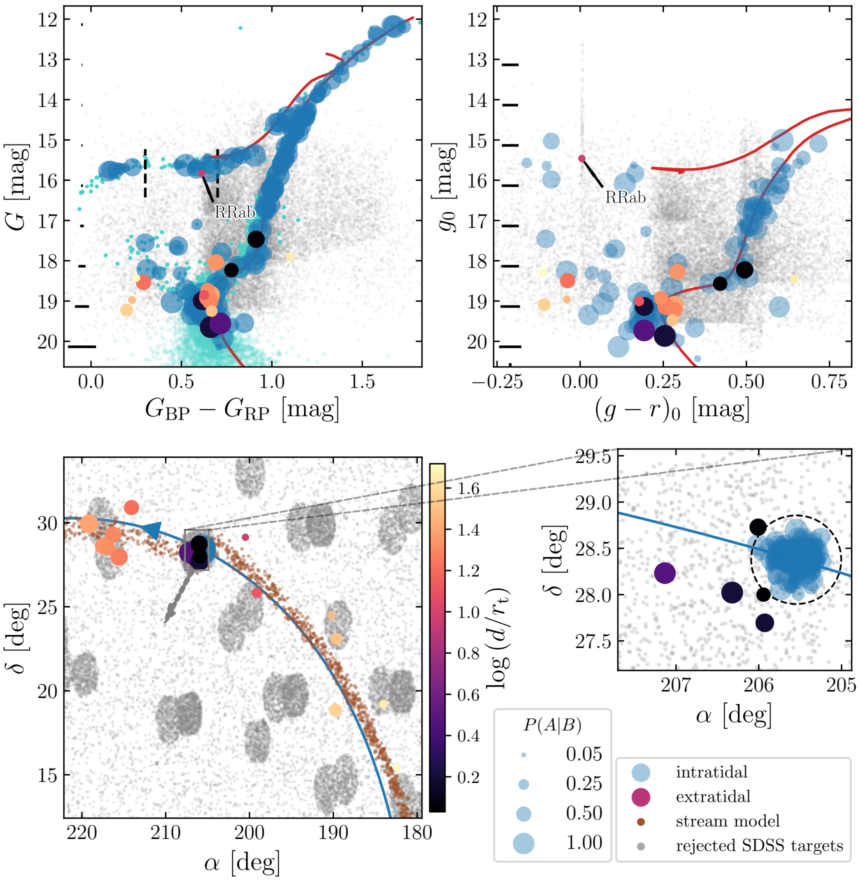

FIGURE IV.10: Same as Figure IV.7, but for M 3. The approximate color range of the instability strip from Clementini et al. (2019) is indicated in the *upper left panel* by vertical, dashed lines and the pulsating variable (see main text) is labeled "RRab". We note that the illustrated color and brightness for the RR Lyrae star are merely mean quantities, which may vary substantially over the pulsation cycle.

Among the presumably bound and unbound candidate stars, several reside blueward of the MSTO and subgiant branch (SGB) as can be seen in Figure IV.10. These could either be connected to false-positive associations or be genuine blue straggler stars (BSS). We favor the latter interpretation, as we do not see any particular reason for all random associations to be preferentially found on the blue- as opposed to the red side of the isochrone, even though the field star population is much more numerous in the red part. Our explanation is bolstered by the fact that the number of true BSS in M 3 is much larger than in M 13 (Ferraro et al. 2003) for example, where our treatment did not associate any potential blue straggler candidate.

Intriguingly, we found a strong degree of spatial alignment between the high-probability extratidal stars and the leading arm of the simulated tidal stream both in the near- and far-field around the cluster. Unfortunately, there are no SDSS plates covering the in-between regions and so the existence of a stream remains uncertain.

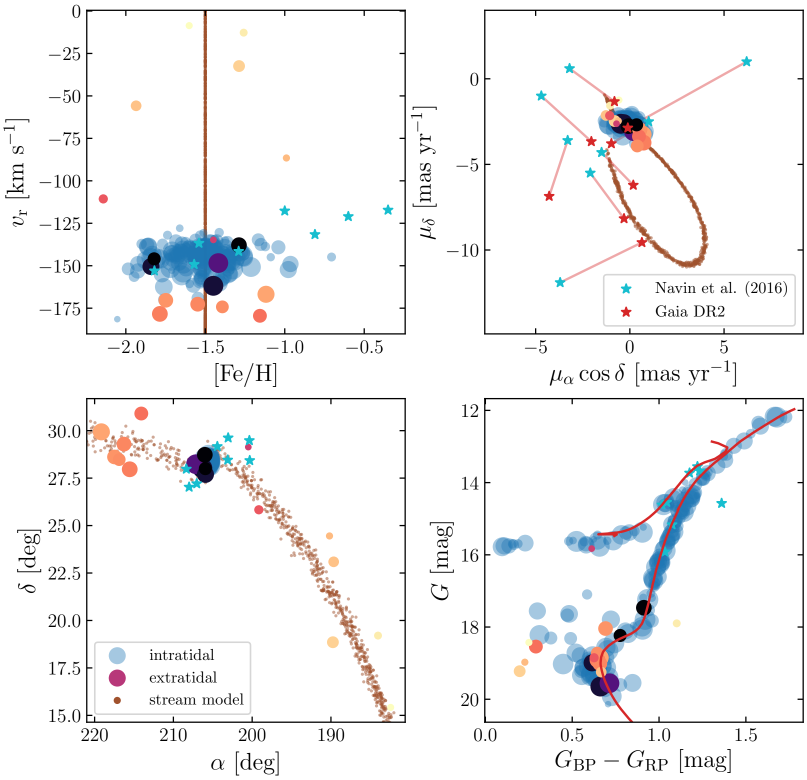

FIGURE IV.11: Same as Figure IV.8, but for M 3.

Navin et al. (2016) also found potential extratidal associates for M 3. Following the same approach and reasoning as in Section 4.1.1, we exclude previous membership for all eight with high confidence. Two stars can even be discarded based on their highly significant *Gaia* parallaxes which render them much closer than the cluster (7 kpc and 5.7 kpc compared to 10.2 kpc distance to M 3). The same graphical representation shown for M 13 in Figure IV.8 is presented in Figure IV.11 for M 3.

4.1.4 M 2 (NGC 7089)

M 2 is a halo ($R_{\mathrm{GC}} \sim 10.1$ kpc) GC with a complex chemical-enrichment history. Yong et al. (2014) and Lardo et al. (2016b), for example, suggested an accretion origin of this cluster, which may be the stripped core of a dwarf spheroidal galaxy based on observed anomalous spreads in iron and neutron-capture elements. Kuzma et al. (2016) detected a photometric stellar envelope surrounding M 2 beyond its tidal radius.

Our formalism yielded 77 associates including 11 extratidal candidates for M 2; three of which are uncertain to be truly unbound because of their small projected separations from the GC ($< 1.2\, r_{\mathrm{t}}$). While ten of the stars might be associated from a

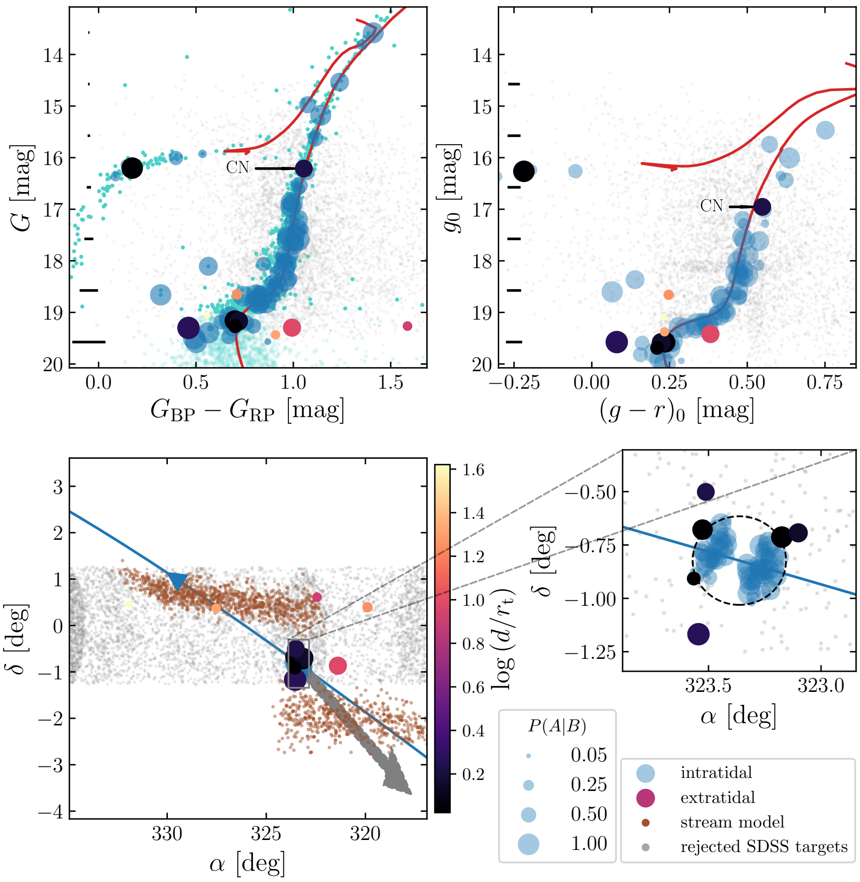

FIGURE IV.12: Same as Figure IV.7, but for M 2. The CN-strong star from Paper I is labeled "CN". The red outlier in the *upper left panel* is outside of the plotting range in the *upper right panel* as showing it ($g_0 = 20.71$ mag, $(g - r)_0 = 1.05$ mag) would strongly distort the diagram.

photometric point of view (see Figure IV.12), one candidate is consistently reported by both *Gaia* and SDSS to be redder than the cluster population at comparable brightness on the MSTO. A further two to three stars reside in the BSS region; at this point we can neither confirm nor reject their BSS nature. Owing to the sparse coverage of SDSS plates around M 2, we cannot draw firm conclusions with respect to the spatial distribution of extratidal halo stars for this GC. However, in the immediate surroundings, we can chemodynamically confirm the finding of Kuzma et al. (2016), who reported on a diffuse stellar envelope that extents out to at least $5\,r_{\rm t}$.

The only identified extratidal giant coincides with the parameter range of – and thus was analyzed in – Paper I; it was found to be CN-enhanced, again suggesting a large fraction of 2P stars in the group of escapees (see Section 4.5 for further discussion).

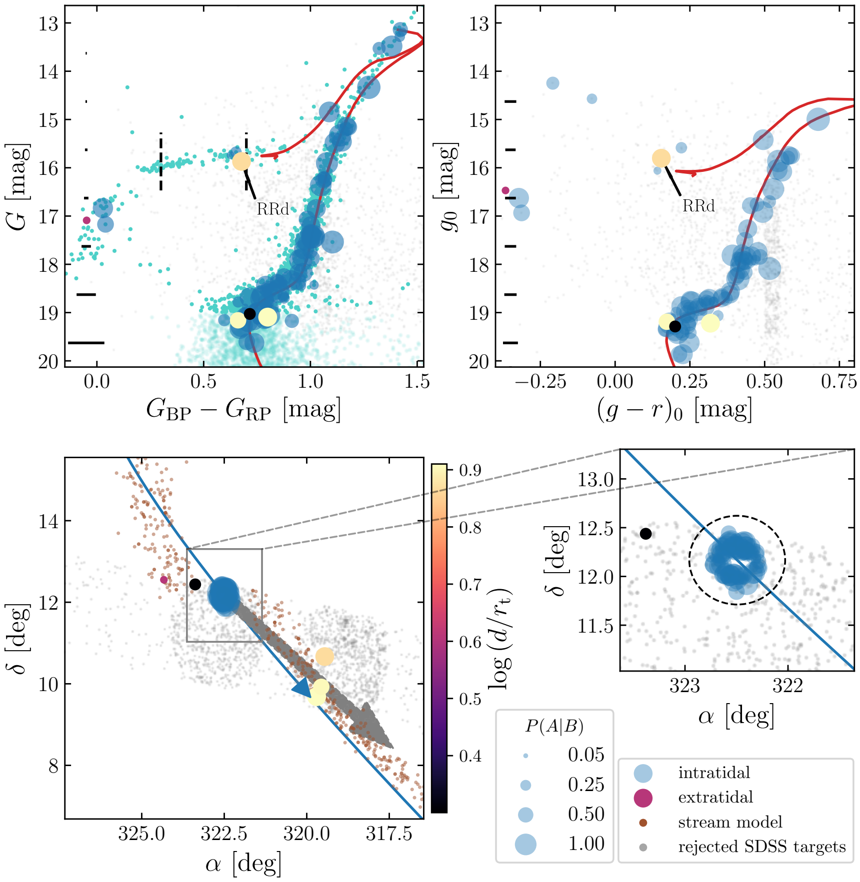

FIGURE IV.13: Same as Figure IV.7, but for M 15.

4.1.5 M 15 (NGC 7078)

At a slightly lower [Fe/H] than M 92, the cluster M 15 is the most metal-poor cluster for which we could identify associations. The region around M 15 is barely covered by SDSS plates (see Figure IV.13). Nevertheless, we find five halo field stars that are a chemodynamical match to this GC. All of them inherit an excellent photometric consistency with the cluster CMD on the MSTO and the blue and red HB. Thus, a cluster origin appears highly feasible.

The star falling in the instability strip is listed as variable in *Gaia* DR2. Nonetheless, it is not tabulated in either of the works by Drake et al. (2013a,b, 2014), nor in Abbas et al. (2014). We therefore performed our own light curve analysis (Appendix A.1) and found this star to be a double-mode RR Lyrae of type d. A distance of 9.5 ± 2.3 kpc was deduced, which places the star at a distance in good agreement with that of M 15.

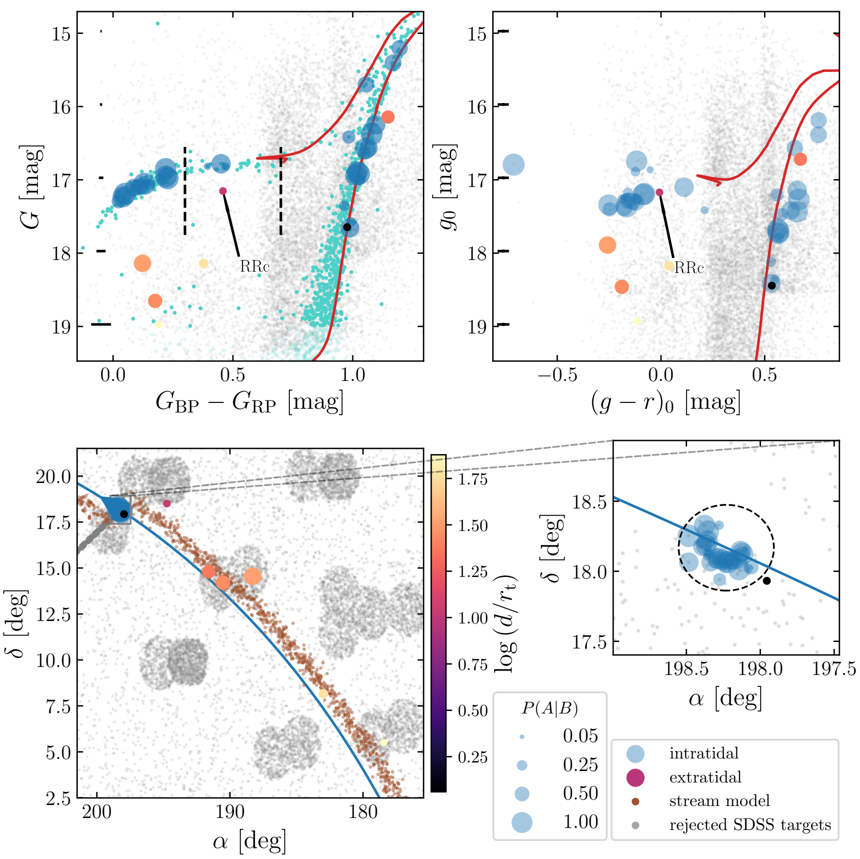

FIGURE IV.14: Same as Figure IV.10, but for M 53.

4.1.6 M 53 (NGC 5024) and NGC 5053

M 53 and NGC 5053 are two GCs at a low angular separation of 0.96 deg, even though their real spatial separation is about 1 kpc (Jordi & Grebel 2010). Law & Majewski (2010a) suggested that both clusters could be possible associates of the Sagittarius stream, while Forbes & Bridges (2010) speculate over the possibility of one or both of them being the nucleus of a disrupted dwarf galaxy. The former hypothesis has been refuted with high confidence by Sohn et al. (2018) using *Hubble* Space Telescope proper motions. Chun et al. (2010) report on extended overdensities for both clusters and claim the detection of a tidal bridge between them. However, Jordi & Grebel (2010) could not reproduce that finding.

Among the extratidal field star population around M 53, we found seven stars that – based on their kinematics and metallicity – may have originated in M 53. As can be seen in Figure IV.14, photometrically, two of the stars can be readily associated with the RGB. One star is fainter than the HB in G while being a perfect match in g_0, thus indicating photometric variability. Indeed, *Gaia* DR2 lists this star as variable and

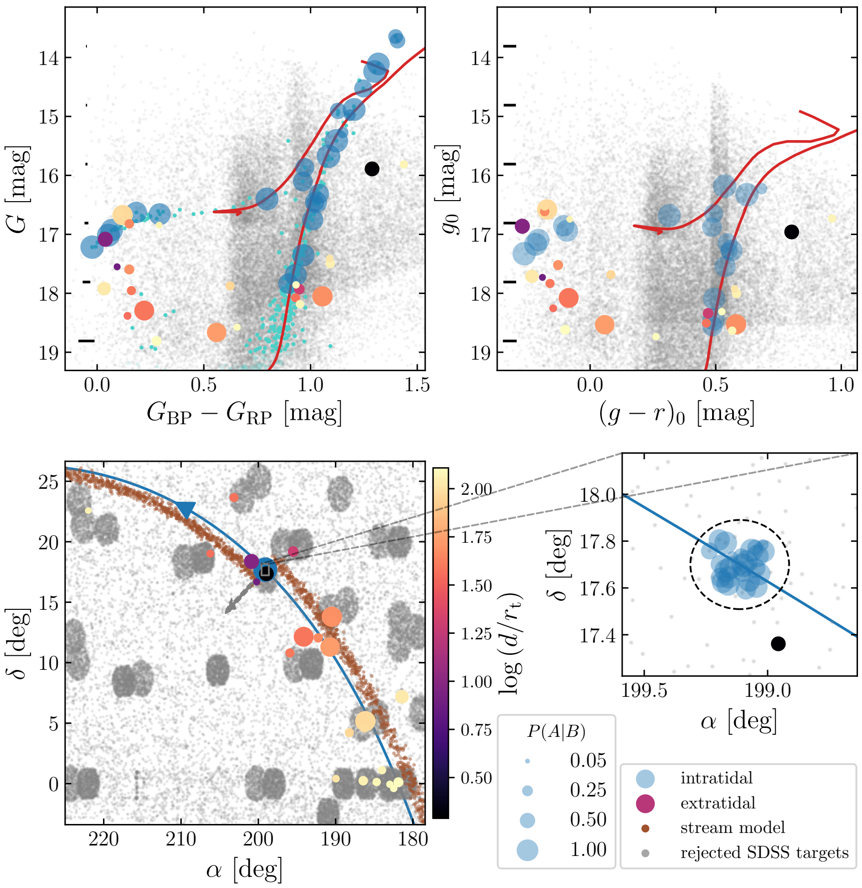

FIGURE IV.15: Same as Figure IV.7, but for NGC 5053.

Abbas et al. (2014) classify it as an RR Lyrae star of type c and provide a distance of 24.07 kpc. This appears marginally consistent with the cluster's distance of 17.9 kpc. Nevertheless, as for the RR Lyrae in Section 4.1.3, a comparison is prohibited in light of missing error margins. Our own analysis showed a distance of 20.1 ± 4.8 kpc, which is in agreement with that of M 53 within one error margin. Kundu et al. (2019) also reported on five extratidal RR Lyrae for M 53. Again, due to their restricting themselves to the immediate cluster vicinity, our target is not part of their list.

The remaining four extratidal associations with M 53 cannot be photometrically matched to either the RGB or the HB. Nevertheless, they cover the same colors and magnitudes as the comparably large number of intratidal stars of the BSS population that we attributed from *Gaia* kinematic properties alone (cyan dots in Figure IV.14).

For NGC 5053, we report on 24 plausible extratidal detections, 12 of which have their chemodynamical membership bolstered by a reasonable photometric match to the populations of intratidal members on the blue HB (five stars) and RGB (seven stars, see Figure IV.15). Two stars are clearly too red to be attributed to the cluster, while

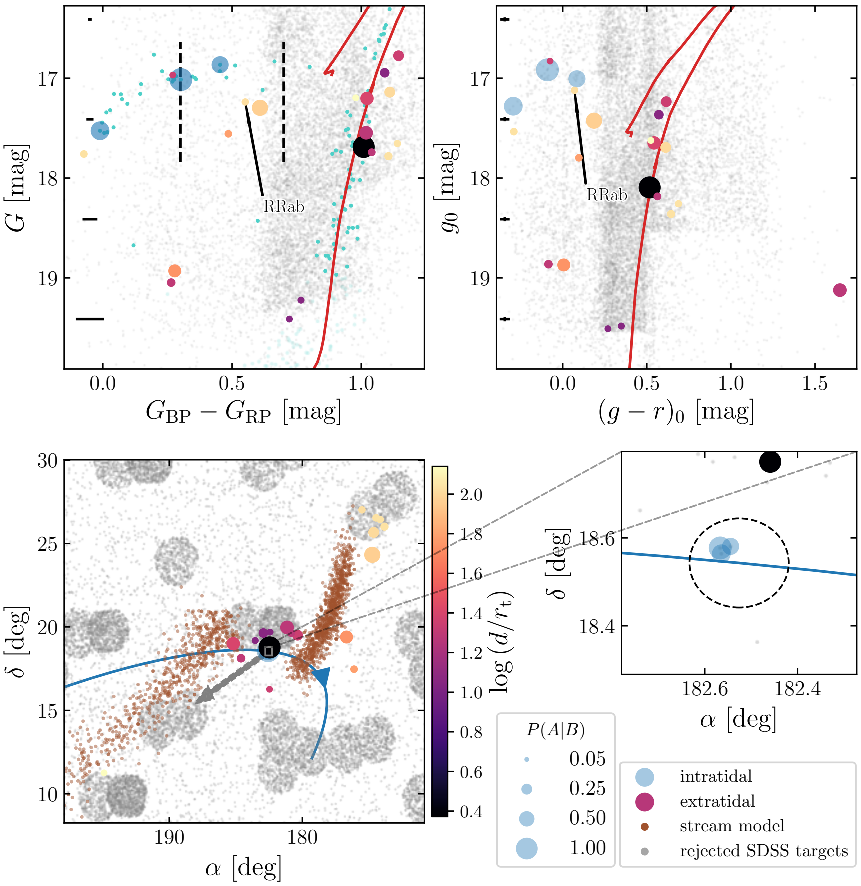

FIGURE IV.16: Same as Figure IV.7, but for NGC 4147.

ten others lie in the BSS region of the CMDs with their affiliation nature remaining spurious.

We emphasize that none of the associations are shared between the two clusters considered in this section. This does not necessarily exclude the possibility of a tidal bridge for two reasons: Firstly, we do not model such tidal interactions when simulating the streams. Hence, in the near-field of the clusters, the streams are spatially almost parallel and do not cross. The differences in v_r between the clusters exclude mutual associations. The second, more important reason is that the intercluster field was only covered by a few ($\sim$ 10) SDSS fibers, thereby tremendously reducing the chance of finding a potential bridge associate.

4.1.7 NGC 4147

NGC 4147 is an outer-halo (R_{GC} = 21.4 kpc) GC that has been suggested to be associated with the Sagittarius stream by Mackey & van den Bergh (2005). However, Villanova et al. (2016) cast some doubt on this by showing that the cluster is a closer match to the Galactic halo in terms of their respective chemical abundances. More recently, proper motion studies firmly rejected an association since the cluster is on a counter-rotating orbit with respect to Sagittarius (Sohn et al. 2018; Riley & Strigari 2020).

Owing to the faint nature of NGC 4147 (horizontal branch magnitude, $V_{\mathrm{HB}} = 17.02$ mag, Harris 1996), our approach can merely test targets that are as bright as the RGB of this GC. Of 19 extratidal candidates, we identified three associations that fall on top of the HB of the cluster. The reddest of these three is an RRab star at a distance of 22.0 ± 5.2 kpc[7]. The latter distance renders it consistent with NGC 4147 at 19.3 kpc. Most of the remaining associations (eight stars) were found to be on the upper RGB, whereas two stars below the HB, two stars redward of the RGB, and the five faintest candidates are likely to be false-positive detections judging from their photometric discrepancy from the intratidal *Gaia* sources.

4.2 Associating CN-strong stars with clusters and major merger events

We explored chemodynamical links of the sample of 112 CN-strong field stars from Paper I with the Galactic GC population through method II. Similar efforts have recently been made by Savino & Posti (2019) who used the similar but smaller sample of Martell et al. (2011). We emphasize that only 27 of the 63 cluster-star pairs reported by Savino & Posti (2019) can be directly compared to our study because the remaining ones lie outside of our stellar metallicity restriction of $-1.8 < \mathrm{[Fe/H]} < -1.3$ dex[8] (Paper I). Of these 27, only one is marginally attributable to their sample of best association candidates (<65% rejection confidence). The reason for the low overall overlap is that we find generally lower probabilities because we use the full distribution of actions instead of marginalized distributions for each of the three components.

Comparing each CN-strong halo star i with each cluster j yields a matrix p_{ij} with 16 800 entries. Figure IV.17 depicts this matrix in a representation where both rows and columns are sorted by increasing metallicity. Once again, we highlight the fact that a value for p close to unity does not necessarily imply high confidence in association, but rather that association cannot be rigidly excluded. In case of considerable ambiguities for the orbital parameters of a particular star – for example due to a highly uncertain distance – almost no cluster can be kinematically excluded

---

[7] (Drake et al. 2013a) reported a distance of 21.36 kpc for this star.

[8] We note that this rejection criterion excludes all potentially CN-strong stars that Savino & Posti (2019) reported to be on highly circular prograde orbits.

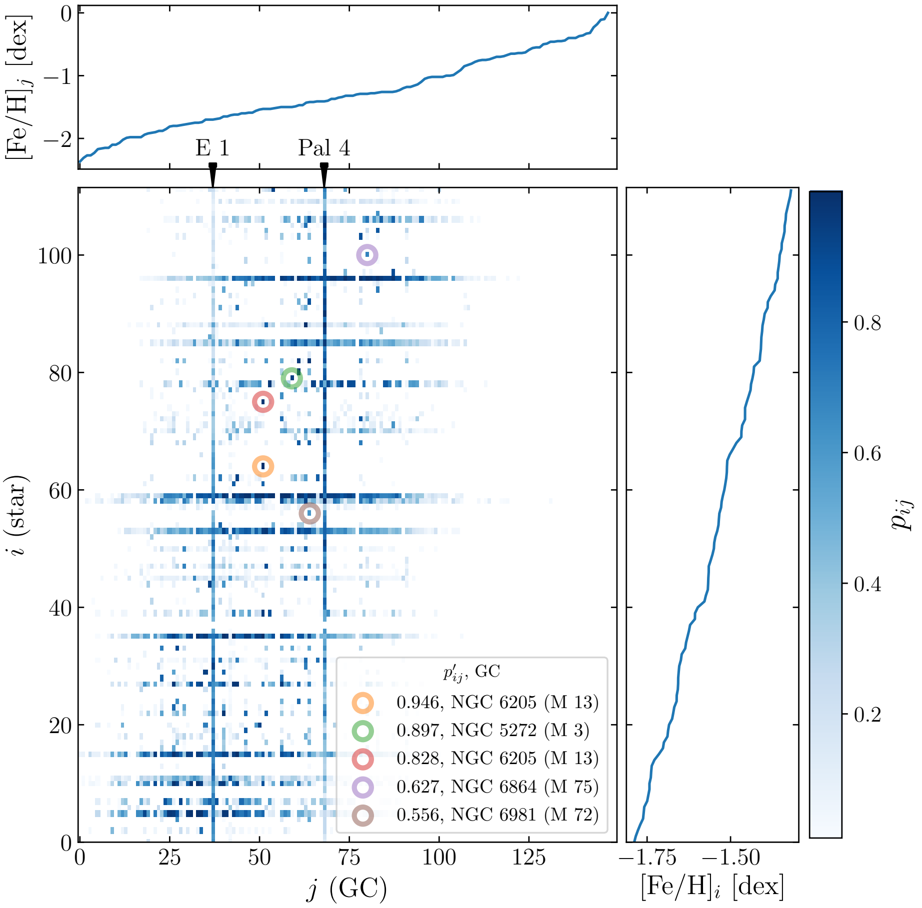

FIGURE IV.17: Graphical representation of the matrix p_{ij} with clusters on the abscissa and CN-strong stars on the ordinate. Both coordinates are sorted by increasing [Fe/H] as indicated by the *top* and *right panels*. The five pairs with highest modified confidence, p'_{ij} (Equation IV.9), are highlighted by colored circles and presented in the legend.

from being a former host. In such cases, p is entirely driven by [Fe/H] alone. In Figure IV.17 those manifest in rows essentially showing broad normal distributions with peak positions at the intersect of the stellar and cluster [Fe/H]. The latter are only occasionally interrupted by low- and high-p columns representing GCs in the outermost regions of the Galaxy and the GCs E 1 and Pal 4, respectively. The latter have loosely constrained orbits themselves, and therefore we do not consider these two clusters in the following.

Inverting the above reasoning implies that pairs (i, j) are good association candidates if they have a high attributed p, while at the same time $p_{ij} / \sum_j p_{ij}$ is strongly peaked. Hence, each cluster can in principle have an arbitrary number of stellar associations whilst to be considered as part of a good pair, each star should have a strongly limited number of attributable clusters. This leads us to the modified quantity:

$$p'_{ij} = \frac{p_{ij}^2}{\sum_j p_{ij}}. \tag{IV.9}$$

In total, 145 pairs were found to satisfy $p'_{ij} > 0.05$, whereas only 15 posses values above 0.32. The five pairs with highest p' are highlighted in Figure IV.17 and the whole list can be found in Table A.1. We recover all four associations of CN-strong stars to the GCs M 13 and M 2 that were presented in Section 4.1. In case of the association with M 2, there are two additional clusters that come into question given their action integrals (M 22 and ESO 280-06). Given the spatial coincidence with M 2 – which did not enter the present analysis – we favor association with this cluster.

Of the 145 reported star-cluster association pairs, 26 involve GCs that were proposed to have possibly been accreted as part of either Gaia-Enceladus (Myeong et al. 2018) or the Sequoia merger event (Myeong et al. 2019); an observation that represents tentative evidence that the involved CN-strong stars were donated by those galaxies. The pairs are indicated in Table A.1. Moreover, among the 15 strongest ($p'_{ij} \geq 0.32$), three pairs involve the bona-fide Enceladus clusters M 75 and NGC 1261. Overall, we found that most, namely 23, pairs are accounted for by Enceladus clusters such as M 2, while only three pairs with low association probability (≤ 0.08) involve Sequoia GCs. We caution that several stars have associations not only with clusters from the two merger events but with other clusters, too. One star, *Gaia* DR2 6032023568562302 72, at the same time shows associations with two Enceladus GCs (M 79 and NGC 1851) and one Sequoia cluster (NGC 3201), although with generally low probabilities.

We confirm the finding by Savino & Posti (2019) that a substantial fraction (here 38%) of the CN-strong stars from the sample seemingly cannot be chemodynamically associated with any of the known GCs. We recall here the three reasons these latter authors proposed for this observation under the restrictive assumption that GCs are the only birth site of these chemically peculiar stars: The first, rather unlikely option is that the hitherto unassociated stars could originate from yet-to-be-discovered clusters that are concealed by the high-extinction regions of the Galactic disk or bulge. Secondly, the stars in question could stem from already entirely dissolved clusters. Finally, the stars could have originated from one of the known GCs without retaining the orbital characteristics of the cluster. For this latter case, Savino & Posti (2019) offer two highly plausible explanations involving high ejection velocities due to three-body interactions or an early escape from the cluster followed by a drastic change of the Galactic potential due to, for example, a major merger. In order to address the former scenarios, it is of utmost importance to establish a ground truth by rigidly confirming the CN-strong nature of the targets using spectroscopic follow-up analyses that could reveal other light-element anomalies.

4.3 Associations around CN-strong field stars

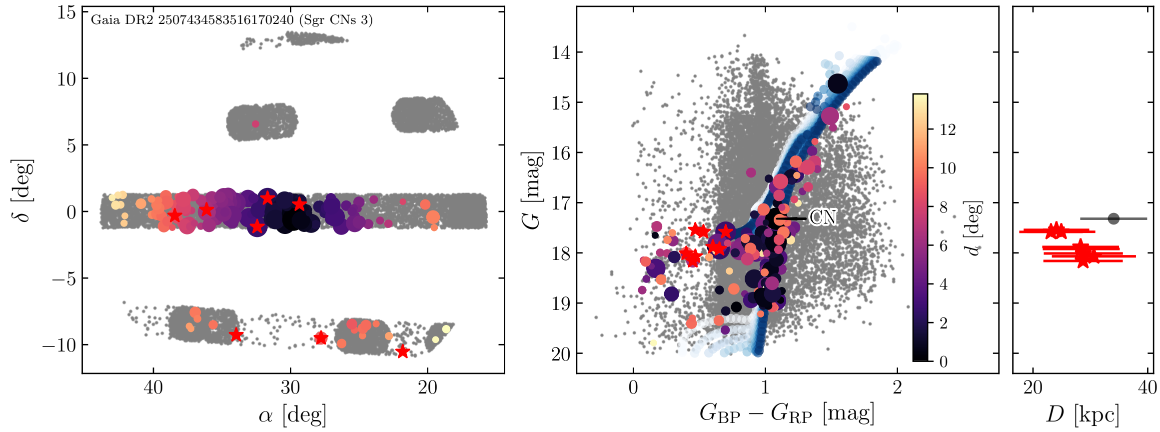

FIGURE IV.18: Graphical representation of the population that was chemodynamically associated with the CN-strong star *Gaia* DR2 2507434583516170240 (Sgr CNs 3). The color coding and circle sizes have the same meaning as in Figure IV.7. Additional red stars indicate the identified RR Lyrae variables (see main text). *Left panel*: position on the sky on top of rejected stars from the SDSS footprint (gray dots). *Middle panel*: photometric associations in the *Gaia* CMD. To guide the eye, isochrones that represent ages from 4 to 13 Gyr (white to dark blue) at the mean [Fe/H] of the population are shown as reference. The CN-strong star is labeled "CN". *Right panel*: RR Lyrae *G* magnitudes and their inferred distances (red stars) in comparison to the spectrophotometric distance of the CN-strong star (black circle, see Section 3.2).

Of the 112 investigated stars, method III revealed 81 groups with at least two – possibly, but not necessarily CN-normal – additionally associated stars. Of these groups, 69 comprise five or more stars, whereas 51 still consist of at least ten stars in excess of their respective CN-strong candidate. Naturally, we recover a large number of intratidal targets for the four extratidal CN-strong stars in the vicinity of M 13 and M 2 that were reported in Section 4.1.

All remaining CN-strong stars have no obvious direct connection to any cluster. Nevertheless, many of the chemodynamically linked groups of stars can be photometrically attributed to the same stellar population even in the absence of a cluster (see Figure IV.18 for an example). Since our selection function is not only spatially inhomogeneous but also strongly biased towards the brighter evolutionary stages, many associated stars coincide with the HB in the CMDs of the latter populations. For candidate variable stars that fall in the instability strip, we performed the analysis outlined in Appendix A.1 and recomputed the Mahalanobis distance using updated values for v_r. This way, we were able to associate 31 already known RR Lyrae stars (Drake et al. 2013a,b, 2014; Abbas et al. 2014) and add one more RRc-type pulsator.

TABLE IV.3: Stars that were chemodynamically associated with CN-strong giants (method III).

Gaia DR2 source ID	$\alpha^{(a)}$ [deg]	$\delta^{(a)}$ [deg]	r [deg]	ϖ [mas]	$\mu_\alpha \cos\delta$ [mas yr^{-1}]	μ_δ [mas yr^{-1}]	v_r [km s^{-1}]	[Fe/H] [dex]	$P(A/B)$	G [mag]	$G_{BP} - G_{RP}$ [mag]	RRx$^{(b)}$	D_{RR} [kpc]
Gaia DR2 4018168336083916800 (Sgr CNs 1)													
4018168336083916800$^{(c)}$	175.083	27.533	0.0	0.05 ± 0.12	-1.4 ± 0.1	-1.0 ± 0.2	-63.0 ± 5.2	-1.40 ± 0.17	1.00	16.67	1.18		
4017874216723852672	175.438	26.772	0.8	0.00 ± 0.18	-1.3 ± 0.3	-1.3 ± 0.2	-67.2 ± 5.4	-1.13 ± 0.18	0.47	17.91	1.07		
4004075586313197312	175.879	23.347	4.2	-0.22 ± 0.34	-1.7 ± 0.4	-1.2 ± 0.3	-53.5 ± 7.4	-1.41 ± 0.16	0.43	18.14	0.90		
3951337858979970560	181.428	20.513	9.1	0.01 ± 0.05	-1.3 ± 0.1	-1.0 ± 0.1	-56.2 ± 5.1	-1.33 ± 0.16	0.41	15.68	1.47		
4017707606352394880	174.097	26.485	1.4	0.04 ± 0.17	-1.4 ± 0.2	-1.2 ± 0.3	-77.0 ± 5.7	-1.61 ± 0.17	0.38	17.60	1.12		
3951642591203760384	182.275	20.433	9.7	-0.00 ± 0.18	-1.3 ± 0.3	-0.9 ± 0.2	-49.9 ± 5.4	-1.39 ± 0.17	0.26	17.94	1.12		
3950619942311040000	183.795	19.849	11.1	0.18 ± 0.18	-1.6 ± 0.3	-1.1 ± 0.2	-71.6 ± 6.2	-1.32 ± 0.16	0.23	18.04	0.85		
3950348916990151296	183.925	19.179	11.6	0.12 ± 0.11	-1.6 ± 0.2	-1.0 ± 0.2	-63.5 ± 5.2	-1.26 ± 0.17	0.23	16.55	1.33		
3999380469799933952	180.989	20.676	8.7	0.08 ± 0.18	-1.7 ± 0.3	-0.9 ± 0.4	-60.2 ± 5.4	-0.94 ± 0.16	0.19	17.87	1.16		
3960517711624629632	188.877	25.658	12.5	-0.07 ± 0.29	-1.7 ± 0.3	-1.0 ± 0.2	-53.0 ± 15.6	-1.45 ± 0.19	0.18	18.40	0.47	RRab^1	34.2 ± 8.3

Notes. The full table will be made publicly available through the CDS. $^{(a)}$ Coordinates are in the *Gaia* DR2 reference epoch J2015.5. $^{(b)}$ RR Lyrae references: (1): Drake et al. (2013a). (2): Drake et al. (2013b). (3): Drake et al. (2014). (4): Abbas et al. (2014), (5): This study. $^{(c)}$ Classified CN-strong in Paper I.

Unfortunately, a number of factors prevented a straightforward automated classification for the degree of belief in true photometric association. Among these are the occasionally high rate of obviously spurious associations and the ambiguity of the distance modulus in the absence of significant parallaxes and/or attributed RR Lyrae stars. We present those 17 groups that passed a visual inspection. Their CMDs and spatial distributions can be found in Figures IV.18 and A.2 through A.17, while the relevant information about individual stars is presented in Table IV.3. Among all CN-strong stars, only *Gaia* DR2 615481011223972736 and *Gaia* DR2 634777096694507776 (cf., Figures A.14 and A.16) were pairwise attributed to each other using method III, which provides evidence that they may share the same birth place.

For five of the groups of associated stars, the CN-strong star was attributed to at least one of the Enceladus clusters through method II. However, four of those only have very low association probabilities, which is why we do not propose an Enceladus membership. The remaining star, *Gaia* DR2 3696548235634359936, generates the sixth strongest among all star-cluster associations ($p^{'}_{ij} = 0.54$), the involved cluster being NGC 1261. Nonetheless, it is noteworthy that Myeong et al. (2018) classified this cluster as merely a possible member of Enceladus whilst eight additional GCs were labeled probable members.

4.4 Associations to the Sagittarius stream and M 54

We found four of our high-confidence groups of associations from the previous section to coincide with the Sagittarius (Sgr) stream. For further reference, we label the groups Sgr CNs 1 to 4. Fortunately, all four have at least one attributed RR Lyrae star, thus enabling a meaningful 6D phase-space characterization. Figure IV.18 exemplarily illustrates the tight photometric consistency for Sgr CNs 3, while in

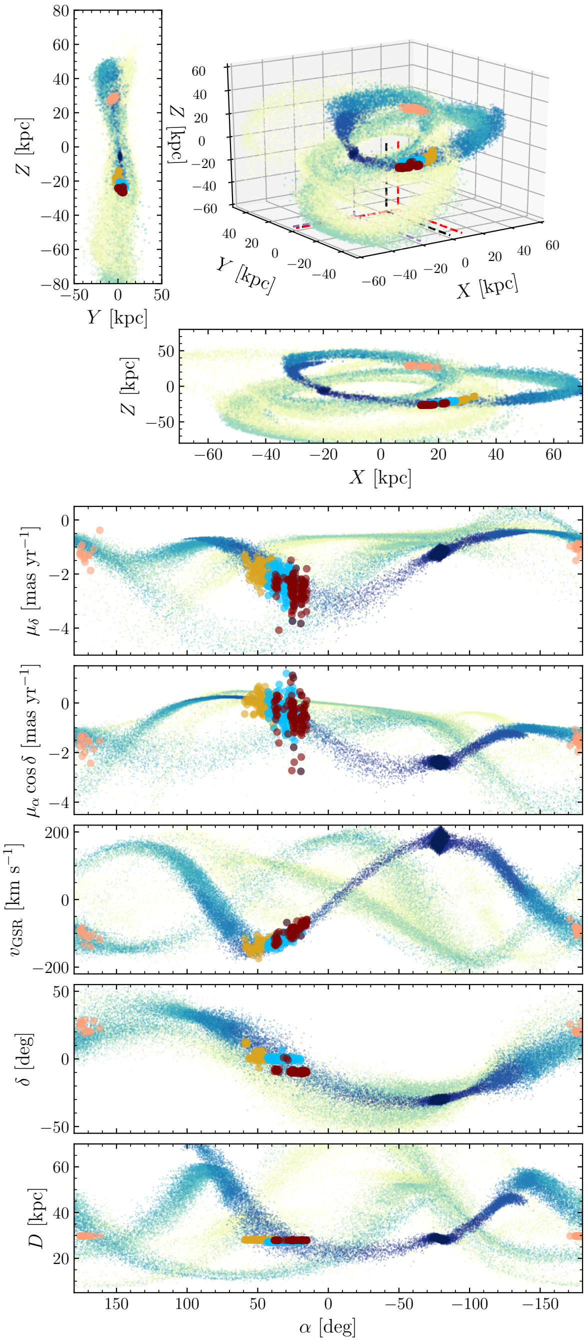

FIGURE IV.19: Multi-parametric representation of four populations of chemodynamical associations with CN-strong giants (salmon, yellow, dark red, and light blue circles) on top of the debris model of the Sgr stream in a triaxial halo by Law & Majewski (2010b). The latter is depicted by dots where increasing color lightness denotes a longer elapsed time since becoming unbound from the Sgr main body. *Top*: 3D position in Cartesian, Galactocentric coordinates. Dashed red, black, and violet lines indicate the positions of the Sun, the Galactic center, and the Sgr main body, respectively. *Bottom panels*: projections in all six dimensions of positional and kinematic observables. For the *bottom panel*, we assumed all stars to reside at exactly the same D as inferred from the mean RR Lyrae distance for each population.

Figure IV.19 we present various population representations on top of the N-body simulation of the tidal disruption of the Sgr dwarf spheroidal galaxy in a triaxial MW halo by Law & Majewski (2010b). The phase-space comparison places our agglomerations right on top of the dynamically young portion of the leading and trailing arms of the stream. On the basis of the simulated model parameters – under the assumption of true association – the stars became unbound from the Sgr main body no longer than 3 Gyr ago.

From a chemical point of view, the metallicities of the four involved CN-strong stars cover a narrow range from -1.51 to -1.40 dex and thus – within their errors – are fully consistent with the mean [Fe/H] of M 54 (-1.45 dex, e.g., Bellazzini et al. 2008). This observation suggests that four chemically altered giants and potentially a considerable fraction of their associates identified here originated from the massive GC M 54. Indeed, one of the four involved CN-strong stars – namely *Gaia* DR2 2507434583516170240, giving rise to the association Sgr CNs 3 – has already been linked to this cluster based on its position in action space (method II), though with very low confidence (0.08). We suspect that the reason for the latter is to be found in the main flaw of the assumptions in Section 4.2, that is, the fact that actions of potential cluster escapees do not necessarily have to be exactly identical to the cluster itself; otherwise, they would never have been able to become unbound in the first place.

4.5 The fraction of chemically altered stars amongst bona-fide escapees

In Paper I we investigated the fraction of CN-strong stars in our sample of analyzed halo stars to estimate the fractional GC contribution to the stellar inventory of the Galactic halo, $f_{\mathrm{h}}^{\mathrm{GC}}$. The outcome of this assessment, among other factors, depends on the assumed fractions of chemically normal 1P stars with respect to the total number of escapees ($N_{\mathrm{1P}}/N_{\mathrm{tot}}$), resulting in a corridor for the overall GC contribution to the halo between 8.5% and 12.5%. As discussed in detail in Paper I, several values for $N_{\mathrm{1P}}/N_{\mathrm{tot}}$ have been proposed for the still bound stellar populations of GCs. For instance, Carretta et al. (2009) and Bastian & Lardo (2015) reported 50% and 32%, respectively, irrespective of GC properties. Milone et al. (2017) found a dependency on the present-day mass of the clusters. Here, for the first time, we elaborate on the average $N_{\mathrm{1P}}/N_{\mathrm{tot}}$ in the collection of escaped stars in the Galactic halo by employing our established chemodynamical links.

Methods I and III revealed new potential GC escapees in the halo field star population

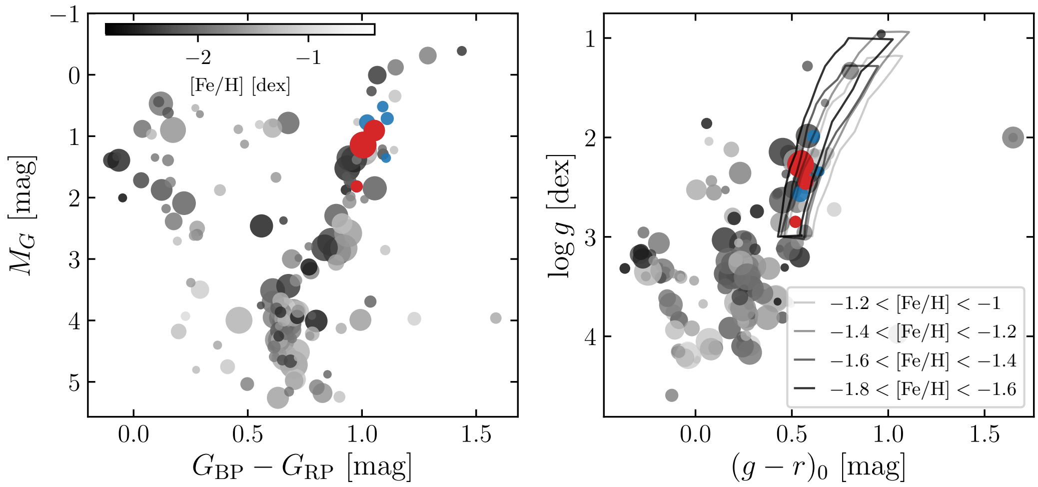

FIGURE IV.20: *Gaia* CMD (*left*) and Kiel diagram (*right*) of all association candidates from method I. For the absolute magnitude, M_G, we computed a distance modulus under the assumption that all stars reside at exactly the same distance as their potential former hosts. Dark gray to light gray colors indicate the stars' metallicity according to the color bar, while the point size mirrors the calculated association probability. The metallicity-dependent polygons used for pre-selection in Paper I are depicted in the *right panel*. Associated stars which at the same time obey these selection cuts are shown in blue. Red circles depict the four CN-strong stars that are likely associated with M 13 and M 2, respectively.

that are either directly chemodynamically linked to a cluster or – adopting the assumption that GCs are the only production sites of CN-strong stars – can be associated with a CN-strong star. Here, we account for the fact that the candidates cover a broad range of evolutionary stages, while Paper I focused exclusively on the RGB. Hence, the newly discovered sample was cleaned to match the selection criteria outlined in section 2.1. of Paper I. Briefly, the targets were split into metallicity bins and the exact same fiducial regions for the RGB in a log g-$(g-r)_0$ diagram were employed. Most RGB stars with an established chemodynamic link in this study are lost for the present analysis as they fall outside of the stringent metallicity corridor applied in Paper I ($-1.8 <$ [Fe/H] < -1.3 dex[9]). As a result, our calculations exclude, for example, the metal-poor cluster M 92 with its many associations on the RGB. Despite reducing the statistical significance, restricting the sample to the RGB confers the coincidental advantage that spurious associations can be considered less likely as the involved stars are brighter than, for example, the upper MS. This results in higher precision in the astrometric quantities [Fe/H] and v_r and therefore stronger discriminatory power.

Figures IV.20 and IV.21 illustrate the subsample obtained in this way for methods I and III. We note that we see no reason to suspect that 1P and 2P stars would have

---

[9] In hindsight, this should have accounted for the tremendously underestimated errors in `SSPP` since even a mono-metallic population (e.g., a GC) at exactly [Fe/H] $= -1.55$ dex would lose a substantial amount of stars just based on this cut.

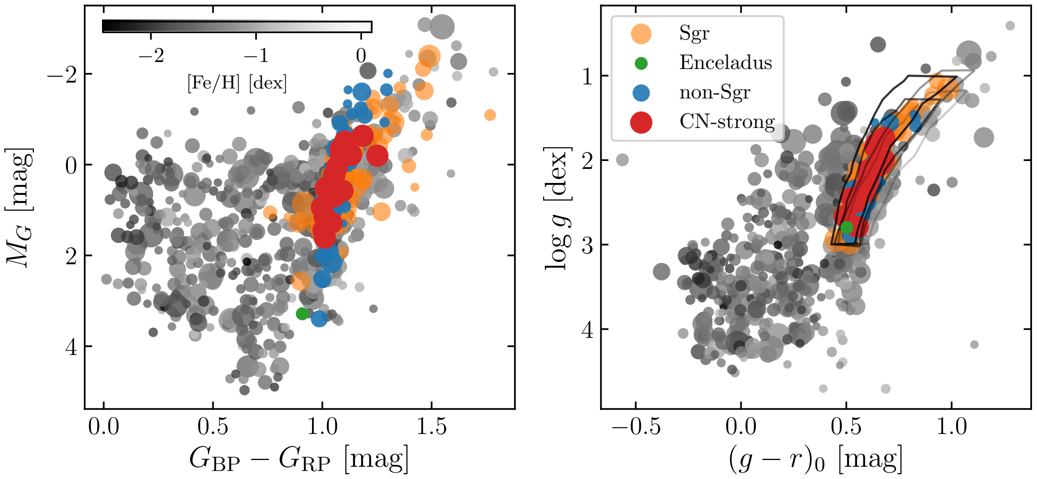

FIGURE IV.21: Same as Figure IV.20 but for associations around CN-strong stars (method III). Here, M_G was computed using the spectrophotometric distances of the CN-strong stars as outlined in Section 3.2. Orange and green circles show the associations with the Sgr stream and Gaia-Enceladus that obey the selection criteria of Paper I but were not considered in estimating the fraction $N_{\mathrm{1P}}/N_{\mathrm{tot}}$.

been subject to different selection functions in the SDSS fiber placement, which was solely based on pre-selection from SDSS photometric broad-band filters which in turn are not sensitive to light-element anomalies. Given that method III cannot firmly distinguish between former 1P GC stars and stars stripped from the Sgr dwarf spheroidal galaxy, we excluded the four involved CN-strong stars and their associations. The same argument holds for the population that was tentatively associated with Gaia-Enceladus (Section 4.3), which is why we exclude the CN-strong star and its one associated giant obeying the selection criteria, too. Having identified four bona-fide 1P and four 2P stars through method I and 48 1P and 12 2P stars from method III, we calculated $N_{\mathrm{1P}}/N_{\mathrm{tot}} = 50.0 \pm 16.7\%$ and $80.2^{+4.9}_{-5.2}\%$, respectively. The values and error margins are taken from the median, 15.9th, and 84.1th percentiles of distributions that were generated in a Monte Carlo (MC) analysis using 10^7 random draws from Poisson distributions for the involved counting statistics. The two resulting distributions can be found in Figure IV.22 where we also show the findings reported for bound cluster stars that were mentioned earlier in this section.

Interestingly, in the near-field around clusters (i.e., using method I), the first-generation fraction appears to balance the second-generation fraction, and is therefore broadly consistent with the present-day cluster findings by Carretta et al. (2009) and Bastian & Lardo (2015), and with the majority of the analyzed clusters of Milone et al. (2017). Moving away from the GCs, that is, to regions in the halo without a direct spatial link to any GC, $N_{\mathrm{1P}}/N_{\mathrm{tot}}$ seems to increase considerably. While it is tempting to claim a solid finding, in particular in light of the low attributed statistical errors from method

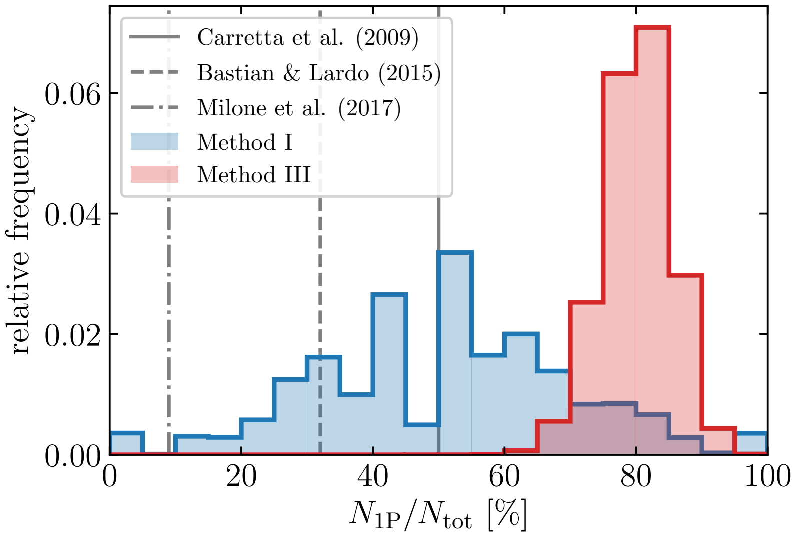

FIGURE IV.22: Result of an MC simulation with 10^7 realizations for the deduced fraction of first-generation stars among all potential GC escapees obeying the selection function in Paper I (Figures IV.20 and IV.21). Here, the blue and red histograms represent the findings from methods I and III, respectively. For comparison, we indicate the fractions for bound cluster stars as reported by Carretta et al. (2009, solid vertical line), Bastian & Lardo (2015, dashed vertical line), and the lowest value from Milone et al. (2017, dash-dotted vertical line).

III, we discuss here two effects that may lead to biases in the estimates.

The first possibility is that some of the CN-strong stars could have originated in a cluster that was part of an accreted, now entirely disrupted dwarf galaxy (other than Sgr, Gaia-Enceladus, and Sequoia) with its own system of GCs. Therefore, much like already seen in the five CN-strong stars of the Sgr stream and (possibly) Gaia-Enceladus, the stars associated with those CN-strong stars would not only share the chemodynamical information of the cluster escapees but that of the stars of the galaxy as well[10]. Vice versa, while being characterizable as ex-situ, associates of the CN-strong stars would not necessarily be of GC origin. As a consequence, the number of chemically normal stars that are erroneously classified as 1P stars would be artificially increased, which in turn would lead to a higher N_{1P}/N_{tot}. Evidence for CN-bimodalities amongst the dSph field star populations is sparse (e.g., Smith & Dopita 1983; Lardo et al. 2016a; Norris et al. 2017; Salgado et al. 2019). However, several GCs in the MW have been associated with dwarf-accretion events. It is equally likely that GCs that were part of dSphs have dissolved into their field star populations (prior to their merger with the MW; see Malhan et al. 2019) meaning that the presence of CN-strong stars within dSphs could be expected, provided that

---

[10] Since the now disrupted galaxy was not necessarily chemically homogeneous, this statement is restricted to those stars from the galaxy's potentially broad metallicity distribution function that share the CN-strong stars' [Fe/H].

the GCs of dSphs follow the same trends as the in-situ population of the MW (e.g., Hendricks et al. 2016).

Another source of increased false-positive rates for 1P stars are spurious associations from the in-situ population of halo stars. However, this latter possibility seems rather unlikely given the independent finding of tight photometric consistency even outside of the selection bounds, whereas halo interlopers could in principle occupy any position in the CMD.

Bearing in mind all the caveats mentioned above, taken at face value, our high N_{1P}/N_{tot} for the halo far away from GCs could imply that 1P stars were preferentially lost during early cluster dissolution while 2P stars were more easily retained. This would provide support for early mass-loss scenarios that commonly assume that only 1P stars are lost (e.g., D'Ercole et al. 2008, see also the review by Bastian & Lardo 2018 and the discussions in Paper I). Alternatively, assuming that GC mass loss affects both 1P and 2P stars to the same extent (Kruijssen 2015) and considering the inverse mass dependency of the now-observed occurrence rate of 1P stars following Milone et al. (2017), low-mass clusters could have contributed the majority of the former GC stars now found in the halo. For the fraction of halo stars donated by GCs, the findings presented here, in concert with the formalism outlined in section 5.1. of Paper I, yield $f_{\rm h}^{\rm GC} = 10.5 \pm 0.7\%$ and $11.8 \pm 0.2\%$, assuming either the 1P fraction for the cluster vicinities or for the general halo, where we adopted an early mass-loss rate of 56% and an average present-day cluster mass of $2.2 \cdot 10^5\,M_\odot$ (see Paper I, for detailed discussions).

5 Summary and Conclusions

In this chapter, we investigate the connection between GCs and the stellar component of the Galactic halo in order to contribute to our understanding of how this old component of the Galaxy was formed. To this end, we explore chemodynamical links between halo field stars and the present-day cluster population using combined data from the SDSS/SEGUE and BOSS surveys as well as from the *Gaia* mission. We created a dataset that allows for the characterization of about $3 \cdot 10^5$ stars through their full phase-space vectors and chemistry (by means of metallicity). As realistic error budgets are key to our probabilistic approaches, uncertainties on SDSS radial velocities and metallicities were reassessed using well-constrained cluster populations and as a consequence considerably increased. The most important ingredient of our study is the characterization of 112 giant stars in the halo that in our previous study (Koch et al. 2019) were found to be chemically peculiar in the sense that they show atypically high nitrogen abundances. In the present investigation, we build upon the assumption that the environmental conditions required for the production of such peculiar chemical characteristics are unique to GCs, the only sites where an abundant occurrence of these 2P stars has been found so far.

Our analysis focuses on three techniques that can be distinguished by the stringency they impose on the precision of the input data. The first approach is restricted to the immediate volumes around current cluster positions, where a solid distance estimate – made using significant parallaxes – is not strictly required. In this case, field stars were associated using only six parameters (two spatial and three velocity coordinates as well as [Fe/H]). The confidence in true association was independently solidified by the fact that the associated stars show a remarkably close match to the still bound populations of stars. The second method uses action integrals to tie CN-strong stars to clusters under the presumption that cluster escapees retain their kinematic memory. A spatial coincidence with the clusters is not required at the expense of a much stronger demand in terms of well-constrained distance estimates. This prohibits a wider applicability for distant halo stars in excess of the 112 CN-strong stars, for which we inferred spectrophotometric distances. Nevertheless, we discuss several persistent systematic uncertainties that may have considerable impact on such measurements. The third and final tagging approach adopted throughout this work was used to single out stellar populations in the near-field of CN-strong stars that share similar chemodynamical properties. It may therefore be feasible that those populations stem from the same birth place, that is, GCs.

In total, we established direct chemodynamical links in the near field of eight clusters (NGC 4147, M 53, M 3, M 13, M 92, M 15, M 2) for 789 stars. While the projected distances of 638 stars are found to reside within the clusters' tidal radii – thereby rendering them likely bound cluster members – 151 can be denoted extratidal. Among the escapees, we qualitatively recover structures that resemble the results of previous photometric studies identifying extratidal envelopes (e.g., Jordi & Grebel 2010). The associations are spread over a wealth of evolutionary stages and metallicities (e.g., four of the eight GCs are more metal-poor than −2 dex). Nonetheless, eight giant stars share the same selection function as required in Koch et al. (2019), and four of these are recognized as being CN-strong. From this, based on the low number statistics at hand, we estimate the fraction of 1P stars among the close-by escapees to be $N_{1P}/N_{tot} = 50.0 \pm 16.7\%$, which is broadly in line with the results of studies that were dedicated to estimating this fraction in nowadays observable cluster populations (Carretta et al. 2009; Bastian & Lardo 2015; Milone et al. 2017).

We further report on 145 possible ($p > 0.05$) pairs of CN-strong stars in the halo field star population and individual GCs. Of these, 15 are presented as probable star-to-cluster connections ($p \geq 0.32$). About 18% of the association pairs involve clusters that were proposed to be attributable to the major merger events Gaia-Enceladus and Sequoia. Three of the high-probability pairs involve Enceladus GCs (M 75 and NGC 1261). We show that 38% of the CN-strong stars cannot be linked to any surviving cluster, which is in marginal agreement with the finding of $\sim 50\%$ by Savino & Posti (2019). Among the possible explanations is a scenario whereby these unassociated stars originate from already destroyed clusters.

The third tagging approach revealed 17 populations of stars that share the same portion of the chemodynamical information space as CN-strong stars. For nine such agglomerations of stars, we are able to attribute already known and newly discovered RR Lyrae stars, for which our refined approach for the distance inference provides more reliable distance estimates than the spectrophotometric distances with their attached caveats. Of particular interest, using this method, four CN-strong targets together with their associated stars are found to be probable members of the Sgr stream. Based on the metallicity overlap with M 54, a GC in the central part of the Sgr dwarf galaxy, we suggest that the four stars may have been stripped from this cluster.

From the identified RGB stars among the stellar populations around CN-strong stars without spatial coincidence with GCs, we again determined $N_{\mathrm{1P}}/N_{\mathrm{tot}}$ and find a value of $80.2^{+4.9}_{-5.2}\%$, which should be regarded as tentative because the statistical uncertainties do not account for all the potential caveats discussed. Nevertheless, it is tempting to argue that a substantial increase of $N_{\mathrm{1P}}/N_{\mathrm{tot}}$ from the vicinity of clusters to the overall halo field points towards either a preferential loss of 1P stars during early cluster dissolution or the birth of a considerable fraction of former GC stars of the halo in since-dissolved clusters. In any case, our findings provide a powerful observational benchmark for theoretical studies of cluster disruption.

As already emphasized in our earlier work, unambiguous confirmation that the identified CN-strong stars are indeed agents of the GC populations showing light-element anomalies remains to be attained. Evidence for imprints from high-temperature proton burning could be gathered through spectroscopic analyses of other key tracer elements such as O, Na, Mg, and Al. Another layer of complexity is added by the open question of whether GCs are genuinely the only sites providing the necessary conditions for the development of abundance anomalies. Bekki (2019), for example, presented a scenario that could explain the substantial fraction of N-rich stars found amongst the Galactic bulge field stars; namely, that these N-rich stars may have formed in the field from an ISM that has been pre-enriched by AGB ejecta. This latter author further envisions a similar mechanism for the halo. However, our – admittedly tentative – observation of an overabundance of CN-strong stars in the cluster surroundings as compared to the halo field challenges this explanation and suggests a mixture of both GC contribution and in-situ formation in the case of the halo.

Our method that is capable of identifying peculiar stars (Paper I) was restricted to the metallicity range $-1.8 < [\mathrm{Fe/H}] < -1.3$ dex. Nevertheless, most of the associates reported in the present study, in particular the ones directly surrounding clusters, are more metal-poor than the lower [Fe/H] limit used in Paper I. For instance, the very metal-poor GC M 92 with its many RGB associates both in the neighboring extratidal envelope and at larger separations remained untouched by our previous approach. Hence, a high-resolution follow up of these moderately faint ($14.5 < G < 17.5$ mag) targets is strongly called for in order to determine the extratidal $N_{\mathrm{1P}}/N_{\mathrm{tot}}$ in the metal-poor regime. Such investigations are paramount to observationally test simulations predicting that the fraction of 1P stars in the halo should increase with decreasing metallicity (Reina-Campos et al. 2020). In addition, not being restricted by the accessibility of CN band indices, high-resolution follow-up studies could target our associated MS, MSTO, SGB, and HB targets as well. This would considerably increase the statistical basis of the fractional estimates. The availability of improved number statistics would allow trends with other parameters such as the cluster age to be investigated (e.g., Martocchia et al. 2019). Finally, in the very near future, ongoing and upcoming large-scale spectroscopic surveys such as APOGEE (Majewski et al. 2017), WEAVE (Dalton et al. 2012), and 4MOST (de Jong et al. 2012; Helmi et al. 2019; Christlieb et al. 2019) will substantially enlarge the sample of chemodynamically characterized stars in the Galactic halo. The exploration of those vast datasets that are not restricted to a handful of chemical elements will ultimately lead to a much refined picture of the connection of GC stellar populations and the Milky Way halo.

> *"The time is gone, the song is over*
> *Thought I'd something more to say"*
>
> Time, PINK FLOYD

CHAPTER V

Concluding remarks and Outlook

1 ATHOS – future prospects of flux ratios in Galactic archaeology

In this thesis, I have introduced an innovative, new, and highly reliable spectroscopic method for the determination of the most important stellar parameters required for chemical abundance studies, which are the effective temperature, the surface gravity, and the metallicity. The revolutionary data-driven approach singled out ratios of spectral fluxes that are sensitive to the desired parameters and I have set up analytical descriptions that can, in turn, predict labels from such ratios. The computational implementation of the method is named `ATHOS`, A Tool for HOmogenizing Stellar parameters, with the name giving away one of its main objectives.

`ATHOS`' main assets can be summarized by its applicability over a wide parameter range (FGK dwarfs and giants at [Fe/H] > -4.5 dex), its independence of resolution (i.e., $R \gtrsim 2000$), and by not requiring a prior continuum placement. Combined with an unprecedented computational speed of just a few ms per spectrum, these features render `ATHOS` not only ideal for the upcoming massive spectroscopic surveys like WEAVE and 4MOST, but can also be easily applied to existing datasets to achieve mitigation of one of the major caveats in the field, that is, cross-survey parameter inhomogeneity (e.g., Kunder et al. 2017; Jofré et al. 2019; Blanco-Cuaresma 2019).

My tests on six independent surveys revealed that `ATHOS`' precisions are highly competitive and that its accuracies are solely limited by the already low uncertainties of the labels of the underlying training sample. Yet, I strive to improve the accuracy even more. To this end, I am currently in the process of compiling a massive update to the originally employed grid. In total, about 1000 stars are envisioned to be included in that new dataset, thereby increasing the sample size by a factor of eight. Whenever possible, I will enlarge the number of interferometric temperature measurements and resort to asteroseismic gravities, mostly using data from TESS (see Section III.3.1) but also from the *Kepler* and K2 missions. Another major improvement is the extension to wavelengths blueward of the current lower limit at 4800 Å. The expectation is that this will open new perspectives in the metal-poor regime since at those wavelengths many spectral lines are pronounced even at very low metallicities. From a methodological point of view, efforts are under way to replace the formerly used analytical relations for the description of flux ratios by more flexible neural nets (cf., e.g., Ting et al. 2019).

Considerable steps forward were already achieved in an entirely different regime of the stellar parameter space, where we successfully devised the by far most precise (<10 K) spectroscopic temperature measure to date for the population of young and massive Cepheid pulsating variables. In doing so, we expanded `ATHOS` by 143 temperature-sensitive FRs for the use in Cepheid spectra. In a series of new papers (Hanke, Lemasle, et al., in prep.), we elaborate on details of the newly determined spectroscopic parameters. This is a vital test to shed new light on chemical abundance gradients among the young Galactic disk stellar populations at unparalleled accuracies. All this could only be achieved because of the foundation that was set in this thesis.

2 HD 20 and the role of benchmarks for nuclear astrophysics

In the study presented in the subsequent chapter, I have performed a state-of-the-art spectroscopic abundance analysis of the metal-poor and *r*-process-enriched halo star HD 20 using exquisite observational material. Specific attention was devoted to the derivation of highly precise and accurate stellar parameters that could then be used to solidify a credible pattern with detections for 54 species of in total 48 chemical elements, 28 of which are ascribed to being produced by neutron-capture processes. Thereby, this study approaches the ground-based limit in terms measurable elements. While typical abundance studies only yield half as many elements, the HD 20 pattern comprises only nine elements less in the important neutron-capture regime than the most complete pattern studied up until now (CS 31082-001; Siqueira Mello et al. 2013). To approach the latter difference, ultraviolet spectra obtained with HST would be needed to get even more exotic elements.

So far, observational benchmark studies have been established for solar twins (e.g., Nissen 2015) or the *Gaia* FGK benchmark stars (Jofré et al. 2014), but hardly any exist in the metal-poor regime, lest for *r*-process patterns (possible exemptions being, e.g., Cowan et al. 2002; Sneden et al. 2003; Honda et al. 2006). Consequently, the study I have conducted in this thesis was highly called for. The inferred pattern was decomposed into its contributions from various nuclesynthetic processes, which are found to be dominated in the light-element regime by ejecta from core-collapse supernovae, whereas for elements beyond the iron peak three distinct processes could be singled out. These are the *s*-process – most likely contributed by a massive star undergoing the AGB phase – as well as the weak and main components of the *r*-process. Facing an apparent lack of a binary companion and therefore a potential polluter, I propose that HD 20 had these imprints already mixed in its natal gas cloud, which poses important observational constraints for mixing in the ISM of the early Galaxy.

The *r*-enhancement and almost complete pattern of HD 20 allows for a vital interpretation of the nature of the *r*-process. The interplay between improved yield predictions and the advanced abundance patterns of benchmark stars like HD 20 paves the way for the first deeper exploration of the role of fission in the *r*-process, which can ultimately allow us to constrain and distinguish between *r*-sites, such as magneto-hydrodynamic supernovae and neutron star mergers. The richness of

HD 20's pattern allowed us to find key fission tracers, which we used in an upcoming project in the framework of the "Chemical Elements as Tracers of the Evolution of the Cosmos" (ChETEC) as part of the European Cooperation in Science and Technology (COST) to set the pivotal direction for a new inter-disciplinary collaboration of the international astrophysics community.

3 Purveyors of fine halos – linking clusters to the Galactic halo

My work has explored the rich possibilities of combining large-scale spectroscopic surveys with kinematic data from the *Gaia* space mission to improve our understanding of the contribution of disrupting globular clusters to the Milky Way halo.

By investigating chemodynamical properties of bona fide second-generation former cluster members with their observed chemical peculiarity, I could trace these objects back to their potential natal hosts, some of which are connected to past merger events with the Milky Way. Furthermore, I linked a sample of chemically unaltered halo field stars to clusters in order to, for the first time, put constraints on the ratio of first- to second-generation stars among the cluster escapees. This information is a decisive missing piece of information that is crucial to advance our knowledge about cluster formation and disruption in the early Universe. By setting up observational constraints on mass loss from different cluster populations, my findings ultimately provided valuable data that can be fed into theories and modeling of the formation (and survival) of multiple stellar populations in globular clusters.

As such, the study laid the foundation for future endeavours that will benefit from upcoming surveys like the SDSS-V, which will unravel a large number of new globular cluster escapees based on abundance information (Na, Al, O) that is, hitherto, not available to the data base we founded our study on (CN). In addition, another future focus needs to lie on deeper investigations of similar populations in the Milky Way bulge, which is thought to have experienced comparable disruption events.

4 Final remarks

Galactic archaeology is at the verge of entering a new exciting era that is characterized by ever larger astrometric and spectroscopic campaigns generating vast datasets with detailed information for millions or even billions of stars. While these offer myriads of possibilities to answer the most fundamental questions in the field, challenges arise with handling the sheer amount of gathered data in a way that is able to compete with the precision and accuracy that astronomers aspire to achieve from more confined samples.

At the same time, it should not be forgotten that such small-scale studies will even in this new, sample-size-driven era gain vital insights in those topics where number statistics at the expense of data quality is not a viable path to pursue. In the scope of this thesis, I have explored the scientific advantages of both worlds by, on the one hand, shedding light on the kinematic and chemical memory of hundred thousands of Galactic halo stars and, on the other hand, by pushing stellar spectroscopy to its limits in the scrupulously precise investigation of a single target. Moreover, I presented a fundamentally new spectroscopic technique that is capable of bridging the seemingly insurmountable distance between the two aforementioned worlds by establishing a common base for sets of fundamental stellar parameters.

This thesis provided major contributions to the fields of developing spectroscopic techniques, nuclear astrophysics, and chemodynamical properties of Milky Way stellar populations. By scrutinizing various aspects of the chemical inventory of stars via the tool of spectroscopy, it fostered our understanding of the buildup and chemical evolution of our home Galaxy, the Milky Way.

CHAPTER A

Additional material for Chapter IV

1 RR Lyrae analysis

This section details the analysis of the RR Lyrae stars mentioned in Chapter IV and was contributed to the respective publication by Zdeněk Prudil.

RR Lyrae stars are pulsating variables residing on the horizontal giant branch within the instability strip. Their pulsation periods are tightly connected to their luminosity through period–metallicity–luminosity relations (see, e.g., Catelan et al. 2004; Muraveva et al. 2018), which makes them invaluable distance indicators within the Local Group. Furthermore, they are part of the old stellar population with ages $>10\,$Gyr due to their exclusive occurrence in old stellar systems such as globular clusters (VandenBerg et al. 2013). RR Lyrae variables are divided into three classes based on the pulsation mode; fundamental mode stars (RRab), first overtone mode

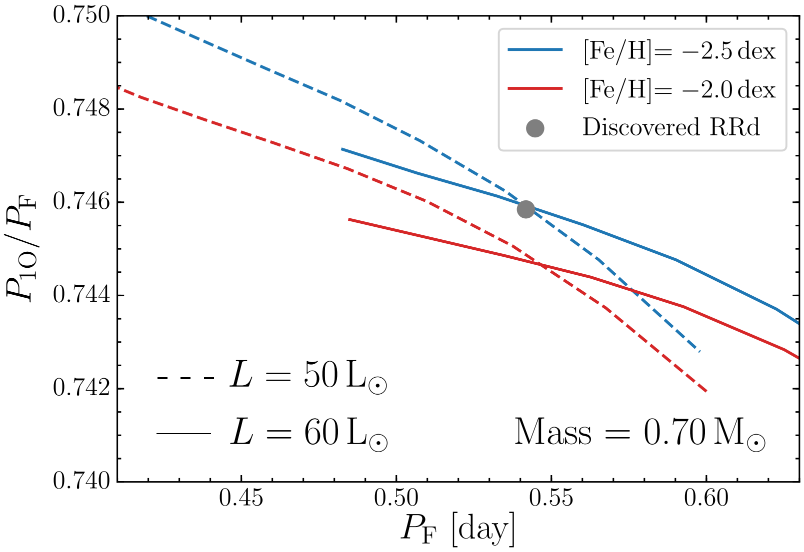

FIGURE A.1: Period ratio vs. fundamental pulsation period (errors on depicted quantities are smaller than the point size) for a discovered RR Lyrae star (gray point) compared to the pulsation models (blue and red colors, Smolec & Moskalik 2008) calculated for a fixed mass (0.7 $M_\odot$), metallicity (−2.0 and −2.5 dex), and a grid of stellar parameters (L and $T_{\rm eff}$) typical for RR Lyrae stars.

pulsators (RRc), and double-mode variables (RRd, pulsating simultaneously in the fundamental and first overtone).

A few hundred stars in our analysis fall inside the fundamental mode RR Lyraes' instability strip boundaries provided by Clementini et al. (2019), intrinsically making them candidates for possible variability. In order to investigate their periodic alternation, we retrieved their photometry from the time domain Catalina sky survey (CSS, Drake et al. 2009). In addition, we used datasets assembled using the data from the CSS (Drake et al. 2013a,b, 2014; Abbas et al. 2014) as a bona fide catalog of RR Lyrae stars in the Galactic halo. The crossmatch of the RR Lyrae candidates with the halo RR Lyrae sample resulted in matches for 65 cases with determined pulsation periods. To verify the nonvariability of the remaining stars, we elaborated on their possible periodicity using the `upsilon` package[1] (Kim & Bailer-Jones 2016), which searches for periodic behavior among photometric data and provides a classification and light curve parameters of identified variables. To ensure reliable classification, we required at least 50 % class probability for stars identified as RR Lyrae pulsators which were fulfilled by nine stars that we denote as newly discovered RR Lyrae variables (three RRab, five RRc and one RRd).

The one RRd variable in our sample is a newly discovered double-mode RR Lyrae star with a dominant first overtone mode (pulsation period $P_{1O} = 0.4040992$ d) and a

---

[1] Available at `https://github.com/dwkim78/upsilon`.

secondary fundamental mode at $P_\mathrm{F} = 0.5417994\,\mathrm{d}$. The period ratio between both modes is $P_{1\mathrm{O}}/P_\mathrm{F} = 0.7458465$, which together with the long fundamental mode period suggests a low metallicity between -2.0 and -2.5 dex (see Fig. A.1 for details) in line with M 15's [Fe/H].

The assembled RR Lyrae light curves (both known and newly discovered) were phased using the stars' ephemerids and decomposed using the Fourier series to determine the time of maximum brightness, the mean magnitude, and the pulsation amplitude:

$$m\left(t\right) = A_0 + \sum_{k=1}^{n} A_k \cdot \cos\left(2\pi k\vartheta + \varphi_k\right), \tag{A.1}$$

where ϑ represents the phase function defined as $\left(MJD - M_0\right)/P$, MJD denotes the observation in the Modified Julian Date, and P and $M0$ are ephemerids of a given star (pulsation period and time of brightness maximum). A_k and φ_k stand for amplitudes and phases, respectively, with n denoting the degree of the Fourier series, and A_0 representing the mean magnitude. Each phased light curve was visually inspected to verify the ephemerids and pulsation amplitudes derived from the Fourier fits.

The absolute magnitudes of RR Lyrae stars in the visual part of the spectrum strongly correlate with their metallicities (see, e.g., Catelan et al. 2004; Muraveva et al. 2018), thus acquiring homogenous absolute magnitudes for all three RR Lyrae classes in our sample can be troubling due to the lack of reliable metallicities (cf., e.g., Smolinski et al. 2011; Hanke et al. 2018; Fabrizio et al. 2019). Hence, for the distance estimates we decided to assume a single absolute magnitude for the entire RR Lyrae sample and allowed a large dispersion $M_\mathrm{V} = 0.6 \pm 0.5\,\mathrm{mag}$.

The single value for the absolute magnitude of all RR Lyrae variables in our sample was derived using a sample of RR Lyrae stars from (Muraveva et al. 2018), *Gaia* parallaxes, 3D dust maps from Green et al. (2019), and mean V-band magnitudes from the ASAS survey (Pojmanski 2002). For the aforementioned quantities, we ran an MC error simulation of the distance modulus assuming two different offsets in *Gaia* parallaxes (-0.057 mas, and -0.029 mas, respectively, Muraveva et al. 2018; Lindegren et al. 2018), and estimated absolute magnitudes for individual RR Lyrae variables. The $\langle M_\mathrm{V} \rangle$ magnitudes clustered around 0.68 ± 0.35 mag and 0.56 ± 0.37 mag for *Gaia* parallax offsets, -0.057 mas and -0.029 mas, respectively. Pursuing a conservative approach, we used $M_\mathrm{V} = 0.6$ mag with a large dispersion of 0.5 mag to account for the offset in both absolute magnitude values derived from parallaxes.

The distances for our sample of RR Lyrae variables were calculated using the MC simulation with 1000 realizations assuming Gaussian error distributions in the reddening (using dust maps from Schlafly & Finkbeiner 2011), absolute magnitudes, and apparent magnitudes[2]. The resulting distances come with errors of around 20-25 %, larger than generally reported based on optical data for RR Lyrae stars (around 8 %, Neeley et al. 2017). This is mainly caused by the conservative assumption for absolute RR Lyrae magnitudes.

Periodic luminosity changes are driven by the variation of the stellar radius and effective temperature. This inevitably affects the radial velocity measurements that comprise a combination of systemic and pulsation velocity. The pulsation effect can be removed from a single radial velocity measurement using radial velocity templates (Sesar 2012)[3] that scale with their photometric counterparts.

We note that for RRc and RRd type RR Lyrae stars, Sesar (2012) does not provide a scaling relation between the amplitudes of v_r and photometric light curves. Thus, we used a sample collected by (Sneden et al. 2017) for radial velocity amplitudes (based on the Hα line) of the first overtone pulsators in the field and compared them with their photometric amplitudes using data from the ASAS survey (Pojmanski 2002). Applying the latter comparison we obtained the following scaling relation between the radial and photometric amplitudes for the first overtone pulsators:

$$A_{\mathrm{rv}}^{\mathrm{H}\alpha} = 95.8 A_V - 5.2. \tag{A.2}$$

The aforementioned relation was also used for the determination of the systemic velocity of the one RRd star in our sample.

In order to determine the systemic velocity of RR Lyrae stars in our sample we extracted single-epoch spectra from the SDSS and measured the radial velocity for the Hα line by cross-correlation with a synthetic template[4] using the `iSpec` package routines (Blanco-Cuaresma et al. 2014; Blanco-Cuaresma 2019) and `MOOG` (Sneden 1973, February 2017 version). Individual radial velocity measurements were phased using the stars' ephemerids with MJDs centered in the middle of the exposure. We scaled the Hα radial velocity template based on the stars amplitude and subtracted the pulsation velocity from the measured radial velocity. The final systemic velocity for a given RR Lyrae star was estimated through the median of individual, pulsation-corrected radial velocity measurements. Errors on the systemic velocities were estimated following the prescriptions by (Sesar 2012).

---

[2] We used the average photometric error of a given RR Lyrae variable as error estimate for the mean magnitude.

[3] Sesar (2012) provides radial velocity templates for measurements based on Hα, Hβ, Hγ, and metallic lines. We note that in our analyses of SDSS spectra we used only the Hα profile due to its high prominence even in the low-quality spectra of faint RR Lyrae stars in our dataset.

[4] Synthesized spectrum of a star with stellar parameters typical for an RR Lyrae star; $T_{\mathrm{eff}} = 6700\,\mathrm{K}$, $\log g = 2.15$, $[\mathrm{Fe/H}] = -1.5\,\mathrm{dex}$

2 Supplemental figures

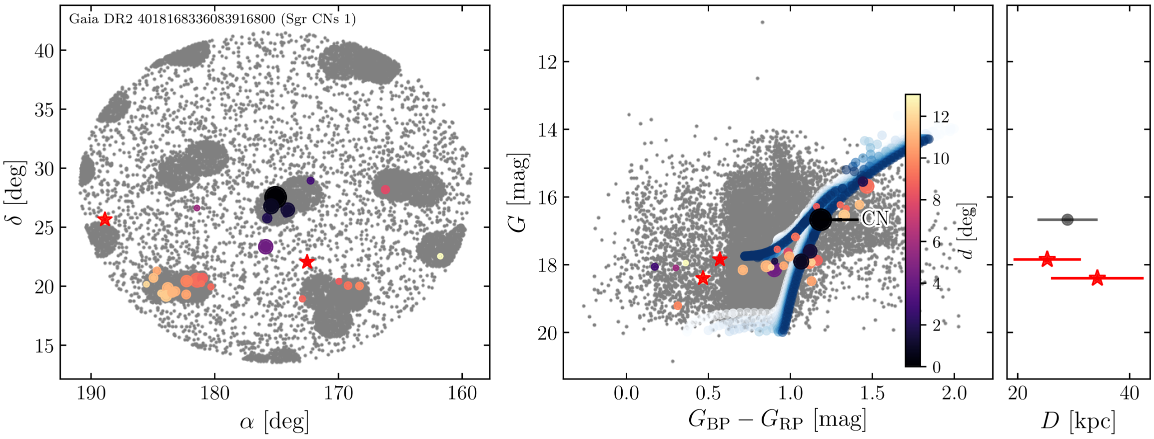

FIGURE A.2: Same as Fig. IV.18 but for associations to the CN-strong star *Gaia* DR2 4018168336083916800 (Sgr CNs 1).

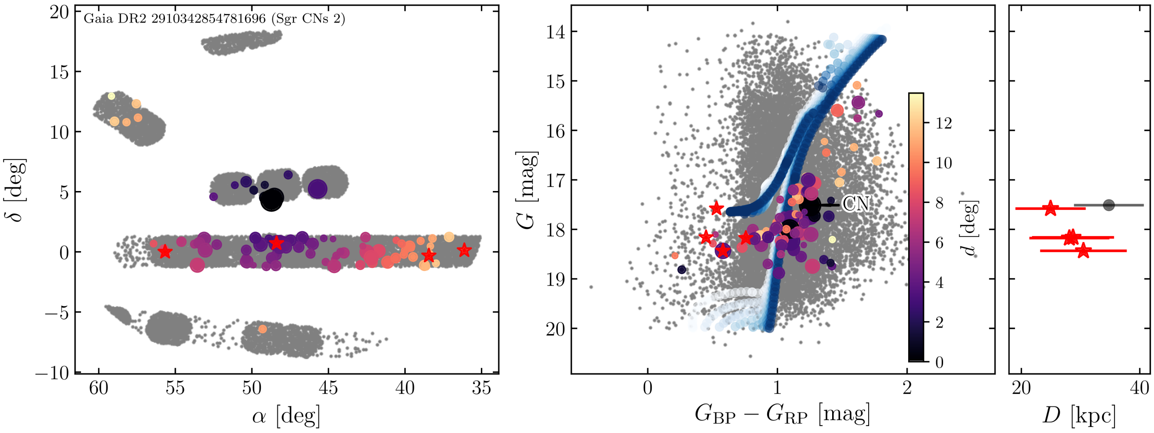

FIGURE A.3: Same as Fig. IV.18 but for associations to the CN-strong star *Gaia* DR2 2910342854781696 (Sgr CNs 2).

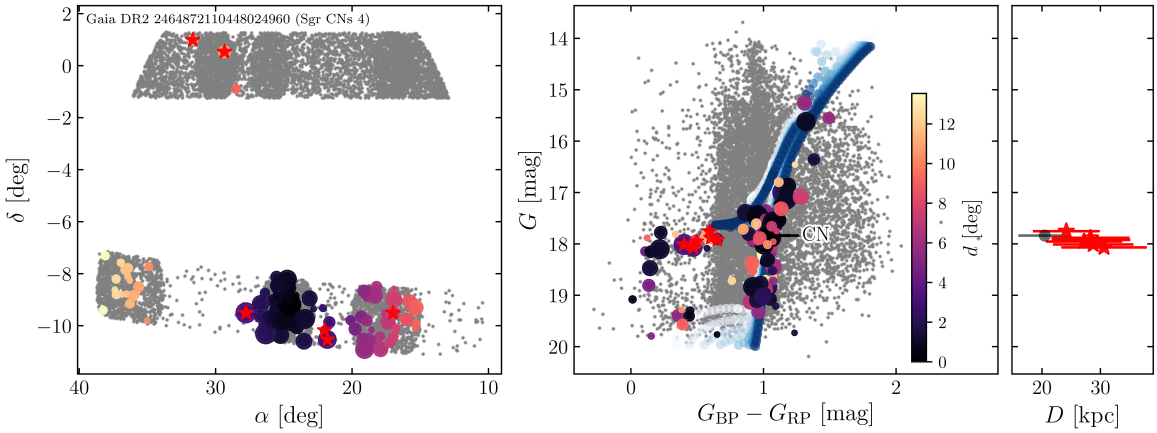

FIGURE A.4: Same as Fig. IV.18 but for associations to the CN-strong star *Gaia* DR2 2464872110448024960 (Sgr CNs 4).

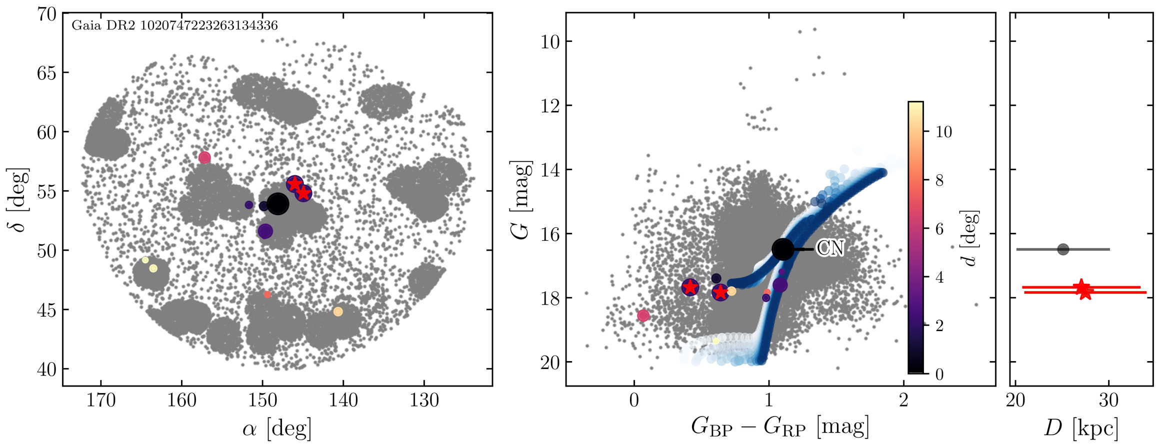

FIGURE A.5: Same as Fig. IV.18 but for associations to the CN-strong star *Gaia* DR2 1020747223263134336.

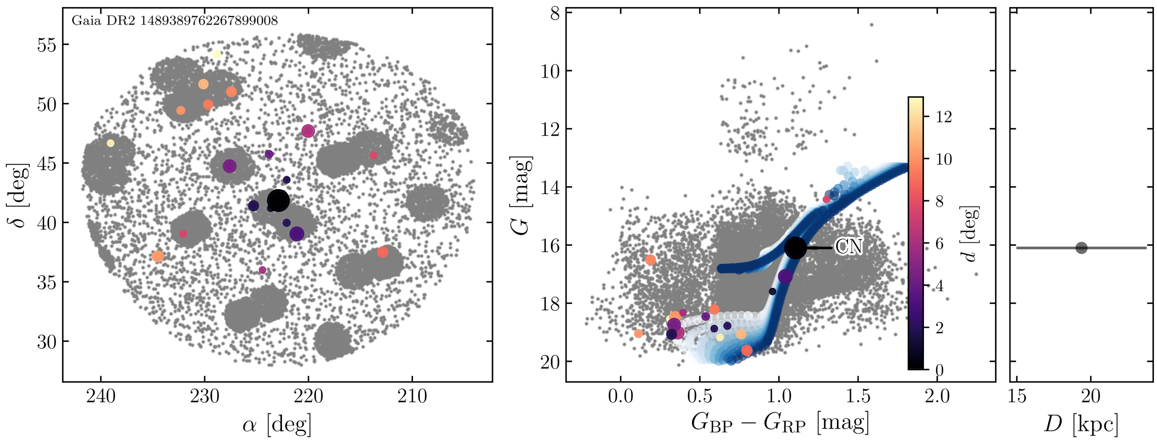

FIGURE A.6: Same as Fig. IV.18 but for associations to the CN-strong star *Gaia* DR2 1489389762267899008.

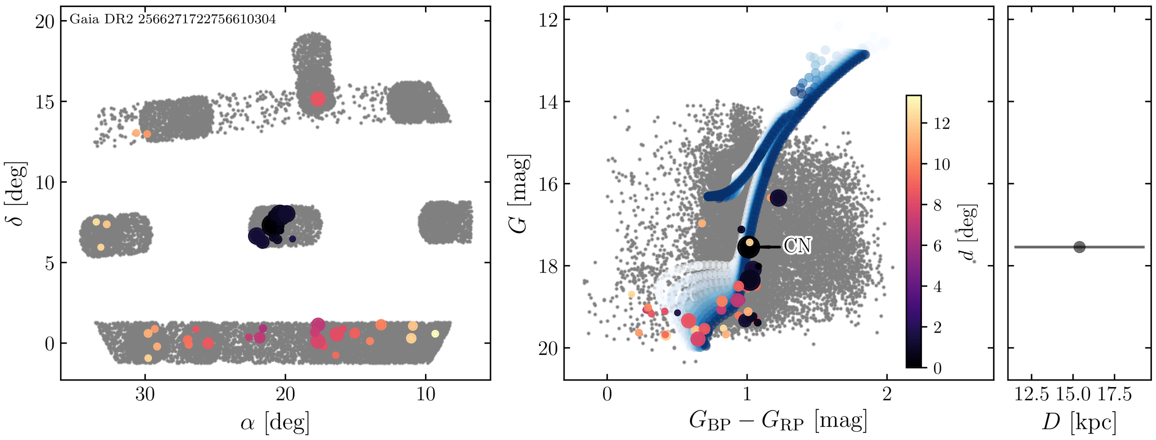

FIGURE A.7: Same as Fig. IV.18 but for associations to the CN-strong star *Gaia* DR2 2566271722756610304.

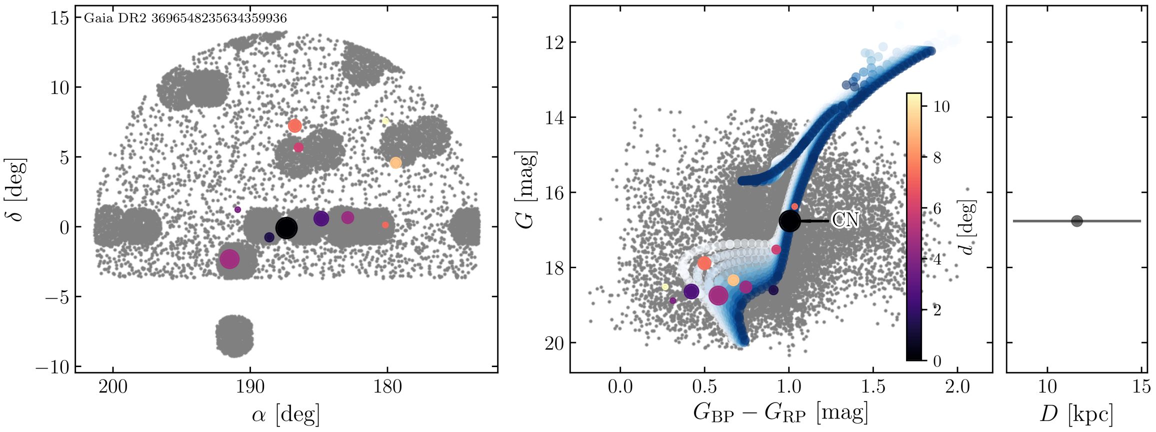

FIGURE A.8: Same as Fig. IV.18 but for associations to the CN-strong star *Gaia* DR2 3696548235634359936. We note that this group of stars may be associated with Gaia-Enceladus through its association with NGC 1261 (Sects. 4.2 and 4.3),

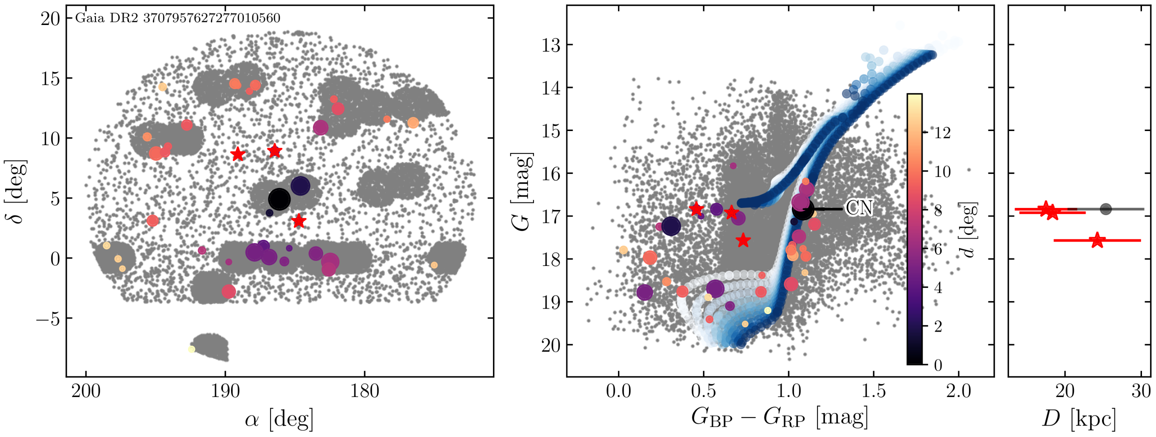

FIGURE A.9: Same as Fig. IV.18 but for associations to the CN-strong star *Gaia* DR2 3707957627277010560.

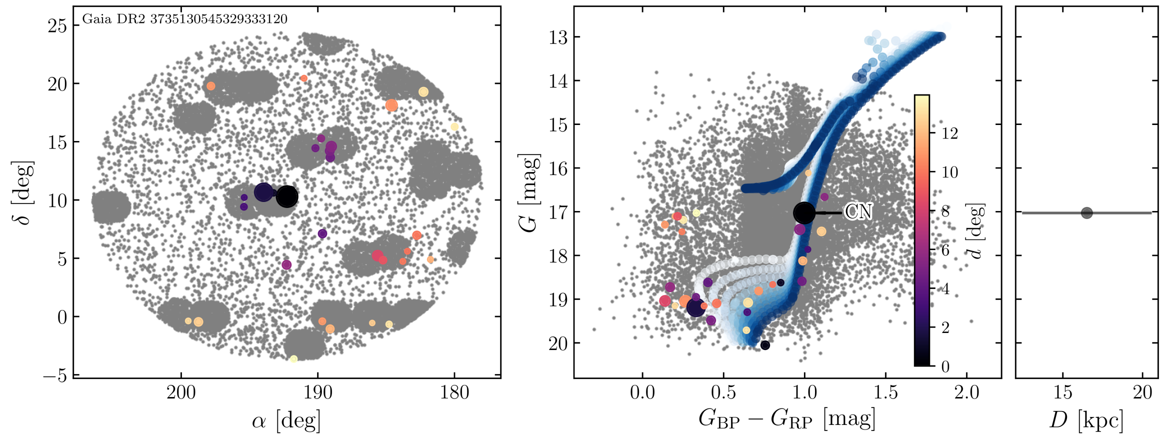

FIGURE A.10: Same as Fig. IV.18 but for associations to the CN-strong star *Gaia* DR2 3735130545329333120.

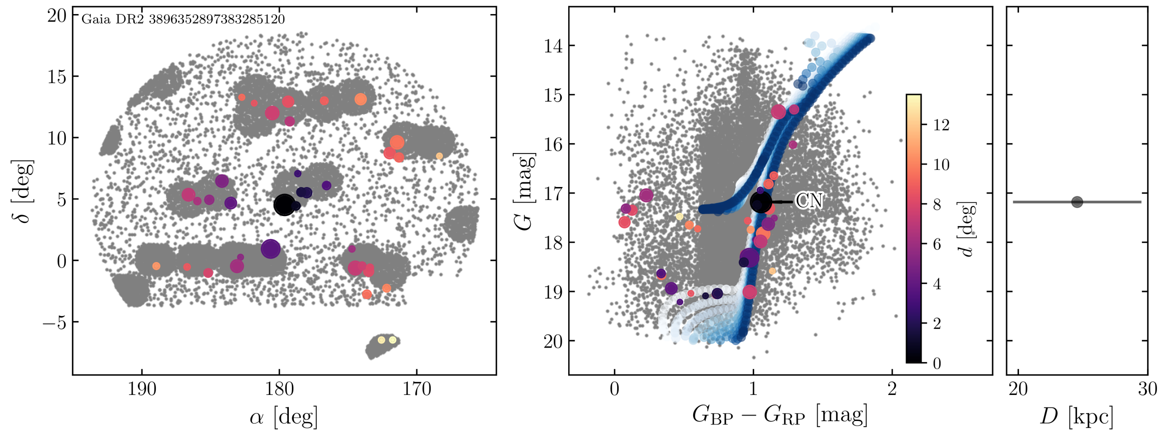

FIGURE A.11: Same as Fig. IV.18 but for associations to the CN-strong star *Gaia* DR2 3896352897383285120.

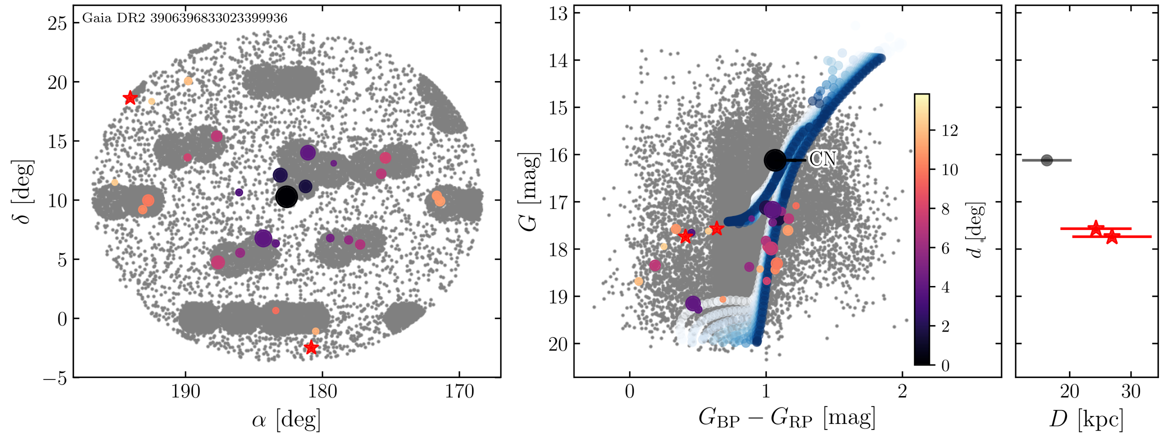

FIGURE A.12: Same as Fig. IV.18 but for associations to the CN-strong star *Gaia* DR2 3906396833023399936.

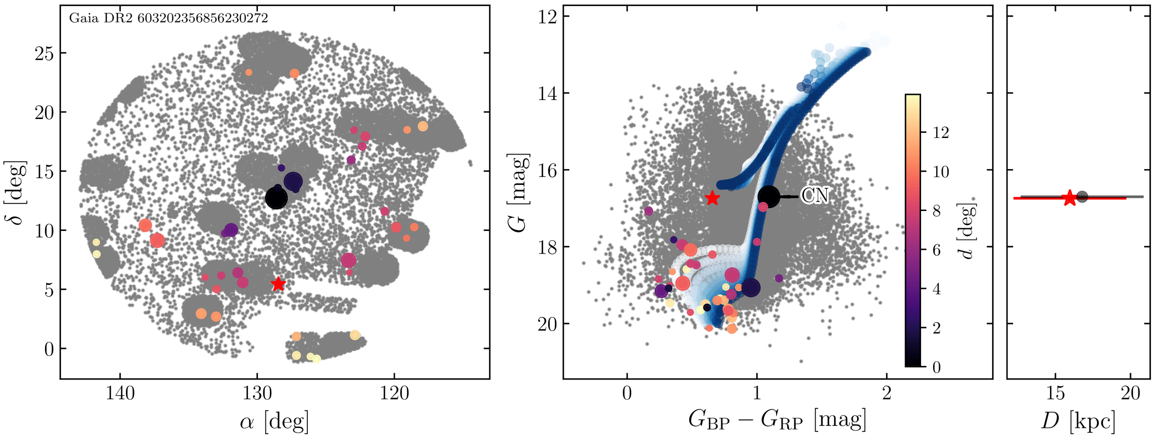

FIGURE A.13: Same as Fig. IV.18 but for associations to the CN-strong star *Gaia* DR2 603202356856230272.

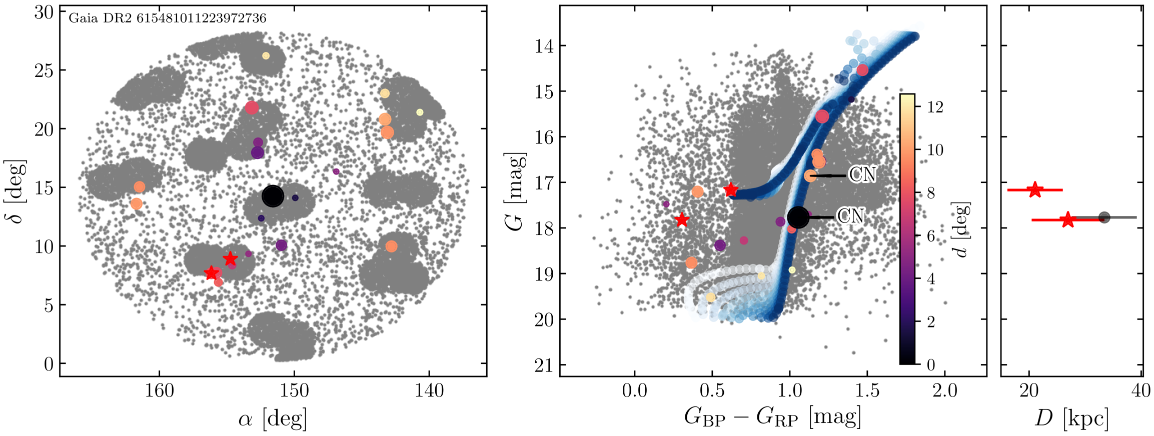

FIGURE A.14: Same as Fig. IV.18 but for associations to the CN-strong star *Gaia* DR2 615481011223972736.

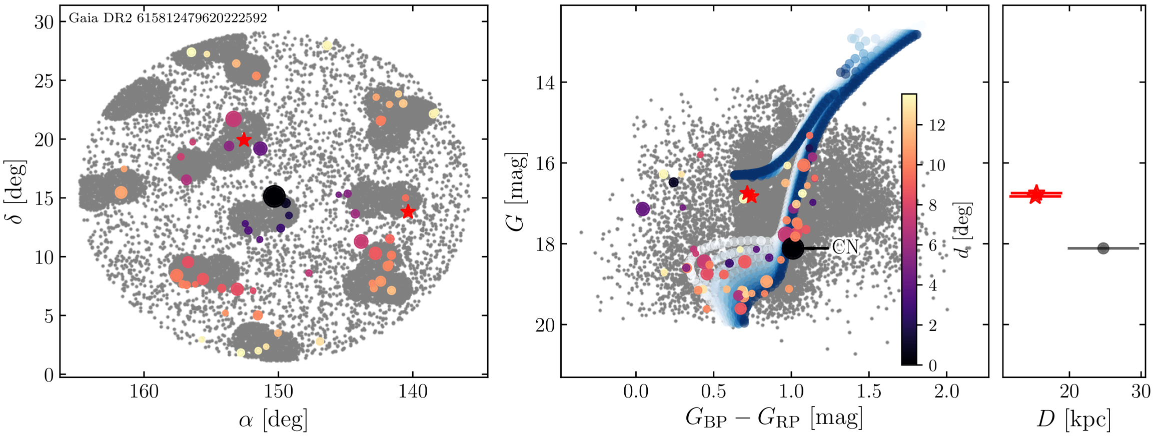

FIGURE A.15: Same as Fig. IV.18 but for associations to the CN-strong star *Gaia* DR2 615812479620222592.

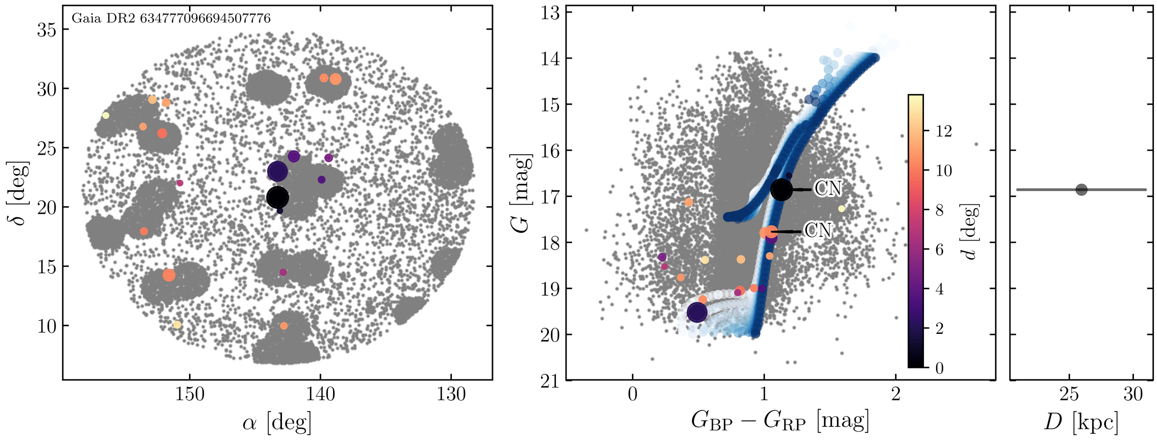

FIGURE A.16: Same as Fig. IV.18 but for associations to the CN-strong star *Gaia* DR2 634777096694507776.

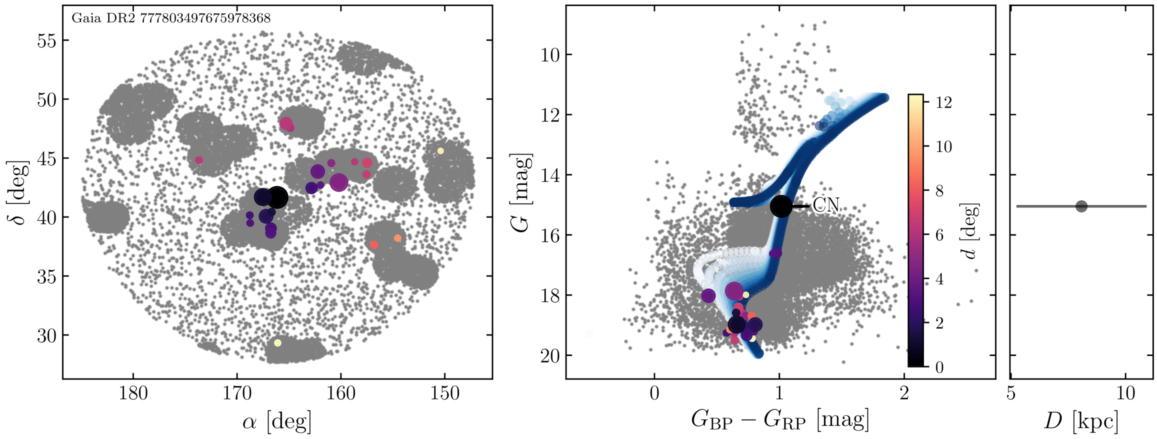

FIGURE A.17: Same as Fig. IV.18 but for associations to the CN-strong star *Gaia* DR2 777803497675978368.

3

Supplemental table

Table A.1: Star-cluster pairs from method II with $p'_{ij} \geq 0.05$.

Gaia DR2 source ID	GC	p'_{ij}	m.m.$^{(a)}$	$p^{(b)}_{\rm ref}$	*Gaia* DR2 source ID	GC	p'_{ij}	m.m.$^{(a)}$	$p^{(b)}_{\rm ref}$
1327315426141900672$^{(c)}$	NGC 6205 (M 13)	0.95	…	…	4564058919924158208	NGC 5904 (M 5)	0.13	…	…
3906396833023399936	NGC 5272 (M 3)	0.90	…	…	2732393700487077504	NGC 7089 (M 2)	0.18	Enc.	…
1314863834914856576$^{(c)}$	NGC 6205 (M 13)	0.83	…	…	2749152495372410880	NGC 5904 (M 5)	0.18	…	…
1464049970616941952	NGC 6864 (M 75)	0.63	Enc.	…	2749152495372410880	NGC 6584	0.15	…	…
2731803537620554112	NGC 6981 (M 72)	0.56	…	…	1532601977988111872	Pal 3	0.17	…	…
3696548235634359936	NGC 1261	0.54	Enc.	…	1532601977988111872	NGC 5824	0.09	…	…
1889299458599695488	IC 1257	0.51	…	…	1532601977988111872	Eridanus	0.07	…	…
1020747223263134336	NGC 6229	0.48	…	…	2464872110448024960	Pal 14 (Arp 1)	0.16	…	…
1020747223263134336	NGC 6981 (M 72)	0.11	…	…	2464872110448024960	Pal 5	0.12	…	…
1020747223263134336	NGC 6584	0.05	…	…	2464872110448024960	Rup 106	0.09	…	…
1266132414419596160	NGC 6284	0.47	…	…	2464872110448024960	Eridanus	0.06	…	…
1266132414419596160	NGC 288	0.13	…	…	2730283398370974208	NGC 2298	0.15	Enc.	…
3938161242913396352	Eridanus	0.42	…	…	603202356856230272	NGC 1904 (M 79)	0.15	Enc.	…
3707957627277010560	NGC 6981 (M 72)	0.39	…	…	603202356856230272	NGC 3201	0.08	Seq.	…
3707957627277010560	NGC 6229	0.12	…	…	603202356856230272	NGC 1851	0.07	Enc.	0.22
4425543651944958848	NGC 6681 (M 70)	0.38	…	…	100528661660795648	Eridanus	0.15	…	…
4425543651944958848	NGC 6205 (M 13)	0.35	…	…	777803497675978368	NGC 6779 (M 56)	0.15	Enc.	…
658003150255826048	NGC 5634	0.36	…	…	777803497675978368	NGC 6656 (M 22)	0.09	…	…
658003150255826048	NGC 6584	0.31	…	…	2732599171722435968	NGC 6584	0.14	…	…
1505296706224813824	NGC 1261	0.32	Enc.	…	2732599171722435968	ESO 280-06	0.10	…	…
1505296706224813824	IC 4499	0.09	…	…	2732599171722435968	NGC 7089 (M 2)	0.05	Enc.	…
1352831345811056384	NGC 6584	0.31	…	…	3065507927991629824	NGC 6981 (M 72)	0.14	…	…
3793673590978231168	Eridanus	0.31	…	…	3065507927991629824	NGC 6229	0.13	…	…
1336539538425553280	NGC 1904 (M 79)	0.30	Enc.	…	3065507927991629824	NGC 5904 (M 5)	0.06	…	…
1336539538425553280	NGC 7089 (M 2)	0.08	Enc.	…	3065507927991629824	IC 4499	0.05	…	…
1336539538425553280	NGC 6981 (M 72)	0.05	…	…	2507434583516170240	Pal 3	0.14	…	…
2619708262744328064	NGC 1261	0.30	Enc.	…	2507434583516170240	Eridanus	0.11	…	…
2619708262744328064	NGC 7089 (M 2)	0.17	Enc.	…	2507434583516170240	NGC 6715 (M 54)	0.08	…	…
1319293939061613312	NGC 362	0.29	…	…	2507434583516170240	Pal 5	0.06	…	…
2686927211051932032$^{(c)}$	NGC 6656 (M 22)	0.28	…	…	2910342854781696	Pal 3	0.13	…	…
2686927211051932032$^{(c)}$	NGC 7089 (M 2)	0.20	Enc.	…	2910342854781696	Eridanus	0.08	…	…
2686927211051932032$^{(c)}$	ESO 280-06	0.10	…	…	3896352897383285120	NGC 7089 (M 2)	0.13	Enc.	0.22
634777096694507776	NGC 5904 (M 5)	0.27	…	…	3896352897383285120	IC 4499	0.09	…	…
634777096694507776	NGC 6229	0.09	…	…	3896352897383285120	NGC 1904 (M 79)	0.08	Enc.	0.14
634777096694507776	NGC 6981 (M 72)	0.07	…	…	4141123766486595200	NGC 6139	0.13	…	…
634777096694507776	NGC 6584	0.05	…	…	4448177751636921088	NGC 6544	0.11	…	…
860782815590943488	Rup 106	0.25	…	…	4448177751636921088	NGC 6273 (M 19)	0.07	…	…
860782815590943488	NGC 7006	0.09	…	…	2470086991019454848	Eridanus	0.10	…	…
860782815590943488	NGC 6934	0.05	…	…	2470086991019454848	Pal 5	0.10	…	…
4602060554337732992$^{(c)}$	NGC 6205 (M 13)	0.25	…	0.35	2470086991019454848	Rup 106	0.09	…	…
764888767240012928	NGC 4147	0.25	…	…	2470086991019454848	Pal 14 (Arp 1)	0.08	…	…
764888767240012928	NGC 6981 (M 72)	0.16	…	…	2720484958765839104	IC 4499	0.10	…	…
3563020451180259456	IC 1257	0.24	…	…	2720484958765839104	NGC 7492	0.06	…	…
3563020451180259456	NGC 7089 (M 2)	0.11	Enc.	…	1592645066735097088	NGC 1904 (M 79)	0.10	Enc.	…
2688138220030361600	NGC 6752	0.24	…	…	1592645066735097088	NGC 6981 (M 72)	0.08	…	…
2688138220030361600	NGC 6656 (M 22)	0.14	…	…	1592645066735097088	NGC 4147	0.06	…	…
2688138220030361600	NGC 6254 (M 10)	0.10	…	…	3591471723298342400	IC 1257	0.10	…	…
2688138220030361600	NGC 6397	0.07	…	…	3932598122098282496	Eridanus	0.10	…	…
3735130545329333120	ESO 280-06	0.23	…	…	3932598122098282496	Pal 14 (Arp 1)	0.08	…	…
3735130545329333120	NGC 7089 (M 2)	0.11	Enc.	…	3932598122098282496	NGC 5272 (M 3)	0.08	…	…
3735130545329333120	NGC 7492	0.10	…	…	3932598122098282496	NGC 7492	0.07	…	…
4425538154386975616	NGC 6273 (M 19)	0.22	…	…	2686860763615798912	NGC 6284	0.10	…	…
4425538154386975616	NGC 6287	0.08	…	…	1325256040863360128	NGC 6205 (M 13)	0.09	…	0.19
1546577767213867136	NGC 6229	0.21	…	…	1325256040863360128	NGC 5139 (omega Cen)	0.08	Seq.	…
1546577767213867136	NGC 4147	0.15	…	…	1325256040863360128	NGC 6681 (M 70)	0.05	…	…
1546577767213867136	NGC 6981 (M 72)	0.12	…	…	1666212668195069184	NGC 5824	0.09	…	…
1546577767213867136	NGC 6584	0.08	…	…	1666212668195069184	Rup 106	0.08	…	…
864027195230709504	NGC 6981 (M 72)	0.21	…	…	1307939316841792512	Pal 3	0.09	…	…
864027195230709504	NGC 1904 (M 79)	0.07	Enc.	…	1307939316841792512	Eridanus	0.06	…	…
864027195230709504	NGC 1851	0.06	Enc.	…	3651209835007571456	Eridanus	0.09	…	…
2566271722756610304	Pal 14 (Arp 1)	0.21	…	…	3651209835007571456	IC 4499	0.06	…	…
2566271722756610304	Rup 106	0.11	…	…	3559140961841845888	NGC 6981 (M 72)	0.09	…	…
2566271722756610304	Eridanus	0.10	…	…	4018168336083916800	Pal 3	0.08	…	…
4141127962669782400	NGC 6093 (M 80)	0.20	…	…	4021877298042177920	NGC 6715 (M 54)	0.08	…	…
4034859648443488896	NGC 4147	0.20	…	…	4021877298042177920	Eridanus	0.07	…	…
4034859648443488896	NGC 5634	0.12	…	…	3697011301828434816	Eridanus	0.07	…	…
4034859648443488896	NGC 5272 (M 3)	0.07	…	…	3697011301828434816	NGC 7089 (M 2)	0.05	Enc.	…
4034859648443488896	NGC 6981 (M 72)	0.07	…	…	3563015262859711744	NGC 7089 (M 2)	0.06	Enc.	…
1678398697300158208	NGC 7006	0.19	…	…	1395074303376247296	Pal 5	0.06	…	…
1678398697300158208	Eridanus	0.10	…	…	3200603517242311808	NGC 6981 (M 72)	0.06	…	…
1678398697300158208	NGC 288	0.06	…	…	3303140501315921152	NGC 6535	0.05	Seq.	…
4564058919924158208	NGC 6229	0.18	…	…	4437207133854765056	Pal 3	0.05	…	…
4564058919924158208	NGC 6981 (M 72)	0.16	…	…					

Notes. $^{(a)}$ Cluster might be associated with the major merger (m.m.) events Gaia-Enceladus (Enc., Myeong et al. 2018) or Sequoia (Seq., Myeong et al. 2019). $^{(b)}$ Confidence attributed to the same pair by Savino & Posti (2019). We note that the values are inverted – that is unity minus reported rejection confidence – with respect to the original study. $^{(c)}$ Associations already reported in Sect. 3.3 and listed in Table IV.2.

List of frequently used Acronyms

1P	chemically “normal” population of globular cluster stars
2P	chemically “enriched” population of globular cluster stars
4MOST	4-meter Multi-Object Spectroscopic Telescope
ADP	Advanced Data Products (ESO)
AGB	asymptotic giant branch
ATHOS	A Tool for HOmogenizing Stellar parameters
APOGEE	Apache Point Observatory Galactic Evolution Experiment
BSS	blue straggler star
CCSN	core-collapse supernova
CEMP	carbon-enhanced metal-poor (star)
CMD	color–magnitude diagram
ESO	European Southern Observatory
EW	equivalent width
FR	flux ratio
FWHM	full width at half maximum
GALAH	GALactic Archaeology with HERMES
GC	globular cluster
GES	*Gaia*-ESO survey
HB	horizontal branch
HST	Hubble Space Telescope
***i*-process**	intermediate neutron-capture process
IRFM	infrared flux method
ISM	interstellar medium
LAMOST	Large Sky Area Multi-Object Fibre Spectroscopic Telescope
LDR	line depth ratio
LTE	local thermodynamic equilibrium
MCMC	Markov chain Monte Carlo (sampling)
MS	main sequence
MSTO	main sequence turnoff
MW	Milky Way
NIST	National Institute of Standards and Technology

NLTE	non-local thermodynamic equilibrium
NSM	neutron star merger
ODR	orthogonal distance regression
***r*-process**	rapid neutron-capture process
RAVE	Radial Velocity Experiment
RGB	red giant branch
rms	root mean square
S/N	signal-to-noise ratio
SN	supernova
***s*-process**	slow neutron-capture process
SDSS	Sloan Digital Sky Survey
SEGUE	Sloan Extension for Galactic Understanding and Exploration
SGB	subgiant branch
SSPP	SEGUE Stellar Parameter Pipeline
TESS	Transiting Exoplanet Survey Satellite
WD	white dwarf
WEAVE	William Herschel Telescope Enhanced Area Velocity Explorer

Publications of Michael Hanke

First- and second-author publications:

- **Hanke, M.**, Lemasle, B., Storm, J., Bono, G., and Grebel, E.K.
  "Atmospheric parameters of Cepheids from flux ratios with ATHOS. II. Comparison of the infrared surface brightness and line depth ratio temperature scales"
  in preparation
- Lemasle, B., **Hanke, M.**, Storm, J., Bono, G., and Grebel, E.K.
  "Atmospheric parameters of Cepheids from flux ratios with ATHOS. I. The temperature scale"
  submitted to Astronomy & Astrophysics
- **Hanke, M.**, Koch, A., Prudil, Z., Grebel, E.K., and Bastian, U.
  "Purveyors of fine halos. II. Chemodynamical association of halo stars with Milky Way globular clusters" (Chapter IV)
  2020b, Astronomy & Astrophysics, in press [arXiv:2004.00018]
- **Hanke, M.**, Hansen, C.J., Ludwig, H.-G., Cristallo, S., McWilliam, A., Grebel, E.K., and Piersanti, L.
  "A high-precision abundance analysis of the nuclear benchmark star HD 20" (Chapter III)
  2020a, Astronomy & Astrophysics, 635, A104
- **Hanke, M.**, Hansen, C.J., Koch, A., and Grebel, E.K.
  "ATHOS: On-the-fly stellar parameter determination of FGK stars based on flux ratios from optical spectra" (Chapter II)
  2018, Astronomy & Astrophysics, 619, A134
- Koch, A., **Hanke, M.**, and Kacharov, N.
  "Kinematics of outer halo globular clusters: M 75 and NGC 6426"
  2018, Astronomy & Astrophysics, 616, A74
- **Hanke, M.**, Koch, A., Hansen, C.J., and McWilliam, A.
  "Insights into the chemical composition of the metal-poor Milky Way halo globular cluster NGC 6426"
  2017, Astronomy & Astrophysics, 599, A97

Co-authored publications:

- Reichert, M., Hansen, C.J., **Hanke, M.**, Skúladóttir, Á., Arcones, A., and Grebel, E.K.
  "Neutron-capture elements in dwarf galaxies. III. A homogenized analysis of 13 dwarf spheroidal and ultra-faint galaxies"
  2020, submitted to Astronomy & Astrophysics, [arXiv:2004.01195]
- Contreras Ramos, R., Minniti, D., Fernández-Trincado, J.G., Alonso-García, J., Catelan, M., Gran, F.; Hajdu, G.; **Hanke, M.**, Hempel, M., Moreno Díaz, E.; Pérez-Villegas, A., Rojas-Arriagada, A., and Zoccali, M.
  "The Orbit of the New Milky Way Globular Cluster FSR1716 = VVV-GC05"
  2018, The Astrophysical Journal, 863, 78

Bibliography

Abbas, M. A., Grebel, E. K., Martin, N. F., et al. 2014, MNRAS, 441, 1230

Abbott, B. P., Abbott, R., Abbott, T. D., et al. 2017, Phys. Rev. Lett., 119, 161101

Abolfathi, B., Aguado, D. S., Aguilar, G., et al. 2018, ApJS, 235, 42

Afşar, M., Sneden, C., & For, B.-Q. 2012, AJ, 144, 20

Ahumada, R., Allende Prieto, C., Almeida, A., et al. 2019, arXiv e-prints, arXiv:1912.02905

Allende Prieto, C. 2003, MNRAS, 339, 1111

Allende Prieto, C., Barklem, P. S., Lambert, D. L., & Cunha, K. 2004, A&A, 420, 183

Allende Prieto, C., Sivarani, T., Beers, T. C., et al. 2008, AJ, 136, 2070

Alonso, A., Arribas, S., & Martinez-Roger, C. 1994, A&AS, 107, 365

Alonso, A., Arribas, S., & Martinez-Roger, C. 1996a, A&AS, 117, 227

Alonso, A., Arribas, S., & Martinez-Roger, C. 1996b, A&A, 313, 873

Alonso, A., Arribas, S., & Martínez-Roger, C. 1999a, A&AS, 139, 335

Alonso, A., Arribas, S., & Martínez-Roger, C. 1999b, A&AS, 140, 261 (AAM99)

Alonso, A., Arribas, S., & Martínez-Roger, C. 2001, A&A, 376, 1039

Amarsi, A. M., Nissen, P. E., & Skúladóttir, Á. 2019, A&A, 630, A104

Amarsi, A. M., Nordlander, T., Barklem, P. S., et al. 2018, A&A, 615, A139

Anderson, R. I., Eyer, L., & Mowlavi, N. 2013, MNRAS, 434, 2238

Andrae, R., Fouesneau, M., Creevey, O., et al. 2018, A&A, 616, A8

Andrievsky, S. M., Bersier, D., Kovtyukh, V. V., et al. 2002a, A&A, 384, 140

Andrievsky, S. M., Kovtyukh, V. V., Luck, R. E., et al. 2002b, A&A, 381, 32

Andrievsky, S. M., Kovtyukh, V. V., Luck, R. E., et al. 2002c, A&A, 392, 491

Andrievsky, S. M., Spite, F., Korotin, S. A., et al. 2011, A&A, 530, A105

Anthony-Twarog, B. J. & Twarog, B. A. 1994, AJ, 107, 1577

Arcones, A., Janka, H. T., & Scheck, L. 2007, A&A, 467, 1227

Arnett, W. D. & Truran, J. W. 1969, ApJ, 157, 339

Arnould, M., Goriely, S., & Jorissen, A. 1999, A&A, 347, 572

Asplund, M. 2005, ARA&A, 43, 481

Asplund, M., Grevesse, N., Sauval, A. J., & Scott, P. 2009, ARA&A, 47, 481

Aurière, M. 2003, in EAS Publications Series, Vol. 9, EAS Publications Series, ed. J. Arnaud & N. Meunier, 105

Baade, W. 1944, ApJ, 100, 137

Bailer-Jones, C. A. L., Rybizki, J., Fouesneau, M., Mantelet, G., & Andrae, R. 2018, AJ, 156, 58

Barbá, R. H., Minniti, D., Geisler, D., et al. 2019, ApJ, 870, L24

Barbuy, B., Chiappini, C., & Gerhard, O. 2018, ARA&A, 56, 223

Bard, A., Kock, A., & Kock, M. 1991, A&A, 248, 315

Bard, A. & Kock, M. 1994, A&A, 282, 1014

Barklem, P. S., Christlieb, N., Beers, T. C., et al. 2005, A&A, 439, 129

Barklem, P. S., Stempels, H. C., Allende Prieto, C., et al. 2002, A&A, 385, 951

Bastian, N., Lamers, H. J. G. L. M., de Mink, S. E., et al. 2013, MNRAS, 436, 2398

Bastian, N. & Lardo, C. 2015, MNRAS, 453, 357

Bastian, N. & Lardo, C. 2018, ARA&A, 56, 83

Battaglia, G., Irwin, M., Tolstoy, E., et al. 2008, MNRAS, 383, 183

Baumgardt, H. & Hilker, M. 2018, MNRAS, 478, 1520

Baumgardt, H., Hilker, M., Sollima, A., & Bellini, A. 2019, MNRAS, 482, 5138

Baumgardt, H. & Sollima, S. 2017, MNRAS, 472, 744

Beasley, M. A. 2020, arXiv e-prints, arXiv:2003.04093

Bedding, T. R., Mosser, B., Huber, D., et al. 2011, Nature, 471, 608

Beers, T. C. & Christlieb, N. 2005, ARA&A, 43, 531

Beers, T. C., Flynn, C., Rossi, S., et al. 2007, ApJS, 168, 128

Beers, T. C., Preston, G. W., & Shectman, S. A. 1985a, AJ, 90, 2089

Beers, T. C., Preston, G. W., & Shectman, S. A. 1985b, AJ, 90, 2089

Bekki, K. 2019, MNRAS, 490, 4007

Bell, E. F., Zucker, D. B., Belokurov, V., et al. 2008, ApJ, 680, 295

Bellazzini, M., Ibata, R. A., Chapman, S. C., et al. 2008, AJ, 136, 1147

Belokurov, V., Erkal, D., Evans, N. W., Koposov, S. E., & Deason, A. J. 2018, MNRAS, 478, 611

Belokurov, V., Zucker, D. B., Evans, N. W., et al. 2006, ApJ, 642, L137

Bensby, T., Bergemann, M., Rybizki, J., et al. 2019, The Messenger, 175, 35

Bensby, T., Feltzing, S., & Lundström, I. 2003, A&A, 410, 527

Bergemann, M. 2011, MNRAS, 413, 2184

Bergemann, M., Collet, R., Amarsi, A. M., et al. 2017a, ApJ, 847, 15

Bergemann, M., Collet, R., Schönrich, R., et al. 2017b, ApJ, 847, 16

Bergemann, M., Gallagher, A. J., Eitner, P., et al. 2019, A&A, 631, A80

Bergemann, M. & Gehren, T. 2008, A&A, 492, 823

Bergemann, M., Hansen, C. J., Bautista, M., & Ruchti, G. 2012a, A&A, 546, A90

Bergemann, M., Kudritzki, R.-P., Würl, M., et al. 2013, ApJ, 764, 115

Bergemann, M., Lind, K., Collet, R., Magic, Z., & Asplund, M. 2012b, MNRAS, 427, 27

Bergemann, M., Pickering, J. C., & Gehren, T. 2010, MNRAS, 401, 1334

Bergemann, M., Serenelli, A., Schönrich, R., et al. 2016, A&A, 594, A120

Bernstein, R., Shectman, S. A., Gunnels, S. M., Mochnacki, S., & Athey, A. E. 2003, in Society of Photo-Optical Instrumentation Engineers (SPIE) Conference Series, Vol. 4841, Proc. SPIE, ed. M. Iye & A. F. M. Moorwood, 1694–1704

Bessell, M. S. 1983, PASP, 95, 480

Biémont, E., Garnir, H. P., Palmeri, P., Li, Z. S., & Svanberg, S. 2000, MNRAS, 312, 116

Biemont, E., Grevesse, N., Kwiatkovski, M., & Zimmermann, P. 1984, A&A, 131, 364

Biemont, E., Quinet, P., & Zeippen, C. J. 1993, A&AS, 102, 435

Binney, J. 2012, MNRAS, 426, 1324

Bisterzo, S., Gallino, R., Straniero, O., Cristallo, S., & Käppeler, F. 2012, MNRAS, 422, 849

Bisterzo, S., Travaglio, C., Gallino, R., Wiescher, M., & Käppeler, F. 2014, ApJ, 787, 10

Bizzarri, A., Huber, M. C. E., Noels, A., et al. 1993, A&A, 273, 707

Blackwell, D. E., Ibbetson, P. A., Petford, A. D., & Shallis, M. J. 1979a, MNRAS, 186, 633

Blackwell, D. E., Petford, A. D., & Shallis, M. J. 1979b, MNRAS, 186, 657

Blackwell, D. E., Petford, A. D., Shallis, M. J., & Simmons, G. J. 1982a, MNRAS, 199, 43

Blackwell, D. E., Petford, A. D., & Simmons, G. J. 1982b, MNRAS, 201, 595

Blackwell, D. E. & Shallis, M. J. 1977, MNRAS, 180, 177

Blackwell, D. E. & Shallis, M. J. 1979, MNRAS, 186, 673

Blackwell, D. E., Shallis, M. J., & Simmons, G. J. 1980, A&A, 81, 340

Blackwell, D. E., Shallis, M. J., & Simmons, G. J. 1982c, MNRAS, 199, 33

Blanco-Cuaresma, S. 2019, MNRAS, 486, 2075

Blanco-Cuaresma, S., Soubiran, C., Jofré, P., & Heiter, U. 2014, A&A, 566, A98 (GBS)

Boeltzig, A., Bruno, C. G., Cavanna, F., et al. 2016, European Physical Journal A, 52, 75

Boesgaard, A. M. & Steigman, G. 1985, ARA&A, 23, 319

Borsato, N. W., Martell, S. L., & Simpson, J. D. 2020, MNRAS, 492, 1370

Borucki, W. J., Koch, D., Basri, G., et al. 2010, Science, 327, 977

Bouvier, A. & Wadhwa, M. 2010, Nature Geoscience, 3, 637

Bovy, J. 2015, ApJS, 216, 29

Bovy, J., Rix, H.-W., Hogg, D. W., et al. 2012, ApJ, 755, 115

Bromm, V. & Larson, R. B. 2004, ARA&A, 42, 79

Bullock, J. S. & Johnston, K. V. 2005, ApJ, 635, 931

Burbidge, E. M., Burbidge, G. R., Fowler, W. A., & Hoyle, F. 1957, Reviews of Modern Physics, 29, 547

Burke, B. F. 1957, AJ, 62, 90

Burnett, B. & Binney, J. 2010, MNRAS, 407, 339

Burris, D. L., Pilachowski, C. A., Armandroff, T. E., et al. 2000, ApJ, 544, 302

Busso, M., Gallino, R., Lambert, D. L., Travaglio, C., & Smith, V. V. 2001, ApJ, 557, 802

Caffau, E., Koch, A., Sbordone, L., et al. 2013, Astronomische Nachrichten, 334, 197

Camargo, D. 2018, ApJ, 860, L27

Camargo, D. & Minniti, D. 2019, MNRAS, 484, L90

Cameron, A. G. W. 1957, PASP, 69, 201

Cameron, A. G. W. 2003, ApJ, 587, 327

Campante, T. L., Corsaro, E., Lund, M. N., et al. 2019, ApJ, 885, 31

Cardelli, J. A., Clayton, G. C., & Mathis, J. S. 1989, ApJ, 345, 245

Carlsson, M. 1986, Uppsala Astronomical Observatory Reports, 33

Carney, B. W., Gray, D. F., Yong, D., et al. 2008, AJ, 135, 892

Carney, B. W., Latham, D. W., Stefanik, R. P., Laird, J. B., & Morse, J. A. 2003, AJ, 125, 293

Carollo, D., Beers, T. C., Chiba, M., et al. 2010, ApJ, 712, 692

Carollo, D., Beers, T. C., Lee, Y. S., et al. 2007, Nature, 450, 1020

Carr, B. J. & Rees, M. J. 1979, Nature, 278, 605

Carretta, E., Bragaglia, A., Gratton, R., & Lucatello, S. 2009, A&A, 505, 139 (C09)

Carretta, E., Bragaglia, A., Gratton, R. G., et al. 2010, A&A, 516, A55

Carter, B. 1974, in IAU Symposium, Vol. 63, Confrontation of Cosmological Theories with Observational Data, ed. M. S. Longair, 291–298

Casagrande, L., Ramírez, I., Meléndez, J., Bessell, M., & Asplund, M. 2010, A&A, 512, A54

Casagrande, L. & VandenBerg, D. A. 2018, MNRAS, 479, L102

Castelli, F. 1996, Astronomical Society of the Pacific Conference Series, Vol. 108, Convection in the ATLAS9 Code, ed. S. J. Adelman, F. Kupka, & W. W. Weiss, 85

Castelli, F. & Kurucz, R. L. 2003, in IAU Symposium, Vol. 210, Modelling of Stellar Atmospheres, ed. N. Piskunov, W. W. Weiss, & D. F. Gray, A20

Castelli, F. & Kurucz, R. L. 2004, ArXiv Astrophysics e-prints [`astro-ph/0405087`]

Catelan, M., Pritzl, B. J., & Smith, H. A. 2004, ApJS, 154, 633

Cayrel, R., Hill, V., Beers, T. C., et al. 2001, Nature, 409, 691

Cayrel, R., van't Veer-Menneret, C., Allard, N. F., & Stehlé, C. 2011, A&A, 531, A83

Chan, C. & Heger, A. 2017, in 14th International Symposium on Nuclei in the Cosmos (NIC2016), 020209

Chen, Y.-P., Trager, S. C., Peletier, R. F., et al. 2014, A&A, 565, A117

Chiappini, C., Minchev, I., Starkenburg, E., et al. 2019, The Messenger, 175, 30

Chornock, R., Berger, E., Kasen, D., et al. 2017, ApJ, 848, L19

Christlieb, N. 2003, Reviews in Modern Astronomy, 16, 191

Christlieb, N., Battistini, C., Bonifacio, P., et al. 2019, The Messenger, 175, 26

Christlieb, N., Beers, T. C., Barklem, P. S., et al. 2004, A&A, 428, 1027

Christlieb, N., Bessell, M. S., Beers, T. C., et al. 2002, Nature, 419, 904

Christlieb, N., Wisotzki, L., Reimers, D., et al. 2001, A&A, 366, 898

Chun, S.-H., Kim, J.-W., Sohn, S. T., et al. 2010, AJ, 139, 606

Clayton, D. D. 1968, Principles of stellar evolution and nucleosynthesis

Clementini, G., Ripepi, V., Molinaro, R., et al. 2019, A&A, 622, A60

Cohen, J. G. 1978, ApJ, 223, 487

Contreras Ramos, R., Minniti, D., Fernández-Trincado, J. G., et al. 2018, ApJ, 863, 78

Cooper, A. P., Parry, O. H., Lowing, B., Cole, S., & Frenk, C. 2015, MNRAS, 454, 3185

Cordero, M. J., Hénault-Brunet, V., Pilachowski, C. A., et al. 2017, MNRAS, 465, 3515

Corliss, C. H. & Bozman, W. R. 1962, Experimental transition probabilities for spectral lines of seventy elements; derived from the NBS Tables of spectral-line intensities

Corsaro, E. & De Ridder, J. 2014, A&A, 571, A71

Corsaro, E., Mathur, S., García, R. A., et al. 2017, A&A, 605, A3

Côté, B., Eichler, M., Arcones, A., et al. 2019, ApJ, 875, 106

Cousins, A. W. J. 1976, MmRAS, 81, 25

Cowan, J. J., Pfeiffer, B., Kratz, K. L., et al. 1999, ApJ, 521, 194

Cowan, J. J. & Rose, W. K. 1977, ApJ, 212, 149

Cowan, J. J., Sneden, C., Beers, T. C., et al. 2005, ApJ, 627, 238

Cowan, J. J., Sneden, C., Burles, S., et al. 2002, ApJ, 572, 861

Cowley, C. R. & Corliss, C. H. 1983, MNRAS, 203, 651

Creevey, O., Grundahl, F., Thévenin, F., et al. 2019, A&A, 625, A33

Cristallo, S., Piersanti, L., Straniero, O., et al. 2011, ApJS, 197, 17

Cristallo, S., Straniero, O., Piersanti, L., & Gobrecht, D. 2015, ApJS, 219, 40

Cropper, M., Katz, D., Sartoretti, P., et al. 2018, A&A, 616, A5

Cyburt, R. H. 2004, Phys. Rev. D, 70, 023505

Dalton, G., Trager, S. C., Abrams, D. C., et al. 2012, Society of Photo-Optical Instrumentation Engineers (SPIE) Conference Series, Vol. 8446, WEAVE: the next generation wide-field spectroscopy facility for the William Herschel Telescope, 84460P

D'Antona, F., Vesperini, E., D'Ercole, A., et al. 2016, MNRAS, 458, 2122

Dawson, K. S., Kneib, J.-P., Percival, W. J., et al. 2016, AJ, 151, 44

de Jong, R. S., Bellido-Tirado, O., Chiappini, C., et al. 2012, Society of Photo-Optical Instrumentation Engineers (SPIE) Conference Series, Vol. 8446, 4MOST: 4-metre multi-object spectroscopic telescope, 84460T

De Lucia, G. & Helmi, A. 2008, MNRAS, 391, 14

De Silva, G. M., Freeman, K. C., Bland-Hawthorn, J., et al. 2015, MNRAS, 449, 2604

Deason, A. J., Belokurov, V., Evans, N. W., & Johnston, K. V. 2013, ApJ, 763, 113

Deason, A. J., Belokurov, V., & Sanders, J. L. 2019, MNRAS, 490, 3426

Dekel, A. & Silk, J. 1986, ApJ, 303, 39

Dekker, H., D'Odorico, S., Kaufer, A., Delabre, B., & Kotzlowski, H. 2000, in Proc. SPIE, Vol. 4008, Optical and IR Telescope Instrumentation and Detectors, ed. M. Iye & A. F. Moorwood, 534–545

Demarque, P., Woo, J.-H., Kim, Y.-C., & Yi, S. K. 2004, ApJS, 155, 667

Den Hartog, E. A., Lawler, J. E., Sneden, C., & Cowan, J. J. 2003, ApJS, 148, 543

Den Hartog, E. A., Lawler, J. E., Sneden, C., & Cowan, J. J. 2006, ApJS, 167, 292

Den Hartog, E. A., Lawler, J. E., Sobeck, J. S., Sneden, C., & Cowan, J. J. 2011, ApJS, 194, 35 den Hartogh, J. W., Hirschi, R., Lugaro, M., et al. 2019, A&A, 629, A123

Denissenkov, P. A. & Hartwick, F. D. A. 2014, MNRAS, 437, L21

D'Ercole, A., Vesperini, E., D'Antona, F., McMillan, S. L. W., & Recchi, S. 2008, MNRAS, 391, 825

Dicke, R. H. 1961, Nature, 192, 440

Djorgovski, S. & Sosin, C. 1989, ApJ, 341, L13

Donati, J. F., Catala, C., Landstreet, J. D., & Petit, P. 2006, Astronomical Society of the Pacific Conference Series, Vol. 358, ESPaDOnS: The New Generation Stellar Spectro-Polarimeter. Performances and First Results, ed. R. Casini & B. W. Lites, 362

Dotter, A., Chaboyer, B., Jevremović, D., et al. 2008, ApJS, 178, 89

Drake, A. J., Catelan, M., Djorgovski, S. G., et al. 2013a, ApJ, 763, 32

Drake, A. J., Catelan, M., Djorgovski, S. G., et al. 2013b, ApJ, 765, 154

Drake, A. J., Djorgovski, S. G., Mahabal, A., et al. 2009, ApJ, 696, 870

Drake, A. J., Graham, M. J., Djorgovski, S. G., et al. 2014, ApJS, 213, 9

Ducati, J. R. 2002, VizieR Online Data Catalog, 2237

Eaton, J. A. 1995, AJ, 109, 1797

Eggen, O. J., Lynden-Bell, D., & Sandage, A. R. 1962, ApJ, 136, 748

Eisenstein, D. J., Weinberg, D. H., Agol, E., et al. 2011, AJ, 142, 72

ESA, ed. 1997, ESA Special Publication, Vol. 1200, The HIPPARCOS and TYCHO catalogues. Astrometric and photometric star catalogues derived from the ESA HIPPARCOS Space Astrometry Mission

Fabrizio, M., Bono, G., Braga, V. F., et al. 2019, ApJ, 882, 169

Fernández-Trincado, J. G., Beers, T. C., Placco, V. M., et al. 2019a, ApJ, 886, L8

Fernández-Trincado, J. G., Beers, T. C., Tang, B., et al. 2019b, MNRAS, 488, 2864

Ferraro, F. R., Sills, A., Rood, R. T., Paltrinieri, B., & Buonanno, R. 2003, ApJ, 588, 464

For, B.-Q. & Sneden, C. 2010, AJ, 140, 1694

Forbes, D. A. & Bridges, T. 2010, MNRAS, 404, 1203

Foreman-Mackey, D., Hogg, D. W., Lang, D., & Goodman, J. 2013, PASP, 125, 306

Fraser, M., Casey, A. R., Gilmore, G., Heger, A., & Chan, C. 2017, MNRAS, 468, 418

Fraunhofer, J. 1817, Annalen der Physik, 56, 264

Frebel, A. & Norris, J. E. 2015, ARA&A, 53, 631

Freytag, B., Steffen, M., Ludwig, H. G., et al. 2012, Journal of Computational Physics, 231, 919

Friel, E. D. 1995, ARA&A, 33, 381

Fuhr, J. R., Martin, G. A., & Wiese, W. L. 1988, Journal of Physical and Chemical Reference Data, 17

Fuhrmann, K., Axer, M., & Gehren, T. 1993, A&A, 271, 451

Fukushima, T., Chiba, M., Tanaka, M., et al. 2019, PASJ, 71, 72

Fulbright, J. P. & Johnson, J. A. 2003, ApJ, 595, 1154

Fulbright, J. P., McWilliam, A., & Rich, R. M. 2006, ApJ, 636, 821

Gai, N., Basu, S., Chaplin, W. J., & Elsworth, Y. 2011, ApJ, 730, 63

Gaia Collaboration, Brown, A. G. A., Vallenari, A., et al. 2018a, A&A, 616, A1

Gaia Collaboration, Helmi, A., van Leeuwen, F., et al. 2018b, A&A, 616, A12

Gaia Collaboration, Katz, D., Antoja, T., et al. 2018c, A&A, 616, A11

Gaia Collaboration, Prusti, T., de Bruijne, J. H. J., et al. 2016, A&A, 595, A1

Gallino, R., Arlandini, C., Busso, M., et al. 1998, ApJ, 497, 388

García-Hernández, D. A., Manchado, A., Lambert, D. L., et al. 2009, ApJ, 705, L31

García Pérez, A. E., Allende Prieto, C., Holtzman, J. A., et al. 2016, AJ, 151, 144

Garz, T. 1973, A&A, 26, 471

Giddings, J. R. 1981, , PhD thesis, -

Gilmore, G., Randich, S., Asplund, M., et al. 2012, The Messenger, 147, 25 (GES)

Gilmore, G. & Reid, N. 1983, MNRAS, 202, 1025

Giribaldi, R. E., Ubaldo-Melo, M. L., Porto de Mello, G. F., et al. 2019, A&A, 624, A10

González Hernández, J. I. & Bonifacio, P. 2009, A&A, 497, 497

Gratton, R., Bragaglia, A., Carretta, E., et al. 2019, A&A Rev., 27, 8

Gratton, R. G., Bonifacio, P., Bragaglia, A., et al. 2001, A&A, 369, 87

Gratton, R. G., Sneden, C., Carretta, E., & Bragaglia, A. 2000, A&A, 354, 169

Gray, D. F. 2005, The Observation and Analysis of Stellar Photospheres

Gray, D. F. & Johanson, H. L. 1991, PASP, 103, 439

Gray, R. O. & Corbally, C. J. 1994, AJ, 107, 742

Green, G. M., Schlafly, E., Zucker, C., Speagle, J. S., & Finkbeiner, D. 2019, ApJ, 887, 93

Grevesse, N., Asplund, M., & Sauval, A. J. 2007, Space Sci. Rev., 130, 105

Grillmair, C. J. & Dionatos, O. 2006, ApJ, 643, L17

Guiglion, G., de Laverny, P., Recio-Blanco, A., et al. 2016, A&A, 595, A18

Guiglion, G., Matijevic, G., Queiroz, A. B. A., et al. 2020, arXiv e-prints, arXiv:2004.12666

Gull, M., Frebel, A., Cain, M. G., et al. 2018, ApJ, 862, 174

Günther, M. N. & Berardo, D. A. 2020, arXiv e-prints, arXiv:2003.14345

Gustafsson, B., Edvardsson, B., Eriksson, K., et al. 2008, A&A, 486, 951

Halley, E. 1715, Philosophical Transactions of the Royal Society of London Series I, 29, 390

Hampel, M., Karakas, A. I., Stancliffe, R. J., Meyer, B. S., & Lugaro, M. 2019, ApJ, 887, 11

Hampel, M., Stancliffe, R. J., Lugaro, M., & Meyer, B. S. 2016, ApJ, 831, 171

Han, W., Zhang, L., Yang, G., Niu, P., & Zhang, B. 2018, ApJ, 856, 58

Hanke, M., Hansen, C. J., Koch, A., & Grebel, E. K. 2018, A&A, 619, A134

Hanke, M., Hansen, C. J., Ludwig, H.-G., et al. 2020a, A&A, 635, A104

Hanke, M., Koch, A., Hansen, C. J., & McWilliam, A. 2017, A&A, 599, A97

Hanke, M., Koch, A., Prudil, Z., Grebel, E. K., & Bastian, U. 2020b, arXiv e-prints, arXiv:2004.00018

Hannaford, P., Lowe, R. M., Grevesse, N., Biemont, E., & Whaling, W. 1982, ApJ, 261, 736

Hansen, C. J., Bergemann, M., Cescutti, G., et al. 2013, A&A, 551, A57

Hansen, C. J., El-Souri, M., Monaco, L., et al. 2018a, ApJ, 855, 83

Hansen, C. J., Montes, F., & Arcones, A. 2014, ApJ, 797, 123

Hansen, C. J., Nordström, B., Bonifacio, P., et al. 2011, A&A, 527, A65

Hansen, C. J., Nordström, B., Hansen, T. T., et al. 2016, A&A, 588, A37

Hansen, C. J., Primas, F., Hartman, H., et al. 2012, A&A, 545, A31 (CJH12)

Hansen, T. T., Andersen, J., Nordström, B., et al. 2015, A&A, 583, A49

Hansen, T. T., Holmbeck, E. M., Beers, T. C., et al. 2018b, ApJ, 858, 92

Harris, W. E. 1996, AJ, 112, 1487

Hartwick, F. D. A. 1976, ApJ, 209, 418

Hauck, B. & Mermilliod, M. 1998, A&AS, 129, 431

Hawkins, K., Jofré, P., Heiter, U., et al. 2016, A&A, 592, A70

Hayden, M. R., Bovy, J., Holtzman, J. A., et al. 2015, ApJ, 808, 132

Haywood, M. 2008, MNRAS, 388, 1175

Heger, A. & Woosley, S. E. 2010, ApJ, 724, 341

Heiter, U., Jofré, P., Gustafsson, B., et al. 2015, A&A, 582, A49

Helmi, A., Babusiaux, C., Koppelman, H. H., et al. 2018, Nature, 563, 85

Helmi, A., Irwin, M., Deason, A., et al. 2019, The Messenger, 175, 23

Hendricks, B., Boeche, C., Johnson, C. I., et al. 2016, A&A, 585, A86

Henon, M. & Heiles, C. 1964, AJ, 69, 73

Herschel, W. 1814, Philosophical Transactions of the Royal Society of London Series I, 104, 248

Hinkle, K., Wallace, L., Valenti, J., & Harmer, D. 2000, Visible and Near Infrared Atlas of the Arcturus Spectrum 3727-9300 A

Hinshaw, G., Larson, D., Komatsu, E., et al. 2013, ApJS, 208, 19

Hobbs, L. M., Thorburn, J. A., & Rebull, L. M. 1999, ApJ, 523, 797

Høg, E., Fabricius, C., Makarov, V. V., et al. 2000, A&A, 355, L27

Honda, S., Aoki, W., Ishimaru, Y., Wanajo, S., & Ryan, S. G. 2006, ApJ, 643, 1180

Howard, C. D., Rich, R. M., Clarkson, W., et al. 2009, ApJ, 702, L153

Howard, C. D., Rich, R. M., Reitzel, D. B., et al. 2008, ApJ, 688, 1060

Howell, S. B., Sobeck, C., Haas, M., et al. 2014, PASP, 126, 398

Hubeny, I. 1988, Computer Physics Communications, 52, 103

Ibata, R., Martin, N. F., Irwin, M., et al. 2007, ApJ, 671, 1591

Ibata, R. A., Gilmore, G., & Irwin, M. J. 1994, Nature, 370, 194

Ibata, R. A., Malhan, K., & Martin, N. F. 2019, ApJ, 872, 152

Ivarsson, S., Andersen, J., Nordström, B., et al. 2003, A&A, 409, 1141

Ivezić, Ž., Kahn, S. M., Tyson, J. A., et al. 2019, ApJ, 873, 111

Jayasinghe, T., Stanek, K. Z., Kochanek, C. S., et al. 2019, MNRAS, 485, 961

Ji, A. P., Drout, M. R., & Hansen, T. T. 2019, ApJ, 882, 40

Jofré, P., Heiter, U., & Soubiran, C. 2019, ARA&A, 57, 571

Jofré, P., Heiter, U., Soubiran, C., et al. 2015, A&A, 582, A81

Jofré, P., Heiter, U., Soubiran, C., et al. 2014, A&A, 564, A133

Johnson, C. I. & Pilachowski, C. A. 2012, ApJ, 754, L38

Johnson, H. L. & Morgan, W. W. 1953, ApJ, 117, 313

Jones, A., Noll, S., Kausch, W., Szyszka, C., & Kimeswenger, S. 2013, A&A, 560, A91

Jordi, K. & Grebel, E. K. 2010, A&A, 522, A71

Kacharov, N., Koch, A., & McWilliam, A. 2013, A&A, 554, A81

Kaiser, N., Burgett, W., Chambers, K., et al. 2010, Society of Photo-Optical Instrumentation Engineers (SPIE) Conference Series, Vol. 7733, The Pan-STARRS wide-field optical/NIR imaging survey, 77330E

Karakas, A. I. & Lattanzio, J. C. 2014, PASA, 31, e030

Karovicova, I., White, T. R., Nordlander, T., et al. 2018, MNRAS, 475, L81

Kelson, D. D. 2003, PASP, 115, 688

Kim, D.-W. & Bailer-Jones, C. A. L. 2016, A&A, 587, A18

Kirchhoff, G. 1860, Annalen der Physik, 185, 275

Kirchhoff, G. & Bunsen, R. 1860, Annalen der Physik, 186, 161

Kjeldsen, H. & Bedding, T. R. 1995, A&A, 293, 87

Kobayashi, C., Leung, S.-C., & Nomoto, K. 2019, arXiv e-prints, arXiv:1906.09980

Koch, A., Grebel, E. K., Gilmore, G. F., et al. 2008a, AJ, 135, 1580

Koch, A., Hanke, M., & Kacharov, N. 2018, A&A, 616, A74

Koch, A., Kunder, A., & Wojno, J. 2017, A&A, 605, A128

Koch, A. & McWilliam, A. 2008, AJ, 135, 1551

Koch, A. & McWilliam, A. 2010, AJ, 139, 2289

Koch, A. & McWilliam, A. 2011, AJ, 142, 63

Koch, A. & McWilliam, A. 2014, A&A, 565, A23

Koch, A., McWilliam, A., Preston, G. W., & Thompson, I. B. 2016, A&A, 587, A124

Koch, A., Reichert, M., Hansen, C. J., et al. 2019, A&A, 622, A159

Koch, A., Rich, R. M., Reitzel, D. B., et al. 2008b, ApJ, 689, 958

Kochukhov, O. P. 2007, in Physics of Magnetic Stars, ed. I. I. Romanyuk, D. O. Kudryavtsev, O. M. Neizvestnaya, & V. M. Shapoval, 109–118

Koppelman, H., Helmi, A., & Veljanoski, J. 2018, ApJ, 860, L11

Koppelman, H. H., Helmi, A., Massari, D., Roelenga, S., & Bastian, U. 2019, A&A, 625, A5

Korotin, S., Andrievsky, S., Caffau, E., & Bonifacio, P. 2017, in Astronomical Society of the Pacific Conference Series, Vol. 510, Stars: From Collapse to Collapse, ed. Y. Y. Balega, D. O. Kudryavtsev, I. I. Romanyuk, & I. A. Yakunin, 141

Korotin, S. A. 2008, Odessa Astronomical Publications, 21, 42

Korotin, S. A. 2009, Astronomy Reports, 53, 651

Korotin, S. A., Andrievsky, S. M., & Zhukova, A. V. 2018, MNRAS, 480, 965

Kovtyukh, V. V., Soubiran, C., Belik, S. I., & Gorlova, N. I. 2003, A&A, 411, 559

Kraft, R. P. 1979, ARA&A, 17, 309

Kramida, A., Yu. Ralchenko, Reader, J., & and NIST ASD Team. 2018, NIST Atomic Spectra Database (ver. 5.6.1), [Online]. Available: `https://physics.nist.gov/asd` [2019, August 19]. National Institute of Standards and Technology, Gaithersburg, MD.

Kratz, K.-L., Farouqi, K., Pfeiffer, B., et al. 2007, ApJ, 662, 39

Krause, M., Charbonnel, C., Decressin, T., Meynet, G., & Prantzos, N. 2013, A&A, 552, A121

Kruijssen, J. M. D. 2015, MNRAS, 454, 1658

Kruijssen, J. M. D., Pfeffer, J. L., Reina-Campos, M., Crain, R. A., & Bastian, N. 2019, MNRAS, 486, 3180

Kunder, A., Koch, A., Rich, R. M., et al. 2012, AJ, 143, 57

Kunder, A., Kordopatis, G., Steinmetz, M., et al. 2017, AJ, 153, 75

Kunder, A., Rich, R. M., Koch, A., et al. 2016, ApJ, 821, L25

Kundu, R., Minniti, D., & Singh, H. P. 2019, MNRAS, 483, 1737

Kurucz, R. L. 1993, SYNTHE spectrum synthesis programs and line data

Kurucz, R. L. & Bell, B. 1995, Atomic line list

Kuzma, P. B., Da Costa, G. S., & Mackey, A. D. 2018, MNRAS, 473, 2881

Kuzma, P. B., Da Costa, G. S., Mackey, A. D., & Roderick, T. A. 2016, MNRAS, 461, 3639

Kwiatkowski, M., Zimmermann, P., Biemont, E., & Grevesse, N. 1982, A&A, 112, 337

Lambert, D. L., Smith, V. V., Busso, M., Gallino, R., & Straniero, O. 1995, ApJ, 450, 302

Langer, N., Heger, A., Wellstein, S., & Herwig, F. 1999, A&A, 346, L37

Lardo, C., Battaglia, G., Pancino, E., et al. 2016a, A&A, 585, A70

Lardo, C., Mucciarelli, A., & Bastian, N. 2016b, MNRAS, 457, 51

Lattimer, J. M. & Schramm, D. N. 1974, ApJ, 192, L145

Law, D. R. & Majewski, S. R. 2010a, ApJ, 718, 1128

Law, D. R. & Majewski, S. R. 2010b, ApJ, 714, 229

Lawler, J. E., Bonvallet, G., & Sneden, C. 2001a, ApJ, 556, 452

Lawler, J. E. & Dakin, J. T. 1989, Journal of the Optical Society of America B Optical Physics, 6, 1457

Lawler, J. E., den Hartog, E. A., Labby, Z. E., et al. 2007, ApJS, 169, 120

Lawler, J. E., Den Hartog, E. A., Sneden, C., & Cowan, J. J. 2006, ApJS, 162, 227

Lawler, J. E., Guzman, A., Wood, M. P., Sneden, C., & Cowan, J. J. 2013, ApJS, 205, 11

Lawler, J. E., Sneden, C., & Cowan, J. J. 2004, ApJ, 604, 850

Lawler, J. E., Sneden, C., Cowan, J. J., Ivans, I. I., & Den Hartog, E. A. 2009, ApJS, 182, 51

Lawler, J. E., Sneden, C., Cowan, J. J., et al. 2008, ApJS, 178, 71

Lawler, J. E., Wickliffe, M. E., Cowley, C. R., & Sneden, C. 2001b, ApJS, 137, 341

Lawler, J. E., Wickliffe, M. E., den Hartog, E. A., & Sneden, C. 2001c, ApJ, 563, 1075

Lawler, J. E., Wood, M. P., Den Hartog, E. A., et al. 2014, ApJS, 215, 20

Lawler, J. E., Wyart, J.-F., & Blaise, J. 2001d, ApJS, 137, 351

Lee, Y. S., Beers, T. C., Allende Prieto, C., et al. 2011, AJ, 141, 90

Lee, Y. S., Beers, T. C., Sivarani, T., et al. 2008a, AJ, 136, 2022

Lee, Y. S., Beers, T. C., Sivarani, T., et al. 2008b, AJ, 136, 2050

Lemasle, B., François, P., Piersimoni, A., et al. 2008, A&A, 490, 613

Li, H., Shen, X., Liang, S., Cui, W., & Zhang, B. 2013, PASP, 125, 143

Lightkurve Collaboration, Cardoso, J. V. d. M., Hedges, C., et al. 2018, Lightkurve: Kepler and TESS time series analysis in Python, Astrophysics Source Code Library

Lind, K., Asplund, M., Barklem, P. S., & Belyaev, A. K. 2011, A&A, 528, A103

Lind, K., Bergemann, M., & Asplund, M. 2012, MNRAS, 427, 50

Lind, K., Korn, A. J., Barklem, P. S., & Grundahl, F. 2008, A&A, 490, 777

Lindegren, L., Hernández, J., Bombrun, A., et al. 2018, A&A, 616, A2

Ljung, G., Nilsson, H., Asplund, M., & Johansson, S. 2006, A&A, 456, 1181

Lodders, K. 2003, ApJ, 591, 1220

Ludwig, H. G., Caffau, E., Steffen, M., Bonifacio, P., & Sbordone, L. 2010, A&A, 509, A84

Lugaro, M., Karakas, A. I., Stancliffe, R. J., & Rijs, C. 2012, ApJ, 747, 2

Luo, A.-L., Zhao, Y.-H., Zhao, G., et al. 2015, Research in Astronomy and Astrophysics, 15, 1095

Mackey, A. D. & van den Bergh, S. 2005, MNRAS, 360, 631

Magic, Z., Collet, R., Asplund, M., et al. 2013, A&A, 557, A26

Majewski, S. R., APOGEE Team, & APOGEE-2 Team. 2016, Astronomische Nachrichten, 337, 863

Majewski, S. R., Schiavon, R. P., Frinchaboy, P. M., et al. 2017, AJ, 154, 94

Malaney, R. A. 1986, MNRAS, 223, 683

Malhan, K., Ibata, R. A., Carlberg, R. G., Valluri, M., & Freese, K. 2019, ApJ, 881, 106

Malhan, K., Ibata, R. A., & Martin, N. F. 2018, MNRAS, 481, 3442

Mamajek, E. E., Torres, G., Prsa, A., et al. 2015, ArXiv e-prints [`arXiv:1510.06262`]

Marigo, P., Girardi, L., Bressan, A., et al. 2017, ApJ, 835, 77

Martell, S. L. & Grebel, E. K. 2010, A&A, 519, A14

Martell, S. L., Shetrone, M. D., Lucatello, S., et al. 2016, ApJ, 825, 146

Martell, S. L., Smolinski, J. P., Beers, T. C., & Grebel, E. K. 2011, A&A, 534, A136

Martin, G., Fuhr, J., & Wiese, W. 1988, J. Phys. Chem. Ref. Data Suppl., 17, 17

Martin, N. F., Ibata, R. A., McConnachie, A. W., et al. 2013, ApJ, 776, 80

Martocchia, S., Dalessandro, E., Lardo, C., et al. 2019, MNRAS, 487, 5324

Mashonkina, L., Gehren, T., Shi, J.-R., Korn, A. J., & Grupp, F. 2011, A&A, 528, A87

Mashonkina, L. I. & Belyaev, A. K. 2019, Astronomy Letters, 45, 341

Masseron, T., Merle, T., & Hawkins, K. 2016, BACCHUS: Brussels Automatic Code for Characterizing High accUracy Spectra

Masseron, T., Plez, B., Van Eck, S., et al. 2014, A&A, 571, A47

Matteucci, F. & Brocato, E. 1990, ApJ, 365, 539

Mayor, M., Pepe, F., Queloz, D., et al. 2003, The Messenger, 114, 20

Mayor, M. & Queloz, D. 1995, Nature, 378, 355

McWilliam, A. 1997, ARA&A, 35, 503

McWilliam, A. 1998, AJ, 115, 1640

McWilliam, A., Preston, G. W., Sneden, C., & Searle, L. 1995, AJ, 109, 2757

McWilliam, A. & Zoccali, M. 2010, ApJ, 724, 1491

Meggers, W. F., Corliss, C. H., & Scribner, B. F. 1975, Tables of spectral-line intensities. Part I, II_- arranged by elements.

Merrill, P. W. 1952, ApJ, 116, 21

Meyer, B. S. 1994, ARA&A, 32, 153

Migdalek, J. 1978, J. Quant. Spectr. Rad. Transf., 20, 81

Milone, A. P., Marino, A. F., Renzini, A., et al. 2018, MNRAS, 481, 5098

Milone, A. P., Piotto, G., Renzini, A., et al. 2017, MNRAS, 464, 3636

Minchev, I. & Famaey, B. 2010, ApJ, 722, 112

Minniti, D., Geisler, D., Alonso-García, J., et al. 2017, ApJ, 849, L24

Mishenina, T., Gorbaneva, T., Pignatari, M., Thielemann, F.-K., & Korotin, S. A. 2015, MNRAS, 454, 1585

Momany, Y., Zaggia, S., Gilmore, G., et al. 2006, A&A, 451, 515

Mosser, B., Goupil, M. J., Belkacem, K., et al. 2012a, A&A, 548, A10

Mosser, B., Goupil, M. J., Belkacem, K., et al. 2012b, A&A, 540, A143

Mösta, P., Roberts, L. F., Halevi, G., et al. 2018, ApJ, 864, 171

Mucciarelli, A., Merle, T., & Bellazzini, M. 2017, A&A, 600, A104

Muraveva, T., Delgado, H. E., Clementini, G., Sarro, L. M., & Garofalo, A. 2018, MNRAS, 481, 1195

Myeong, G. C., Evans, N. W., Belokurov, V., Sand ers, J. L., & Koposov, S. E. 2018, ApJ, 863, L28

Myeong, G. C., Vasiliev, E., Iorio, G., Evans, N. W., & Belokurov, V. 2019, MNRAS, 488, 1235

Navin, C. A., Martell, S. L., & Zucker, D. B. 2016, ApJ, 829, 123

Neeley, J. R., Marengo, M., Bono, G., et al. 2017, ApJ, 841, 84

Ness, M., Freeman, K., Athanassoula, E., et al. 2013a, MNRAS, 430, 836

Ness, M., Freeman, K., Athanassoula, E., et al. 2013b, MNRAS, 432, 2092

Ness, M., Freeman, K., Athanassoula, E., et al. 2012, ApJ, 756, 22

Ness, M., Hogg, D. W., Rix, H.-W., Ho, A. Y. Q., & Zasowski, G. 2015, ApJ, 808, 16

Nilsson, H., Ivarsson, S., Johansson, S., & Lundberg, H. 2002a, A&A, 381, 1090

Nilsson, H., Zhang, Z. G., Lundberg, H., Johansson, S., & Nordström, B. 2002b, A&A, 382, 368

Nissen, P. E. 2015, A&A, 579, A52

Nissen, P. E., Akerman, C., Asplund, M., et al. 2007, A&A, 469, 319

Nitz, D. E., Wickliffe, M. E., & Lawler, J. E. 1998, ApJS, 117, 313

Noll, S., Kausch, W., Barden, M., et al. 2012, A&A, 543, A92

Nomoto, K., Tominaga, N., Umeda, H., Kobayashi, C., & Maeda, K. 2006, Nucl. Phys. A, 777, 424

Nordlander, T. & Lind, K. 2017, A&A, 607, A75

Norris, J. E., Yong, D., Venn, K. A., et al. 2017, ApJS, 230, 28

O'Brian, T. R., Wickliffe, M. E., Lawler, J. E., Whaling, W., & Brault, J. W. 1991, Journal of the Optical Society of America B Optical Physics, 8, 1185

O'Connell, J. E., Johnson, C. I., Pilachowski, C. A., & Burks, G. 2011, PASP, 123, 1139

Odenkirchen, M., Grebel, E. K., Rockosi, C. M., et al. 2001, ApJ, 548, L165

Önehag, A., Gustafsson, B., Eriksson, K., & Edvardsson, B. 2009, A&A, 498, 527

Pancino, E., Romano, D., Tang, B., et al. 2017, A&A, 601, A112

Parkinson, W. H., Reeves, E. M., & Tomkins, F. S. 1976, Journal of Physics B Atomic Molecular Physics, 9, 157

Pasquini, L., Avila, G., Allaert, E., et al. 2000, in Proc. SPIE, Vol. 4008, Optical and IR Telescope Instrumentation and Detectors, ed. M. Iye & A. F. Moorwood, 129–140

Pehlivan Rhodin, A., Hartman, H., Nilsson, H., & Jönsson, P. 2017, A&A, 598, A102

Penzias, A. A. & Wilson, R. W. 1965, ApJ, 142, 419

Pérez-Mesa, V., Zamora, O., García-Hernández, D. A., et al. 2017, A&A, 606, A20

Pian, E., D'Avanzo, P., Benetti, S., et al. 2017, Nature, 551, 67

Pickering, J. C., Thorne, A. P., & Perez, R. 2001, ApJS, 132, 403

Piersanti, L., Cristallo, S., & Straniero, O. 2013, ApJ, 774, 98

Pignatari, M., Gallino, R., Heil, M., et al. 2010, ApJ, 710, 1557

Pillepich, A., Madau, P., & Mayer, L. 2015, ApJ, 799, 184

Pinnington, E. H., Ji, Q., Guo, B., et al. 1993, Canadian Journal of Physics, 71, 470

Piotto, G., Bedin, L. R., Anderson, J., et al. 2007, ApJ, 661, L53

Piskunov, N. E., Kupka, F., Ryabchikova, T. A., Weiss, W. W., & Jeffery, C. S. 1995, A&AS, 112, 525

Pitts, R. E. & Newsom, G. H. 1986, J. Quant. Spectr. Rad. Transf., 35, 383

Placco, V. M., Frebel, A., Beers, T. C., et al. 2016, ApJ, 833, 21

Planck, M. 1901, Annalen der Physik, 309, 553

Planck Collaboration, Akrami, Y., Arroja, F., et al. 2018, arXiv e-prints, arXiv:1807.06205

Plez, B. 2012, Turbospectrum: Code for spectral synthesis

Poggio, E., Drimmel, R., Andrae, R., et al. 2020, Nature Astronomy [`arXiv:1912.10471`]

Pojmanski, G. 2002, Acta Astron., 52, 397

Pourbaix, D., Nidever, D., McCarthy, C., et al. 2002, A&A, 386, 280

Prantzos, N., Abia, C., Cristallo, S., Limongi, M., & Chieffi, A. 2019, MNRAS, 2748

Prantzos, N., Charbonnel, C., & Iliadis, C. 2007, A&A, 470, 179

Prantzos, N., Charbonnel, C., & Iliadis, C. 2017, A&A, 608, A28

Preston, G. W., Sneden, C., Chadid, M., Thompson, I. B., & Shectman, S. A. 2019, AJ, 157, 153

Prugniel, P. & Soubiran, C. 2001, A&A, 369, 1048

Prugniel, P., Soubiran, C., Koleva, M., & Le Borgne, D. 2007, ArXiv Astrophysics e-prints [`astro-ph/0703658`]

Prša, A., Harmanec, P., Torres, G., et al. 2016, AJ, 152, 41

Queloz, D., Henry, G. W., Sivan, J. P., et al. 2001, A&A, 379, 279

Raassen, A. J. J. & Uylings, P. H. M. 1998, A&A, 340, 300, (RU)

Raiteri, C. M., Busso, M., Gallino, R., & Picchio, G. 1991, ApJ, 371, 665

Ramírez, I., Allende Prieto, C., Redfield, S., & Lambert, D. L. 2006, A&A, 459, 613

Ramírez, I. & Meléndez, J. 2005, ApJ, 626, 446

Ramírez, I. & Meléndez, J. 2005, ApJ, 626, 465

Rauer, H., Catala, C., Aerts, C., et al. 2014, Experimental Astronomy, 38, 249

Recio-Blanco, A., Bijaoui, A., & de Laverny, P. 2006, MNRAS, 370, 141

Reichert, M., Hansen, C. J., Hanke, M., et al. 2020, arXiv e-prints, arXiv:2004.01195

Reina-Campos, M., Hughes, M. E., Kruijssen, J. M. D., et al. 2020, MNRAS, 493, 3422

Rich, R. M. 2013, The Galactic Bulge, ed. T. D. Oswalt & G. Gilmore, Vol. 5, 271

Ricker, G. R., Winn, J. N., Vanderspek, R., et al. 2015, Journal of Astronomical Telescopes, Instruments, and Systems, 1, 014003

Riley, A. H. & Strigari, L. E. 2020, MNRAS [`arXiv:2001.11564`]

Roederer, I. U. 2012, ApJ, 756, 36

Roederer, I. U., Hattori, K., & Valluri, M. 2018a, AJ, 156, 179

Roederer, I. U., Karakas, A. I., Pignatari, M., & Herwig, F. 2016, ApJ, 821, 37

Roederer, I. U., Kratz, K.-L., Frebel, A., et al. 2009, ApJ, 698, 1963

Roederer, I. U., Preston, G. W., Thompson, I. B., et al. 2014, AJ, 147, 136 (R14)

Roederer, I. U., Sakari, C. M., Placco, V. M., et al. 2018b, ApJ, 865, 129

Roederer, I. U., Sneden, C., Lawler, J. E., & Cowan, J. J. 2010, ApJ, 714, L123

Ryabchikova, T., Piskunov, N., Kurucz, R. L., et al. 2015, Phys. Scr, 90, 054005

Ryabchikova, T. A., Hill, G. M., Landstreet, J. D., Piskunov, N., & Sigut, T. A. A. 1994, MNRAS, 267, 697

Sakari, C. M., Placco, V. M., Farrell, E. M., et al. 2018, ApJ, 868, 110

Salgado, C., Da Costa, G. S., Norris, J. E., & Yong, D. 2019, MNRAS, 484, 3093

Savino, A., Massari, D., Bragaglia, A., Dalessandro, E., & Tolstoy, E. 2018, MNRAS, 474, 4438

Savino, A. & Posti, L. 2019, A&A, 624, L9

Schatz, H., Toenjes, R., Pfeiffer, B., et al. 2002, ApJ, 579, 626

Schiavon, R. P., Zamora, O., Carrera, R., et al. 2017, MNRAS, 465, 501

Schlafly, E. F. & Finkbeiner, D. P. 2011, ApJ, 737, 103

Schnabel, R., Schultz-Johanning, M., & Kock, M. 2004, A&A, 414, 1169

Schuler, S. C., King, J. R., & The, L.-S. 2009, ApJ, 701, 837

Searle, L. & Zinn, R. 1978, ApJ, 225, 357

Sesar, B. 2012, AJ, 144, 114

Shen, J., Rich, R. M., Kormendy, J., et al. 2010, ApJ, 720, L72

Shi, J. R., Yan, H. L., Zhou, Z. M., & Zhao, G. 2018, ApJ, 862, 71

Shirai, T., Reader, J., Kramida, A. E., & Sugar, J. 2007, Journal of Physical and Chemical Reference Data, 36, 509

Siess, L., Goriely, S., & Langer, N. 2004, A&A, 415, 1089

Sigut, T. A. A. & Landstreet, J. D. 1990, MNRAS, 247, 611

Siqueira Mello, C., Spite, M., Barbuy, B., et al. 2013, A&A, 550, A122

Sitnova, T. M., Mashonkina, L. I., & Ryabchikova, T. A. 2013, Astronomy Letters, 39, 126

Sitnova, T. M., Mashonkina, L. I., & Ryabchikova, T. A. 2016, MNRAS, 461, 1000

Sivarani, T., Bonifacio, P., Molaro, P., et al. 2004, A&A, 413, 1073

Skrutskie, M. F., Cutri, R. M., Stiening, R., et al. 2006, AJ, 131, 1163

Smiljanic, R., Korn, A. J., Bergemann, M., et al. 2014, A&A, 570, A122

Smith, G. 1981, A&A, 103, 351

Smith, G. 1988, Journal of Physics B Atomic Molecular Physics, 21, 2827

Smith, G. & O'Neill, J. A. 1975, A&A, 38, 1

Smith, G. & Raggett, D. S. J. 1981, Journal of Physics B Atomic Molecular Physics, 14, 4015

Smith, G. H. & Dopita, M. A. 1983, ApJ, 271, 113

Smith, V. V. & Lambert, D. L. 1988, ApJ, 333, 219

Smith, W. H. & Liszt, H. S. 1971, Journal of the Optical Society of America (1917-1983), 61, 938

Smolec, R. & Moskalik, P. 2008, Acta Astron., 58, 193

Smolinski, J. P., Lee, Y. S., Beers, T. C., et al. 2011, AJ, 141, 89

Sneden, C., Cowan, J. J., & Gallino, R. 2008, ARA&A, 46, 241

Sneden, C., Cowan, J. J., Lawler, J. E., et al. 2003, ApJ, 591, 936

Sneden, C., Kraft, R. P., Guhathakurta, P., Peterson, R. C., & Fulbright, J. P. 2004, AJ, 127, 2162

Sneden, C., Lawler, J. E., Cowan, J. J., Ivans, I. I., & Den Hartog, E. A. 2009, ApJS, 182, 80

Sneden, C., Preston, G. W., Chadid, M., & Adamów, M. 2017, ApJ, 848, 68

Sneden, C. A. 1973, Carbon and Nitrogen Abundances in Metal-Poor Stars., PhD thesis, THE UNIVERSITY OF TEXAS AT AUSTIN.

Sobeck, J. S., Kraft, R. P., Sneden, C., et al. 2011, AJ, 141, 175

Sobeck, J. S., Lawler, J. E., & Sneden, C. 2007, ApJ, 667, 1267

Sohn, S. T., Watkins, L. L., Fardal, M. A., et al. 2018, ApJ, 862, 52

Soker, N. 2019, arXiv e-prints, arXiv:1912.01550

Soubiran, C., Jasniewicz, G., Chemin, L., et al. 2018, A&A, 616, A7

Sousa, S. G., Adibekyan, V., Delgado-Mena, E., et al. 2018, A&A, 620, A58

Spergel, D. N., Verde, L., Peiris, H. V., et al. 2003, ApJS, 148, 175

Spite, M., Cayrel, R., Hill, V., et al. 2006, A&A, 455, 291

Spite, M., Cayrel, R., Plez, B., et al. 2005, A&A, 430, 655

Stanek, K. Z., Mateo, M., Udalski, A., et al. 1994, ApJ, 429, L73

Steigman, G. 2010, J. Cosmology Astropart. Phys., 2010, 029

Steinmetz, M., Zwitter, T., Siebert, A., et al. 2006, AJ, 132, 1645

Stetson, P. B. & Pancino, E. 2008, PASP, 120, 1332

Straniero, O., Gallino, R., Busso, M., et al. 1995, ApJ, 440, L85

Straniero, O., Gallino, R., & Cristallo, S. 2006, Nucl. Phys. A, 777, 311

Strömgren, B. 1966, ARA&A, 4, 433

Tanabashi, M., Hagiwara, K., Hikasa, K., et al. 2018, Phys. Rev. D, 98, 030001

Testa, V., Zaggia, S. R., Andreon, S., et al. 2000, A&A, 356, 127

Ting, Y.-S., Conroy, C., Rix, H.-W., & Cargile, P. 2019, ApJ, 879, 69

Tonry, J. & Davis, M. 1979, AJ, 84, 1511

Travaglio, C., Gallino, R., Arnone, E., et al. 2004, ApJ, 601, 864

Tyson, J. A. 2002, Society of Photo-Optical Instrumentation Engineers (SPIE) Conference Series, Vol. 4836, Large Synoptic Survey Telescope: Overview, ed. J. A. Tyson & S. Wolff, 10–20

Uitenbroek, H. 1998, ApJ, 498, 427

Valenti, J. A. & Piskunov, N. 1996, A&AS, 118, 595

van Raai, M. A., Lugaro, M., Karakas, A. I., García-Hernández, D. A., & Yong, D. 2012, A&A, 540, A44

VandenBerg, D. A., Brogaard, K., Leaman, R., & Casagrande, L. 2013, ApJ, 775, 134

Vasiliev, E. 2019, MNRAS, 484, 2832

Velichko, A. B., Mashonkina, L. I., & Nilsson, H. 2010, Astronomy Letters, 36, 664

Venn, K. A., Irwin, M., Shetrone, M. D., et al. 2004, AJ, 128, 1177

Villanova, S., Monaco, L., Moni Bidin, C., & Assmann, P. 2016, MNRAS, 460, 2351

Wanajo, S. 2013, ApJ, 770, L22

Warner, B. 1968a, MNRAS, 139, 115

Warner, B. 1968b, MNRAS, 140, 53

Watkins, L. L., Evans, N. W., Belokurov, V., et al. 2009, MNRAS, 398, 1757

Watson, D., Hansen, C. J., Selsing, J., et al. 2019, Nature, 574, 497

Wegg, C. & Gerhard, O. 2013, MNRAS, 435, 1874

Werner, K. & Herwig, F. 2006, PASP, 118, 183

Whaling, W. & Brault, J. W. 1988, Phys. Scr, 38, 707

Wickliffe, M. E. & Lawler, J. E. 1997, Journal of the Optical Society of America B Optical Physics, 14, 737

Wickliffe, M. E., Lawler, J. E., & Nave, G. 2000, J. Quant. Spectr. Rad. Transf., 66, 363

Wickliffe, M. E., Salih, S., & Lawler, J. E. 1994, J. Quant. Spectr. Rad. Transf., 51, 545

Wien, W. 1893, Annalen der Physik, 285, 633

Wiescher, M., Käppeler, F., & Langanke, K. 2012, ARA&A, 50, 165

Wiese, W. L., Smith, M. W., & Glennon, B. M. 1966, Atomic transition probabilities. Vol.: Hydrogen through Neon. A critical data compilation

Wiese, W. L., Smith, M. W., & Miles, B. M. 1969, Atomic transition probabilities. Vol. 2: Sodium through Calcium. A critical data compilation

Wilson, O. C. & Vainu Bappu, M. K. 1957, ApJ, 125, 661

Wood, M. P., Lawler, J. E., Den Hartog, E. A., Sneden, C., & Cowan, J. J. 2014a, ApJS, 214, 18

Wood, M. P., Lawler, J. E., Sneden, C., & Cowan, J. J. 2013, ApJS, 208, 27

Wood, M. P., Lawler, J. E., Sneden, C., & Cowan, J. J. 2014b, ApJS, 211, 20

Woosley, S. E. & Weaver, T. A. 1995, ApJS, 101, 181

Yan, H. L., Shi, J. R., & Zhao, G. 2015, ApJ, 802, 36

Yang, J., Turner, M. S., Steigman, G., Schramm, D. N., & Olive, K. A. 1984, ApJ, 281, 493

Yanny, B., Rockosi, C., Newberg, H. J., et al. 2009, AJ, 137, 4377

Yong, D., Roederer, I. U., Grundahl, F., et al. 2014, MNRAS, 441, 3396

York, D. G., Adelman, J., Anderson, John E., J., et al. 2000, AJ, 120, 1579

Youakim, K., Starkenburg, E., Martin, N. F., et al. 2020, MNRAS, 492, 4986

Yuan, H. B., Liu, X. W., & Xiang, M. S. 2013, MNRAS, 430, 2188

Zacharias, N., Finch, C. T., Girard, T. M., et al. 2013, AJ, 145, 44

Zennaro, M., Milone, A. P., Marino, A. F., et al. 2019, MNRAS, 487, 3239

Zhao, G., Zhao, Y.-H., Chu, Y.-Q., Jing, Y.-P., & Deng, L.-C. 2012, Research in Astronomy and Astrophysics, 12, 723

Zinn, R. 1993, Astronomical Society of the Pacific Conference Series, Vol. 48, The Galactic Halo Cluster Systems: Evidence for Accretion, ed. G. H. Smith & J. P. Brodie, 38

Zoccali, M., Hill, V., Lecureur, A., et al. 2008, A&A, 486, 177

Zoccali, M., Renzini, A., Ortolani, S., et al. 2003, A&A, 399, 931

Zolotov, A., Willman, B., Brooks, A. M., et al. 2009, ApJ, 702, 1058

> *"Wrong! Do it again!*
> *Wrong! Do it again!*
> *If you don't eat your meat you can't have any pudding!*
> *How can you have any pudding if you don't eat your meat?"*
>
> Another Brick In The Wall, PINK FLOYD

Acknowledgements

There is a considerable number of people I would like to thank, without whom this thesis would probably have been finished half a year ago and be twice as thorough. All jokes aside, I am eternally grateful to so many people that I am seriously worried about forgetting any of you in my current, coffee-induced delirious state.

First and 4MOST, I would like to thank you, **Eva**, for providing a more than enjoyable and fruitful supervisor-supervisee atmosphere, for your confidence in my work, for the freedom to pursue my projects, and, not the least, for the financial support throughout these last four years. I am a bit sorry about how that window cleaning story turned out. But, on the other hand, I didn't get my bathtub filled with ru(h)m or a Batmobile, either. So I guess we are... even? Ouh yes and my deepest apologies, again, for you actually having to read this thing!

To **Camilla** and **Andreas**: I honestly have no idea how to thank the two of you in a manner that reflects how much I owe you (i.e., pretty much everything). I will at least try to lessen my debt with lots of "Modschaidos". **Camilla**, about 105.4% of this thesis would be entirely unthinkable without you coming up with the projects and providing patient guidance throughout. Thank you so much for all the science-related stuff but many times more for being a great friend! **Andreaaas**, (ne keine Angst diesmal leite ich damit keine last-minute Bitte zum Korrekturlesen ein) I just counted and it has been impressive six years already (another nine and... well you can guess the rest)! It has been a pleasure to have you as a friend, mentor, supervisor, thesis advisor, colleague, source for funny comics and definitely not funny jokes, etc. pp., schleim schleim, und niemals vergessen: Nudeln stinken beim Kochen nicht so doll und werden auch weicher wenn man in den Topf ein bisschen Wasser macht. for so many years. Vice versa, it tells a lot about my teaching skills that it took me as long to convince you that Python is not some witches' brew... Even though you crossed out my "ironischsten Blödsinn", I am very grateful that you spent so much time for proofreading major parts of this thesis and for providing invaluable comments.

I further would like to thank **Norbert Christlieb** for agreeing to be a referee of this thesis, and **Björn Malte Schäfer** and **Mario Trieloff** for being part in my board of examiners. A warm thank you goes out to **Anna** for taking part in my thesis committee and therefore helping to keep these projects on track.

To **my family, Mama, Papa, Marcel, Oma** and **Opa** (wherever you are now), I am forever grateful for your constant love and support and for always being there for me.

To **Zdenek** (a.k.a. my Jägermeister buddy): Dude, this is the second time you had a major contribution to one of my theses, be it due to being an amazing friend and colleague or because you actually wrote an entire section! I wouldn't want to miss a single one of our sessions with batshit crazy discussions about all kinds of things in life. You're the best office mate one could think of. In a sense, I guess you are the worst one, too, because let's face it: Our constant, mutually reinforced, pedantic OCDing the s**t out of things (mostly plots) doesn't exactly localize us on the mentally healthy part of the normal distribution, but hey, at least we're having lots of fun in the process!

To **Shahrzad** and **Sergej**, thank you for always being there for me, not only but especially in the current times. You are my oldest and best friends in Heidelberg and my life would be a much sadder place without you guys in it.

To **Jonas**, thank you for our amazing coffee breaks, for our football sessions, for being my swimming buddy (I hope we can do that again, soon), and for being a true friend!

To **Paula**, thanks for making sure I didn't get dehydrated by remotely checking that I had enough liquid consumption (beer) during these final stages of writing my thesis.

To **Faezeh**, NOPE!

To **Bertrand**, thank you for our extended coffee... I am a bit hesitant to call them breaks... let's say... marathons? I am having a great time talking and working with you and I think we have a very productive collaboration going there :-)

To the **greatest office ARI has to offer, Bahar, Gustavo,** and (well, again) **Zdenek**. I enjoyed spending major parts of my days with you guys. Thank you for making ARI such a special (you guys know how I would have pronounced this one ;-)) place to be.

To the **ARI Gang (Jonas, Matteo, Marta, Sarah,** and **Zdenek)** and the "cool" **MPIA peeps (Asmita, Manuel,** and **Paula)**, thank you for being such an amazing group of people to spend time with. I sincerely hope we will have the chance to revive our legendary music nights, soon!

To **Chantal, Tanja, Johann,** and **Markus**, Ich bin ein Grashüpfer!

To **Marcö** and **Prestel**, thank you for staying in contact and keeping our friendship going even after so many years. This kitesurfing thing is not entirely dead yet... just postponed for who knows how long...

Finally, I would like to acknowledge financial support by the Deutsche Forschungsgemeinschaft (DFG, German Research Foundation) – SFB 881 ("The Milky Way System").

“Where I go I do not know
I only know the place I’ve been
Dreams they come and go, ever shall be so
Nothing’s real until you feel”

Ghost of the Navigator, IRON MAIDEN